ELECTROCHEMICAL AND SOLAR PHOTOELECTROCATALYTIC OXIDATION OF SELECTED ORGANIC COMPOUNDS AT CARBON-SEMICONDUCTOR BASED ELECTRODES

by

MOSES GBENGA PELEYEJU

Student Number: 201495046

Dissertation in fulfilment of the requirement for the degree of

PHILOSOPHIAE DOCTOR

in

CHEMISTRY

in the

FACULTY OF SCIENCE

of the

UNIVERSITY OF JOHANNESBURG

Supervisor : PROF. O. A. AROTIBA

Co-supervisor : PROF. J. O. BABALOLA

OCTOBER 2017

DECLARATION

I hereby declare that this dissertation, which I herewith submit for the research qualification

PHILOSOPHIAE DOCTOR IN CHEMISTRY

to the University of Johannesburg, Department of Applied Chemistry, is, apart from the recognised assistance of my supervisors, my own work and has not previously been submitted by me to another institution to obtain a research diploma or degree.

_____ on this ____ day of _____

(Candidate)

_____ on this ____ day of _____

(Supervisor)

_____ on this ____ day of _____

(Co-supervisor)

_____ on this ____ day of _____

(Co-supervisor)

DEDICATION

This dissertation is dedicated to:

God, the Father of my Lord Jesus Christ

My mother, Mrs Phebean Morisola, and father, Mr Samson Akinremi Peleyeju

My wife, Mrs Grace Busayo Peleyeju

ACKNOWLEDGEMENTS

"Bless the LORD, O my soul, and forget not all his benefits... Who redeemeth thy life from destruction..." I have come this far only by the grace of the LORD. Thank you Father for bringing the plan to pass.

I am immensely grateful to my supervisors:

Prof. Omotayo Ademola Arotiba for his academic mentorship, for believing in me and for supporting me and my immediate family beyond the call of a PhD advisor. I must appreciate you for the several hours you gave, the love you demonstrated and the understanding you showed in the course of the journey. Thank you for being such a great blessing. May the good Lord continue to prosper you and all yours.

Prof. Jonathan Oyebamiji Babalola for his intellectual and moral contributions to the success of this PhD. You stood and acted when it was needed most. Thank you for your understanding and care. My story would be incomplete without a mention of you.

My heartfelt gratitude goes to my mother, Mrs Phebean Morisola Peleyeju, for her numerous sacrifices for my cause.

My wife, Mrs Grace Busayo Peleyeju, is gratefully acknowledged for her understanding and contributions to the realisation of this goal. Thank you for being there. My Son, Babalola and daughter, Babanifemi are also appreciated for bearing with daddy when he was 'immersed' in research.

My pastor, Dr Tayo Ololade and his wife Dr (Mrs) Shola Ololade and the entire RCCG Celebration Centre, Auckland Park, JHB are appreciated for their prayers and supports.

I wish to thank all the academic, administrative and technical staff of the Department of Applied Chemistry, University of Johannesburg, who contributed to the success of my PhD programme.

All the members of the Electrochemistry Research Group, University of Johannesburg are appreciated for the precious time we had together.

I am thankful to the Nanotechnology Innovation Centre (NIC)/Mintek, South Africa, for funding my PhD.

PRESENTATIONS AND PUBLICATIONS

Presentations

The following are the academic meetings where the results in this dissertation have been presented:

1. Topical Meeting of the International Society of Electrochemistry, Electrochemical Properties and Applications of Advanced Carbon Materials, the Vila Gale Eco Resort of Angra dos Reis, Angra dos Reis, Brazil. 22-26 March, 2015. **Poster Presentation** "Electrochemical Application of Exfoliated Graphite-Diamond Mixed Carbon Electrodes in Water Treatment"
2. 3rd International Symposium on Electrochemistry **(**Materials, Analytical and Physical Electrochemistry Today), University of the Western Cape, Bellville, South Africa. 26-28 May, 2015. **Oral presentation** "Electrochemical oxidation of acid blue 40 at expanded graphite-diamond electrode"
3. 6th Annual DST/MINTEK NIC workshop, Rhodes University, Grahamstown, South Africa. 28-29 October, 2015. **Oral presentation** "Electrochemical degradation of synthetic dyes at mixed carbon electrode"
4. 67th Annual Meeting of the International Society of Electrochemistry, World Forum, The Hague, Netherlands. 21 - 26 August, 2016. **Poster presentation** "Oxidation of sulfamethoxazole at a carbon-titania electrode in a photoelectrochemical reactor"
5. 6th Annual Gauteng Nanosciences Young Researchers' Symposium, Conference Centre, Mintek, Randburg, South Africa. 18 November, 2016. **Oral presentation** "Photo-assisted electrochemical degradation of sulfamethoxazole at a carbon-titania nanocomposite anode"
6. 7th Annual DST/MINTEK NIC workshop, University of the Western Cape, SA Medical Research Council, Cape Town, South Africa. 25-26 January, 2017. **Poster**

presentation " Oxidation of sulfamethoxazole at a carbon-titania electrode in a photoelectrochemical reactor"

Publications

The following are the journal articles published as a PhD student. Articles 1, 2 and 3 form chapters 4, 5 and 6 respectively of this dissertation.

1. **MG Peleyeju**, EH Umukoro, JO Babalola, OA Arotiba (2016). Electrochemical degradation of an anthraquinonic dye on an expanded graphite-diamond composite electrode. *Electrocatalysis* 7:132-139
2. **MG Peleyeju,** EH Umukoro, JO Babalola, OA Arotiba (2017). Electrochemical detection of 2,4-dichlorophenol on a ternary composite of diamond, graphene and polyaniline. *ChemElectroChem 4 (5):1074-1080*
3. **MG Peleyeju**, EH Umukoro, L Tshwenya, R Moutloali, JO Babalola, OA Arotiba (2017). Photoelectrocatalytic water treatment systems: Degradation, kinetics and intermediate products studies of sulfamethoxazole on a TiO_2-exfoliated graphite electrode**.** *RSC Advances 7:40571-50580*
4. EH Umukoro, **MG Peleyeju**, JC Ngila, OA Arotiba (2016). Photocatalytic degradation of acid blue 74 in water using Ag–Ag_2O–ZnO nanostructures anchored on graphene oxide. *Solid State Sciences* 51: 66-73
5. B Ntsendwana, **MG Peleyeju**, OA Arotiba (2016). The application of exfoliated graphite electrode in the electrochemical degradation of *p*-nitrophenol in water. *Journal of Environmental Science and Health, Part A* 51:571-578
6. EH Umukoro, **MG Peleyeju**, JC Ngila, OA Arotiba (2016). Photoelectrochemical degradation of orange II dye in wastewater at a silver–zinc oxide/reduced graphene oxide nanocomposite photoanode. *RSC Advances* **6**:52868-52877

7. EH Umukoro, **MG Peleyeju**, JC Ngila, OA Arotiba (2017). Towards wastewater treatment: Photo-assisted electrochemical degradation of 2-nitrophenol and orange II dye at a tungsten trioxide-exfoliated graphite composite. *Chemical Engineering Journal 317:290-301*

Article to be submitted for publication

Photoelectrocatalytic Application Of CND/B-$BiVO_4$/WO_3 Nanostructured Electrode For Degradation Of Orange II Dye.

ABSTRACT

This study explored preparation, characterisation and applications of different types of carbon and metal oxide semiconductors-based anodes for the electrochemical/photoelectrocatalytic oxidation of some selected organic contaminants. Exfoliated graphite (EG), a form of carbon, was prepared by acids intercalation of natural graphite flakes and thermal treatment. Expanded graphite – diamond (EG-diamond) composite prepared by solution mixing of EG and diamond powder was fabricated into electrodes and characterised. Raman spectrometry and x-ray diffraction (XRD) patterns revealed peaks that are characteristic of EG and diamond. Scanning electron microscopy (SEM) images showed that the diamond particles were well dispersed within sheets of EG. Cyclic voltammetry (CV) showed that the EG electrode exhibited faster electron transfer while the composite electrode gave enhanced current peak. The electrolysis of acid blue 40 (AB 40) in 0.1 M Na_2SO_4 electrolyte resulted in ca. 80% dye removal at the EG-Diamond electrode and 66% removal at the pristine EG electrode at a current density of 20 $mAcm^{-2}$ after 4 h. However, in a chlorine mediated electrolysis (NaCl as supporting electrolyte), the decolourisation of the dye was very rapid with over 98% decolourisation in 25 min. The extent of mineralisation was measured by total organic carbon (TOC). EG-Diamond and EG electrodes yielded TOC removal of 44% and 26% respectively in the electrochemical cell with Na_2SO_4 supporting electrolyte. While NaCl cell presented faster decoulorisation, the TOC decay was much slower compared to the Na_2SO_4 cell. The degradation of AB 40 follows pseudo first-order kinetic model with apparent rate constants of 2.34×10^{-3} min^{-1} and 4.41×10^{-3} min^{-1} obtained at EG and EG-diamond electrodes respectively. The EG-diamond electrode was further applied in the degradation of orange II dye (OG II) and a mixture of OG II and AB 40 with a TOC removal of 49 % for the dye mixture.

Diamond-based material was further explored as a platform for electro-oxidation of organic molecules. A ternary composite electrode which consists of diamond, graphene and polyaniline was synthesised. The composite, obtained via oxidative polymerisation of aniline in the presence of graphene and diamond, was characterised by fourier transform infrared (FTIR) spectroscopy, Raman spectroscopy, XRD and Brunauer–Emmett–Teller (BET) surface area analyser. Glassy carbon electrode (GCE) was modified with the composite material and the electrochemical properties of the bare and modified electrodes were investigated using cyclic voltammetry, square wave voltammetry and electrochemical impedance spectroscopy. The results obtained showed that the modified electrode exhibited far better electrochemical properties than the bare GCE. Determination of 2,4-DCP in 0.1 M HNO_3 was carried using square wave voltammetry and the oxidation peak of the analyte was found to increase linearly with increasing concentration with a detection limit of 0.25 μM. The electrode exhibited antifouling capabilities during the electro-oxidation of 2,4-DCP. The sensor was utilised for the detection of 2,4-DCP in domestic wastewater.

To explore semiconductor-based anodes for photoelectrocatalytic degradation of organic contaminants, TiO_2-exfoliated graphite (TiO_2-EG) nanocomposite was synthesised by sol-gel and microwave methods. The materials were then characterised by XRD, Raman and FTIR spectroscopies, SEM and transmission electron microscopy (TEM). The cyclic voltammograms of the fabricated electrodes were obtained in $[Fe(CN)_6]^{3-}$ redox probe and the electron transfer kinetics was studied. Degradation of an antibiotic -, sulfamethoxazole - was carried out at the electrodes in the presence of simulated sunlight. Concentration abatement of the compound was monitored on UV-Visible spectrophotometer and the possible intermediates were investigated using liquid chromatography-mass spectrometry (LCMS). After 6 h of the photoelectrocatalytic process, almost 100% of the drug has been degraded and a 90%

COD decay was achieved. The photoelectrocatalytic degradation of sulfamethoxazole entailed γ-, β-, δ- and ε- cleavages, hydroxylation and rings opening.

A heterostructured photocatalyst comprising carbon nanodots (CND) and Boron co-doped $BiVO_4$ and WO_3 was also synthesised by hydrothermal method. The materials were characterised by Raman, FTIR, diffuse reflectance, energy dispersive x-ray spectroscopies and SEM and TEM. The catalysts were immobilised on treated titanium sheets by drop-casting. The fabricated electrodes were characterised by linear sweep voltammetry (LSV) and chronoamperometry. The diffuse reflectance spectroscopy of the catalysts reveals that the incorporation of CND and B into the structure of the monoclinic $BiVO_4$ enhanced its optical absorption. The LSV measurement carried out in 0.1 M Na_2SO_4 showed that the $BiVO_4$ and WO_3 based photoelectrode demonstrated significant photoactivity. The performance of the electrodes towards degradation of orange II sodium salt was in the order $BiVO_4$ < WO_3 < CND/B-$BiVO_4$ < CND/B-$BiVO_4$/WO_3. The apparent rate constants obtained by fitting the experimental data into the Langmuir Hinshelwood kinetic model are 0.0924, 0.1812, 0.254 and 0.845 h^{-1} for $BiVO_4$, WO_3, CND/B-$BiVO_4$ and CND/B-$BiVO_4$/WO_3 respectively. The COD abatement after 3 h of electrolysis at the best performing photoanode was 58%.

The outcomes of this study show that low-cost and easy-to-prepare anodes prepared from diamond and other relatively new forms of carbon are effective for the degradation of organic pollutants in water. In addition diamond-based anodes can serve as platforms for the sensitive determination of organic analytes. Furthermore, semiconductor-based anodes are effective for the destruction of emerging organic contaminants via photoelectrocatalytic process.

Table of contents

Table of figures

Abbreviation

AOP	Advanced oxidation process
AB	Acid blue
BET	Brunauer-Emmet-Teller
BDD	Boron-doped diamond
CND	Carbon nanodots
COD	Chemical oxygen demand
CV	Cyclic voltammetry
DCP	Dichlorophenol
DGP	Diamond-graphene-polyaniline
DMF	Dimethylformamide
DRS	Diffuse reflectance spectroscopy
DSA	Dimensionally stable anodes
EDS	Energy dispersive x-ray spectroscopy
EG	Exfoliated/Expanded graphite
EIS	Electrochemical impedance spectroscopy
ESR	Electron spin resonance
FTIR	Fourier-transform infrared
FTO	Fluorine doped tin oxide
GCE	Glassy carbon electrode
GIC	Graphite intercalated compounds
GO	Graphene oxide
GP	Graphene-polyaniline
IC	Inorganic carbon
JPCDS	Joint committee of powder diffraction standards
LC	Liquid chromatography

LCMS	Liquid chromatography and mass spectrometry
LSV	Linear sweep voltammetry
OER	Oxygen evolution reactions
OG	Orange
PANI	Polyaniline
PEC	Photoelectrocatalysis
PEG	Polyethylene glycol
rGO	Reduced graphene oxide
SEM	Scanning electron microscope
SMX	Sulfamethoxazole
TC	Total carbon
TCE	Total current efficiency
TEM	Transmission electron microscopy
Ti	Titanium
TOC	Total organic carbon
UV	Ultraviolet
XRD	X-ray diffraction

CHAPTER ONE

1.0 INTRODUCTION

1.1 Background and statement of the problem

Water is indispensable for the survival of man, animals and plants on earth. Global demand for water is undoubtedly on the increase in the main areas of water use: household, agriculture and industry [1]. Incidentally, as many as one-fifth of the world's population experience water crisis, and a higher number of people are faced with economic water shortage [2]. The need to manage this natural resource in terms of quantity and quality cannot be overstressed. One key area that deserves serious attention is the adequate treatment of industrial effluents prior to discharge into the environment. As industrial activities grow, it is certain that the amount of wastewater generated will increase and consequently the quantity of contaminants that may get discharged to the surface water and groundwater will continue to rise. In its environmental outlook, OECD (2012) projected that the amount of wastewater returned to the environment untreated will dramatically increase by the year 2050 [3]. This is particularly more critical for developing countries where industry has had enormous impact on the economy in the last few decades. In the continent of Africa, pollution is about the most disturbing part of industrial water use and industrial growth is bound to have significant effect on water quality, with potentially harmful outcomes on human health.

The constituents of wastewater depend on the industries from where the water emanates. Oftentimes, the effluents contain soluble and solid substances which may pose risks to man and the environment. For instance, typical wastewater from textile

industries is a complex mixture of organic compounds and inorganic ions [4-6]. The effluent is usually very coloured because it contains a high concentration of dyes. Dyes and some other organic compounds such as pentachlorophenol, surfactants, softeners and solvents that may be present in dye effluents are xenobiotic and may pose serious hazards to both aquatic and terrestrial entities[7-10]. Pharmaceutical wastewater is one of the most complex industrial effluents. It is characterised by high chemical oxygen demand, biological oxygen demand and toxicity[11]. The detection of pharmaceuticals in therapeutically significant quantity in the environment is a concern to the scientific community. Similarly, municipal wastewater contains a variety of substances such as phenols, personal care products, pharmaceuticals, etc [12]. Also, release of organic contaminants such as pesticides and herbicides during agricultural activities increases the organic load of our water bodies. In addition, many organic substances can find their way into our water from the activities of many other industries including those dealing with petrochemicals, pesticides and herbicides, disinfectants, and so on.

From the above, it is obvious that organic compounds are at the core of many industrial and agricultural enterprises, and thus they represent a major category of pollutants commonly found in water bodies. It is therefore pertinent to treat wastewater to remove organic contaminants before it is released into the environment. In this regard, a lot of efforts have been directed at the development of technologies for the treatment of wastewaters. Scientists and researchers have employed physical, chemical and biological processes to remove a variety of contaminants from wastewaters. Processes such as coagulation and flocculation, membrane filtration, ion-exchange, adsorption, aerobic and anaerobic degradation, etc. have been advanced and utilised for the remediation of water polluted by organic substances. Some significant successes have been recorded with these traditional approaches to water treatment. However, notable drawbacks are associated with them. Coagulation and flocculation, for instance,

requires chemical inputs and there is a transfer of toxic substances from solution to solid phase. The sludge generated also constitutes secondary pollution. Membrane filtration is attractive, but the challenges of fouling and secondary pollution are major disadvantages. The major demerit of adsorption methods is secondary pollution. Biological treatment is also ineffective for the treatment of recalcitrant organic pollutants.

These shortcomings have led to the quest for other water treatment approaches. One of the upcoming alternatives for complementing water treatment methodologies is a group of methods called advanced oxidation processes (AOPs). There exist a number of AOPs commonly employed in wastewater treatment: they include ozonation, Fenton reaction, photo-Fenton system, UV/H_2O_2, heterogeneous photocatalysis, electrochemical advanced oxidation system (EAOP), etc. All these processes are characterised by the *in situ* production of hydroxyl radical which possesses a very strong oxidising power, and which reacts with many organic species until they are completely degraded [13, 14]. AOPs have been applied for the oxidation of a myriad of organic contaminants including dyes, phenols, pharmaceuticals, pesticides and so on, and in most cases great degradation efficiencies were achieved [15-18]. AOPs are particularly well suited for the treatment of water contaminated by recalcitrant organic pollutants, organic substances in this class are not easily biodegradable and thus they persist in the environment [19]. Most often, AOPs are carried out at ambient conditions and are deemed to be environmentally benign. In recent years, application of electrochemical technologies to water remediation has attracted much attention [20] and electrochemical advanced oxidation processes, in particular, have been shown to be promising for the destruction of refractory organic pollutants in water [21]. In EAOPs, formation of hydroxyl radicals occurs at the anode via water oxidation. The quantity and the effectiveness/availability of the OH radicals produced are greatly influenced by the nature of the anode

materials. Several anodes have been employed for the anodic oxidation of organics, these include boron-doped diamond (BDD), SnO_2, PbO_2, RuO_2-TiO_2 etc. [22]. Innovative additions have been made to anodic oxidation, these include incorporation of Fenton process (where H_2O_2 is electrochemically generated at graphite cathodes by two electron reduction of O_2 in acidic medium) and application of light energy to photolyse possible Fe complexes that may be formed. Another upcoming EAOP is the photoelectrocatalytic process in which photoactive materials are used as anodes, and both electrical and light energies are utilised for degradation of the targeted pollutant. This process presents an exciting alternative approach to wastewater remediation as it offers the synergistic benefits of combining anodic potential and light irradiation.

1.2 Rationale/Motivation

The need for quality and copious amount of water for the health and economic prosperity of mankind cannot be overemphasised. And effective treatment of contaminated water to satisfy this need is a necessity. EAOP, a subset of AOPs, has been indicated to hold huge potential for the effective decontamination of water polluted by organics. One of the most important components of the EAOP set up is the anodic material, where the oxidising species are generated. Till date, diamond based electrode (BDD) remains the best anode for the electrochemical destruction of organic pollutants [23]. The excellent properties of diamond that made it a material of choice for many electrochemical applications include wide potential window, low signal-to-background current ratio, tunable electrical resistivity, high oxygen evolution potential, excellent chemical stability, and minimal susceptibility to fouling. For EAOP, the desirable properties of BDD are high oxygen overvoltage and weak interaction with generated hydroxyl radicals and targeted organics [24]. The high cost of BDD, however, remains a

major drawback. It would be interesting to explore cheaper and easy-to-fabricate diamond-based electrodes for anodic oxidation/electro-oxidation of organic substances. On the other hand, since photoelectrocatalytic process has prospects for water remediation because of the inherent benefits of combining electrolysis and photocatalysis, some photocatalytic semiconductors and/or their composites would be investigated as anodic materials for the oxidation of selected organic contaminants. It is well known that the efficiency of heterogeneous photocatalysis is often hampered by low quantum yield and rapid recombination of photo-generated charges. Recombination of holes and electrons can be overcome in a photoelectrocatalytic process because the applied potential enhances separation of the charges, leading to improved degradation of the organic pollutants in wastewater. Also, the challenge of recovering catalysts in a typical photocatalytic process is mitigated as the materials are immobilised onto conductive substrates. Of note is the fact that a photoanode subjected to anodic potential and irradiated with light of suitable wavelength will not only degrade organic compounds by photolytic process but also by electrochemical oxidation. It should be noted that the energy requirement of the anodic oxidation would be drastically reduced. Moreover, for large scale applications, utilisation of solar energy will be of great benefit and the overall process will be efficient and cost-effective for removal of organic pollutants from water.

1.3 Hypothesis

Anodes/photoanodes prepared from diamond (and other forms of carbon) and semiconductors are efficient for the oxidation/degradation of organic pollutants in water.

1.4 Aim of the study

This study aims at investigating the applicability of carbon and metal oxide semiconductors based anodes for the electrochemical and photoelectrocatalytic oxidation of selected organic pollutants.

1.5 Objectives

The specific objectives of the study are as follows:

i. To prepare expanded graphite, and the composite of diamond and expanded graphite

ii. To prepare diamond, graphene and polyaniline composite (DGP)

iii. To prepare a nanocomposite of TiO_2 and expanded graphite

iv. To synthesise $BiVO_4$ nanocomposites

v. To fabricate the materials into electrodes

vi. To characterise the materials and the electrodes using Raman spectroscopy, FTIR spectroscopy, XRD, SEM/EDS, TEM, BET, DRS, CV, EIS, LSV and chronoamperometry.

vii. To evaluate the performance of the fabricated electrodes in the electrochemical and photoelectrocatalytic oxidation of some selected organic compounds

viii. To investigate the intermediate products formed during the degradation of some of the pollutants using chromatographic and spectroscopic techniques.

1.6 Thesis outline

This thesis has eight chapters.

- Chapter 2 presents a review of studies and various concepts related to and dealing with electrochemical and photoelectrocatalytic oxidation processes.

- Chapter 3 discusses general characterisation techniques employed in this study, including descriptions of analysis conditions where necessary.

- Chapter 4 is a report of investigation dealing with application of diamond and exfoliated graphite composite electrode for electrochemical degradation of an anthraquinonic dye.

- Chapter 5 deals with the electro-oxidation of 2,4-dichlorophenol at a novel electrode comprising nanocomposite of diamond, graphene and PANI.

- Chapter 6 contains a report on the synthesis, fabrication and application of EG-TiO_2 photoanode for the oxidation a pharmaceutical.

- Chapter 7 deals with synthesis, characterisation and application of $BiVO_4$ nanocomposite electrode for the degradation of dyes via photoelectrocatalytic process.

- Chapter 8 presents general conclusions and recommendations.

1.7 References

[1] R.B. Jackson, S.R. Carpenter, C.N. Dahm, D.M. McKnight, R.J. Naiman, S.L. Postel, S.W. Running, Water in a changing world, Ecological Applications 11 (2001) 1027-1045.

[2] http://www.un.org/waterforlifedecade/scarcity.shtml Accessed 28 April 2017

[3] https://www.oecd.org/env/indicators-modelling-outlooks/49846090.pdf Accessed 28 April 2017

[4] M. Zeiner, T. Rezić, B. Šantek, I. Rezić, S. Hann, G. Stingeder, Removal of Cr, Mn, and Co from textile wastewater by horizontal rotating tubular bioreactor, Environmental Science & Technology 46 (2012) 10690-10696.

[5] J. Jadhav, D. Kalyani, A. Telke, S. Phugare, S. Govindwar, Evaluation of the efficacy of a bacterial consortium for the removal of color, reduction of heavy metals, and toxicity from textile dye effluent, Bioresource Technology 101 (2010) 165-173.

[6] C.A. Somensi, E.L. Simionatto, S.L. Bertoli, A. Wisniewski, C.M. Radetski, Use of ozone in a pilot-scale plant for textile wastewater pre-treatment: physico-chemical efficiency, degradation by-products identification and environmental toxicity of treated wastewater, Journal of Hazardous Materials 175 (2010) 235-240.

[7] V.M. Correia, T. Stephenson, S.J. Judd, Characterisation of textile wastewaters-a review, Environmental Technology 15 (1994) 917-929.

[8] C. Frijters, R. Vos, G. Scheffer, R. Mulder, Decolorizing and detoxifying textile wastewater, containing both soluble and insoluble dyes, in a full scale combined anaerobic/aerobic system, Water Research 40 (2006) 1249-1257.

[9] S.B. Jadhav, A.S. Chougule, D.P. Shah, C.S. Pereira, J.P. Jadhav, Application of response surface methodology for the optimization of textile effluent biodecolorization and its toxicity perspectives using plant toxicity, plasmid nicking assays, Clean Technologies and Environmental Policy 17 (2015) 709-720.

[10] K. Paździor, J. Wrębiak, A. Klepacz-Smółka, M. Gmurek, L. Bilińska, L. Kos, J. Sójka-Ledakowicz, S. Ledakowicz, Influence of ozonation and biodegradation on toxicity of industrial textile wastewater, Journal of Environmental Management (2016).

[11] K.K. Ng, X. Shi, S.L. Ong, C.-F. Lin, H.Y. Ng, An innovative of aerobic bio-entrapped salt marsh sediment membrane reactor for the treatment of high-saline pharmaceutical wastewater, Chemical Engineering Journal 295 (2016) 317-325.

[12] L. Lishman, S.A. Smyth, K. Sarafin, S. Kleywegt, J. Toito, T. Peart, B. Lee, M. Servos, M. Beland, P. Seto, Occurrence and reductions of pharmaceuticals and personal care products and estrogens by municipal wastewater treatment plants in Ontario, Canada, Science of the Total Environment 367 (2006) 544-558.

[13] B. Bethi, S.H. Sonawane, B.A. Bhanvase, S.P. Gumfekar, Nanomaterials-based advanced oxidation processes for wastewater treatment: A review, Chemical Engineering and Processing: Process Intensification 109 (2016) 178-189.

[14] M. Cheng, G. Zeng, D. Huang, C. Lai, P. Xu, C. Zhang, Y. Liu, Hydroxyl radicals based advanced oxidation processes (AOPs) for remediation of soils contaminated with organic compounds: a review, Chemical Engineering Journal 284 (2016) 582-598.

[15] M. Antonopoulou, E. Evgenidou, D. Lambropoulou, I. Konstantinou, A review on advanced oxidation processes for the removal of taste and odor compounds from aqueous media, Water Research 53 (2014) 215-234.

[16] A. Klančar, J. Trontelj, A. Kristl, A. Meglič, T. Rozina, M.Z. Justin, R. Roškar, An advanced oxidation process for wastewater treatment to reduce the ecological burden from pharmacotherapy and the agricultural use of pesticides, Ecological Engineering 97 (2016) 186-195.

[17] F.C. Moreira, R.A. Boaventura, E. Brillas, V.J. Vilar, Electrochemical advanced oxidation processes: A review on their application to synthetic and real wastewaters, Applied Catalysis B: Environmental 202 (2017) 217-261.

[18] A.D. Bokare, W. Choi, Review of iron-free Fenton-like systems for activating H 2 O 2 in advanced oxidation processes, Journal of Hazardous Materials 275 (2014) 121-135.

[19] A.R. Ribeiro, O.C. Nunes, M.F. Pereira, A.M. Silva, An overview on the advanced oxidation processes applied for the treatment of water pollutants defined in the recently launched Directive 2013/39/EU, Environment International 75 (2015) 33-51.

[20] C.A. Martinez-Huitle, S. Ferro, Electrochemical oxidation of organic pollutants for the wastewater treatment: direct and indirect processes, Chemical Society Reviews 35 (2006) 1324-1340.

[21] B.P. Chaplin, Critical review of electrochemical advanced oxidation processes for water treatment applications, Environmental Science: Processes & Impacts 16 (2014) 1182-1203.

[22] C.A. Martínez-Huitle, L.S. Andrade, Electrocatalysis in wastewater treatment: recent mechanism advances, Quimica Nova 34 (2011) 850-858.

[23] C. Bruguera-Casamada, I. Sirés, E. Brillas, R.M. Araujo, Effect of electrogenerated hydroxyl radicals, active chlorine and organic matter on the electrochemical

inactivation of Pseudomonas aeruginosa using BDD and dimensionally stable anodes, Separation and Purification Technology 178 (2017) 224-231.

[24] A. El-Ghenymy, F. Centellas, J.A. Garrido, R.M. Rodríguez, I. Sirés, P.L. Cabot, E. Brillas, Decolorization and mineralization of Orange G azo dye solutions by anodic oxidation with a boron-doped diamond anode in divided and undivided tank reactors, Electrochimica Acta 130 (2014) 568-576.

CHAPTER TWO

2.0 LITERATURE REVIEW

2.1 Introduction

This chapter presents a general literature review on the various concepts relevant to this study. Specific attention is given to electrochemical advanced oxidation processes including anodic oxidation and photoelectrocatalytic process. A brief review on the electro-oxidation of phenols at different nanostructured surfaces and an overview of the electrode materials explored in this work are also presented. In addition to the review in this chapter, the result chapters also have a brief review of literature relevant to them.

2.2 Advanced oxidation processes

Advanced oxidation processes (AOPs) refer to a collection of oxidation processes in aqueous media involving certain highly reactive and powerful species for the destruction of target organic substances. AOPs are characterised by the generation of hydroxyl radicals, ·OH. After fluorine, hydroxyl radical is the strongest oxidant known (2.8 V vs. SHE). These radicals are able to attack and destroy organic compounds until their mineralisation [1]. Hydroxyl radicals are nonselective, thus they are capable of oxidising a wide range of organic contaminants into carbon dioxide and inorganic ions. Interaction of ·OH with organic molecules have been shown to proceed by radical addition, hydrogen abstraction, electron transfer and radical combination [2, 3] There are a number of processes in which the hydroxyl radicals can be generated, examples are Fenton and Fenton-like processes, heterogeneous photocatalysis, electrochemical techniques and so on. The Fenton reaction was first described by the British scientist, Henry John Horstman Fenton, in 1894. He observed that tartaric acid was oxidised by

H_2O_2 in the presence of ferrous salt [4, 5]. Further investigation by Haber and Weiss led to the proposition that hydroxyl radicals generated *in situ* during the interaction of hydrogen peroxide and iron salts [1, 6, 7] were responsible for the oxidation of the organic compound in the process. Since then, there have been improvements to the traditional Fenton process and also attention has been given to the development of Fenton-like technologies. In this regard, there have emerged processes such as photo-Fenton, electro-Fenton, sono-Fenton and so on. The Fenton and Fenton-like processes have been extensively employed for the treatment of water contaminated by organic substances [8-10]. The Fenton reaction is usually conducted under acidic conditions and the process can be represented by the following equation:

$$Fe^{2+} + H_2O_2 \longrightarrow Fe^{3+} + OH^- + {}^{\cdot}OH \qquad (2.1)$$

Heterogeneous photocatalysis is another advanced oxidation process that has received tremendous attention for the remediation of water polluted by organic compounds [11-13]. In this process, photons strike the surface of a photocatalytic material in aqueous medium to produce hydroxyl radicals via one-electron oxidation of adsorbed water molecules by photogenerated holes. The photogenerated holes are also powerful oxidants which can react with organic molecules until they are completely degraded. More details on this process are presented in section 2.4.

Over the last few decades, there has been an increasing interest in the development of electrochemical technologies for wastewater treatment. In particular, there has been a great deal of advances in the utilisation of electrochemical processes for the destruction of organic substances in water since it was discovered that hydroxyl radicals are produced at the surface of certain materials upon application of electrical energy. The processes in which hydroxyl radicals can be generated in situ in electrochemical reactors are termed electrochemical advanced oxidation processes (EAOPs). The

fundamentals and an overview of the recent works done in the area of EAOPs are presented in the subsequent section.

2.3 Electrochemical Advanced Oxidation Processes

As stated earlier, EAOPs are methods based on the production of oxidants such as hydroxyl radicals for the oxidation of organic pollutants in an electrochemical cell. These technologies can be considered 'green' because electron, which is the reagent involved, is clean. Consequently, EAOPs are environmentally benign and do not present post-treatment concerns. In EAOPs, hydroxyl radicals are formed via oxidation of water molecules at the surface of the anode [14, 15]. The formation of this potent oxidant was studied and communicated by Comninellis and group in 2003. In their study, they used electron spin resonance (ESR) technique, with 5,5-dimethyl-1-pyrroline-*N*-oxide as free radical trapping agent, to confirm the electrogeneration of hydroxyl radicals at a synthetic boron-doped diamond electrode (BDD) [16]. This finding led to the confirmation of electrochemical oxidation as advanced oxidation process [17]. The hydroxyl radicals formed in this electrochemical process are capable of reacting with the organic molecules in solution until their complete mineralisation. In addition, in electrochemical oxidation, decomposition of the target compound can also occur via direct electron transfer reactions which occur when electrons are released from the organic molecule to the anode. These electron transfer reactions have been noted as an important pathway in the degradation of recalcitrant compounds such as fluorinated organics which are unreactive towards hydroxyl radicals [14, 18]. Anodic oxidation of water and direct electron transfer reactions can be represented by equations 2.2 and 2.3 shown below.

$$H_2O \longrightarrow {\cdot}OH + H^+ + e^- \qquad (2.2)$$

$$R \longrightarrow (\cdot R)^{+} + e^{-} \qquad (2.3)$$

The quantity and the reactivity of the hydroxyl radicals produced are largely dependent on the nature of the anode materials. On this basis, anodic materials have been classified into two main categories: 'active' and 'non-active' [19]. The 'active' anodes are characterised by strong adsorption of the hydroxyl radicals to the electrode surface while the 'inactive' anodes interact weakly with the hydroxyl radicals formed [20]. Owing to the strong interaction of the electrogenerated hydroxyl radicals with the surfaces of the 'active' anodes, the concentration of the oxidant species is usually very low at the electrode surface resulting in selective/incomplete oxidation of the target compound [21]. Pt, IrO_2, RuO_2 and graphite electrodes have been classified as 'active' anodes based on their oxidation performance [22]. Furthermore, active anodes show good electrocatalytic properties for oxygen evolution reactions (OER) and at high anodic potential, OER competes with the formation of hydroxyl radicals. Effective oxidation of organics can be achieved at these anodes at low current densities, although the reaction rate is usually very sluggish. 'Non-active' anodes, on the other hand, promote complete combustion of the target analyte due to the accumulation of substantial amount of the hydroxyl radicals at their surfaces. They are poor electrocatalyst for OER, and thus the mineralisation of refractory organics to CO_2, H_2O and inorganic ions can be realised via physisorbed hydroxyl radicals generated at high anode potential. As a result, 'non-active' anodes are considered promising electrodes for wastewater treatment. BDD, SnO_2 and PbO_2 are classified as 'non-active' anodes [23].

There are several reports dealing with the degradation of a wide range of organic contaminants at both the 'active' and 'non-active anodes'. In these studies, the oxidation powers of the anodes to induce conversion or combustion of the target contaminants were demonstrated. For instance, Martinez-Huitle *et al.* [24] reported the degradation of the toxic pesticide, methamidophos, at Pb/PbO_2, Ti/SnO_2 and Si/BDD anodes. The

performance of these electrodes for the removal of the compound was evaluated and BDD displayed the highest degradation rate under similar experimental conditions. The removal efficiency followed the order Si/BDD >> Pb/PbO_2 > Ti/SnO_2. In a study by Gargouri *et al.* [25], table olive wastewater, which is characterised by high organic content, including phenol, was electrochemically treated at BDD and PbO_2. Chemical oxygen demand (COD) measurement after 2 h electrolysis time revealed that a very significant amount of the organic content of the water has been destroyed at both anodes. BDD however displayed a more rapid and improved degradation. The study affirmed both anodes as possessing high oxidation power for organics. A comparative investigation by Brillas *et al.* [26] revealed that BDD is far superior to Pt in the anodic oxidation of an acidic solution of dopamine. Dissolved organic carbon (DOC) abatement at the 'active' anode was much less than that recorded at the 'non-active' anode under the same experimental conditions. Similarly, the work of Fajardo *et al.* [27] showed that BDD offered better mineralisation efficiency than IrO_2 based anode when both electrodes were employed for the anodic oxidation of Amaranth dye. The decolourisation and incineration of this azo dye was not only better but was also much faster at the diamond electrode. In a related study by Sopaj *et al.* [28], two 'non-active' anodes (BDD and PbO_2) and four active anodes (Pt, carbon-fiber, carbon-graphite, carbon-felt and DSA) were employed for the electrochemical oxidation of amoxillin. The results obtained showed that the pharmaceutical was better mineralised at BDD. Of the sp^2 carbon electrodes, carbon-felt gave the best degradation performance at relatively low current densities. It is known that electrolytic process can be performed on active anodes at lower current densities to avoid oxygen evolution reactions, although a longer time is then required to achieve removal of the organic substance. Many other researchers have reported on the oxidation performance of both 'active' and 'non-active' anodes towards the removal of organic carbon from synthetic and real wastewater [29-31]. Other interesting anodic materials are the sub-stoichiometric

titanium oxides which have been shown to be promising for electro-oxidation of refractory organic pollutants. They are produced from TiO_2, a very abundant material, thus they are much cheaper than most electrodes discussed earlier. Sub-stoichiometric titanium oxides ceramic electrodes exhibit high electrical conductivity at normal room conditions and excellent stability in aqueous environment. The nature of the hydroxyl radicals produced at Ti_4O_7 has been studied. Compared to other non-active anodes, this sub-stoichiometric ceramic anode yielded less amount but more reactive hydroxyl radicals [32]. A few studies have reported on degradation of organic contaminants at these electrodes [33-35].

2.3.1 Influence of supporting electrolytes on the oxidation of organic pollutants

Studies have shown that the chemical nature of the substance used to enhance the conductivity of the contaminant solution can exert significant effect on the degradation/mineralisation of the contaminant. The use of certain salts leads to the generation of some reactive species which can attack the organic molecules in solution. Sulphate (SO_4^{2-}) is one of the most commonly used supporting electrolytes in electrochemical oxidation process [3]. Electrogeneration of persulfate ($S_2O_8^{2-}$), a weak oxidant from SO_4^{2-}, and its possible participation in anodic oxidation process have been reported [36-38]. The mechanism of formation of the sulphate oxidising species as proposed by Davis *et al.* [39] is as follows:

$$HSO_4^- + {\cdot}OH \longrightarrow SO_4^{-\cdot} + H_2O \qquad (2.4)$$

$$H_2SO_4 + {\cdot}OH \longrightarrow SO_4^{-\cdot} + H_3O^+ \qquad (2.5)$$

$$SO_4^{2-} \longrightarrow SO_4^{-\cdot} + H_3O^+ + e^- \qquad (2.6)$$

$$SO_4^{-\cdot} + SO_4^{-\cdot} \longrightarrow S_2O_8^{2-} \qquad (2.7)$$

Furthermore, mediated electrochemical oxidation of organic contaminants by active chlorine has been widely investigated since it is known that chloride is often present in wastewater. Transformation of Cl^- at the surface of the anode and subsequent formation of oxidising species are given in the equations below:

$$2Cl^- \longrightarrow Cl_2 + 2e^- \quad (2.8)$$

$$Cl_2 + H_2O \longrightarrow HOCl + H^+ + Cl^- \quad (2.9)$$

$$HOCl \longrightarrow OCl^- + H^+ \quad (2.10)$$

The predominant chlorine oxidant formed is a function of pH of the electrolysis solution. Cl_2 is predominantly present at pH < 3, HOCl at 3 < pH < 8 while OCl^- predominates at pH > 8 [40, 41]. These active chlorine species possess considerable oxidising powers to degrade organic molecules in solution. The oxidising ability is in the order $OCl^- < Cl_2 <$ HOCl (The standard oxidation potentials are 0.42, 1.36 and 1.63V respectively against SHE). In a study by Boudreau *et al.* [42], the electrochemical oxidation of sulfamethoxazole was carried out in the presence and absence of chloride at BDD. The concentration of the drug was found to decrease with increasing amount of chloride and mineralisation was uninhibited at the early stage of the process. Chlorinated by-products were formed but it was observed that these compounds were susceptible to anodic oxidation via hydroxyl radicals attack. It followed that the reaction pathways in anodic oxidation and chlorine-mediated electrochemical oxidation are not mutually exclusive: the oxidation products of anodic oxidation can undergo electrochemical hypochlorination and vice-versa. A report by Ammar *et al.* [43] also showed that the abatement of metronidazole concentration was significantly accelerated in the presence of NaCl during the electrochemical oxidation of the drug at BDD, with over 90% COD removal in 120 min. The study by Rocha *et al.* also demonstrated that decolourisation of Novacron Yellow C-RG, a textile dye, was more rapidly achieved at

both BDD and platinum anode when NaCl was used as supporting electrolyte. Interestingly, TOC decay was improved at both electrodes when the salt was used. It was also observed that the rate of decolourisation was higher at the Pt electrode, although the extent of mineralisation was smaller. Salazar *et al.* [44] also observed that electrochemical cell equipped with BDD (and chloride as supporting electrolyte) resulted in higher initial mineralisation of the antihypertensive drug, losartan, than the cell in which sulphate was used as supporting electrolyte. However, further electrolysis revealed that the extent of mineralisation in the sulphate supported cell was better. Furthermore, it has been observed in some studies that generation of active chlorine (and consequently degradation process in the presence of Cl^-) is more favoured at the 'active' anodes than at the 'non-active' anodes [45, 46]. The major concern with the utilisation of chorine-mediated electrolysis is the formation of chlorinated intermediates [47], although longer electrolysis time has been suggested as a possible approach to ensuring the by-products are mineralised [42]. So complete concentration abatement of the target compound should not be taken as an indication of the success of the remediation process.

2.3.2 Electro-Fenton and Photoelectro-Fenton Processes

In order to improve the efficiency of EAOP, researchers have made efforts to couple Fenton reaction to anodic oxidation. In this electrochemical set-up, a cathode at which significant amount of H_2O_2 can be generated by two electron reduction of oxygen is used. This electrochemical process whereby H_2O_2 is generated *in situ* at the cathode in the presence of oxygen, with Fe^{2+} added to the electrolytic solution to induce Fenton reaction is termed electro-Fenton. There are other variations of electro-Fenton process: i) H_2O_2 is added and sacrificial Fe anode is used, ii) H_2O_2 is electrogenerated at the cathode and Fe sacrificial anode is used and iii) Both H_2O_2 and Fe^{2+} are added to electrolytic cell [5, 48-50]. Unlike the traditional Fenton reaction where the Fe^{2+} is

consumed and cannot be re-used in the system, electro-Fenton offers the benefit of regeneration of the oxidised Fe^{2+} by cathodic reduction [51]. The challenge of sludge formation (which causes secondary pollution) in classical Fenton process is avoided. The main reactions involved in electro-Fenton process can be given as shown below:

$$O_2 + 2H^+ + 2e^- \longrightarrow H_2O_2 \quad \textit{(at the cathode)} \qquad (2.11)$$

$$H_2O_2 + Fe^{2+} + H^+ \longrightarrow Fe^{3+} + H_2O + {\cdot}OH \qquad (2.12)$$

$$Fe^{3+} + e^- \longrightarrow Fe^{2+} \qquad (2.13)$$

Fenton reaction is usually carried out at a pH value of around 3, although higher pH is possible [52]. The rate of production and the quantity of H_2O_2 produced depend on the nature of the cathode used. Carbonaceous materials such as graphite, carbon sponge, carbon felt, carbon fiber, carbon nanotubes, reticulated vitreous carbon, etc. are known to be suitable as cathodes for electro-generation of H_2O_2 [53-55].

The efficiency of electro-Fenton process can be improved by UV or visible light [56, 57]. This is called UV or solar photoelectro-Fenton. The use of UV or solar irradiation is advantageous for the decarboxylation of Fe(III)-carboxylate complex (equation 2.14), an intermediate formed during the oxidation process. In addition, the light source aids regeneration of Fe^{2+} by photoreduction of $[Fe(OH)]^{2+}$ (equation 2.15). It has also been suggested that the light irradiation can promote homolytic fission of H_2O_2 to produce more hydroxyl radicals according to equation (2.16) [57, 58].

$$[Fe(OOCR)]^{2+} + h\nu \longrightarrow Fe^{2+} + CO_2 + {\cdot}R \qquad (2.14)$$

$$[Fe(OH)]^{2+} + h\nu \longrightarrow Fe^{2+} + {\cdot}OH \qquad (2.15)$$

$$H_2O_2 + h\nu \longrightarrow 2\,{\cdot}OH \qquad (2.16)$$

In essence, whether used in a mediated process (such as indirect oxidation with active chlorine) or in a coupled process (such as the electro-Fenton process), BDD appears to be the most promising anodic material for the oxidation of organic pollutants into carbon dioxide and inorganic ions. This is evident from the TOC removal efficiencies recorded at this anode in several studies where it has been compared to others. The major drawback with the utilisation of this anode is the high cost. It also requires a relatively high electrical potential to achieve the needed degradation. SnO_2 and PbO_2 electrodes are also effective for mineralisation of organic substances in water but the service life of SnO_2 electrode is short and Pb ions can leach into solution from PbO_2 electrode posing health risks. Furthermore, 'active anodes' are known to favour conversion rather than mineralisation. Exploring a hybrid of 'active' and 'non-active' anodes for the degradation of organic pollutants may present exciting results. Such anode should be a compromise between the major drawbacks of the two categories of anodic materials.

2.4 Electro-oxidation of phenols

Electro-oxidation of phenolic compounds provides a simple approach for their detection and quantification in aqueous media. Electrochemical methods are a viable and attractive alternative to analysing phenols in environmental samples because electrochemical devices provide high sensitivity and good reliability; can be miniaturised and thus allows for on-site analysis; give rapid response and are simple to operate [59-61]. As such, research in the development of anodic materials for the electrochemical oxidation (and consequently detection and quantification) of many analytes of interest has received considerable attention. The determination of phenols at the anode presents one major challenge - the formation of polymeric films on the surface of the anode (Figure 2.1) [62-64] which reduces the electrochemical signal of the

analyte. During electroanalysis, a molecule of phenol is oxidised to phenoxy radicals, which undergo further oxidation to polymeric products [65]. These polymeric products lead to the passivation of the anode surface.

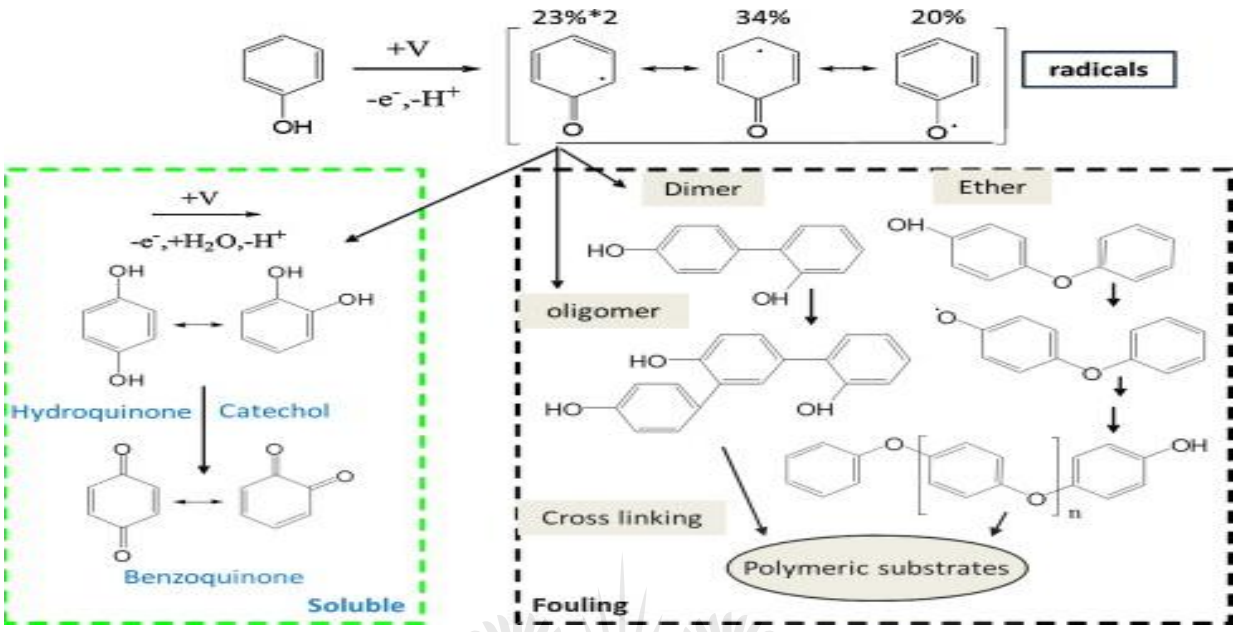

Fig. 2. 1. Possible schemes of the chemical reactions that occur during the electro-oxidation of phenol [64]**.**

In view of this passivation challenge, research efforts are being directed at fabricating anodes that are resistant to deactivation by these oxidation products. Talarico *et al.* [66] reported the detection of phenolic compounds at a screen printed electrode modified by carbon black dispersion. The modified electrode was not only more sensitive than the bare electrode; it also exhibited better resistance to fouling. The less susceptibility of the carbon black modified electrode to fouling was attributed to the high number of defect sites provided by the modifier. In a related study by Sharma *et al.* [67], electrochemical oxidation of catechol and dopamine was investigated on glassy carbon electrode modified by a composite of electrochemically reduced graphene oxide and multi-walled carbon nanotubes. The evaluation of the anti-fouling properties of the modified electrodes revealed that the composite modified electrodes showed the best fouling

resistance compared to the bare, reduced graphene oxide modified and multi-walled carbon nanotubes modified electrodes during the electroanalysis of the compounds. Furthermore, Quynh *et al.* [68] examined the electro-oxidation of phenol and catechol at the surface of a nanoporous gold electrode. The electrode reportedly showed well-defined amperometric responses toward the substances at neutral and acidic pH. While repeatability of catechol sensing at the nanoporous electrode was very good in both acidic and neutral media, the repeatability of phenol detection was found to be better in acidic medium than in neutral solution. The stable sensitivity of the anode to the analyte is thought to be as a result of favourable formation of soluble products such as quinones when the electrolyte is acidic. Acidic medium is preferred for electrochemical oxidation of phenols since it could prevent electrode deactivation due to polymeric contamination. In a similar study by Pirvu *et al.* [69], the anti-fouling abilities of Au, polypyrrole(PPy)/Au and sodium polystyrene sulfonate (NaPSS) modified PPy/Au electrodes in phenols oxidation were evaluated. The rate of accumulation of reaction products on these electrodes is in the order Au > PPy/Au > Au/PPy/NaPSS. The poor adhesion of phenol oxidation products to the surface of the NaPSS surfactant modified electrode was attributed to the orientation and distribution of the polymeric surfactant. In another report by Al-Qasmi *et al.* [70], multi-walled carbon nanotubes (MWCNTs) was composited with nafion and used as a modifier for glassy carbon electrode (GCE). The GCE/MWCNTs/nafion electrode showed significant anti-passivating property compared to the bare electrode which readily lost activity. The authors asserted that the fouling resistance ability of the composite modified electrode was as a result of the protection offered by the nafion component. Also, Ganesh *et al.* [71] showed that eosin Y film modified paste electrode exhibited anti-fouling characteristic during the electro-oxidation of dihydroxy benzene isomers, catechol and hydroquinone. Wang *et al.* also reported that ionic liquids coated Ni/$CdFe_2O_4$ sensing platform produced reproducible electrochemical signals of bisphenol S and bisphenol AP [72]. In a similar work, Cheng

and co-workers [73] showed that conducting polymer modified by ionic liquid provide excellent sensing platform for reproducible signals of bisphenol A in aqueous medium. There are a number of other articles which have reported on the preparation of different mediating surfaces for the electrochemical determination of phenolic compounds. A few of these materials include polycarbazole/N-doped graphene [74], α-MnO_2 nanorod/graphene [75], Au/Cu nanoparticles [76], Ag/chitosan [77], Ag/reduced graphene oxide [78], V_2O_5/reduced graphene oxide [79], smectite-chitosan [80] and BDD [81, 82]. Apart from electrode-based modifications, solution-phase mediation has also been indicated to be a plausible approach to overcoming fouling during electroanalysis of phenolic compounds. Hossain *et al.* [83] reported that addition of polyoxometalates to the solution of phenol can significantly suppress electrode passivation in the course of electroanalysis. The polyoxometalates are believed to act as electrocatalytic mediator by oxidising the intermediate products formed and themselves getting re-oxidised. It is noteworthy that the thermodynamics of the oxidation of the phenolic molecule remains largely the same.

2.5 Photoelectrocatalytic process

Photoelectrocatalysis (PEC) is an advanced oxidation process which couples both photocatalytic oxidation process and electrochemical oxidation process. Simply, a photoactive semiconducting material is employed as anodic material and both light of suitable wavelength and electrical energy are applied to achieve the degradation of the target organic compound. In this process, recombination of photogenerated electrons and holes which occurs in photocatalytic process is retarded by the applied bias potential. This leads to longer lifespan of the charges and consequently improvement of the photocatalytic degradation process. In addition, production of hydroxyl radicals via water oxidation at the anode surface and the possible occurrence of direct electron

transfer reactions are bound to increase the oxidation rate of the pollutant. On the other hand, the challenge of catalyst recovery after treatment in a photocatalytic setup is absent as the catalyst is localised on a conducting substrate in PEC.

When light (hν) of sufficient energy strikes the surface of a semiconductor (S), the process in equation (2.17) occurs,

$$S + h\nu \longrightarrow e^{-}_{CB} + h^{+}_{VB} \qquad (2.17)$$

The schematic representation of the photocatalytic process is shown in figure 2.2. The photogenerated charge pairs are transient, with estimated lifetime in the order of nanoseconds [84]. These charges are capable of interacting with species in the heterogeneous system. For instance, the holes are powerful oxidant which can react with organics and water molecules which are adsorbed onto the surface of the catalyst.

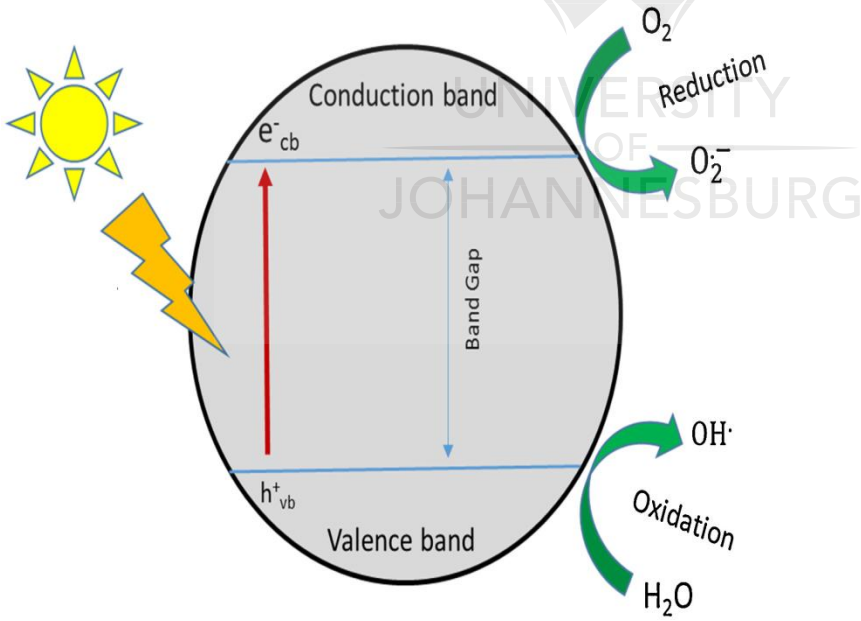

Fig. 2. 2. Schematic representation of semiconductor photocatalytic process [85].

The oxidative degradation of organic compounds by valence-bound holes has been documented [86]. Furthermore, the trapped holes have been indicated to undergo one-electron oxidation step with water molecules to generate the highly oxidising hydroxyl radicals. The formation of hydroxylated intermediates during the photocatalytic degradation of organic molecules has been given as evidence for the involvement of hydroxyl radicals [84]. These intermediates were found to be consistent with those obtained when similar molecules were reacted with a known source of hydroxyl radicals. In addition, electron spin resonance studies have been conducted in support of the existence of hydroxyl radicals upon light irradiation of TiO_2 [87, 88]. It should also be noted that some reactive species such as coumarin, p-chlorobenzoic, p-benzoquinone and terephthalic acid have been employed as fluorescent probes to establish the formation of hydroxyl radicals in aqueous media in advanced oxidation processes [89-92] At present, photoluminescence study of the interaction between terephthalic acid and hydroxyl radicals in solution is often provided as evidence for the formation of hydroxyl radicals in photocatalytic processes [90, 93-95]. The Equations (2.18) and (2.19) depict the interaction of photogenerated holes with organics and water molecule. In addition, it is assumed that the positive holes can also oxidise hydroxide ions to produce hydroxyl radicals [96] as shown in equation (2.20).

$$R + h^+ \longrightarrow {\cdot}R \qquad (2.18)$$

$$H_2O + h^+ \longrightarrow {\cdot}OH + H^+ \qquad (2.19)$$

$$OH^- + h^+ \longrightarrow {\cdot}OH \qquad (2.20)$$

The electrons at the conduction band can interact with adsorbed or dissolved oxygen in the reaction system to form superoxide ion as shown in equation (2.21). The superoxide ions are also known to possess considerable oxidising power. Further reactions can take place between the various species in the mixture as depicted by equations (2.22- 2.23).

$$e^- + O_2 \longrightarrow O_2^{\cdot -} \qquad (2.21)$$

$$O_2^{\cdot -} + H^+ \longrightarrow OOH^{\cdot} \qquad (2.22)$$

$$OOH^{\cdot} + H^+ + e^- \longrightarrow H_2O_2 \qquad (2.23)$$

As shown in equation (2.16), the H_2O_2 so formed in equation (2.23) can undergo cleavage upon light irradiation to produce more hydroxyl radicals.

In a typical electrolytic cell, oxidation of water occurs at the anode surface upon application of electrical energy according to equation (2.2). In photoelectrocatalytic system, therefore, oxidant species can be generated via photocatalytic process and electrolytic process. The applied bias potential minimises electron-hole recombination phenomenon and the photogenerated electrons are channeled away via the counter electrode. Direct electron transfer reactions, in which there is a transfer of electrons from the target pollutant to the anode, are also a possibility. In essence, the oxidation routes of organic contaminants in a photoelectrocatalytic set-up are multiple. Figure 2.3 gives an example of a photoelectrocatalytic cell.

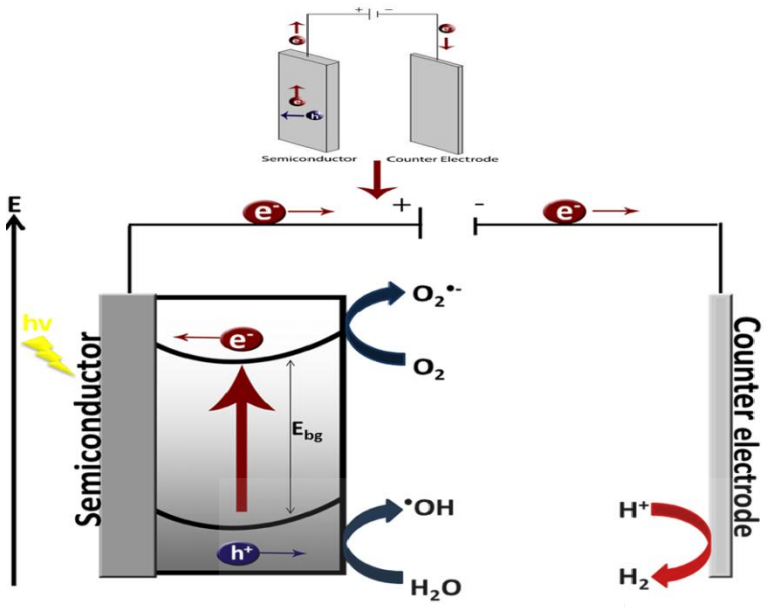

Fig. 2. 3. A diagrammatic representation of a photoelectrochemical/photoelectrocatalytic cell

As in anodic oxidation process, the nature of the electrode material also plays an important role in the photoelectrocatalytic process. Expectedly, any semiconductor that would be used as photoanode should have a suitable band gap and exhibit photochemical stability in aqueous media. Such material should offer high quantum yield and considerable adsorptive capability for the organic contaminant. It is also desirable that such photoanode material is capable of harvesting substantial portion of the visible spectrum, as this is important to address the question of sustainability and overall cost implications of the process.

There exist a substantial number of reports on photoelectrocatalytic/photoelectrochemical oxidation of organic pollutants at certain semiconducting materials. Most commonly, the films of these semiconductors are obtained on conductive substrates such as titanium sheets, indium tin oxide (ITO) glass and fluorine doped tin oxide (FTO) glass. Photoelectrocatalytic degradation of organic pollutants have been studied at semiconductors such as TiO_2 [97-99], ZnO [100, 101] ,

$BiVO_4$ [102, 103], WO_3 [104, 105] and/or their composites. Considerable attention has been given to improving the visible light absorption characteristics of semiconductors such as TiO_2 and ZnO which are only sensitive under UV irradiation. Specifically, tuning of the synthesis routes/procedures [106-108], incorporation of metallic and non-metallic impurities and band-gap engineering [109-113], coupling of two or more semiconductors [114-116] etc. to obtain catalysts with practicable solar light utilisation have been extensively investigated.

2.6 Electrode materials for electrochemical and photoelectrocatalytic oxidation

In this section, the descriptions and applications of the anode materials used in this study are reviewed.

2.6.1 Diamond

Diamond is an exciting allotrope of carbon and a rare gemstone which has been largely explored for various applications in various fields of science and engineering. The motivation for these investigations can be attributed, principally, to the many outstanding properties of diamond which include excellent mechanical strength, high thermal conductivity, electrical resistance, wide spectral range optical transparency, large band gap and chemical inertness [117, 118]. The extremely hard nature of diamond is as a result of its giant molecular structure, with each carbon atom in the structure covalently bonding to four other carbon atoms in a tetrahedral arrangement (Fig 2.4). Over a past few decades, diamond has been an attractive and promising material for innovative research in electrochemistry. It has been used in the development of electrodes for a myriad of purposes in electrochemical applications

such as sensing [119], electrochemical advanced oxidation processes, supercapacitors [120], electrosynthesis [121], photoelectrochemistry [122] and so on.

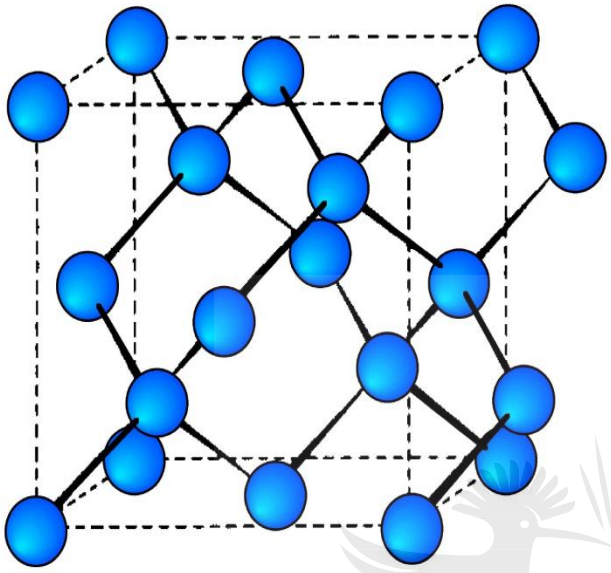

Fig. 2. 4. Structure of diamond [123]

Diamond-based electrodes offer suitable platform for many electrochemical studies because of the wide potential window, low signal-to-background current ratio, tunable electrical resistivity, high oxygen evolution potential, excellent chemical stability, and minimal susceptibility to fouling of diamond [124, 125]. However, pristine diamond is uninteresting to an electrochemist given its completely sp^3 hybridised structure which makes it electrically non-conductive. Iwaki *et al.* [126] and Pleskov *et al.* [127] conducted the early research on the use of diamond as electrode material. The former authors obtained electrically conductive diamond by argon and nitrogen implantation. The growth of high-quality diamond films via chemical vapour deposition (CVD) on conductive substrates have led to substantial advancements in diamond electrochemistry. With appropriate level of doping, semi-conductive, semi-metallic or superconductive diamond films can be obtained via CVD. Impurities such as boron,

nitrogen and phosphorus have been introduced into the lattices of diamond to induce electrical conductivity, with boron being the preferred dopant [128, 129]. Low-level boron doping (approximately 10^7 atoms cm^{-3}) of diamond produces p-type semiconducting diamond material and high-level doping (approximately 10^{20} atoms cm^{-3}) gives diamond with semi-metallic conductivity [14], with boron acting as an electron acceptor due to an electron deficiency in its external shell [130]. The widely used substrate for diamond films electrodes is p-silicon. This is primarily due to the facts that Si can form a compact self-limiting oxide and has a relatively low electrochemical activity, which prevents delamination. Si however is fragile and thus unsuitable for large-scale applications. Other substrates such as Nb, W, Zr, Ta etc. have been explored [14], but the questions of high costs and stability still remain unanswered. Ti substrate is cheap but poor adhesion of the diamond film to its surface is a drawback. While efforts are on to address these challenges, alternative electrode materials can be explored.

2.6.2 Graphene

Graphene is a one-atom thick and two-dimensional carbon sheet which has received enormous attention in the scientific community in the last few years. Considered single layer (Fig. 2.5 (a)) of stacked graphite sheets [131], stable sheets of graphene were first isolated in 2004 by Novoselov et al. using scotch tape method [132]. Monolayer graphene possesses excellent electrical, optical and mechanical properties and this makes it a candidate for many technological applications. These applications require bulk quantity of graphene which cannot be practically obtained by the simple scotch tape method [133]. Consequently, many researchers have been devoting lots of efforts to large-scale production of 'graphene' which can meet the demand. These graphene-related materials are not graphene in the real sense of it but the term has been extensively used in the literature to describe them. They often consist of few/multiple layers of graphene (Fig. 2.5 (b)) and sometimes hetero atoms (Fig. 2.5 (c)) and other

impurities (as is the case with those obtained by chemical treatment of graphite). These materials do not exhibit exactly the same properties of single layer graphene [134].

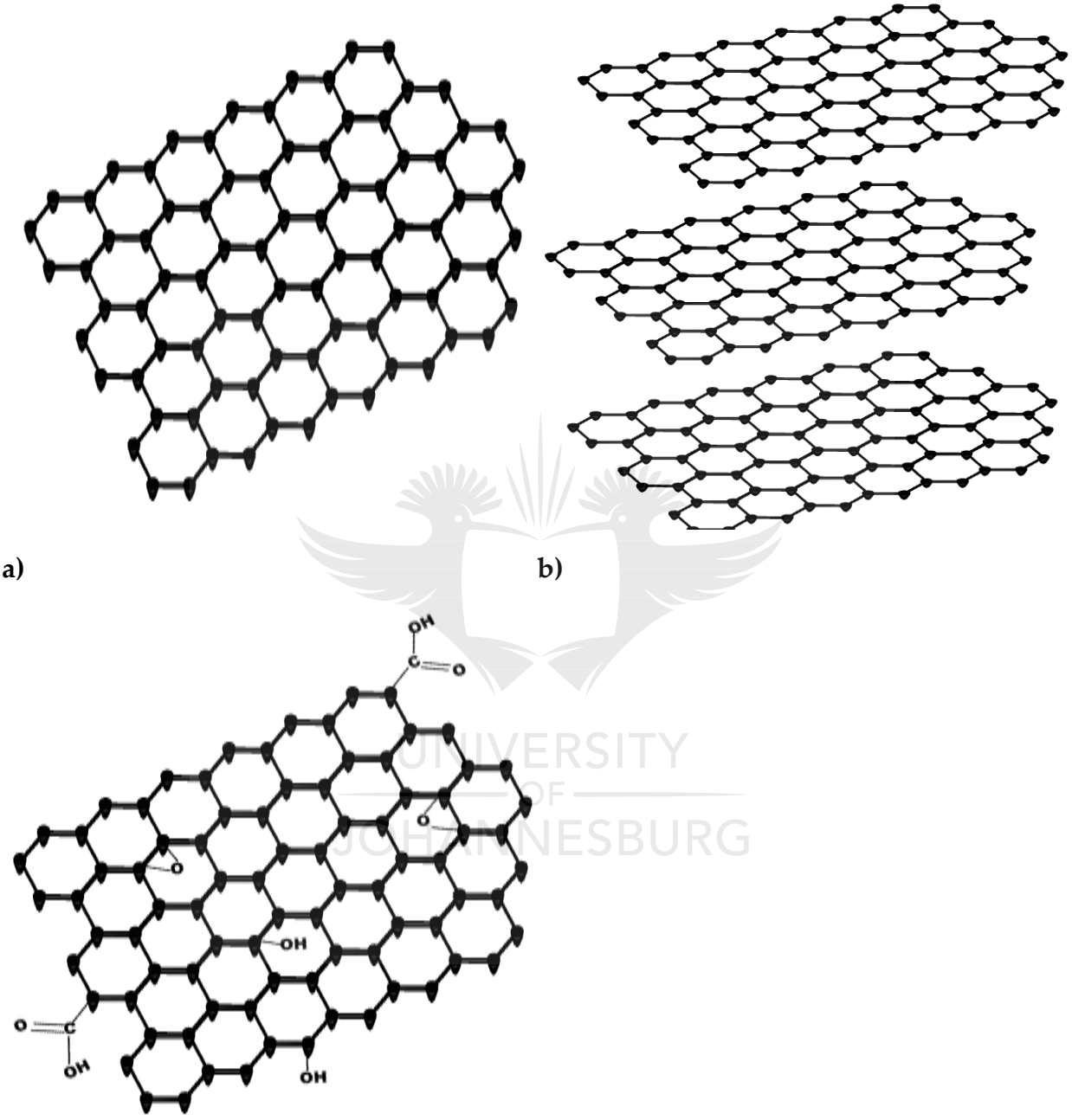

Fig. 2. 5. a) Single-layer, b) multiple-layer and c) chemically produced graphene.

The two properties of graphene which make it a desirable material for electrochemical applications are its excellent electrical conductivity and impressively large surface area. A single-layer graphene has a conductivity of 64 mS cm^{-1}, it can be considered a zero-gap semiconductor or a metal since it presents no gap between the valence band and conduction band [135]. The theoretical surface area of single-layer graphene is 2630 m^2/g [136], a value much larger for most carbon nanomaterials. Despite the exciting properties of pristine graphene, the particularly low density of defects present on it may present a major shortcoming when it comes to electron transfer properties. It has been reported that electron transfer kinetics is much better at defects or edge-like portions of carbon materials than at basal or defect-free planes [134, 137-139]. In electrochemical applications, particularly applications dealing with electro-oxidation of environmental analytes, chemically modified graphene materials have been largely utilised. The structural defects and the functional groups present on these materials have been found to be advantageous for electrochemical reactions [135, 140]. Such materials also exhibit impressive conductivity and considerably large surface area. The synthesis approach involves chemical oxidation of graphite to yield graphite oxide; the graphite oxide is then exfoliated via physical methods such as ultrasonic exfoliation or thermal shock. The graphene oxide obtained can then be subjected to chemical or thermal treatment to produce reduced graphene oxide. Graphene oxide and reduced graphene oxide have been widely applied for electro-oxidation (electrochemical sensing) of many analytes of environmental significance, including organics [141-143]. It is believed that compositing graphene with some other functional materials may offer synergistic benefits for electroanalysis. Hence, research efforts are still being geared towards obtaining graphene-based composites with improved electrochemical properties for oxidation of organic pollutants.

2.6.3 Exfoliated graphite

Natural graphite flakes can be intercalated by treatment with intercalating species which enter between the carbon layers of the graphite to yield what is called graphite intercalated compounds (GICs) [144]. Subjecting GICs to a thermal shock produces a worm-like, low-density carbon material known as exfoliated graphite (EG). The expansion of GICs occurs along the crystallographic c-axis when the intercalated species vapourise during heating process resulting in a puffed-up material [145]. EG possesses some splendid characteristics including low bulk density, large pore volume, high specific surface area, excellent electron transport property and high temperature resistance [146]. Bulk EG has been shown to be an excellent adsorbent for cleaning oil spills [147], it has been used for making gasket, thermal insulators, fire-resistant composite, conductive resin composites etc. [148]. EG has many pores into which nanoparticles can be accommodated, hence it is very useful for forming composite materials. In addition, EG particles can be compressed or compacted under a high pressure without the use of a binder. This compressible nature of EG allows its fabrication into electrodes. Its impressive electrical conductivity lends credence to its utilisation as electrode material. There are a few reports on the application of EG-based electrodes for electrochemical sensing/oxidation of heavy metals and organic substances [149-152].

2.6.4 Polyaniline

Polyaniline (PANI) is an electrically conductive polymer which has been explored for a variety of applications. Among the intrinsically conducting polymers, PANI has received tremendous attention because of its outstanding electrochemical and optical activities, stability in aggressive media, high thermal stability, unique doping/dedoping mechanism and ease of preparation [153, 154]. In addition, PANI is inexpensive and it gives a high yield of the polymerisation reaction [155]. Like other electrically

conducting polymers, PANI has a backbone of π-conjugated chain, a sequence of alternating single and double bonds which results in delocalization of π-electrons along the entire polymer chain [156-158]. The movement of electrons within the π system gives rise to conduction in the polymer [159].

PANI exhibits three redox states in its neutral base form, these include emeraldine base (Fig. 2.6 (a)), leucoemeraldine base (Fig. 2.6 (b)) and pernigraniline base (Fig. 2.6 (c)) [157, 160]. The emeraldine base displays the highest stability under ambient conditions. The leucoemeraldine base and pernigraniline base are products of complete oxidation and reduction respectively, of the emeraldine base. Exposure of the emeraldine base to strong acids leads to the formation of the green emeraldine salt of PANI. This protonation induces a change in the electronic structure of PANI; the quinoid ring is converted to benzenoid structure with associated spin unpairing. That is, the electronic structure now has a half-filled band and a metallic state [161]. As a result, the conductivity of the emelradine base progresses from that of a semiconductor to that of a metal. The emeraldine salt (Fig 2.6 (d)) is up to ten orders of magnitude more conductive than the unprotonated PANI [160]. PANI can be produced chemically or electrochemically by oxidative polymerisation of aniline. Upon oxidation of aniline monomer, a resonantly stabilised anilium radical is formed. The reaction is propagated in acidic media by the joining of anilium radical cations preferentially at the para-position [160]. While electrochemical approach offers advantage such as easier control over morphology and conductivity, it is unsuitable for mass production. Chemical synthesis, on the other hand, allows for morphology and conductivity control, and is suited for large-scale production [162].

PANI, given its unique properties, has been used in the manufacture of rechargeable batteries, catalysts, electromagnetic shielding materials, antistatic and anticorrosive coatings, separation membranes, electrooptic and electrochromic devices, supercapacitors, fuel, solar cells, actuators and sensors [163, 164].

In a study by Sha *et al.* [165], electro-oxidation of urea was carried out at the surface of graphene-PANI film. The high current response obtained at the composite film in the presence of the urea was attributed to the π electron system and large number of micropores present at the electrode which enhanced the interaction between analyte and the electrode surface. Hou *et al.* [166] also employed a nanocomposite of PANI for simultaneous electrochemical determination of uric acid and ascorbic acid in aqueous medium. The authors explained that the interaction between the cationic emeraldine salt and the ascorbic acid at the physiological pH promotes the detection of the analyte at the electrode surface. In another report by Karolia *et al.* [167], a composite of PANI and multi-walled carbon nanotubes was used to modify a glassy carbon electrode for sensitive the detection of omeprazole (a pharmaceutical). The authors claimed that the PANI in the composite allowed for the selective detection of the pharmaceutical. In the same vein, Zhang *et al.* [168] also reported the electrochemical detection of 4-nitrophenol at the surface of a glassy carbon modified with PANI and Ag nanoparticles. The authors observed a decrease in the reduction potential of the analyte and credited to the strong electrostatic interaction and hydrogen bonding between PANI and the phenolic compound.

In essence, the charges on PANI and the aromatic backbone are advantageous for interaction between PANI based composites and many target organic pollutants. Thus, PANI-based composites would offer a sensitive platform for electrochemical detection of organic molecules.

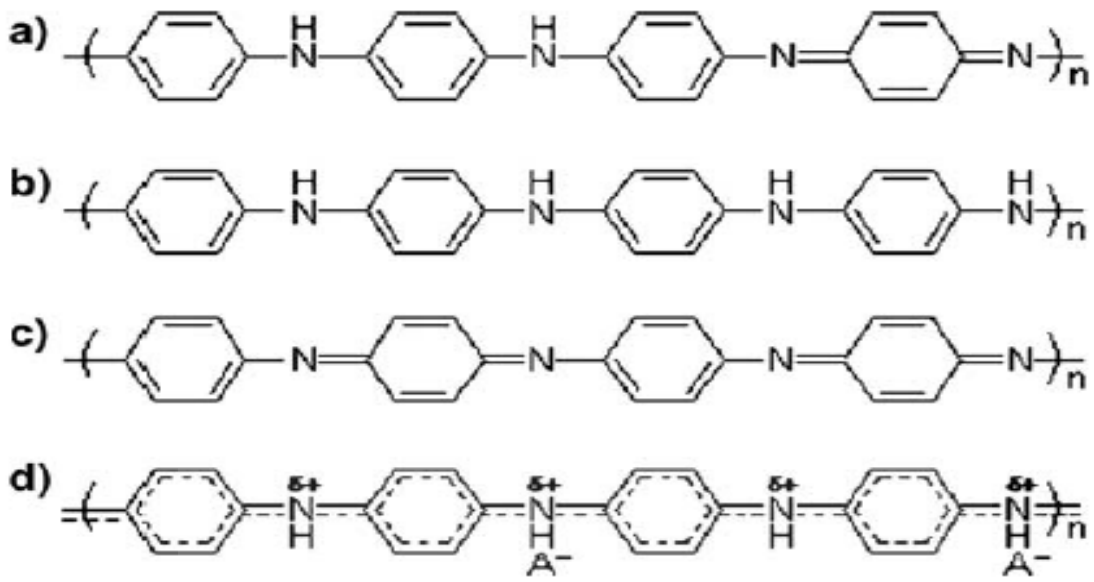

Fig. 2. 6. a) Emeraldine base, b) Leucoemeraldine base, c) Pernigraniline base, and d) Emeraldine salt [160].

2.6.5 Titanium dioxide

Titanium dioxide (TiO_2) is a semiconductor which has been widely used in many fields of science and technology. It is consumed in large quantities in the industrial production of paints, plastic and paper. It has been extensively explored as a photocatalyst for environmental and energy applications. Undoubtedly, TiO_2 still remains the most studied single-crystalline system in the surface science of metal oxide semiconductors. The outstanding properties of TiO_2 that make it a material of choice for many applications include chemical stability, non-toxicity and biocompatibility, and availability and low-cost. A vast body of literature exists on the use of TiO_2 in heterogeneous photocatalysis. Since the publication of the first report on water splitting at TiO_2 electrodes by Fujishima and Honda in 1972 [169], tremendous advances have been made in TiO_2 photocatalysis. This is connected to the high photocatalytic activity of TiO_2 which surpasses those of comparable semiconductors.

TiO_2 is an n-type semiconductor having a typical band-gap energy of 3.2 eV. This relatively wide gap requires high energy for the excitation of electron from the valence band of TiO_2. The catalyst must absorb photon with energy equal or higher than its band-gap energy for electron to be promoted from the valence band to the conduction band, leaving behind holes in the valence band. This energy requirement limits the application of TiO_2 with visible light as the energy obtainable within the visible region is inadequate. Doping of TiO_2 with metal and non-metal impurities has been indicated to extend its optical absorption to the visible region [170, 171]. Similarly, the crystalline phase of TiO_2 has also been shown to influence its photo-response under both the UV and visible light irradiation. TiO_2 exists in three crystalline phases, namely, rutile, anatase and brookite (Fig 2.7). Of these three polymorphs, the anatase has been shown to exhibit the best photocatalytic activity [170]. The photocatalytic performance of the rutile phase is relatively poor while the brookite phase has received little attention as a photocatalyst owing to its thermodynamic meta-stability [172]. Surface properties of the anatase phase possibly play a role in its superior photocatalytic activity. There are reports in which two phases combined (most commonly anatase and rutile) have been reported to display excellent photocatalytic activity [172, 173]. It is believed, for instance, that appropriate anatase/rutile ratio lead to improved photoactivity because of enhanced charge separation achieved in the catalyst structure. A junction is formed between the two crystalline phases which is beneficial for separation of photo-induced charges [174].

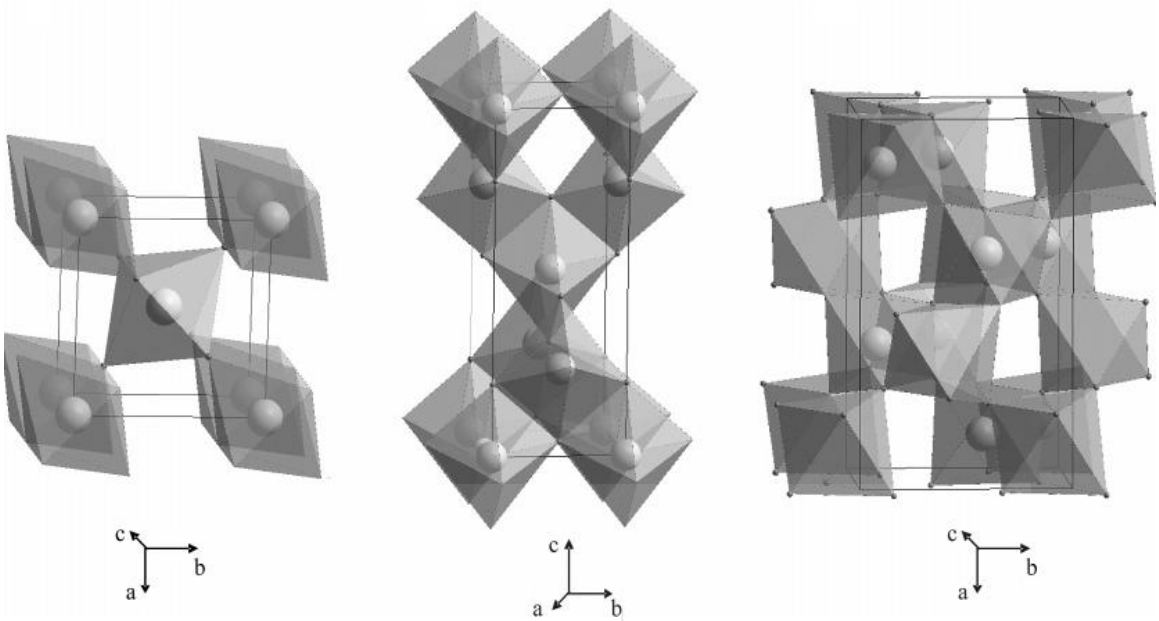

a) **b)** **(c**

Fig. 2. 7. The bulk structures of a) rutile, b) anatase, and (c brookite [175]

TiO_2 films for photoeletrocatalytic applications are prepared using a variety of methods including anodisation, sol-gel and coating, magnetron sputtering, chemical vapour deposition, cathodic deposition etc.

A porous or nanotube arrays (NTAs) of TiO_2 can be prepared by anodization of Ti metal in certain electrolytes. The titanium substrate is first cleaned and then introduced into the electrolytic solution. The anodisation is carried out using appropriate potentials for a specific duration. After anodisation process is complete, the Ti substrate is dried and annealed to obtain the crystalline TiO_2. Yajin JI [176] reported the preparation of TiO_2 NTAs by anodisation of Ti foil in a NH_4F/ethylene glycol solution at 120, 40 V for different time intervals. The obtained crystalline double-walled and bamboo-type structure was found to show superior photocatalyitc performance to single-layer TiO_2 NTAs. Adan *et al.* [177], in a related study, prepared TiO_2 NTAs by anodisation of Ti sheets in an electrolytic solution comprising ethylene glycol, water and NH_4F. The authors observed the effects of anodisation potentials and times on the morphology of

the photocatalyst formed and they reported that the thickness and the length of the nanotubes are linked to their photocatalytic and photoelectrocatalytic behaviours. In another interesting work by Dong *et al.* [178], a tubular-structure layer of TiO_2 was produced by two-step anodisation of Ti foil. After sintering, the top oxide layer was removed leaving exposed an inner layer of black TiO_2. The hexagonally dimpled layer of the black oxide, although has less surface area than the nanotubes, was said to display higher photocatalytic activity under visible light irradiation. Joseph and Sagayaraj [179] also studied the outcome of hydrogen peroxide (as a component of electrolytic solution) and potentials on the morphology of the TiO_2 NTAs synthesised via anodisation. Their results indicated that the pore diameter and the length of the nanotubes formed are dependent on the concentration of the H_2O_2 used. In addition, higher concentration of the peroxide was found to lead to the loss of the tubular structure of the TiO_2 produced. It was also inferred that applied potential influences the geometrical features of the nanotubes.

Anodisation has been shown to enable production of TiO_2 photoanodes with controllable nanoscale features and considerably high surface area. Stability of the NTAs is a key factor that is given due consideration when optimising anodisation conditions.

Furthermore, sol-gel is a well explored method to obtaining TiO_2 photocatalyst. In this approach, the precursors of the metal oxide is prepared and then hydrolysed. The titanium source can be inorganic or titanium alkoxide. The sol is subsequently coated onto a conductive substrate, dried and annealed to obtain the crystalline catalyst. Pablos *et al.* [98] prepared TiO_2 films on the surfaces of Ti and ITO glass by dipping the supports in a suspension of P25-TiO_2. The photoelectrocatalytic performance of the TiO_2/Ti and TiO_2/ITO electrodes were evaluated against that of a TiO_2 electrode prepared by annealing of Ti. Although the thermally prepared electrode was found to display superior properties for charge carrier separation upon application of bias

potential, the particulate TiO_2 electrodes appeared to be more effective for charge carrier transfer on TiO_2 and thus favour formation of hydroxyl radicals. TiO_2/Ti was reported to be most suitable for the degradation of the selected organic compound. The outstanding performance of this electrode was attributed firstly to the good charge carrier properties resulting from its particulate nature and then to the good interaction between the catalyst layer and the Ti substrate, which promotes charge carriers separation when an electric bias potential is applied. Islam and Basu [97] prepared a TiO_2/Ti electrode by dip-coating technique. Prior to coating, diethylene glycol was added to the TiO_2 sol and the mixture was thoroughly mixed. Citing Kajitvichyanukul and Amornchat [180], the authors submitted that the presence of the additive in the sol enhances the adhesion of the thin film to the surface of the substrate, improving the stability of the electrode. Sol-gel technique allows for flexible control of synthesis parameters and thus easy tunability of the properties of TiO_2 produced. In addition, other materials can be readily introduced into the reaction mixture to form composites or doped TiO_2.

Thin films of TiO_2 can also prepared using methods such as magnetron sputtering, chemical vapour deposition (CVD) and cathodic deposition. Magnetron sputtering involves the bombardment of a target material with energetic ions in the presence of a magnetic field at defined sputtering power, deposition time and gas partial pressure; leading to the deposition of the target material particles onto a given substrate. There exist a number of reports in which this technique was employed to prepare TiO_2 films for photoelectrocatalytic remediation of water contaminated by organics [181-185]. Chemical vapour deposition has also been employed to prepare TiO_2 photoanodes for oxidation of organics [186-188]. Here, the film is produced by the condensation of the catalyst onto a substrate when the catalyst volatile precursor is subjected to a high temperature and pressure under an inert atmosphere. In a study by Wu *et al.* [189], thin films of TiO_2 were prepared by cathodic deposition technique and used for the

destruction of orange G dye. TiO_2 for photoelectrocatalytic application have also been achieved by thermal treatment of Ti surface, resulting in the oxidation of the surface to yield the metal oxide [190, 191]. Materials such as graphite rods and exfoliated graphite have also been used as supports for nanoparticulate TiO_2 to fabricate TiO_2-based photoanodes for oxidation of organic pollutants [151, 192, 193].

In essence, the choice of preparation technique for TiO_2 thin film electrodes should be premised on factors such as film thickness control, electrode stability and service life, up-scalability, cost implications and simplicity amongst others.

2.6.6 Tungsten trioxide

Tungsten trioxide (WO_3) is notable as a semiconductor for electrochromic applications owing to its good stability in acidic media, strong adherence to immobilisation supports and large optical modulation [194]. It has also found applications in gas sensing and photocatalytic systems. WO_3 is found in five crystalline phases in the temperature range of -180 to 900 °C. These include tetragonal (α-WO_3, > 740 °C), orthorhombic (β-WO_3, 330 - 740°C), monoclinic I (γ-WO_3, 17 - 330 °C), triclinic (δ-WO_3, -43 - 17 °C) and monoclinic II (ε-WO_3, < -43 °C). Of these phases, γ-WO_3 exhibits the greatest stability in bulk WO_3 at room temperature [195, 196]. WO_3 is an n-type semiconductor with a fairly narrow band gap (2.4 -2.8 eV). WO_3, because of its narrow band gap, has visible light absorption capability close to about 500 nm of the solar spectrum [105, 197]. This makes it a candidate of interest for visible-light driven catalytic processes.

WO_3 has a valence band edge of about +3.1 V (vs NHE at pH = 0), which is sufficiently positive to drive water and/or organics oxidation [198]. The potential at the bottom of the conduction band is approximately +0.4 V (vs NHE at pH = 0). This value is below the hydrogen redox potential ($E_{H2/H2O}$ = 0 V vs NHE at pH = 0) [199, 200], hence hydrogen evolution or one-electron reduction of molecular oxygen is not energetically favoured at WO_3 [201, 202]. Build-up of electrons in WO_3 photocatalytic system

encourages rapid recombination of electron-hole pairs leading to poor photocatalytic activity especially of pristine WO_3.

However, the relatively high conductivity, low susceptibility to photocorrosion and considerable oxidation power of the valence band of WO_3 [203] holes have drawn attention to it as a potential anodic material for water purification. Given the fact that the bias potential which is usually applied in the photoelectrocatalytic system will serve to counter the recombination of charges at the semiconductor, WO_3 therefore may represent an impressive photoanode for organic pollutants oxidation.

Thin films of WO_3 have been prepared by a number of methods. Kim *et al.* [204] prepared a dispersion of WO_3 by mixing measured amounts of the catalyst, ethylene glycol and triton. The dispersion was drop-cast onto a titanium support, dried and thermally treated. Mohite *et al.* [104] also sythesised a film of WO_3 on a conductive substrate by dissolving tungsten powder in hydrogen peroxide and mixing the resulting peroxotungstic acid with ethanol to form the precursor solution. The WO_3 precursor was subsequently sprayed onto the preheated FTO glass substrate and annealed in air to produce the crystalline film. Longobucco *et al.* [105] reported preparation of two WO_3 films electrodes via colloidal solution and anodisation. The colloidal solution, which was obtained using sodium tungstate as starting material, was deposited onto cleaned FTO glass by spin-coating. The other electrode was prepared by accelerated potentiostaic anodisation of W sheet. The surface of the FTO glass coated with WO_3 suspension showed the presence of homogeneous and spherical particles with small size distribution while the surface of the anodised W sheet displayed roughly spherical and strongly fused particles with larger size. It is noteworthy however that the photoelectrocatalytic activities of both electrodes are comparable. In another work by Zhu *et al.* [197], WO_3/FTO electrode was prepared by doctor-blade method. The WO_3 paste was obtained by mixing the catalyst powder, previously prepared by hydrothermal process, with terpineol and ethyl cellulose. The cellulose

played the role of a binder. Vidyarthi *et al.* [205] prepared a polycrystalline WO_3 films by reactive magnetron sputtering using a very pure metallic tungsten target and a Ti coated silicon wafers substrate. The micro-structural features of the thin films produced were found to be dependent upon the applied sputter pressures. And the photocurrent responses of the films were influenced by their structures. There is also a report in which WO_3 nanoparticles were trapped in the pores of exfoliated graphite. The nanocomposite was pressed into pellets and subsequently fabricated into electrodes for photoelectrocatalytic degradation of a phenolic compound and a synthetic dye [206].

2.6.7 Bismuth vanadate

Layered bismuth vanadate ($BiVO_4$) exists in three crystal modifications: the monoclinic scheelite type and the tetragonal scheelite and zircon types (Fig. 2.8). The monoclinic $BiVO_4$ is an n-type semiconductor with a band-gap energy of 2.4 eV. It has been shown to exhibit superior photocatalytic activity compared with the other forms [207-209]. The valence band edge is favourably located for water oxidation while the conduction band edge is positioned just short of the energy level for hydrogen evolution [210, 211].

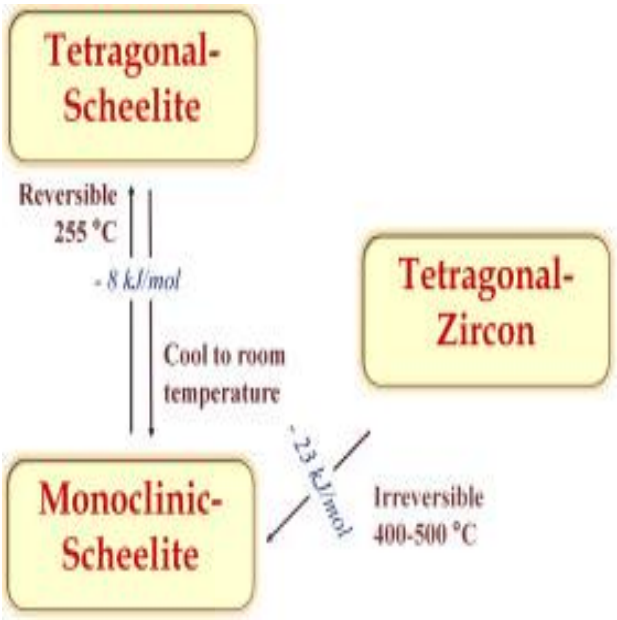

Fig. 2. 8. Diagrammatic representation of polymorphic transitions in $BiVO_4$ along with their formation enthalpies [212].

$BiVO_4$ is gaining attention as a photocatalyst for harvesting sunlight energy in photoelectrochemical water oxidation process [213-215], owing to its relatively small band-gap energy. Furthermore, $BiVO_4$ is stable to photocorrosion, non-toxic and consists of earth-abundant elements [216]. The major factor hampering its utilisation is its low photo-efficiency, resulting from the poor charges separation and transport properties, and poor water oxidation kinetics [216-218]. Much effort have been directed at ameliorating this challenge and exciting results have been reported in the literature, especially in the areas of water oxidation for hydrogen generation. However, reports on the use of $BiVO_4$ as photoanodes for degradation of organic contaminants are still very sparse. Xia et al.[102] reported on the photoelectrochemical performance of $BiVO_4$ and α-Fe_2O_3/$BiVO_4$. The photoanodes, fabricated by coating the precursor solutions of $BiVO_4$ and Fe_2O_3 onto FTO glass in a successive manner, displayed impressive incident photon-to-current efficiency (ICPE). Photoelectrocatalytic degradation of phenol at

these electrodes yielded very significant abatement in the chemical oxygen demand (COD) of the aqueous solution of the compound. Monfort *et al.* [103] also synthesised pure and Nb doped $BIVO_4$ by sol- gel method using Triton X-100 as structure-controlling agent. The films of the materials were deposited onto FTO glass by doctor-blade method. Both materials did not only show promise for hydrogen generation but also for degradation of Rhodamine B and stearic acid. There exist other articles in which $BiVO_4$ is combined with other well explored semiconductors for photoelectrocatalytic water treatment [114, 219].

2.7 References

[1] S. Malato, P. Fernández-Ibáñez, M.I. Maldonado, I. Oller, in: New and Future Developments in Catalysis, (Elsevier, Amsterdam, 2013).

[2] A. Heponiemi, U. Lassi, Advanced oxidation processes in food industry wastewater treatment-A review (INTECH Open Access Publisher, 2012).

[3] I. Sirés, E. Brillas, M.A. Oturan, M.A. Rodrigo, M. Panizza, Electrochemical advanced oxidation processes: today and tomorrow. A review, Environmental Science and Pollution Research 21 (2014) 8336-8367.

[4] J. Fenton , Oxidation of tartaric acid in presence of iron, Journal of the Chemical Society, Transactions 65 (1894) 899-910.

[5] A. Babuponnusami, K. Muthukumar, A review on Fenton and improvements to the Fenton process for wastewater treatment, Journal of Environmental Chemical Engineering 2 (2014) 557-572.

[6] F. Haber, J. Weiss, in: Proceedings of the Royal Society of London A: Mathematical, Physical and Engineering Sciences, (The Royal Society, 1934).

[7] A. Fischbacher, C. von Sonntag, T.C. Schmidt, Hydroxyl radical yields in the Fenton process under various pH, ligand concentrations and hydrogen peroxide/Fe (II) ratios, Chemosphere 182 (2017) 738-744.

[8] M. Usman, K. Hanna, S. Haderlein, Fenton oxidation to remediate PAHs in contaminated soils: A critical review of major limitations and counter-strategies, Science of the Total Environment 569 (2016) 179-190.

[9] L. Clarizia, D. Russo, I. Di Somma, R. Marotta, R. Andreozzi, Homogeneous photo-Fenton processes at near neutral pH: a review, Applied Catalysis B: Environmental (2017).

[10] D. Gümüş, F. Akbal, Comparison of Fenton and electro-Fenton processes for oxidation of phenol, Process Safety and Environmental Protection 103 (2016) 252-258.

[11] S. Ahmed, M. Rasul, W.N. Martens, R. Brown, M. Hashib, Heterogeneous photocatalytic degradation of phenols in wastewater: a review on current status and developments, Desalination 261 (2010) 3-18.

[12] U.I. Gaya, A.H. Abdullah, Heterogeneous photocatalytic degradation of organic contaminants over titanium dioxide: a review of fundamentals, progress and problems, Journal of Photochemistry and Photobiology C: Photochemistry Reviews 9 (2008) 1-12.

[13] M.N. Chong, B. Jin, C.W. Chow, C. Saint, Recent developments in photocatalytic water treatment technology: a review, Water Research 44 (2010) 2997-3027.

[14] B.P. Chaplin, Critical review of electrochemical advanced oxidation processes for water treatment applications, Environmental Science: Processes & Impacts 16 (2014) 1182-1203.

[15] W. Khongthon, G. Jovanovic, A. Yokochi, P. Sangvanich, V. Pavarajarn, Degradation of diuron via an electrochemical advanced oxidation process in a microscale-based reactor, Chemical Engineering Journal 292 (2016) 298-307.

[16] B. Marselli, J. Garcia-Gomez, P.-A. Michaud, M. Rodrigo, C. Comninellis, Electrogeneration of hydroxyl radicals on boron-doped diamond electrodes, Journal of the Electrochemical Society 150 (2003) D79-D83.

[17] R. Dewil, D. Mantzavinos, I. Poulios, M.A. Rodrigo, New perspectives for Advanced Oxidation Processes, Journal of Environmental Management 195 (2017) 93-99.

[18] J.-F. Zhi, H.-B. Wang, T. Nakashima, T.N. Rao, A. Fujishima, Electrochemical incineration of organic pollutants on boron-doped diamond electrode. Evidence for direct electrochemical oxidation pathway, The Journal of Physical Chemistry B 107 (2003) 13389-13395.

[19] E. Brillas, C.A. Martínez-Huitle, Decontamination of wastewaters containing synthetic organic dyes by electrochemical methods. An updated review, Applied Catalysis B: Environmental 166 (2015) 603-643.

[20] C.A. Martínez-Huitle, M.A. Rodrigo, I. Sirés, O. Scialdone, Single and coupled electrochemical processes and reactors for the abatement of organic water pollutants: a critical review, Chemical Reviews 115 (2015) 13362-13407.

[21] C. Comninellis, Electrocatalysis in the electrochemical conversion/combustion of organic pollutants for waste water treatment, Electrochimica Acta 39 (1994) 1857-1862.

[22] C.A. Martínez-Huitle, L.S. Andrade, Electrocatalysis in wastewater treatment: recent mechanism advances, Quimica Nova 34 (2011) 850-858.

[23] T. González, J.R. Domínguez, P. Palo, J. Sánchez-Martín, E.M. Cuerda-Correa, Development and optimization of the BDD-electrochemical oxidation of the antibiotic trimethoprim in aqueous solution, Desalination 280 (2011) 197-202.

[24] C.A. Martínez-Huitle, A. De Battisti, S. Ferro, S. Reyna, M.n. Cerro-López, M.A. Quiro, Removal of the pesticide methamidophos from aqueous solutions by

electrooxidation using Pb/PbO_2, Ti/SnO_2, and Si/BDD electrodes, Environmental Science & Technology 42 (2008) 6929-6935.

[25] B. Gargouri, O.D. Gargouri, I. Khmakhem, S. Ammar, R. Abdelhèdi, M. Bouaziz, Chemical composition and direct electrochemical oxidation of table olive processing wastewater using high oxidation power anodes, Chemosphere 166 (2017) 363-371.

[26] E. Brillas, A. Thiam, S. Garcia-Segura, Incineration of acidic aqueous solutions of dopamine by electrochemical advanced oxidation processes with Pt and BDD anodes, Journal of Electroanalytical Chemistry 775 (2016) 189-197.

[27] A.S. Fajardo, R.C. Martins, C.A. Martínez-Huitle, R.M. Quinta-Ferreira, Treatment of Amaranth dye in aqueous solution by using one cell or two cells in series with active and non-active anodes, Electrochimica Acta 210 (2016) 96-104.

[28] F. Sopaj, M.A. Rodrigo, N. Oturan, F.I. Podvorica, J. Pinson, M.A. Oturan, Influence of the anode materials on the electrochemical oxidation efficiency. Application to oxidative degradation of the pharmaceutical amoxicillin, Chemical Engineering Journal 262 (2015) 286-294.

[29] Y. He, W. Huang, R. Chen, W. Zhang, H. Lin, H. Li, Anodic oxidation of aspirin on PbO_2, BDD and porous Ti/BDD electrodes: Mechanism, kinetics and utilization rate, Separation and Purification Technology 156 (2015) 124-131.

[30] F. Guenfoud, M. Mokhtari, H. Akrout, Electrochemical degradation of malachite green with BDD electrodes: Effect of electrochemical parameters, Diamond and Related Materials 46 (2014) 8-14.

[31] F.C. Moreira, R.A. Boaventura, E. Brillas, V.J. Vilar, Electrochemical advanced oxidation processes: a review on their application to synthetic and real wastewaters, Applied Catalysis B: Environmental 202 (2017) 217-261.

[32] D. Bejan, E. Guinea, N.J. Bunce, On the nature of the hydroxyl radicals produced at boron-doped diamond and Ebonex® anodes, Electrochimica Acta 69 (2012) 275-281.

[33] S.O. Ganiyu, N. Oturan, S. Raffy, G. Esposito, E.D. van Hullebusch, M. Cretin, M.A. Oturan, Use of Sub-stoichiometric Titanium Oxide as a Ceramic Electrode in Anodic Oxidation and Electro-Fenton Degradation of the Beta-blocker Propranolol: Degradation Kinetics and Mineralization Pathway, Electrochimica Acta 242 (2017) 344-354.

[34] A.M. Zaky, B.P. Chaplin, Porous substoichiometric TiO_2 anodes as reactive electrochemical membranes for water treatment, Environmental Science & Technology 47 (2013) 6554-6563.

[35] O. Scialdone, A. Galia, G. Filardo, Electrochemical incineration of 1, 2-dichloroethane: effect of the electrode material, Electrochimica Acta 53 (2008) 7220-7225.

[36] A.S. Fajardo, H.F. Seca, R.C. Martins, V.N. Corceiro, I.F. Freitas, M.E. Quinta-Ferreira, R.M. Quinta-Ferreira, Electrochemical oxidation of phenolic wastewaters using a batch-stirred reactor with NaCl electrolyte and Ti/RuO_2 anodes, Journal of Electroanalytical Chemistry 785 (2017) 180-189.

[37] J. Radjenovic, M. Petrovic, Sulfate-mediated electrooxidation of X-ray contrast media on boron-doped diamond anode, Water Research 94 (2016) 128-135.

[38] A.Y. Bagastyo, D.J. Batstone, K. Rabaey, J. Radjenovic, Electrochemical oxidation of electrodialysed reverse osmosis concentrate on Ti/Pt–IrO_2, Ti/SnO_2–Sb and boron-doped diamond electrodes, Water Research 47 (2013) 242-250.

[39] J. Davis, J.C. Baygents, J. Farrell, Understanding persulfate production at boron doped diamond film anodes, Electrochimica Acta 150 (2014) 68-74.

[40] S.D. Jojoa-Sierra, J. Silva-Agredo, E. Herrera-Calderon, R.A. Torres-Palma, Elimination of the antibiotic norfloxacin in municipal wastewater, urine and seawater by electrochemical oxidation on IrO_2 anodes, Science of the Total Environment 575 (2017) 1228-1238.

[41] C.A. Martínez-Huitle, E. Brillas, Decontamination of wastewaters containing synthetic organic dyes by electrochemical methods: a general review, Applied Catalysis B: Environmental 87 (2009) 105-145.

[42] J. Boudreau, D. Bejan, S. Li, N.J. Bunce, Competition between electrochemical advanced oxidation and electrochemical hypochlorination of sulfamethoxazole at a boron-doped diamond anode, Industrial & Engineering Chemistry Research 49 (2010) 2537-2542.

[43] H.B. Ammar, M.B. Brahim, R. Abdelhédi, Y. Samet, Green electrochemical process for metronidazole degradation at BDD anode in aqueous solutions via direct and indirect oxidation, Separation and Purification Technology 157 (2016) 9-16.

[44] C. Salazar, N. Contreras, H.D. Mansilla, J. Yáñez, R. Salazar, Electrochemical degradation of the antihypertensive losartan in aqueous medium by electro-oxidation with boron-doped diamond electrode, Journal of Hazardous Materials 319 (2016) 84-92.

[45] F.L. Guzmán-Duque, R.E. Palma-Goyes, I. González, G. Peñuela, R.A. Torres-Palma, Relationship between anode material, supporting electrolyte and current density during electrochemical degradation of organic compounds in water, Journal of hazardous materials 278 (2014) 221-226.

[46] C. Ridruejo, C. Salazar, P.L. Cabot, F. Centellas, E. Brillas, I. Sirés, Electrochemical oxidation of anesthetic tetracaine in aqueous medium. Influence of the anode and matrix composition, Chemical Engineering Journal 326 (2017) 811-819.

[47] H. Zöllig, A. Remmele, C. Fritzsche, E. Morgenroth, K.M. Udert, Formation of chlorination byproducts and their emission pathways in chlorine mediated electro-oxidation of urine on active and nonactive type anodes, Environmental Science & Technology 49 (2015) 11062-11069.

[48] C.-C. Su, A.-T. Chang, L.M. Bellotindos, M.-C. Lu, Degradation of acetaminophen by Fenton and electro-Fenton processes in aerator reactor, Separation and Purification Technology 99 (2012) 8-13.

[49] M. Hassan, N. Pous, B. Xie, J. Colprim, M.D. Balaguer, S. Puig, Influence of iron species on integrated microbial fuel cell and electro-Fenton process treating landfill leachate, Chemical Engineering Journal 328 (2017) 57-65.

[50] H. Zhang, X. Ran, X. Wu, Electro-Fenton treatment of mature landfill leachate in a continuous flow reactor, Journal of Hazardous Materials 241 (2012) 259-266.

[51] S. Lanzalaco, I. Sirés, M.A. Sabatino, C. Dispenza, O. Scialdone, A. Galia, Synthesis of polymer nanogels by electro-Fenton process: investigation of the effect of main operation parameters, Electrochimica Acta 246 (2017) 812-822.

[52] F.C. Moreira, R.A. Boaventura, E. Brillas, V.J. Vilar, Degradation of trimethoprim antibiotic by UVA photoelectro-Fenton process mediated by Fe (III)–carboxylate complexes, Applied Catalysis B: Environmental 162 (2015) 34-44.

[53] A. Bedolla-Guzman, I. Sirés, A. Thiam, J.M. Peralta-Hernández, S. Gutiérrez-Granados, E. Brillas, Application of anodic oxidation, electro-Fenton and UVA photoelectro-Fenton to decolorize and mineralize acidic solutions of Reactive Yellow 160 azo dye, Electrochimica Acta 206 (2016) 307-316.

[54] F.C. Moreira, S. Garcia-Segura, V.J. Vilar, R.A. Boaventura, E. Brillas, Decolorization and mineralization of Sunset Yellow FCF azo dye by anodic oxidation, electro-Fenton, UVA photoelectro-Fenton and solar photoelectro-Fenton processes, Applied Catalysis B: Environmental 142 (2013) 877-890.

[55] Y. Wang, Y. Liu, K. Wang, S. Song, P. Tsiakaras, H. Liu, Preparation and characterization of a novel KOH activated graphite felt cathode for the electro-Fenton process, Applied Catalysis B: Environmental 165 (2015) 360-368.

[56] B. Garza-Campos, E. Brillas, A. Hernández-Ramírez, A. El-Ghenymy, J.L. Guzmán-Mar, E.J. Ruiz-Ruiz, Salicylic acid degradation by advanced oxidation processes. Coupling of solar photoelectro-Fenton and solar heterogeneous photocatalysis, Journal of Hazardous Materials 319 (2016) 34-42.

[57] L.C. Almeida, B.F. Silva, M.V. Zanoni, Photoelectrocatalytic/photoelectro-Fenton coupling system using a nanostructured photoanode for the oxidation of a textile dye: kinetics study and oxidation pathway, Chemosphere 136 (2015) 63-71.

[58] M. Saquib, M.A. Tariq, M. Haque, M. Muneer, Photocatalytic degradation of disperse blue 1 using UV/TiO_2/H_2 O_2 process, Journal of Environmental Management 88 (2008) 300-306.

[59] T. Gan, Z. Wang, Y. Wang, X. Li, J. Sun, Y. Liu, Flexible graphene oxide− wrapped SnO_2 hollow spheres with high electrochemical sensing performance in simultaneous determination of 4− aminophenol and 4− chlorophenol, Electrochimica Acta 250 (2017) 1-9.

[60] T. Spătaru, N. Spătaru, Voltammetric detection of phenol at platinum–polytyramine composite electrodes in acidic media, Journal of hazardous materials 180 (2010) 777-780.

[61] J. Ahmed, M.M. Rahman, I.A. Siddiquey, A.M. Asiri, M.A. Hasnat, Efficient Bisphenol-A detection based on the ternary metal oxide (TMO) composites by electrochemical approaches, Electrochimica Acta 246 (2017) 597-605.

[62] T.S. Cheng, M.Z.M. Nasir, A. Ambrosi, M. Pumera, 3D-printed metal electrodes for electrochemical detection of phenols, Applied Materials Today 9 (2017) 212-219.

[63] A.N. Kawde, M.A. Morsy, N. Odewunmi, W. Mahfouz, From electrode surface fouling to sensitive electroanalytical determination of phenols, Electroanalysis 25 (2013) 1547-1555.

[64] X. Yang, J. Kirsch, J. Fergus, A. Simonian, Modeling analysis of electrode fouling during electrolysis of phenolic compounds, Electrochimica Acta 94 (2013) 259-268.

[65] R. Sha, S.K. Puttapati, V.V. Srikanth, S. Badhulika, Ultra-sensitive phenol sensor based on overcoming surface fouling of reduced graphene oxide-zinc oxide composite electrode, Journal of Electroanalytical Chemistry 785 (2017) 26-32.

[66] D. Talarico, F. Arduini, A. Constantino, M. Del Carlo, D. Compagnone, D. Moscone, G. Palleschi, Carbon black as successful screen-printed electrode modifier for phenolic compound detection, Electrochemistry Communications 60 (2015) 78-82.

[67] V.V. Sharma, I. Gualandi, Y. Vlamidis, D. Tonelli, Electrochemical behavior of reduced graphene oxide and multi-walled carbon nanotubes composites for catechol and dopamine oxidation, Electrochimica Acta 246 (2017) 415-423.

[68] B.T.P. Quynh, J.Y. Byun, S.H. Kim, Non-enzymatic amperometric detection of phenol and catechol using nanoporous gold, Sensors and Actuators B: Chemical 221 (2015) 191-200.

[69] C. Pirvu, C.C. Manole, Electrochemical surface plasmon resonance for in situ investigation of antifouling effect of ultra thin hybrid polypyrrole/PSS films, Electrochimica Acta 89 (2013) 63-71.

[70] N. Al-Qasmi, M.T. Soomro, I.M. Ismail, E.Y. Danish, A.A. Al-Ghamdi, An enhanced electrocatalytic oxidation and determination of 2, 4-dichlorophenol on multilayer deposited functionalized multi-walled carbon nanotube/Nafion composite film electrode, Arabian Journal of Chemistry (2015).

[71] P. Ganesh, B.K. Swamy, Voltammetric resolution of catechol and hydroquinone at eosin Y film modified carbon paste electrode, Journal of Molecular Liquids 220 (2016) 208-215.

[72] Q. Wang, D. Zhang, L. Yang, L. Zhang, Constructed ILs@ hollow porous spherical Ni-loaded $CdFe_2O_4$ modified electrode for highly sensitive simultaneous electrochemical analysis of bisphenols, Sensors and Actuators B: Chemical 246 (2017) 800-808.

[73] J.-Y. Wang, Y.-L. Su, B.-H. Wu, S.-H. Cheng, Reusable electrochemical sensor for bisphenol A based on ionic liquid functionalized conducting polymer platform, Talanta 147 (2016) 103-110.

[74] Y. Zhang, L. Wu, W. Lei, X. Xia, M. Xia, Q. Hao, Electrochemical determination of 4-nitrophenol at polycarbazole/N-doped graphene modified glassy carbon electrode, Electrochimica Acta 146 (2014) 568-576.

[75] Y. Haldorai, K. Giribabu, S.-K. Hwang, C.H. Kwak, Y.S. Huh, Y.-K. Han, Facile synthesis of α-MnO_2 nanorod/graphene nanocomposite paper electrodes using a 3D precursor for supercapacitors and sensing platform to detect 4-nitrophenol, Electrochimica Acta 222 (2016) 717-727.

[76] A. Shah, M. Akhtar, S. Aftab, A.H. Shah, H.-B. Kraatz, Gold copper alloy nanoparticles (Au-Cu NPs) modified electrode as an enhanced electrochemical sensing platform for the detection of persistent toxic organic pollutants, Electrochimica Acta 241 (2017) 281-290.

[77] C.A. de Lima, P.S. da Silva, A. Spinelli, Chitosan-stabilized silver nanoparticles for voltammetric detection of nitrocompounds, Sensors and Actuators B: Chemical 196 (2014) 39-45.

[78] N.I. Ikhsan, P. Rameshkumar, N.M. Huang, Controlled synthesis of reduced graphene oxide supported silver nanoparticles for selective and sensitive electrochemical detection of 4-nitrophenol, Electrochimica Acta 192 (2016) 392-399.

[79] K. Rajesh, J. Santhanalakshmi, Design and development of graphene intercalated V_2O_5 nanosheets based electrochemical sensors for effective determination of potentially hazardous 3, 5–Dichlorophenol, Materials Chemistry and Physics 199 (2017) 497-507.

[80] N. Jović-Jovičić, Z. Mojović, M. Darder, P. Aranda, E. Ruiz-Hitzky, P. Banković, D. Jovanović, A. Milutinović-Nikolić, Smectite-chitosan-based electrodes in electrochemical detection of phenol and its derivatives, Applied Clay Science 124 (2016) 62-68.

[81] A. Azevedo, F. Souza, J. Matsushima, M. Baldan, N. Ferreira, Detection of phenol at boron-doped nanocrystalline diamond electrodes, Journal of Electroanalytical Chemistry 658 (2011) 38-45.

[82] M. Brycht, P. Lochyński, J. Barek, S. Skrzypek, K. Kuczewski, K. Schwarzova-Peckova, Electrochemical study of 4-chloro-3-methylphenol on anodically pretreated boron-doped diamond electrode in the absence and presence of a cationic surfactant, Journal of Electroanalytical Chemistry 771 (2016) 1-9.

[83] M.M. Hossain, L. Aldous, Polyoxometalates as solution-phase electrocatalytic mediators for reduced electrode fouling and the improved oxidative response of phenols, Electrochemistry Communications 69 (2016) 32-35.

[84] M.R. Hoffmann, S.T. Martin, W. Choi, D.W. Bahnemann, Environmental applications of semiconductor photocatalysis, Chemical reviews 95 (1995) 69-96.

[85] R. Ahmad, Z. Ahmad, A.U. Khan, N.R. Mastoi, M. Aslam, J. Kim, Photocatalytic systems as an advanced environmental remediation: Recent developments, limitations and new avenues for applications, Journal of Environmental Chemical Engineering 4 (2016) 4143-4164.

[86] E.R. Carraway, A.J. Hoffman, M.R. Hoffmann, Photocatalytic oxidation of organic acids on quantum-sized semiconductor colloids, Environmental science & technology 28 (1994) 786-793.

[87] M. Grela, M. Coronel, A. Colussi, Quantitative spin-trapping studies of weakly illuminated titanium dioxide sols. Implications for the mechanism of photocatalysis, The Journal of Physical Chemistry 100 (1996) 16940-16946.

[88] C.D. Jaeger, A.J. Bard, Spin trapping and electron spin resonance detection of radical intermediates in the photodecomposition of water at titanium dioxide particulate systems, Journal of Physical Chemistry 83 (1979) 3146-3152.

[89] H. Czili, A. Horváth, Applicability of coumarin for detecting and measuring hydroxyl radicals generated by photoexcitation of TiO_2 nanoparticles, Applied Catalysis B: Environmental 81 (2008) 295-302.

[90] Y. Jing, B.P. Chaplin, Mechanistic Study of the Validity of Using Hydroxyl Radical Probes To Characterize Electrochemical Advanced Oxidation Processes, Environmental science & technology 51 (2017) 2355-2365.

[91] J. Farner Budarz, A. Turolla, A.F. Piasecki, J.-Y. Bottero, M. Antonelli, M.R. Wiesner, Influence of aqueous inorganic anions on the reactivity of nanoparticles in TiO_2 photocatalysis, Langmuir 33 (2017) 2770-2779.

[92] S. Issarapanacheewin, K. Wetchakun, S. Phanichphant, W. Kangwansupamonkon, N. Wetchakun, Efficient photocatalytic degradation of Rhodamine B by a novel CeO_2/Bi_2WO_6 composite film, Catalysis Today 278 (2016) 280-290.

[93] K.-i. Ishibashi, A. Fujishima, T. Watanabe, K. Hashimoto, Detection of active oxidative species in TiO_2 photocatalysis using the fluorescence technique, Electrochemistry Communications 2 (2000) 207-210.

[94] T. Charbouillot, M. Brigante, G. Mailhot, P.R. Maddigapu, C. Minero, D. Vione, Performance and selectivity of the terephthalic acid probe for OH as a function of temperature, pH and composition of atmospherically relevant aqueous media, Journal of Photochemistry and Photobiology A: Chemistry 222 (2011) 70-76.

[95] Q. Xiao, L. Ouyang, Photocatalytic activity and hydroxyl radical formation of carbon-doped TiO_2 nanocrystalline: effect of calcination temperature, Chemical Engineering Journal 148 (2009) 248-253.

[96] D. Robert, S. Malato, Solar photocatalysis: a clean process for water detoxification, Science of the Total Environment 291 (2002) 85-97.

[97] M.M. Islam, S. Basu, Understanding photoelectrochemical degradation of methyl orange using TiO_2/Ti mesh as photocathode under visible light, Journal of Environmental Chemical Engineering 4 (2016) 3554-3561.

[98] C. Pablos, J. Marugán, R. van Grieken, C. Adán, A. Riquelme, J. Palma, Correlation between photoelectrochemical behaviour and photoelectrocatalytic activity and scaling-up of P25-TiO_2 electrodes, Electrochimica Acta 130 (2014) 261-270.

[99] C.-F. Liu, C. Huang, C.-C. Hu, Y. Juang, C. Huang, Photoelectrochemical degradation of dye wastewater on TiO_2-coated titanium electrode prepared by electrophoretic deposition, Separation and Purification Technology 165 (2016) 145-153.

[100] Z.-Q. Liu, P.-Y. Kuang, R.-B. Wei, N. Li, Y.-B. Chen, Y.-Z. Su, BiOBr nanoplate-wrapped ZnO nanorod arrays for high performance photoelectrocatalytic application, RSC Advances 6 (2016) 16122-16130.

[101] M. Fan, C. Yang, W. Pu, J. Zhang, Liquid phase deposition of ZnO film for photoelectrocatalytic degradation of p-nitrophenol, Materials science in semiconductor processing 17 (2014) 104-109.

[102] L. Xia, J. Bai, J. Li, Q. Zeng, L. Li, B. Zhou, High-performance BiVO 4 photoanodes cocatalyzed with an ultrathin α-Fe_2 O_3 layer for photoelectrochemical application, Applied Catalysis B: Environmental 204 (2017) 127-133.

[103] O. Monfort, S. Sfaelou, L. Satrapinskyy, T. Plecenik, T. Roch, G. Plesch, P. Lianos, Comparative study between pristine and Nb-modified $BiVO_4$ films employed for photoelectrocatalytic production of H_2 by water splitting and for photocatalytic degradation of organic pollutants under simulated solar light, Catalysis Today 280 (2017) 51-57.

[104] S. Mohite, V. Ganbavle, K. Rajpure, Solar photoelectrocatalytic activities of rhodamine-B using sprayed WO_3 photoelectrode, Journal of Alloys and Compounds 655 (2016) 106-113.

[105] G. Longobucco, L. Pasti, A. Molinari, N. Marchetti, S. Caramori, V. Cristino, R. Boaretto, C.A. Bignozzi, Photoelectrochemical mineralization of emerging contaminants at porous WO_3 interfaces, Applied Catalysis B: Environmental 204 (2017) 273-282.

[106] G. Meenakshi, A. Sivasamy, Synthesis and characterization of zinc oxide nanorods and its photocatalytic activities towards degradation of 2, 4-D, Ecotoxicology and environmental safety 135 (2017) 243-251.

[107] G. Byzynski, C. Melo, D.P. Volanti, M.M. Ferrer, A.F. Gouveia, C. Ribeiro, J. Andrés, E. Longo, The interplay between morphology and photocatalytic activity in ZnO and N-doped ZnO crystals, Materials & Design 120 (2017) 363-375.

[108] Q. Li, X. Sun, K. Lozano, Y. Mao, Dependence of Photoelectrochemical Properties on Geometry Factors of Interconnected "Caterpillar-like" ZnO Networks, Electrochimica Acta 222 (2016) 232-245.

[109] R. Asahi, T. Morikawa, T. Ohwaki, K. Aoki, Y. Taga, Visible-light photocatalysis in nitrogen-doped titanium oxides, science 293 (2001) 269-271.

[110] Y. Ma, L. Han, H. Ma, J. Wang, J. Liu, L. Cheng, J. Yang, Q. Zhang, Improving the visible-light photocatalytic activity of interstitial carbon-doped TiO_2 with electron-withdrawing bidentate carboxylate ligands, Catalysis Communications 95 (2017) 1-5.

[111] Q. Chen, H. Liu, Y. Xin, X. Cheng, Coupling immobilized TiO_2 nanobelts and Au nanoparticles for enhanced photocatalytic and photoelectrocatalytic activity and mechanism insights, Chemical Engineering Journal 241 (2014) 145-154.

[112] M. Salem, I. Massoudi, S. Akir, Y. Litaiem, M. Gaidi, K. Khirouni, Photoelectrochemical and opto-electronic properties tuning of ZnO films: Effect of Cu doping content, Journal of Alloys and Compounds (2017).

[113] I. Khan, A.A. Ibrahim, M. Sohail, A. Qurashi, Sonochemical assisted synthesis of RGO/ZnO nanowire arrays for photoelectrochemical water splitting, Ultrasonics Sonochemistry 37 (2017) 669-675.

[114] R. Wang, J. Bai, Y. Li, Q. Zeng, J. Li, B. Zhou, $BiVO_4/TiO_2$(N2) Nanotubes Heterojunction Photoanode for Highly Efficient Photoelectrocatalytic Applications, Nano-Micro Letters 9 (2017) 14.

[115] J. Li, S. Lv, Y. Liu, J. Bai, B. Zhou, X. Hu, Photoeletrocatalytic activity of an n-ZnO/p-Cu_2O/n-TNA ternary heterojunction electrode for tetracycline degradation, Journal of hazardous materials 262 (2013) 482-488.

[116] T. Guaraldo, V. Goncales, B. Silva, S. de Torresi, M. Zanoni, Hydrogen production and simultaneous photoelectrocatalytic pollutant oxidation using a TiO_2/WO_3 nanostructured photoanode under visible light irradiation, Journal of Electroanalytical Chemistry 765 (2016) 188-196.

[117] R. Balmer, J. Brandon, S. Clewes, H. Dhillon, J. Dodson, I. Friel, P. Inglis, T. Madgwick, M. Markham, T. Mollart, Chemical vapour deposition synthetic diamond: materials, technology and applications, Journal of Physics: Condensed Matter 21 (2009) 364221.

[118] J. Field, The mechanical and strength properties of diamond, Reports on Progress in Physics 75 (2012) 126505.

[119] P. Samiec, Ľ. Švorc, D.M. Stanković, M. Vojs, M. Marton, Z. Navrátilová, Mercury-free and modification-free electroanalytical approach towards bromazepam and alprazolam sensing: A facile and efficient assay for their quantification in pharmaceuticals using boron-doped diamond electrodes, Sensors and Actuators B: Chemical 245 (2017) 963-971.

[120] S. Yu, N. Yang, H. Zhuang, J. Meyer, S. Mandal, O.A. Williams, I. Lilge, H. Schönherr, X. Jiang, Electrochemical supercapacitors from diamond, The Journal of Physical Chemistry C 119 (2015) 18918-18926.

[121] T.A. Ivandini, Y. Einaga, Polycrystalline boron-doped diamond electrodes for electrocatalytic and electrosynthetic applications, Chemical Communications 53 (2017) 1338-1347.

[122] S. Pehlivanova, C. Petkov, C. Popov, P. Petkov, V. Boev, T. Petkova, in: Nanoscience Advances in CBRN Agents Detection, Information and Energy Security, (Springer, 2015).

[123] http://butane.chem.uiuc.edu/pshapley/GenChem2/C3/1.html. Accessed on 17 September 2017.

[124] J.V. Macpherson, A practical guide to using boron doped diamond in electrochemical research, Physical Chemistry Chemical Physics 17 (2015) 2935-2949.

[125] K. Cinková, C. Batchelor-McAuley, M. Marton, M. Vojs, Ľ. Švorc, R.G. Compton, The activity of non-metallic boron-doped diamond electrodes with sub-micron scale heterogeneity and the role of the morphology of sp^2 impurities, Carbon 110 (2016) 148-154.

[126] M. Iwaki, S. Sato, K. Takahashi, H. Sakairi, Electrical conductivity of nitrogen and argon implanted diamond, Nuclear Instruments and Methods In Physics Research 209 (1983) 1129-1133.

[127] Y.V. Pelskov, A.Y. Sakharova, M. Krotova, L. Bouilov, B. Spitsyn, Photoelectrochemical properties of semiconductor diamond, Journal of electroanalytical chemistry and interfacial electrochemistry 228 (1987) 19-27.

[128] Y. Zhang, S. Yoshihara, T. Shirakashi, T. Kyomen, Electrochemical characteristics of boron-doped, undoped and nitrogen-doped diamond films, Diamond and Related Materials 14 (2005) 213-219.

[129] M. Nesladek, Conventional n-type doping in diamond: state of the art and recent progress, Semiconductor Science and Technology 20 (2005) R19.

[130] F. Souza, C. Saez, M. Lanza, P. Canizares, M. Rodrigo, The effect of the sp 3/sp 2 carbon ratio on the electrochemical oxidation of 2, 4-D with P-Si BDD anodes, Electrochimica Acta 187 (2016) 119-124.

[131] A. Morgan, G. Somorjai, Low energy electron diffraction studies of gas adsorption on the platinum (100) single crystal surface, Surface Science 12 (1968) 405-425.

[132] K.S. Novoselov, A.K. Geim, S.V. Morozov, D. Jiang, Y. Zhang, S.V. Dubonos, I.V. Grigorieva, A.A. Firsov, Electric field effect in atomically thin carbon films, Science 306 (2004) 666-669.

[133] Y. Gogotsi, Controlling Graphene Properties through Chemistry, Guest Commentary, The Journal of Physical Chemistry Letters 2(19) (2011) 2509-2510.

[134] A. Ambrosi, C.K. Chua, A. Bonanni, M. Pumera, Electrochemistry of graphene and related materials, Chemical reviews 114 (2014) 7150-7188.

[135] A. Martin, A. Escarpa, Graphene: the cutting–edge interaction between chemistry and electrochemistry, TrAC Trends in Analytical Chemistry 56 (2014) 13-26.

[136] S. Stankovich, D.A. Dikin, G.H.B. Dommett, K.M. Kohlhaas, E.J. Zimney, E.A. Stach, R.D. Piner, S.T. Nguyen, R.S. Ruoff, Graphene-based composite materials, Nature 442 (2006) 282-286.

[137] D.K. Kampouris, C.E. Banks, Exploring the physicoelectrochemical properties of graphene, Chemical Communications 46 (2010) 8986-8988.

[138] D.A. Brownson, L.J. Munro, D.K. Kampouris, C.E. Banks, Electrochemistry of graphene: not such a beneficial electrode material?, RSC Advances 1 (2011) 978-988.

[139] L. Wang, M. Pumera, Electrochemical catalysis at low dimensional carbons: Graphene, carbon nanotubes and beyond–A review, Applied Materials Today 5 (2016) 134-141.

[140] S. Szunerits, R. Boukherroub, Electrochemistry of graphene: The current state of the art, in: Electrochemistry 12 (2013) 211-242.

[141] Q. Sun, L. Wang, L. Qi, C. Gu, J. Huang, Enhanced Electrochemical Determination of Trinitrophenol Based on Pyrenecyclodextrin Functionalized Reduced Graphene Oxide, Sensor Letters 11 (2013) 2227-2232.

[142] P. Kanyong, S. Rawlinson, J. Davis, A Voltammetric Sensor Based on Chemically Reduced Graphene Oxide-Modified Screen-Printed Carbon Electrode for the Simultaneous Analysis of Uric Acid, Ascorbic Acid and Dopamine, Chemosensors 4 (2016) 25.

[143] Y. Xiaowen, S. Kaixuan, C. Ji, L. Chun, S. Gaoquan, Electrochemical Biosensing Based on Graphene Modified Electrodes, Acta Chimica Sinica 72 (2014) 319-332.

[144] G. Chen, D. Wu, W. Weng, C. Wu, Exfoliation of graphite flake and its nanocomposites, Carbon 41 (2003) 619-621.

[145] A. Celzard, J. Mareche, G. Furdin, Modelling of exfoliated graphite, Progress in Materials Science 50 (2005) 93-179.

[146] M. Saidaminov, N. Maksimova, N. Sorokina, V. Avdeev, Effect of graphite nitrate exfoliation conditions on the released gas composition and properties of exfoliated graphite, Inorganic Materials 49 (2013) 883-888.

[147] F. Vieira, I. Cisneros, N. Rosa, G. Trindade, N. Mohallem, Influence of the natural flake graphite particle size on the textural characteristic of exfoliated graphite used for heavy oil sorption, Carbon 44 (2006) 2590-2592.

[148] T. Wei, Z. Fan, G. Luo, C. Zheng, D. Xie, A rapid and efficient method to prepare exfoliated graphite by microwave irradiation, Carbon 47 (2009) 337-339.

[149] J. Mafa, N. Mabuba, O. Arotiba, An Exfoliated Graphite Based Electrochemical Sensor for As (III) in Water, Electroanalysis 28 (2016) 1462-1469.

[150] T. Ndlovu, O.A. Arotiba, S. Sampath, R.W. Krause, B.B. Mamba, An exfoliated graphite-based bisphenol A electrochemical sensor, Sensors 12 (2012) 11601-11611.

[151] B. Ntsendwana, S. Sampath, B. Mamba, O. Arotiba, Photoelectrochemical oxidation of p-nitrophenol on an expanded graphite–TiO_2 electrode, Photochemical & Photobiological Sciences 12 (2013) 1091-1102.

[152] X. Guo, D. Li, J. Wan, X. Yu, Preparation and electrochemical property of TiO 2/nano-graphite composite anode for electro-catalytic degradation of ceftriaxone sodium, Electrochimica Acta 180 (2015) 957-964.

[153] X. Li, H. Zhang, G. Wang, Z. Jiang, A novel electrode material based on a highly homogeneous polyaniline/titanium oxide hybrid for high-rate electrochemical capacitors, Journal of Materials Chemistry 20 (2010) 10598-10601.

[154] L. Wang, X. Lu, S. Lei, Y. Song, Graphene-based polyaniline nanocomposites: preparation, properties and applications, Journal of Materials Chemistry A 2 (2014) 4491-4509.

[155] S.J. Son, H.S. Kim, D.J. Lee, Y.H. Lee, H.D. Kim, Surface graft polymerization of conducting polyaniline on waterborne poyurethane-urea film and its phenol sensing, Journal of Applied Polymer Science 127 (2013) 1643-1652.

[156] T. Sen, S. Mishra, N.G. Shimpi, Synthesis and sensing applications of polyaniline nanocomposites: a review, RSC Advances 6 (2016) 42196-42222.

[157] Y. Bu, Z. Chen, Role of polyaniline on the photocatalytic degradation and stability performance of the polyaniline/silver/silver phosphate composite under visible light, ACS applied materials & interfaces 6 (2014) 17589-17598.

[158] X. Lu, W. Zhang, C. Wang, T.-C. Wen, Y. Wei, One-dimensional conducting polymer nanocomposites: synthesis, properties and applications, Progress in Polymer Science 36 (2011) 671-712.

[159] S. Bhadra, D. Khastgir, N.K. Singha, J.H. Lee, Progress in preparation, processing and applications of polyaniline, Progress in Polymer Science 34 (2009) 783-810.

[160] J. Tarver, Y.-L. Loo, in: Conjugated Polymers: A Practical Guide to Synthesis, (The Royal Society of Chemistry, 2014).

[161] J. Anand, S. Palaniappan, D. Sathyanarayana, Conducting polyaniline blends and composites, Progress in Polymer Science 23 (1998) 993-1018.

[162] H.R. Tantawy, D.E. Aston, J.R. Smith, J.L. Young, Comparison of electromagnetic shielding with polyaniline nanopowders produced in solvent-limited conditions, ACS applied materials & interfaces 5 (2013) 4648-4658.

[163] G. Ćirić-Marjanović, Recent advances in polyaniline research: Polymerization mechanisms, structural aspects, properties and applications, Synthetic Metals 177 (2013) 1-47.

[164] A.A. Rakić, S. Trifunović, G. Ćirić-Marjanović, Dopant-free interfacial oxidative polymerization of aniline, Synthetic Metals 192 (2014) 56-65.

[165] R. Sha, K. Komori, S. Badhulika, Graphene–Polyaniline composite based ultra-sensitive electrochemical sensor for non-enzymatic detection of urea, Electrochimica Acta 233 (2017) 44-51.

[166] T. Hou, P. Gai, M. Song, S. Zhang, F. Li, Synthesis of a three-layered SiO_2@Au nanoparticle@ polyaniline nanocomposite and its application in simultaneous

electrochemical detection of uric acid and ascorbic acid, Journal of Materials Chemistry B 4 (2016) 2314-2321.

[167] P. Karolia, D. Tiwari, R. Jain, Electrocatalytic sensing of omeprazole, Ionics 21 (2015) 2355-2362.

[168] C. Zhang, S. Govindaraju, K. Giribabu, Y.S. Huh, K. Yun, AgNWs-PANI nanocomposite based electrochemical sensor for detection of 4-nitrophenol, Sensors and Actuators B: Chemical 252 (2017) 616-623.

[169] A. Fujishima, K. Honda, Electrochemical photolysis of water at a semiconductor electrode, Nature 238 (1972) 37-38.

[170] H. Zangeneh, A. Zinatizadeh, M. Habibi, M. Akia, M.H. Isa, Photocatalytic oxidation of organic dyes and pollutants in wastewater using different modified titanium dioxides: a comparative review, Journal of Industrial and Engineering Chemistry 26 (2015) 1-36.

[171] L.G. Devi, R. Kavitha, A review on non metal ion doped titania for the photocatalytic degradation of organic pollutants under UV/solar light: role of photogenerated charge carrier dynamics in enhancing the activity, Applied Catalysis B: Environmental 140 (2013) 559-587.

[172] Y. Cao, X. Li, Z. Bian, A. Fuhr, D. Zhang, J. Zhu, Highly photocatalytic activity of brookite/rutile TiO_2 nanocrystals with semi-embedded structure, Applied Catalysis B: Environmental 180 (2016) 551-558.

[173] C. Jia, X. Zhang, P. Yang, Construction of anatase/rutile TiO_2 hollow boxes for highly efficient photocatalytic performance, Applied Surface Science (2017).

[174] W.-K. Wang, J.-J. Chen, M. Gao, Y.-X. Huang, X. Zhang, H.-Q. Yu, Photocatalytic degradation of atrazine by boron-doped TiO_2 with a tunable rutile/anatase ratio, Applied Catalysis B: Environmental 195 (2016) 69-76.

[175] A. Beltran, L. Gracia, J. Andres, Density functional theory study of the brookite surfaces and phase transitions between natural titania polymorphs, The Journal of Physical Chemistry B 110 (2006) 23417-23423.

[176] J. Yajun, Growth mechanism and photocatalytic performance of double-walled and bamboo-type TiO 2 nanotube arrays, RSC Advances 4 (2014) 40474-40481.

[177] C. Adán, J. Marugán, E. Sánchez, C. Pablos, R. van Grieken, Understanding the effect of morphology on the photocatalytic activity of TiO_2 nanotube array electrodes, Electrochimica Acta 191 (2016) 521-529.

[178] J. Dong, J. Han, Y. Liu, A. Nakajima, S. Matsushita, S. Wei, W. Gao, Defective black TiO_2 synthesized via anodization for visible-light photocatalysis, ACS applied materials & interfaces 6 (2014) 1385-1388.

[179] S. Joseph, P. Sagayaraj, A cost effective approach for developing substrate stable TiO_2 nanotube arrays with tuned morphology: a comprehensive study on the role of H_2O_2 and anodization potential, New Journal of Chemistry 39 (2015) 5402-5409.

[180] P. Kajitvichyanukul, P. Amornchat, Effects of diethylene glycol on TiO_2 thin film properties prepared by sol–gel process, Science and technology of advanced materials 6 (2005) 344-347.

[181] C. Montero-Ocampo, A. Gago, G. Abadias, B. Gombert, N. Alonso-Vante, In situ photoelectrochemical/photocatalytic study of a dye discoloration in a microreactor

system using TiO_2 thin films, Environmental Science and Pollution Research 19 (2012) 3751-3762.

[182] R. Daghrir, P. Drogui, N. Delegan, M.A. El Khakani, Electrochemical degradation of chlortetracycline using N-doped Ti/TiO_2 photoanode under sunlight irradiations, Water research 47 (2013) 6801-6810.

[183] C.W. Yeh, K.R. Wu, in: Advanced Materials Research, (Trans Tech Publ, 2013) .

[184] M. Qamar, Q. Drmosh, M.I. Ahmed, M. Qamaruddin, Z.H. Yamani, Enhanced photoelectrochemical and photocatalytic activity of WO_3-surface modified TiO_2 thin film, Nanoscale research letters 10 (2015) 54.

[185] R. Daghrir, P. Drogui, N. Delegan, M.A. El Khakani, Removal of chlortetracycline from spiked municipal wastewater using a photoelectrocatalytic process operated under sunlight irradiations, Science of the Total Environment 466 (2014) 300-305.

[186] S. Han, X. Zhang, Q. Yu, L. Lei, Preparation of B-doped TiO_2/ITO film electrode by MOCVD and its visible-lightdriven photoelectrocatalytic properties, J. Chem. Eng. Chin. Univ 27 (2013) 488-493.

[187] C.-Y. Chang, Y.-H. Hsieh, Y.-Y. Chen, Photoelectrocatalytic degradation of sodium oxalate by TiO_2/Ti thin film electrode, International Journal of Photoenergy 2012 (2012).

[188] S. Han, X. Zhang, Q. Yu, L. Lei, Preparation of TiO_2/ITO film electrode by AP-MOCVD for photoelectrocatalytic application, Science China Chemistry (2012) 1-9.

[189] T.-F. Wu, W.-C. Lin, Y.-C. Hsiao, C.-H. Su, C.-C. Hu, C.-P. Huang, R. Muniyandi, Electrochemical Photocatalytic Degradation of Orange G Using TiO_2 Films Prepared by Cathodic Deposition, Journal of The Electrochemical Society 161 (2014) H762-H769.

[190] L. Özcan, S. Yurdakal, V. Augugliaro, V. Loddo, S. Palmas, G. Palmisano, L. Palmisano, Photoelectrocatalytic selective oxidation of 4-methoxybenzyl alcohol in water by TiO_2 supported on titanium anodes, Applied Catalysis B: Environmental 132 (2013) 535-542.

[191] D. Li, X. Cheng, X. Yu, Z. Xing, Preparation and characterization of TiO_2-based nanosheets for photocatalytic degradation of acetylsalicylic acid: influence of calcination temperature, Chemical Engineering Journal 279 (2015) 994-1003.

[192] G. Palmisano, V. Loddo, H.H. El Nazer, S. Yurdakal, V. Augugliaro, R. Ciriminna, M. Pagliaro, Graphite-supported TiO_2 for 4-nitrophenol degradation in a photoelectrocatalytic reactor, Chemical Engineering Journal 155 (2009) 339-346.

[193] D. Li, J. Jia, Y. Zhang, N. Wang, X. Guo, X. Yu, Preparation and characterization of Nano-graphite/TiO_2 composite photoelectrode for photoelectrocatalytic degradation of hazardous pollutant, Journal of hazardous materials 315 (2016) 1-10.

[194] M. Nunes, C. Moura, A.R. Hillman, C. Freire, Novel hybrid based on a poly [Ni (salen)] film and WO_3 nanoparticles with electrochromic properties, Electrochimica Acta 238 (2017) 142-155.

[195] J.Y. Zheng, G. Song, J. Hong, T.K. Van, A.U. Pawar, D.Y. Kim, C.W. Kim, Z. Haider, Y.S. Kang, Facile fabrication of WO_3 nanoplates thin films with dominant crystal facet of (002) for water splitting, Crystal Growth & Design 14 (2014) 6057-6066.

[196] Y. Li, Z. Tang, J. Zhang, Z. Zhang, Defect engineering of air-treated WO_3 and its enhanced visible-light-driven photocatalytic and electrochemical performance, The Journal of Physical Chemistry C 120 (2016) 9750-9763.

[197] J. Zhu, W. Li, J. Li, Y. Li, H. Hu, Y. Yang, Photoelectrochemical activity of $NiWO_4/WO_3$ heterojunction photoanode under visible light irradiation, Electrochimica Acta 112 (2013) 191-198.

[198] D. Raptis, V. Dracopoulos, P. Lianos, Renewable energy production by photoelectrochemical oxidation of organic wastes using WO_3 photoanodes, Journal of hazardous materials 333 (2017) 259-264.

[199] P. Dong, B. Yang, C. Liu, F. Xu, X. Xi, G. Hou, R. Shao, Highly enhanced photocatalytic activity of WO_3 thin films loaded with Pt–Ag bimetallic alloy nanoparticles, RSC Advances 7 (2017) 947-956.

[200] J.Y. Zheng, Z. Haider, T.K. Van, A.U. Pawar, M.J. Kang, C.W. Kim, Y.S. Kang, Tuning of the crystal engineering and photoelectrochemical properties of crystalline tungsten oxide for optoelectronic device applications, CrystEngComm 17 (2015) 6070-6093.

[201] A. Tanaka, K. Hashimoto, H. Kominami, Visible-light-induced hydrogen and oxygen formation over $Pt/Au/WO_3$ photocatalyst utilizing two types of photoabsorption due to surface plasmon resonance and band-gap excitation, Journal of the American Chemical Society 136 (2014) 586-589.

[202] S. Mohite, V. Ganbavle, V. Patil, K. Rajpure, Photoelectrocatalytic degradation of benzoic acid using immobilized tungsten trioxide photocatalyst, Materials Chemistry and Physics 183 (2016) 439-446.

[203] B. Weng, J. Wu, N. Zhang, Y.-J. Xu, Observing the role of graphene in boosting the two-electron reduction of oxygen in graphene–WO_3 nanorod photocatalysts, Langmuir 30 (2014) 5574-5584.

[204] G. Kim, E.T. Igunnu, G.Z. Chen, A sunlight assisted dual purpose photoelectrochemical cell for low voltage removal of heavy metals and organic pollutants in wastewater, Chemical Engineering Journal 244 (2014) 411-421.

[205] V.S. Vidyarthi, M. Hofmann, A. Savan, K. Sliozberg, D. König, R. Beranek, W. Schuhmann, A. Ludwig, Enhanced photoelectrochemical properties of WO_3 thin films fabricated by reactive magnetron sputtering, international journal of hydrogen energy 36 (2011) 4724-4731.

[206] E.H. Umukoro, M.G. Peleyeju, J.C. Ngila, O.A. Arotiba, Towards wastewater treatment: Photo-assisted electrochemical degradation of 2-nitrophenol and orange II dye at a tungsten trioxide-exfoliated graphite composite electrode, Chemical Engineering Journal 317 (2017) 290-301.

[207] P. Madhusudan, M.V. Kumar, T. Ishigaki, K. Toda, K. Uematsu, M. Sato, Hydrothermal synthesis of meso/macroporous $BiVO_4$ hierarchical particles and their photocatalytic degradation properties under visible light irradiation, Environmental Science and Pollution Research 20 (2013) 6638-6645.

[208] A. Kudo, K. Omori, H. Kato, A novel aqueous process for preparation of crystal form-controlled and highly crystalline $BiVO_4$ powder from layered vanadates at room temperature and its photocatalytic and photophysical properties, J. Am. Chem. Soc. 121 (1999) 11459-11467.

[209] S. Tokunaga, H. Kato, A. Kudo, Selective preparation of monoclinic and tetragonal $BiVO_4$ with scheelite structure and their photocatalytic properties, Chemistry of Materials 13 (2001) 4624-4628.

[210] P.S. Archana, Z. Shan, S. Pan, A. Gupta, Photocatalytic water oxidation at bismuth vanadate thin film electrodes grown by direct liquid injection chemical vapor deposition method, International Journal of Hydrogen Energy 42 (2017) 8475-8485.

[211] Y. Park, K.J. McDonald, K.-S. Choi, Progress in bismuth vanadate photoanodes for use in solar water oxidation, Chemical Society Reviews 42 (2013) 2321-2337.

[212] G. Nagabhushana, A. Tavakoli, A. Navrotsky, Energetics of bismuth vanadate, Journal of Solid State Chemistry 225 (2015) 187-192.

[213] K.R. Tolod, S. Hernández, N. Russo, Recent advances in the $BiVO_4$ photocatalyst for sun-driven water oxidation: Top-performing photoanodes and scale-up challenges, Catalysts 7 (2017) 13.

[214] C.M. Suarez, S. Hernández, N. Russo, $BiVO_4$ as photocatalyst for solar fuels production through water splitting: A short review, Applied Catalysis A: General 504 (2015) 158-170.

[215] B. Anke, M. Rohloff, M.G. Willinger, W. Hetaba, A. Fischer, M. Lerch, Improved photoelectrochemical performance of bismuth vanadate by partial O/F-substitution, Solid State Sciences 63 (2017) 1-8.

[216] J. Quiñonero, T. Lana–Villarreal, R. Gómez, Improving the photoactivity of bismuth vanadate thin film photoanodes through doping and surface modification strategies, Applied Catalysis B: Environmental 194 (2016) 141-149.

[217] H.W. Jeong, T.H. Jeon, J.S. Jang, W. Choi, H. Park, Strategic modification of $BiVO_4$ for improving photoelectrochemical water oxidation performance, The Journal of Physical Chemistry C 117 (2013) 9104-9112.

[218] J. Su, Z. Bai, B. Huang, X. Quan, G. Chen, Unique three dimensional architecture using a metal-free semiconductor cross-linked bismuth vanadate for efficient photoelectrochemical water oxidation, Nano Energy 24 (2016) 148-157.

[219] L. Xia, J. Bai, J. Li, Q. Zeng, X. Li, B. Zhou, A highly efficient $BiVO_4/WO_3/W$ heterojunction photoanode for visible-light responsive dual photoelectrode photocatalytic fuel cell, Applied Catalysis B: Environmental 183 (2016) 224-230.

CHAPTER THREE

3.0 METHODOLOGY

3.1 Introduction

This chapter gives a brief information about the basics and the application of various techniques used in this work.
The experimental methodologies followed to achieve the aims of the study are detailed in the experimental section of each result chapter.

3.2 Characterisation techniques

3.2.1 X-ray diffractometry

X-ray diffractometry (XRD) is an analytical technique which can provide both qualitative and quantitative information about a crystalline material. It is a versatile, non-destructive tool that can be used to gain insights into the crystal structure, crystal phase and crystal orientation of a material. In addition, information such as crystallinity, crystal defects, average grain size and strain of a powder can be obtained from XRD analysis. X-rays are produced when high-energy electrons hit a matter at a very high speed and their kinetic energy is converted into radiation. In practice, x-rays are generated when electrons emitted from a hot filament (cathode) are accelerated by an applied potential towards the anode. They are short-wavelength radiation, occupying the region between the gamma and the ultraviolet rays in the electromagnetic spectrum. The wavelength of x-rays are comparable with the size of atoms, hence, they are very appropriate for investigating the arrangement of atoms in a variety of crystalline materials. The energetic x-rays are capable of penetrating deep into the materials, providing useful information about the bulk structure.

In x-ray diffraction analysis, a beam of monochromatic x-rays is incident on a target sample (Fig. 3.1). The interaction between the atoms (electrons in the atom) of the sample and the x-rays produces constructive interference (and diffracted rays) when the Bragg's law is satisfied. The x-ray patterns generated during an analysis are characteristic of the crystals present in the sample. The intensity of the diffracted x-rays is collected as the sample is scanned over a range of 2θ angles.

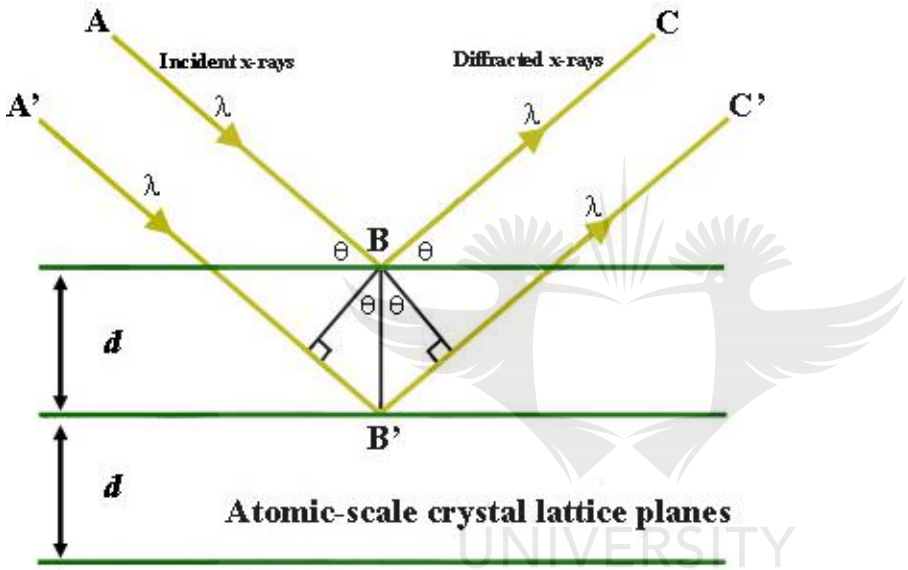

Fig. 3. 1. Incidence and diffraction of x-rays at the planes of a crystalline material [1]

The conditions of the Bragg's law include: The angle of incidence must be equal to the angle of scattering and the difference between the pathlengths must be an integer number of wavelength. The law provides general relationship between the wavelength of the incident x-rays, the angle of incidence and the spacing between the crystal lattice planes of atoms. It is expressed as:

$$n\lambda = 2d \sin\theta \qquad (3.1)$$

where n = a positive integer referred to as the order of diffraction and is often unity.

λ = wavelength of the radiation used

d = the lattice inter-planar spacing of the crystal, and

θ = is the angle between the incident (or diffracted) ray and the crystal plane (Bragg's angle)

2θ is defined as the scattering angle. The possible 2θ values where reflections can occur depend on the unit cell dimensions and the intensities of the reflections are determined by the nature of the atoms and their position in the unit cell.

X-ray diffraction analysis was used in this study to investigate the crystal planes and the crystal size of the materials used for the fabrication of the electrodes. The diffractometers were equipped with Cu Kα radiation source.

3.2.2 Infrared spectroscopy

Infrared (IR) spectroscopy is a versatile, non-destructive and non-contact analytical technique which provides a wealth of information on the chemical functional groups present in a sample. It is based on absorption of infrared radiation by molecules. The infrared radiation is that part of electromagnetic spectrum which lies between the visible and microwave regions. Irradiation of a molecule with infrared light induces vibrations within the molecule. Fundamentally, the bonds stretch or bend in response to the light. Chemical compounds absorb infrared radiation with energy corresponding to the energy involved in the vibrations of their bonds. Consequently, different functional groups absorb characteristic frequencies of the infrared radiation. Molecular vibrations appear as bands in the IR spectrum; these bands can be taken as fingerprints of the analysed sample. A change in electric dipole moment of a molecule during vibration is necessary for IR activity. The IR spectrum of any sample can be obtained within a few seconds and no elaborate sample preparation is required. The introduction of the

Fourier Transform principle in Fourier Transform Infrared (FTIR) spectrometers has upped the utilisation of IR spectroscopy to solve a wide range of analytical problems involving solid, liquid or gaseous samples [2]. This study utilised FTIR to obtain the characteristic IR peaks of the materials used to fabricate electrodes.

3.2.3 Raman spectroscopy

Raman spectroscopy is based on scattering of radiation by matter. When a beam of monochromatic light (from a laser) is incident on a chemical substance, the light is scattered. Most of the scattered radiation possesses the same frequency as that of the incident radiation (elastic scattering), while a very small fraction of the scattered radiation has a frequency different from that of the incident radiation (inelastic scattering) [3]. The inelastic scattering constitutes the Raman scattering. The Raman fraction is scattered with either lower or higher frequency than the incident light. Lower frequencies are called stokes scattering and higher frequencies are anti-stokes scattering. The anti-Stokes line is much less intense than the Stokes line. This occurs because only molecules that are vibrationally excited prior to irradiation can give rise to the anti-Stokes line. Hence, in Raman spectroscopy, only the more intense Stokes line is normally measured [4]. The energy change between the incident light and the inelastically scattered light relates to the transition between initial and final states of the scattering sample. This provides insights into the vibrational modes of the molecules. Active Raman vibrations are possible only in molecules that undergo change in polarizability during vibrations. Polarizability is related to electron cloud distribution within a molecule. Raman spectroscopy is complementary to IR spectroscopy, while IR tends to emphasise polar functional groups, Raman considers aromatic and carbon backbone in molecules. Raman spectroscopy is particularly well suited for examining the sp^2 and sp^3 hybridised structures of carbon materials. It can however be used for both qualitative and quantitative measurements of many other inorganic and organic

materials. In fact, Raman spectroscopy has been used for probing structure, dynamics and function of biological molecules [5, 6], for distinguishing between malignant tumors and normal body tissue [7, 8], for analysing pigments/inks in artworks [9] etc.
In this study, Raman spectroscopy was employed to investigate the chemical nature of and structural changes in some of the materials used.

3.2.4 UV-Visible spectroscopy

UV-Visible spectroscopy is based on the changes in the electronic states of a molecule upon irradiation with UV/visible light. When a sample with certain chemical group (chromophores) absorbs sufficient amount of light energy in the UV/visible region (200 - 800 nm) of the electromagnetic spectrum, there occurs an excitation of electrons from highest occupied molecular orbital (HOMO) to lowest unoccupied molecular orbital (LUMO). Various electron transitions are possible between the non-bonding orbital, bonding and anti-bonding sigma and pi orbitals. But most absorptions of UV/Visible light by organic molecules are based on excitation of non-bonding or bonding pi electrons to the anti-bonding pi orbital. These transitions result in absorbance bands at wavelengths highly characteristic of the difference in energy levels of the absorbing species [10]. The extent of absorption at different wavelengths is recorded and the wavelength of maximum absorption (λ_{max}) provides qualitative information about the molecule. The UV-Vis spectrum is a plot of optical absorbance against a wavelength range. The identity of a substance can be confirmed by comparing its spectrum with a standard/reference spectrum, although UV-vis spectra cannot be solely used to identify an unknown substance.
Quantitative measurement is possible with UV-Vis spectroscopy and it is guided by the Beer-Lambert's law. The law states that the extent of absorption by a molecule is directly proportional to the path length and the concentration of the molecule.
Mathematically,

$$A = \varepsilon cl \qquad (3.2)$$

where A is the absorbance which can be defined as $log\ (I_0/I)$, I_0 is the intensity of the incident light and I is the intensity of the transmitted light.

ε is molar absorptivity (extinction coefficient), which is constant for an organic compound at a given wavelength. It is determined by the nature and number of chromophores in the sample.

c is the molar concentration of the sample, and

l is the path length (in cm) of light through the sample

From the above the molar amount of a substance can be calculated from the absorbance values.

Unlike substances dissolved in liquid which allows transmission of incident light, solid substances are opaque and thus reflect UV-Vis light when incident on their surfaces. The incident light scattered in different directions is referred to as diffuse reflection. Electronic transition from the valence band to the conduction band within the solid is also possible upon light irradiation. The absorbance/reflectance data provide insights into the absorption features of the material in the UV/Visible region. Such data can be used, for instance, to compute the optical band-gap of a semiconductor using the popular Tauc's relation [11, 12]:

$$(\alpha h\upsilon) = A(h\upsilon - E_g)^n \qquad (3.3)$$

Where α is the absorption coefficient, h is the Planck's constant, υ is the photon frequency, A is a constant, E_g is the allowed energy gap, n = 1/2 for allowed direct transition n = 2 for allowed indirect transition [13]. The average band gap can be estimated from the intercept of linear portion of the $(\alpha h\upsilon)$ vs ($h\nu$) plot on $h\nu$ axis.

In this study, UV-Vis. spectroscopy was used to monitor the concentration abatement of the studied organic contaminants, and to study the optical absorption of the semiconductors.

3.2.5 Total Organic Carbon Analysis and Chemical Oxygen Demand

3.2.5.1 Total Organic Carbon

Total organic carbon (TOC) analysis is one way of monitoring the quality of water by measuring the overall amount of its carbon content. The TOC analysis is non-specific as it gives no information regarding the nature of the organic molecules present in the matrix, but gives the sum of the organic carbon in the molecules. It is thus useful for confirming the presence of organic contaminants in water. A typical polluted water sample often contains inorganic and organic substances. The total carbon in such sample comprises the organic carbon and the inorganic carbon. Analysis of TOC can be done by differential method or by direct approach. In the differential method the total carbon content and the inorganic carbon content of the water sample are measured separately. The TOC is then obtained by using the relation below:

$$TOC = TC - IC \qquad (3.4)$$

Where TC represents the total carbon content and IC is the total inorganic carbon

In the direct approach the inorganic carbon content is removed by purging the acidified sample with a pure gas, and the TOC is subsequently measured. This approach is unsuitable when the water sample contains purgeable organic substances such as benzene, toluene etc.

There exist a number of methods for measuring TOC, but the processes involved in these methods are the same. They include:

1. oxidation of the organic carbon to CO_2, and

2. measurement of the amount of the CO_2

To achieve number 1 above, common oxidation approaches including the use of chemical oxidising agents, catalytic combustion, exposure to ionising radiation etc. are employed. The concentration of the carbon dioxide produced can be quantified using a non-dispersive infrared gas (NDIR) analyser or by conductivity measurement.

In this study, Teledyne Tekmar TOC analyser (Fusion TOC analyser) was used to monitor TOC decay in treated water samples. The analyser utilises UV supported persulfate oxidant and NDIR detector. Standard solutions of potassium hydrogen phthalate (KHP) were used for instrument calibration. The procedure for the preparation of the reagents used for the TOC analysis is as follows:

i. Preparation of acid reagent: 188 mL of ultrapure water was measured into a clean glass bottle and 37 mL of 85% phosphoric acid was added to the water.

ii. Preparation of persulfate solution: 50 g of 98% sodium persulfate ($Na_2S_2O_8$) was weighed into a clean glass bottle, 426 mL of ultrapure water was added and the mixture was shaken until the salt was completely dissolved. Subsequently, 18 mL of 85% phosphoric acid was added to the solution.

The TOC values were reported in part per million (ppm).

3.2.5.2 Chemical Oxygen Demand

Chemical oxygen demand represents another means of measuring the amount of carbon content in water sample. COD method determines the amount of oxygen required to oxidise the dissolved organic matter under the conditions of oxidant, temperature and time. The quantity of oxidant consumed by the sample is equivalent to the amount of oxygen required to oxidise the organic matter. The amount of oxidant is chosen to be in excess of sample COD. Most COD testing systems now come with vials containing the oxidant solution (potassium dichromate, mercury sulfate and

sulfuric acid) and digestion unit. The sample is added to the test vial and both sample vial and blank vial are heated for a specified period. After cooling, the blank vial is used to zero a colorimeter/spectrophotometer and the sample reading is taken. The colorimeter/spectrophotometer reads the absorbance of the sample after digestion to determine how much of the dichromate is remaining or how much of the reduced form of the salt is formed [14]. This is then correlated to the COD concentration of the sample.

In this study, Hach COD testing system was used to determine the COD decay of the simulated wastewater after photoelectrocatalytic treatment.

3.2.6 Liquid Chromatography and Mass Spectrometry

Liquid chromatography-mass spectrometry (LC-MS) is a coupled technique which provides a platform for the sensitive detection and quantification of many analytes of interest. LC-MS combines the specificity of column liquid chromatography and the sensitivity of mass spectrometry to accurately analyse a myriad of chemical substances. Column liquid chromatography (LC) is a versatile technique for separating compounds in a mixture. The sample gets fractionated by differential migration through the stationary phase when the mobile phase flows through the stationary phase. Elution of the components of the sample occurs at different times because they have different migration rate which is determined by their interaction with the mobile phase and stationary phase [15]. The different fractions are then collected and directed to a detector which produces an electrical signal in form of a graph (chromatogram). In mass spectrometry, a neutral atom/molecule is bombarded with high-energy electrons resulting in ejection of electron(s) from the molecule. The radical cation (molecular ion) formed can undergo fragmentation to product ions, which in turn can fragment further into ions. The ions are then accelerated through a magnetic field where they are

deflected along circular paths according to their mass to charge ratio (m/e), and are detected in proportion to their abundance. The detector converts the electrical signals into a plot of ion abundance against m/e. In LC-MS, the liquid chromatograph is attached to a mass spectrometer via an appropriate interface. The compounds are separated in the LC and then passed to the MS for mass analysis. LC-MS is useful for the analysis of a complex matrix. It is very suitable for the analysis of non-volatile, thermally unstable and ionic molecules without the need for chemical modification of the sample.

In this study, LC-MS (Shimadzu LCMS 8030 (triple quad)) was used to investigate the intermediate products formed during the degradation of sulfamethoxazole. Details of the analysis are contained in chapter 6.

3.2.7 Scanning electron microscopy

Scanning electron microscopy (SEM) is an imaging technique which gives information on the surface morphology and composition of a material. The instrument is used to obtain information on an electrically conductive material by focusing a beam of high-energy electron on the surface of the material. A non-conductive surface is usually covered with a conductive layer (carbon or gold) prior to SEM analysis. The electron beam which is emitted from an electron gun and focused by electromagnetic lenses and an objective lens on a small spot on the specimen surface scans the surface in a rastal fashion [16]. The electron gun produces a divergent electron beam which is reconverged and focused by the electromagnetic lenses. The objective lens finally focuses the beam on the smallest possible spot on the surface of the specimen. The electron source is often demagnified up to about 5000x before hitting the sample [17]. The whole system from electron source, through the lenses, to the detector operates under a high vacuum. This is to avoid the loss of the emitted electrons to air. The incident electrons interact with the atoms of the sample to produce signals which are collected and processed by the

detector to provide information on the surface morphology and composition of the sample [18]. The interaction of the electron beam with the specimen atoms result in a number of signal types such as backscattered electrons, secondary electrons, Auger electrons, x-rays, plasmons etc.. Secondary electrons (SE) imaging mode is mostly used for imaging in SEM. Secondary electrons have low energy (less than 50 eV), thus they are generated from regions around the specimen surface and produce high lateral resolution signal.

In this work, SEM was used to investigate the morphology of the electrode materials.

3.2.8 Transmission electron microscopy

TEM operates basically on the same principle as SEM. The major difference lies in the interaction of the sample with the incident electrons. While the electrons are deflected away at the sample surface in SEM, they penetrate and pass through the sample in TEM. Because of the need for the electrons to penetrate the sample, TEM uses a higher accelerating voltage. The transmitted electrons are focused and projected onto the viewing device. The energy loss by electrons beam in the course of interaction with the specimen provides information about the elemental, chemical, and electronic states of the sample atoms. TEM presents a significantly higher magnification power than SEM. TEM imaging requires a very small sample but the sample preparation method is more intricate. The specimen must be electron-transparent, in other words, it must be thin enough for electron to pass through [19].

This study used TEM to obtain morphological data on some of the materials explored. Fine powders of the materials were dispersed in ethanol and sonicated for 60 min. Subsequently, a carbon-coated copper grid was carefully placed on a filter paper and a drop of the suspension was cast onto the copper grid. It was then allowed to dry under room conditions before analysis.

3.2.9 Energy Dispersive X-ray spectroscopy

Energy dispersive x-ray spectroscopy (EDS/EDX) is an analytical technique which is used for the identification of element(s) that are contained in a material. The EDS system is often coupled to electron microscopes (SEM or TEM) [20]. The x-rays generated from the impact of electron beam on the solid sample in SEM/TEM imaging are analysed by EDS system to provide information on the elemental composition of the material. This is so because the energy of the emitted x-rays is characteristic of the atoms in the bombarded specimen. EDS can also be used for quantitative measurement using appropriate standard. The intensity of the spectrum lines corresponding to the element is measured against calibration standards. In addition, EDS is useful for elemental mapping, an exercise to determine the relative concentration of the elements present in the scanned area. In this study EDS analysis was used to confirm the presence of constituent elements in prepared semiconducting materials.

3.2.10 Brunauer-Emmet-Teller analysis

Brunauer-Emmet-Teller (BET) analysis is used to measure the specific surface area of materials. It is based on the theory of gas adsorption onto a solid surface that was put forward by Stephen **Brunauer**, Paul **Emmet** and Edward **Teller** in 1938 [21]. BET theory is an extension of Irving Langmuir adsorption theory [22]. BET theory considers multilayer adsorption of gas molecules onto a solid surface. The amount of gas molecules adsorbed depends on the exposed surface and on factors such as temperature, gas pressure and the strength of the interaction between the adsorbate and the adsorbent. In a typical BET analysis, nitrogen gas is adsorbed onto the surface of the test sample at the boiling temperature of liquid nitrogen (77 K) and certain pressure conditions created by partial vacuum. The adsorption progresses until saturation is

achieved and no more adsorption of the gas molecules onto the solid surface can occur at elevated pressure. The adsorbed gas molecules are then desorbed at elevated temperature and quantified. BET isotherm can be obtained from the plot of the volume of the adsorbed gas molecules against the relative pressure (P/P_0). The BET surface area of the powder sample is determined from the isotherm. Pore volume and pore size distribution of a material can also be deduced from a BET analysis [23]. Nitrogen gas is used in BET analysis because of its availability and considerable interaction with most solids, although other gases such as argon and carbon dioxide are also used in some cases. Prior to analysis, the measured sample is degassed under vacuum at high temperature (at which the sample is still thermally stable). This is to remove adsorbed water molecules and other contaminants which can introduce error to the analysis.

In this study, Shimadzu (Micromeritics ASAP 2010) BET surface analyser was used to determine the surface area of some of the explored materials. About 0.3 g of the sample was used for each analysis. Degassing and analysis conditions were chosen according to the nature of each material.

3.3 Electrochemical techniques

3.3.1 Cyclic voltammetry

Cyclic voltammetry is a versatile technique which offers qualitative information about electrochemical reactions. It can be used to study the thermodynamics of redox processes, kinetics of heterogeneous electron-transfer reactions, analysis of coupled electrochemical reactions or adsorption processes [24, 25]. Cyclic voltammetry (CV) experiment is usually carried out using three-electrode system. The system consists of the working electrode on which the reaction of interest occurs or which possesses the interface of interest; the reference electrode which has a known potential and thus allows the measurement of the potential at the working electrode; and the

counter/auxiliary electrode which serves to close the current circuit in an electrochemical cell. The electrochemical cell (Fig. 3.2) contains the chosen electrolyte (the liquid interface or solution of the substance under investigation), with the three electrodes inside it and the electrodes are connected to appropriate lines on the potentiostat. The electrodes are stationary and the electrolyte is undisturbed/unstirred.

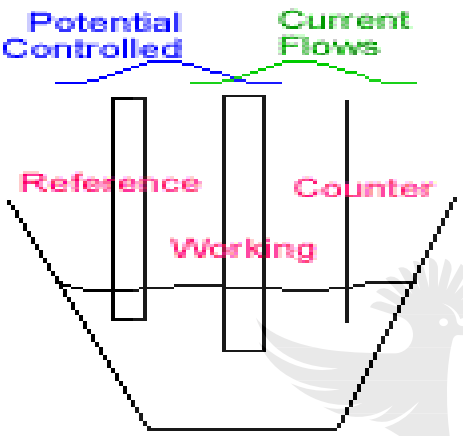

Fig. 3. 2. A typical three-electrode electrochemical cell [26]

In CV experiment, a potential which changes with time is applied to the working electrode [27]. The potential of the working electrode is scanned from an initial value, E_1 to a final value E_2 and then in a reverse direction to complete the cycle. The starting potential is determined such that the chemical species of interest are not initially oxidised or reduced. Also the upper limit potential is chosen so that the oxidation/reduction of the species under investigation occurs within the potential interval E_2 -E_1 [27]. The cycle can be repeated depending on the information needed from the experiment. The applied potential gives rise to a current response which is plotted against the voltage (potential). This plot of current vs voltage is referred to as cyclic voltammogram (Fig. 3.3). The voltammogram formed often depends on the standard rate constant, the formal redox potential and the diffusion coefficient of the

redox couple, the selected lower and upper potentials and the potential scan rate amongst others [27].

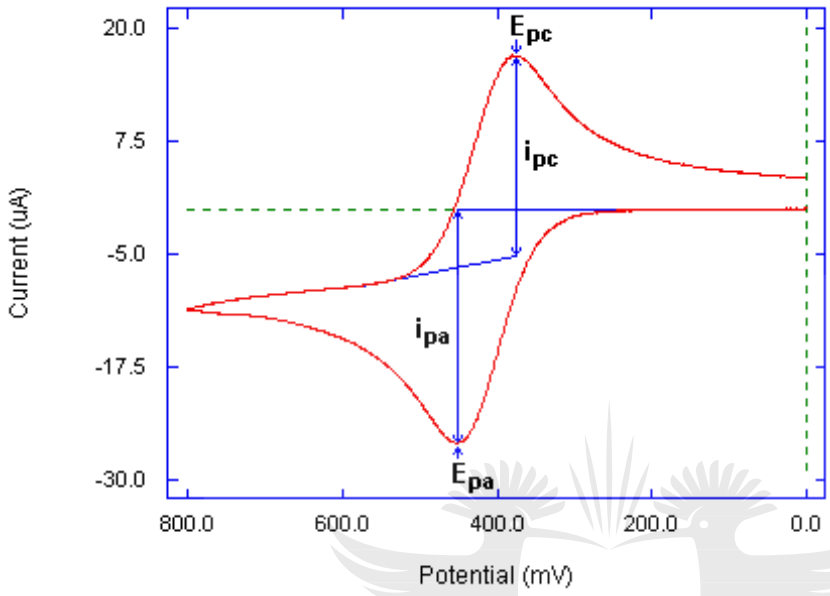

Fig. 3. 3. A typical cyclic voltammogram [28]

A cyclic voltammogram contains important data which provide insights into the nature of electrodes or electro-active substance under investigation. These include the peak potentials (anodic, E_{pa} and cathodic, E_{pc}) and peak currents (anodic, I_{pa} and cathodic, I_{pc}) (Fig. 3.3). A cyclic voltammogram can be reversible, quasi-reversible or irreversible.

For electrochemical reversibility, the following conditions are satisfied [29]:

1. The ratio of anodic peak current to cathodic peak current is unity (i.e. $I_{pa} = I_{pc}$). The peak current for a reversible couple at 298 K can be calculated using the Randles-Sevcik equation:

$$i_p = (2.69 \times 10^5).\, n^{3/2}.ACD^{1/2}.v^{1/2} \qquad (3.5)$$

where i_p is the peak current, n is number of electrons, A is area (cm^2) of the electrode, C is concentration ($mol.cm^{-3}$), D is the diffusion coefficient ($cm^2.s^{-1}$) and v is the scan rate

(Vs^{-1}). From this equation, it is clear that peak current varies directly with the concentration

2. Peak current is directly proportional to the square root of scan rate

3. The formal potential of the redox couple is centered between the anodic peak potential and the cathodic peak potential (i.e. $E^0 = (E_{pa} + E_{pc})/2$).

4. The separation between the peak potentials, E_{pa} - E_{pc} (ΔE_p) = 0.059V/n for an n-electron couple. This peak separation can be used to determine the number of electrons transferred and as a criterion for Nernstian behaviour.

5. The peak potentials are not dependent on the scan rate.

While the current in a reversible process is a function of charge transfer, that of a quasi-reversible process is controlled by both charge transfer and mass transport. The separation of the peak potentials is larger and the voltammogram is more drawn out compared to that of the reversible process [30]. As the peak potentials separation increases, the process approaches irreversibility. A totally irreversible system is characterised by a shift in the peak potential with scan rate. The peak current is given by

$$i_p = (2.99 \times 10^5).n\,(\alpha n_a)^{1/2}.ACD^{1/2}.v^{1/2} \qquad (3.6)$$

where α is the transfer coefficient and n_a is the number of electrons involved in the charge transfer step. The peak current is still directly related to the concentration of the analyte but the height is lower and dependent on the transfer coefficient [30].

In this work, CV experiments were conducted to investigate the electrochemical behaviours of the fabricated and modified electrodes.

3.3.2 Square wave voltammetry

Square wave voltammetry (SWV) is a pulse voltammetric technique in which a potential waveform is applied to the working electrode and pairs of current measurements are then made for each wave period [29]. A square wave is superimposed on a staircase, with the forward pulse of the square wave coinciding with the staircase step (Fig. 3.4) [31]. The square wave has pulse height/square wave amplitude, the staircase height, the pulse time and the cycle period [27]. The difference between the current associated with the forward pulse and the current of the reverse pulse gives the net current response [32]. A plot of the net current against applied potential gives the square wave voltammogram. The peak height is directly proportional to the concentration of the electro-active species in solution.

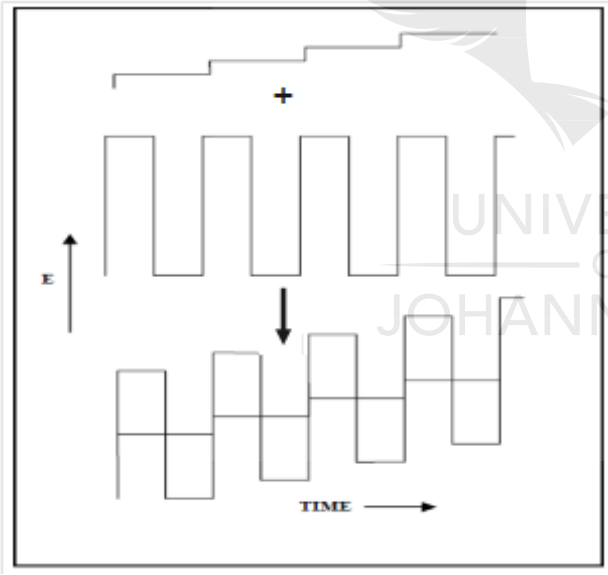

Fig. 3. 4. Schematic illustration of superimposition of a square wave on a potential staircase in SWV [33].

SWV has gained tremendous attention as a technique for quantitative analysis. This is owing to its excellent sensitivity (with detection limit as low as 10^{-8} M) to surface-

confined electrode reactions and significant elimination of capacitive contribution to current [27, 34]. In addition, SWV is preferred to other pulse voltammetric techniques such as the normal pulse voltammetry and differential pulse voltammetry because it offers more rapid analysis [35].

In this study SWV was employed for the quantitative analysis of phenols in aqueous media.

3.3.3 Electrochemical impedance spectroscopy

Electrochemical impedance spectroscopy (EIS) is a technique in which a sinusoidal potential excitation is applied to an electrochemical cell and the resulting alternating current signal is measured and analysed. Usually an electrochemical system is probed by applying a small amplitude sinusoidal excitation signal over a broad range of frequencies. The applied potential can be expressed as:

$$E_t = E_0 \, Sin(\omega t) \qquad (3.7)$$

Where E_t is the potential at time t, E_0 is the amplitude of the signal, ω is the radial frequency. The radial frequency is defined as follows:

$$\omega = 2\pi f \qquad (3.8)$$

where f is the frequency in Hertz.

A sinusoidal potential produces a sinusoidal current having the same frequency as the applied potential but with characteristic phase-shift. For small excitations, the response is pseudo-linear (Fig. 3.5).

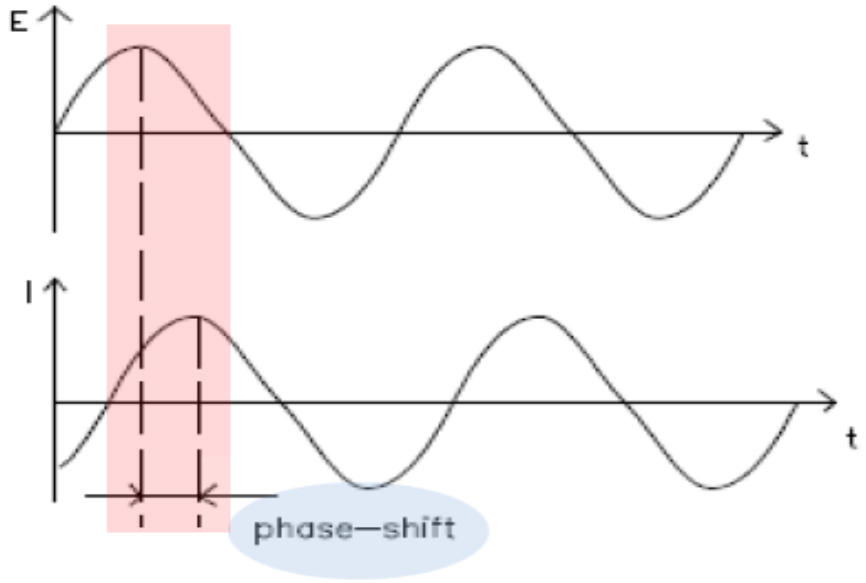

Fig. 3. 5. Sinusoidal current response to a small excitation signal as a function of time [36]

The response signal can be expressed as:

$$I_t = I_0 \sin(\omega t + \phi) \qquad (3.9)$$

Where I_t is the response at time t, I_0 is the amplitude and ϕ is the phase shift.

The resistance of an electrical circuit can be determined from Ohm's law (R = V/I). Impedance is a frequency-dependent resistance. Thus, impedance (Z) can be defined in terms of alternating potential and current as functions of time [37].

$$Z = \frac{E_t}{I_t} \qquad (3.10)$$

Substituting (3.7) and (3.9) into (3.10) give

$$Z = \frac{E_0 \sin(\omega t)}{I_0 \sin(\omega t + \phi)} \qquad (3.11)$$

Equation (3.11) can be simplified to:

$$Z = Z_0 \frac{Sin(\omega t}{Sin(\omega t + \phi)} \qquad (3.12)$$

Equation (3.12) defines the impedance in terms of magnitude of Z_0 and phase angle, ϕ. Impedance can also be represented as a complex quantity using Euler's relationship (Equation 3.13). This is mathematically equivalent to the vector representation described by equation 3.12.

$$e^{j\phi} = Cos\phi + jSin\phi \text{ (where } j = (-1)^{1/2}) \qquad (3.13)$$

$$Z(\omega) = Z_0 \frac{e^{j\omega t}}{e^{j(\omega t-\phi)}} = Z_0 (Cos\phi + jSin\phi) \text{ (where } E_t = e^{j\omega t} \text{ and } I_t = e^{j(\omega t-\phi)}) \qquad (3.14)$$

Impedance, $Z(\omega)$ comprises a real ($ReZ = Z' = Z_0Cos\phi$) and an imaginary part ($ImZ = Z'' = Z_0Sin\phi$).

A plot of the imaginary part against the real part gives a Nyquist plot (Fig. 3.6)

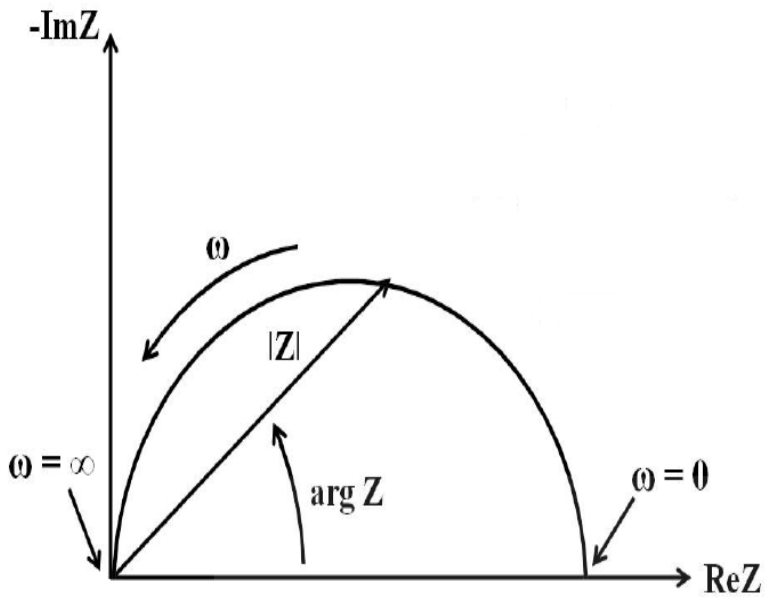

Fig. 3. 6. A typical Nyquist plot **[38]**

Each point on the Nyquist plot is impedance at one frequency. Impedance can be represented as a vector with length |Z| and the angle between the vector and x-axis is the phase angle, ϕ (arg Z). Nyquist plots are based on equivalent circuits. An equivalent circuit is composed of elements such as resistor, capacitor and inductors. Each element in the circuit corresponds to an activity in the electrochemical cell. Parameters such as electrolytic solution resistance, electrode polarization resistance, double layer capacitance etc. can be evaluated using Nyquist plots. Nyquist plot, however, offers no information on frequency. Another useful way of presenting EIS data is Bode plots. In Bode plots, the x-axis contains the logarithm of frequency while the y-axis has both the absolute values of impedance and the phase shift (Fig. 3.7). Bode plots provide clearer description of the frequency-dependent behaviour of electrochemical cell compared to Nyquist plot [37].

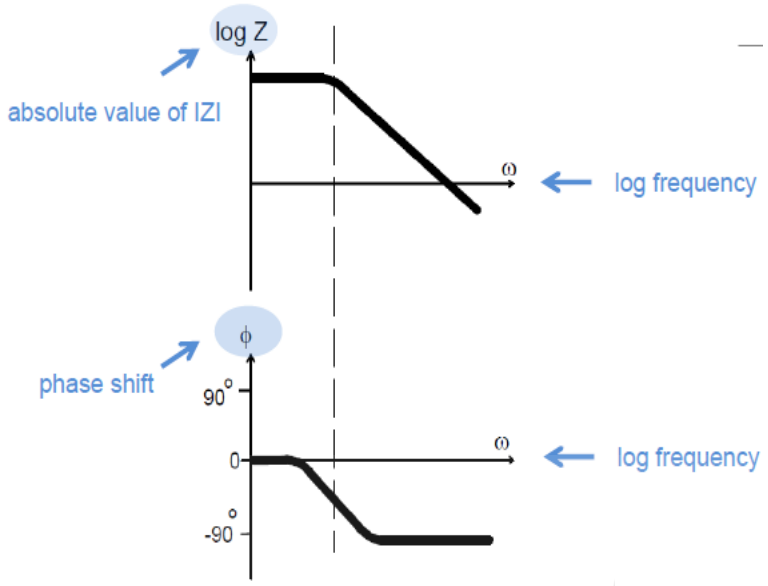

Fig. 3. 7. Diagrammatic representation of Bode plot [36]

3.3.4 Chronopotentiometry

Chronopotentiometry is an electrochemical technique in which a current is applied to the working electrode and the resulting voltage is measured against a reference electrode as a function of time [40]. In chronopotentiometry, a constant current can be applied to the working electrode to effect the oxidation/reduction of the species in an electrolytic solution. The species in solution diffuse to the surface of the electrode where they are oxidised/reduced. The solution is stirred to enhance the rate of mass transfer to the electrode surface. The magnitude of the current is often inversely related to the electrolysis time, although an optimum value may be reached. In addition, the rate of decomposition of the analyte is also largely affected by the area of the electrode. Large electrodes tend to favour rapid degradation.

3.4 References

[1] https://serc.carleton.edu/research_education/geochemsheets/BraggsLaw.html (Accessed 25 September 2017)

[2] Z. Bacsik, J. Mink, G. Keresztury, FTIR spectroscopy of the atmosphere. I. Principles and methods, Applied Spectroscopy Reviews 39 (2004) 295-363.

[3] A. Kudelski, Analytical applications of Raman spectroscopy, Talanta 76 (2008) 1-8.

[4] G.S. Bumbrah, R.M. Sharma, Raman spectroscopy–Basic principle, instrumentation and selected applications for the characterization of drugs of abuse, Egyptian Journal of Forensic Sciences 6 (2016) 209-215.

[5] N. Gierlinger, M. Schwanninger, The potential of Raman microscopy and Raman imaging in plant research, Spectroscopy 21 (2007) 69-89.

[6] M. Baranska, H. Schulz, P. Rösch, M.A. Strehle, J. Popp, Identification of secondary metabolites in medicinal and spice plants by NIR-FT-Raman microspectroscopic mapping, Analyst 129 (2004) 926-930.

[7] P.R. Jess, D.D. Smith, M. Mazilu, K. Dholakia, A.C. Riches, C.S. Herrington, Early detection of cervical neoplasia by Raman spectroscopy, International journal of cancer 121 (2007) 2723-2728.

[8] R.E. Kast, G.K. Serhatkulu, A. Cao, A.K. Pandya, H. Dai, J.S. Thakur, V.M. Naik, R. Naik, M.D. Klein, G.W. Auner, Raman spectroscopy can differentiate malignant tumors from normal breast tissue and detect early neoplastic changes in a mouse model, Biopolymers 89 (2008) 235-241.

[9] L. Bellot-Gurlet, C. Coupry, Raman spectroscopy in art and archaeology, Journal of Raman Spectroscopy 37 (2006) 962-965.

[10] T. Owen, Fundamentals of modern UV-visible spectroscopy 2000, Agilent technologies 73.

[11] J. Tauc, A. Menth, States in the gap, Journal of Non-Crystalline Solids 8 (1972) 569-585.

[12] S. Mehta, S. Kumar, S. Chaudhary, K. Bhasin, Nucleation and growth of surfactant-passivated CdS and HgS nanoparticles: time-dependent absorption and luminescence profiles, Nanoscale 2 (2010) 145-152.

[13] A. Tumuluri, K.L. Naidu, K.J. Raju, Band gap determination using Tauc's plot for $LiNbO_3$ thin films, Chem Tech 6 (2014) 3353-3356.

[14] A.M. Jirka, M.J. Carter, Micro semiautomated analysis of surface and waste waters for chemical oxygen demand, Analytical chemistry 47 (1975) 1397-1402.

[15] B. Ismail, S.S. Nielsen, in: Food Analysis, (Springer, 2010).

[16] in: CIRP Encyclopedia of Production Engineering, eds L. Laperrière, G. Reinhart (Springer Berlin Heidelberg, Berlin, Heidelberg, 2014).

[17] R. Reichelt, in: Science of microscopy, (Springer, 2007).

[18] Y. Zhu, H. Inada, in: Encyclopedia of Nanotechnology, ed B. Bhushan (Springer Netherlands, Dordrecht, 2012).

[19] D.B. Williams, C.B. Carter, in: Transmission electron microscopy, (Springer, 1996).

[20] C. Hollerith, D. Wernicke, M. Bühler, F. Feilitzsch, M. Huber, J. Höhne, T. Hertrich, J. Jochum, K. Phelan, M. Stark, Energy dispersive X-ray spectroscopy with microcalorimeters, Nuclear Instruments and Methods in Physics Research Section A: Accelerators, Spectrometers, Detectors and Associated Equipment 520 (2004) 606-609.

[21] S. Brunauer, P.H. Emmett, E. Teller, Adsorption of gases in multimolecular layers, Journal of the American Chemical Society 60 (1938) 309-319.

[22] I. Langmuir, The adsorption of gases on plane surfaces of glass, mica and platinum, Journal of the American Chemical Society 40 (1918) 1361-1403.

[23] M. Lawrence, Y. Jiang, in: Bio-aggregates Based Building Materials, (Springer, 2017).

[24] D.A. Brownson, C.E. Banks, in: The Handbook of Graphene Electrochemistry, (Springer, 2014).

[25] F. Marken, A. Neudeck, A.M. Bond, in: Electroanalytical methods, (Springer, 2010).

[26] https://www.kutztown.edu/academics/colleges-and-departments/liberal-arts-and sciences/departments/physical-sciences/chemistry-and biochemistry/instrumentation/voltammetry.htm (Accessed 05 October 2017)

[27] R.G. Compton, C.E. Banks, Understanding voltammetry (World Scientific, 2011).

[28] https://www.basinc.com/manuals/EC_epsilon/Techniques/CycVolt/cv_analysis Accessed 05 October 2017

[29] P. Monk, Fundamentals of electroanalytical chemistry. 2001, England: John Wiley & Sons Ltd.

[30] J. Wang, Analytical electrochemistry (John Wiley & Sons, 2006).

[31] S.P. Kounaves, (Prentice Hall, Upper Saddle River, NJ, USA, 1997).

[32] M. Lovrić, in: Electroanalytical Methods, (Springer, 2010).

[33]http://www.ameteksi.com//media/ameteksi/download_links/documentations/library/princetonappliedresearch/application_note_s-7.pdf?la=en Accessed 5 October 2017

[34] L. Ramaley, M.S. Krause, Theory of square wave voltammetry, Analytical chemistry 41 (1969) 1362-1365.

[35] B. Dogan-Topal, S.A. Ozkan, B. Uslu, The analytical applications of square wave voltammetry on pharmaceutical analysis, The Open Chemical and Biomedical Methods Journal 3 (2010) 56-73.

[36]http://www.fhiberlin.mpg.de/acnew/department/pages/teaching/pages/teaching__wintersemester__2012_2013/cornelia_breitkopf__impedance_spectroscopy__121207.pdf. (Accessed 06 October 2017)

[37] A.I. Zia, S.C. Mukhopadhyay, in: Electrochemical Sensing: Carcinogens in Beverages, (Springer, 2016).

[38] W.E. Lee, T. Tang, D. Lin, A.M. Mohammed, D.J. Harrison, A.B. Jemere, Self-assembled nanostructures for bioanalysis, (2015).

[39] S.-I. Pyun, H.-C. Shin, J.-W. Lee, J.-Y. Go, in: Electrochemistry of Insertion Materials for Hydrogen and Lithium, (Springer Berlin Heidelberg, Berlin, Heidelberg, 2012).

CHAPTER FOUR

ELECTROCHEMICAL DEGRADATION OF AN ANTHRAQUINONIC DYE ON AN EXPANDED GRAPHITE-DIAMOND COMPOSITE ELECTRODE[1]

4.1 Introduction

Pollution of water bodies resulting from industrial activities is a major challenge to our modern world. Water contamination is particularly more pronounced in developing countries where 70% of industrial waste is reportedly being dumped untreated into waters where they pollute usable water sources [1]. A number of water pollutants which include organics and heavy metals have been implicated in many health-related issues [2-4]. In a very recent study by Fernandes *et al.*, disperse red 1 (an azo dye) was reported as being capable of inducing reproductive health problems [5]. Synthetic dyes represent a major class of organic pollutants. Apart from the health hazards which may be posed by these organics, they also adversely affect the aquatic ecosystems owing to their colour [6, 7]. Textile industries consume a large amount of water in the dyeing process, thus generate much effluents which contain considerably high concentration of dye [8]. Treatment of these effluents prior to discharge into the environment is therefore a necessity. Given the importance of water to life, there has been an ever growing interest in the development of techniques for water remediation. Physical and chemical processes have been and are being explored. These include coagulation, sorption, ion-exchange process, biological treatment and advanced oxidation processes. Some of

[1] This chapter has been published as: "Peleyeju, M.G., Umukoro E., Babalola, J.O. Arotiba, O.A.*. Electrochemical Degradation of Anthraquinonic Dye on an Expanded Graphite-Diamond Composite Electrode. *Electrocatalysis.* **2016,** 7, 132-139"

these methods either lead to secondary pollution or are ineffective in the treatment of recalcitrant organic pollutants [9-11]

Advanced oxidation processes (AOPs) refer to processes in which organic pollutants are oxidised primarily by their interaction with hydroxyl radicals in aqueous medium.

$$n\,^{\bullet}OH + R \rightarrow \textit{oxidation products} \qquad (4.1)$$

Hydroxyl radicals are generated according to the following examples:

$$TiO_2 + h\nu \rightarrow e^-_{cb} + h^+_{vb}$$

$$h^+_{vb} + H_2O \rightarrow {}^{\bullet}OH + H^+ \qquad \textit{Photocatalysis} \qquad (4.2)$$

$$Fe^{2+} + H_2O_2 \rightarrow Fe^{3+} + {}^{\bullet}OH + OH^- \qquad \textit{Fenton process} \qquad (4.3)$$

$$H_2O \rightarrow {}^{\bullet}OH + H^+ + e^- \qquad \textit{Electrochemical (on the surface of the anode)} \qquad (4.4)$$

After fluorine, hydroxyl radical is the most powerful oxidant known. It reacts unselectively with most organic pollutants with the capability of completely mineralising them [12, 13]

Electrochemical advanced oxidation process (EAOP) can be considered a subset of AOPs in which hydroxyl is generated from the oxidation of water on the surface of the anode [13]. EAOP is particularly attractive because the main reagent involved (i.e. electron) is clean. EAOPs are also carried out at ambient conditions and are amenable to automation [14-16]. An important component of the EAOP is the electrode material, the anode material especially. The nature of the electrode material strongly influences the efficiency of the process [17].

Anode materials for electrochemical oxidation of organic species have been classified into active and non-active. Hydroxyl radicals formed tend to adsorbs strongly on the surface of active anodes, leading to a low concentration of the radicals at the electrode surface, thus, only a small quantity are available for the oxidation of the target pollutants. Oxygen evolution reaction (an undesirable side reaction which affects the efficiency of the process) is favoured at active anodes especially at high current densities [17, 18]. Consequently, organic contaminants are partially oxidised at the surface of active anodes. Electrode materials such as graphite, platinum, IrO_2 and ruthenium-based oxides have been grouped as active anodes. On the other hand, hydroxyl radicals are physisorbed on the surface of non-active anodes. These anodes are poor electrocatalysts for oxygen evolution reaction. Complete mineralisation of organic pollutants is therefore possible at the non-active electrodes. Boron-doped diamond (BDD), PbO_2 and SnO_2 are typical examples. Up till date, BDD is the most promising anode for electrochemical oxidation of organics. However, there is a need to explore potential electrode materials which are inexpensive and are easy to fabricate [19, 20].

In this work, we present the electrochemical oxidation of an anthraquinone-based dye, acid blue 40 (AB 40) at an expanded graphite-diamond anode. Anthraquinone dyes are known for their brightness, fastness and durability. They are resistant to solar radiation and ambient conditions [11]. Expanded graphite (EG) is a graphitic material with low density and high temperature resistance. EG has been applied for electrochemical sensing and electro-oxidation of organics. It has been indicated to possess good electrocatalytic property which is promising for the electrochemical degradation of organic contaminants [21, 22]. However, its low oxygen evolution potential is a drawback for its use for complete mineralisation of organics. Diamond, on the other hand, possesses high oxygen evolution potential and thus presents an excellent

platform for the electrochemical oxidation of organics. Nevertheless, it cannot be used alone; it requires doping to enhance its conductivity.

Herein, we explored the applicability of this composite electrode material for the degradation of dye molecule

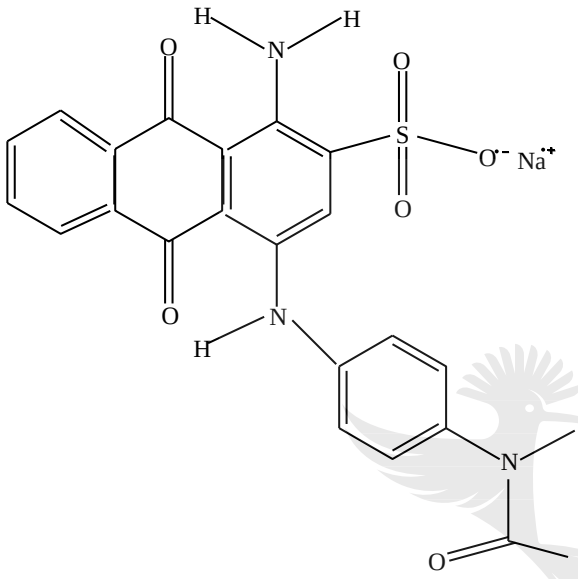

Fig. 4. 1. Chemical structure of acid blue 40

4.2 Experimental

4.2.1 Chemical reagents and materials

Natural graphite flakes, conductive silver paint, and diamond powder were supplied by Sigma-Aldrich, Agar scientific and Element Six (South Africa) respectively. Acid blue 40 (50% content), Orange II sodium salt, Sodium sulphate, Sodium chloride, Sulphuric acid, Nitric acid, Potassium ferricyanide and Isopropanol were purchased from Sigma-Aldrich. All reagents were of analytical grade and were used as received. Deionised water was used to prepare all solutions.

4.2.2 Characterisations

Raman spectra of the electrode materials were recorded on Raman Microscope (PerkinElmer RamanMicro 200) with 50x objective. X-ray diffraction (XRD) data were collected on X'Pert Pro PANalytical diffractometer operated at 40 kV and 40 mA, using Cu Kα radiation as the source. Scanning electron microscopy (SEM) images were obtained from TESCAN VEGA microscopy (VEGA3SEM) operated at 20.0 kV.

Decolourisation of AB 40 solution was followed from the decrease in absorbance at the wavelength of maximum absorption of the dye (λ_{max} = 620 nm) with UV-Vis spectrophotometer (Agilent Technologies Cary 60) and extent of mineralisation of the dye was determined from total organic carbon (TOC) decay, measured on Teledyne Tekmar TOC fusion.

4.2.3 Preparation of EG and EG-diamond composite

Natural graphite flakes were immersed in a mixture of concentrated sulphuric acid and concentrated nitric acid (H_2SO_4:HNO_3 = 3:1) and the mixture was left at room temperature and pressure for 24 h. The material was then washed with deionised water until the pH was neutral. The graphite intercalated compounds (GIC) was air-dried and subsequently placed in a microwave oven operated at 900 W for 60 seconds. Under microwave irradiation the precursor expanded rapidly accompanied by small light flashes, giving a puffed-up material called expanded graphite (EG).

To prepare the composite material, equal amounts of EG and diamond powder (1 g each for example) were measured into a given volume of propan-2-ol and the mixture stirred and thoroughly mixed. It was then dried in oven at 60 °C overnight.

4.2.4 Fabrication of electrodes

The composite material was compressed into pellets at 6000 psi for 1 h with a pressing machine. The pellets obtained were used to prepare the electrodes. The electrode fabrication was as follows: a clean copper wire was coiled at one end to form a flat surface; the pellet was then placed on the surface on which conductive silver paint had been initially applied. It was left to air dry, and then carefully placed in a glass rod. The edges of the electrode were covered with non-conducting epoxy to exclude current contribution from the edges.

4.2.5 Electrochemical measurements and degradation experiment

All electrochemical experiments were done on autolab potentiostat/galvanostat (PGSTAT 302N model), the anodic oxidation of the pollutant was carried out in galvanostatic mode. Electrochemical characterisation of the working electrodes was done using cyclic voltammetry with 5 mM $K_3Fe(CN)_6$ as a redox probe. The electrochemical oxidation of 20 ppm AB 40 (75 mL) was done in an undivided electrochemical cell using chronopotentiometry. The set up consists of three-electrode configuration with EG and EG-diamond as working electrodes (diameter 1.3 cm), Ag/AgCl (3.0 M KCl) as reference electrode and platinum foil as counter electrode. The electrolytic solution was continuously stirred using a magnetic stirrer to ensure uniform concentration. Aliquots were drawn from the electrochemical cell at fixed time intervals.

4.3 Results and discussion

4.3.1 XRD analysis

EG shows an intense characteristic reflection peak at 2θ = 26.57° (002) with corresponding interlayer spacing of 0.345 nm (Fig. 4.2a). The crystallite size from the broadening of the characteristic peak was estimated using Scherrer's equation:

$$L = \frac{K\lambda}{\beta Cos\theta}$$

where K represents the dimensionless shape factor, having a typical value of about 0.9, λ is the Cu K_α radiation wavelength (0.154 nm), β is the crystallite size contribution to the peak width (integral or full width at half maximum) in radians, and θ is the scattering angle (Bragg angle) [23-25]. The crystallite size of the EG was calculated to be 59 nm.

XRD pattern of the composite in Fig. 4.2b presents sharp and well-defined peaks at 2θ = 43.97 and 75.30 ° corresponding to diamond (111) and (220) reflections respectively [26]; while still retaining the characteristic peaks of EG. This clearly shows the presence of both EG and diamond in the composite. The XRD pattern of diamond powder only is shown in the inset of Fig 4.2b

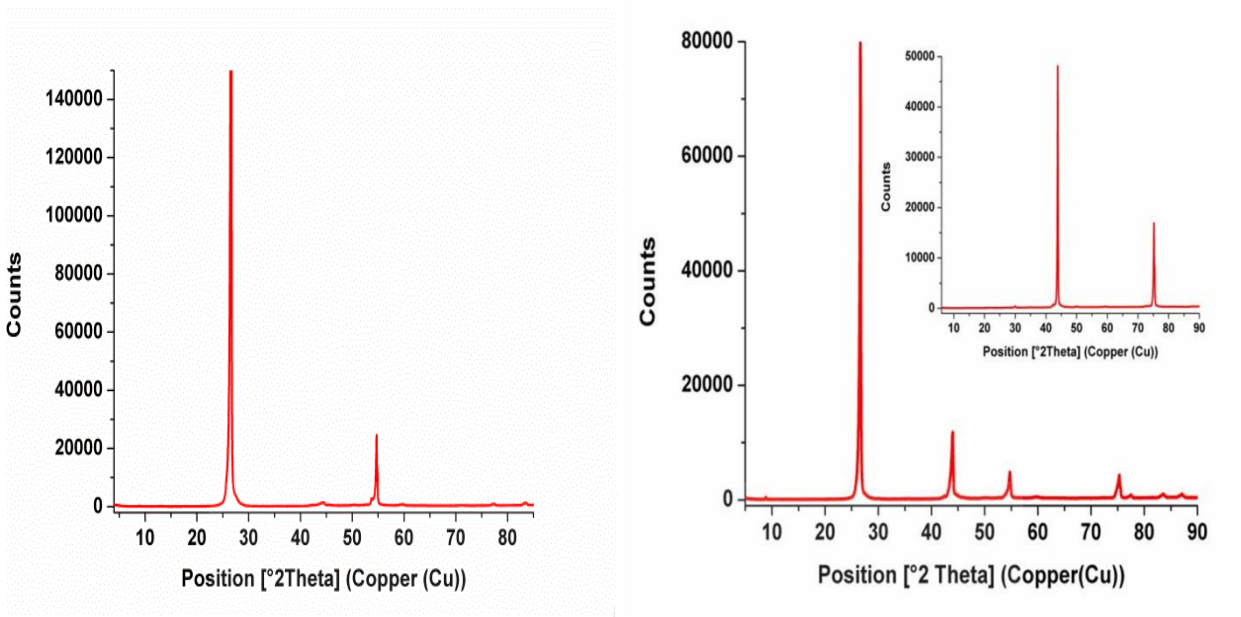

a) b)

Fig. 4. 2. XRD patterns of a) EG and b) EG-diamond composite and diamond (inset).

4.3.2 Raman spectroscopy

Raman spectra of diamond powder, EG and EG-diamond composite are presented in Fig. 4.3. The Raman spectrum of EG shows two distinct bands, the G (graphitic) band centred at about 1578 cm^{-1} and the D (disorder) band at 1334 cm^{-1} (Fig. 4.3b (inset)). The G band has been attributed to the first-order scattering of the E_{2g} mode; it is due to the bond stretching of all sp^2 atoms. The D peak corresponds to the A_{1g} breathing mode; it arises when there is disruption in the symmetrical hexagonal graphitic lattice [27-29]. Given the very small value of the I_D/I_G (ratio of D band intensity to G band intensity), the EG can be said to be very crystalline.

The Raman spectrum of the diamond powder shows a very intense and sharp D band around 1330 cm^{-1} (Fig. 4.3a), this peak relates to the sp^3 bonds in diamond. The Raman spectrum of diamond has only one band because all of the bonds in the crystal are of the same orientation and strength, thus, a single vibrational frequency [30, 31]. The

intensity of the G band (at 1589 cm^{-1}) of EG in the EG-diamond composite is comparatively small owing to the very intense peak of the diamond. The broadening and the upward shift of this G band can be attributed to the significant decrease of the in-plane sp^2 domains due to the presence of sp^3 domains. Similar spectrum was obtained by Wen *et al.* in a study aimed at synthesizing diamond from nano-graphite [32].

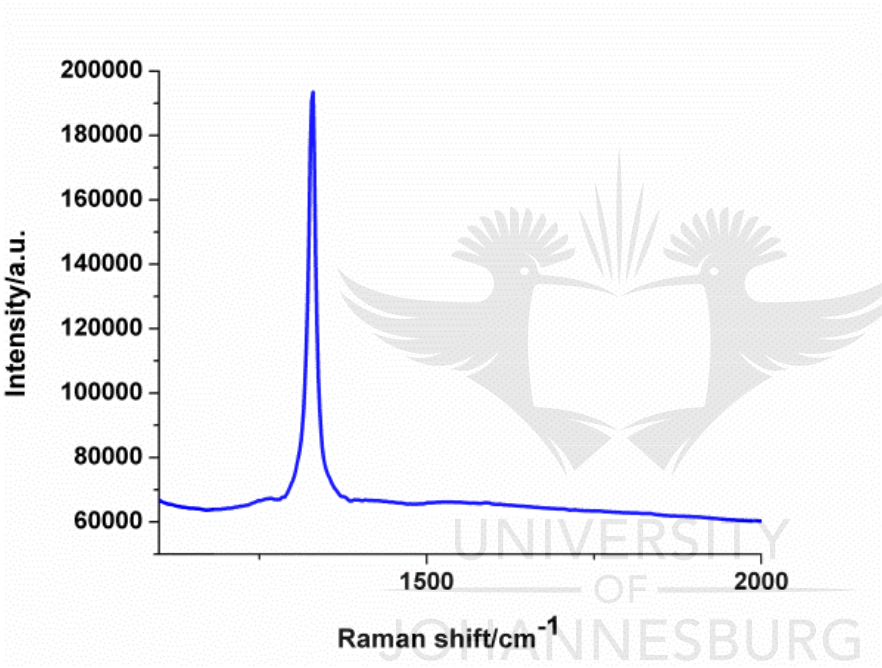

a)

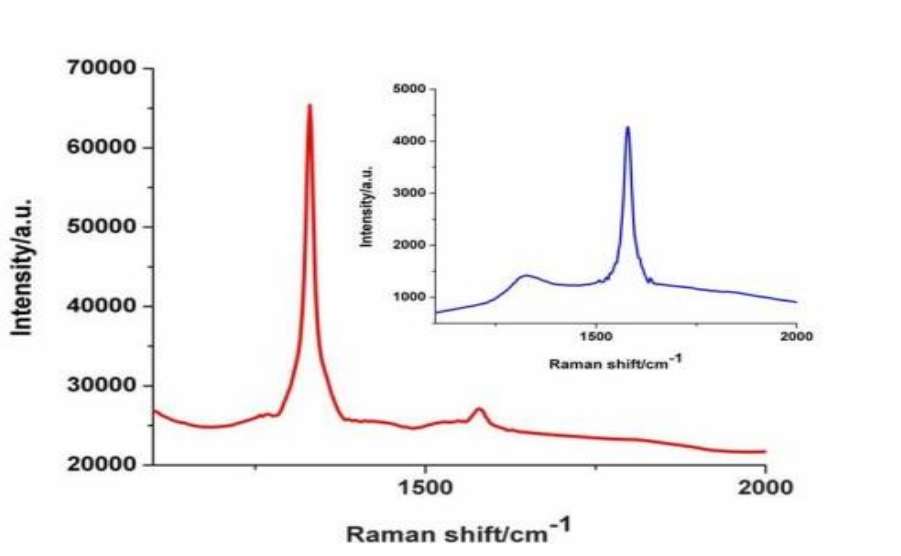

b)

Fig. 4. 3. Raman spectra of a) diamond and b) EG-diamond (inset is EG only)

4.3.3 Scanning electron microscopy

SEM images confirm the formation of expanded graphite – diamond composite (EG-D) as observed in Figure 4.4. The expanded layers of EG (Fig 4.4a) can be seen to be decorated with diamond particles (Fig 4.4b).

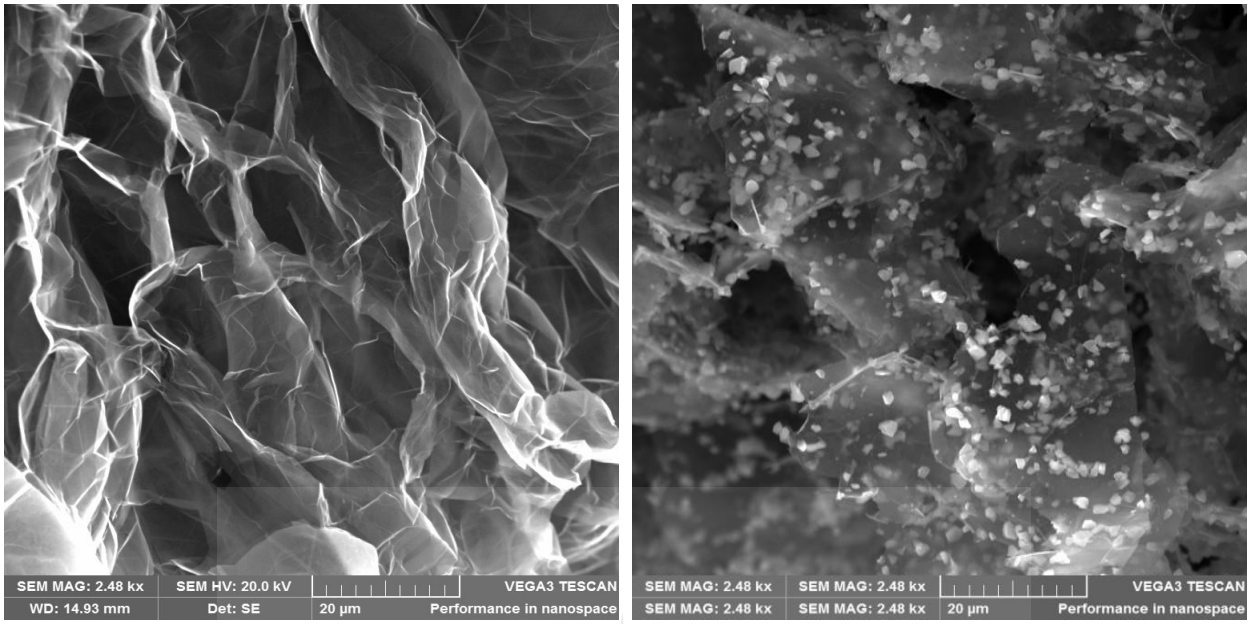

Fig. 4. 4. SEM image of a) EG and b) EG-D

4.3.4 Cyclic voltammetric measurement

The electrochemical responses of the electrodes in the presence of ferrocyanide redox probe were investigated. The voltammograms obtained at the EG and composite electrodes are shown in figure 4.5. The oxidation/reduction peaks are clearly defined in this solution: ~0.25 V/0.15 V and 0.28 V/0.12 V for EG and EG-diamond respectively. The separations between the anodic peak and the cathodic peak (ΔE_p) were estimated to be 106 mV and 166 mV for EG and EG-diamond respectively. While a more sluggish kinetics is expected on the EG-diamond electrode (because of the non-catalytic behaviour of diamond), surface oxides introduced during intercalation as well as the dilution effect of diamond tend to have significant effects on the electron-transfer kinetics on the EG electrode [33, 34]. Also of note is that EG-diamond gave enhanced current peak when compared with EG. The probable reason for this is that the diamond

acted as spaces in between the lattices of the EG exposing more of the edge planes as against the predominant basal planes.

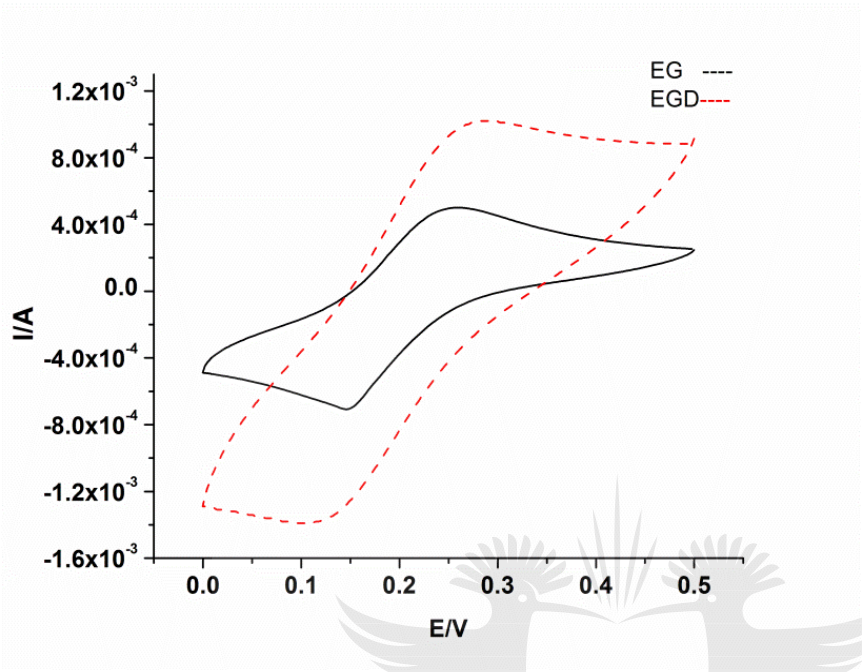

Fig. 4. 5. Cyclic voltammograms of EG and EG-diamond (EGD) in 5 mM Ferrocyanide redox probe at a scan rate of 0.02 Vs^{-1}

4.3.5 Electrochemical degradation at EG and EG-diamond electrodes

The bulk electrolysis of AB 40 was carried out in 0.1 M Na_2SO_4 supporting electrolyte at neutral pH. Decline in the absorbance of the substrate with time at λ = 620 nm as shown in Figure 4.6a, confirms its decay at the composite electrode. This decay is current density dependent (Fig. 4.6b). Decolourisation increases with increasing current densities at both EG and EG-diamond. After 4 hours of electrolysis at 20 mA cm^{-2}, 66% (not shown) and 81% colour removal were obtained at EG and EG-diamond respectively.

Figure 4.6c shows the total organic carbon (TOC) abatement where the extent of mineralisation increases with increase in current density. The increase in the extent of

mineralisation with increasing current density can be thought to be as a result of production of larger amount of hydroxyl radicals from the anodic oxidation of water, which can enhance the degradation of the parent pollutant as well as the transformation products. After 4 hours of electrolysis, 26% TOC removal was obtained at EG while EG-diamond gave 44% mineralisation. The enhanced performance of the composite electrode can be attributed to the presence of diamond which possesses high oxygen evolution overpotential and thus is believed to minimise oxygen evolution reactions.

The robustness of this composite electrode was further explored by its application to an azo dye, Orange II (OG II), and a mixture of AB 40 and OG II. A 20 ppm solution of OG II was prepared in 0.1 M Na_2SO_4 and electrolysed at 20 mA cm^{-2}. More than 50% colour removal was obtained in the first 30 min of electrolysis, reaching over 98% in 3 h (Fig. 4.6e), with 52% TOC decay. This implies that the chromophore, which is responsible for the colour, in the azo dye is rapidly cleaved. A mixture containing 20 ppm each of the anthraquinoinic and the azo dyes was also oxidised at the electrode. The rate of decolourisation of each of the components was slightly impeded as presented in figure 4.6f. This is expected as there would be competition for the available hydroxyl radicals by the dye molecules. The rate of decline of the absorbance of OG II at 484 nm is higher compared to that of AB 40 and this confirms the faster decolourisation obtained when the two dyes were electrolysed individually. After 4 h electrolysis of the mixture, approximately 60% and 90% degradation were achieved for AB 40 and OG II respectively. The TOC removal was 49%.

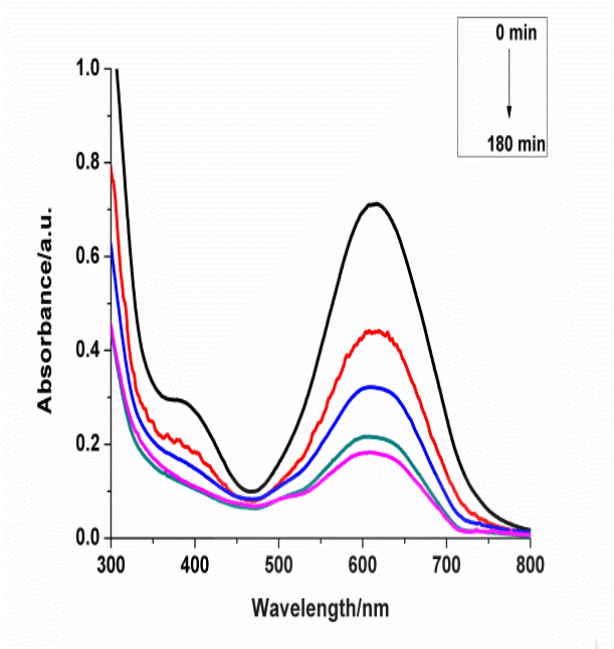

a)

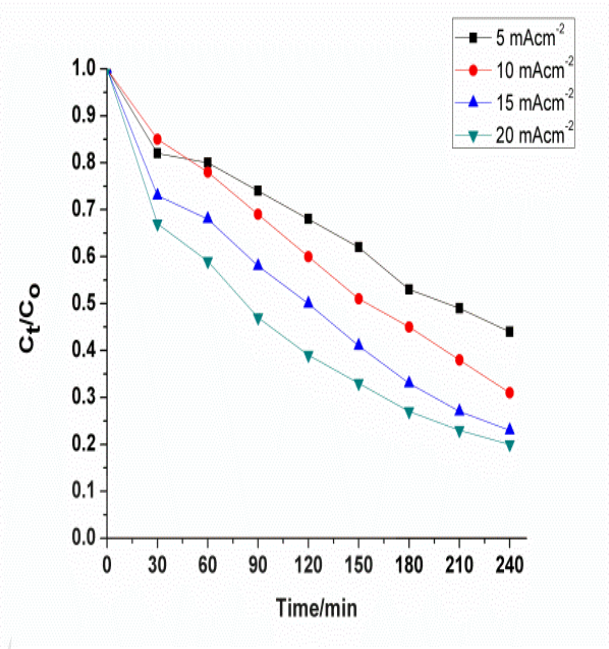

b)

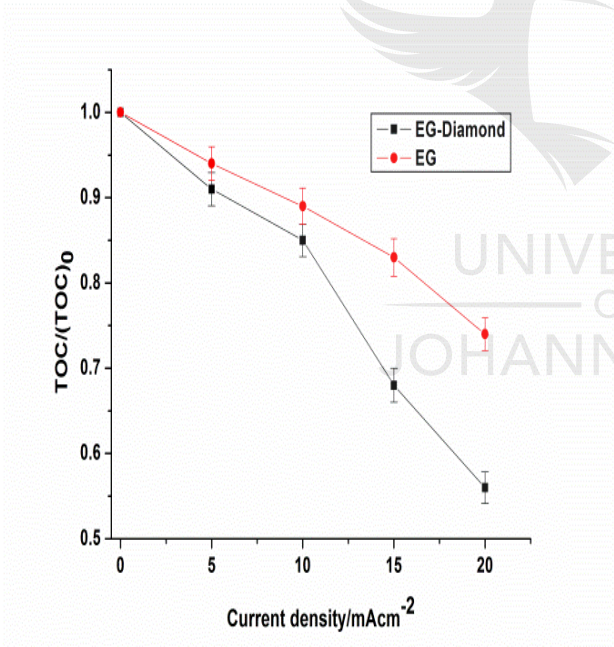

c)

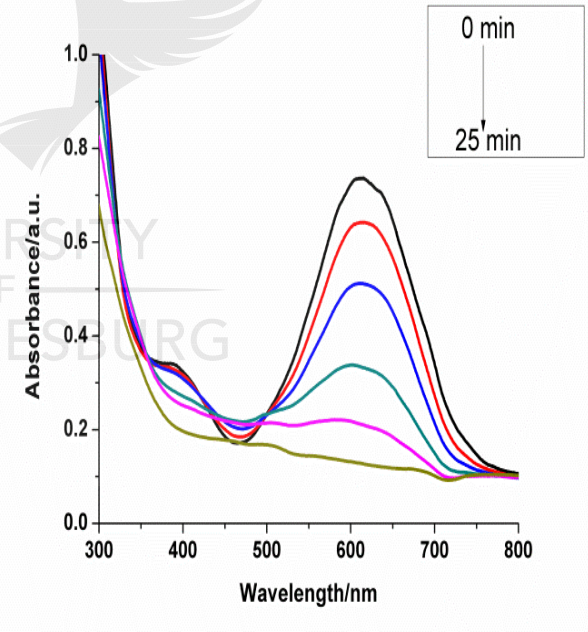

d)

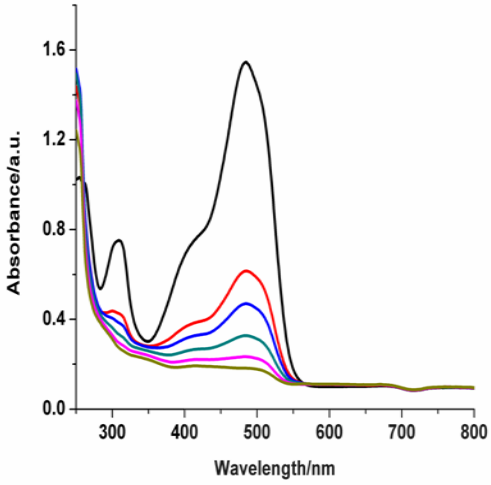

e)

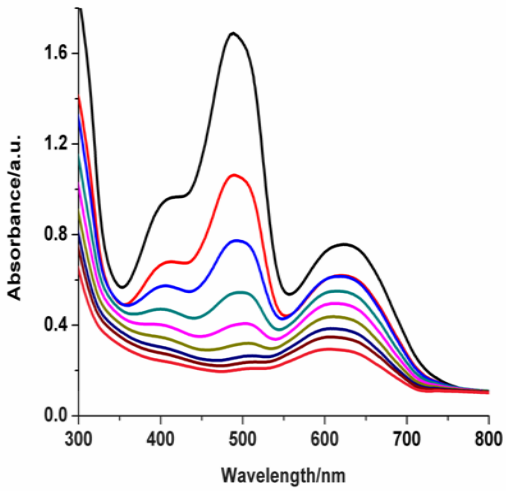

f)

Fig. 4. 6. (a) UV-Vis spectra showing the degradation of AB 40 with time at EG-diamond anode. (b) Effect of current density on the oxidation (decolourisation) of AB 40 at EG-diamond anode. (c) Plot of normalised TOC abatement for EG and EG-diamond at different current densities after 4 h (n = 3). UV-Vis spectra of (d) AB 40 in 0.1 M NaCl, (e) Orange II in 0.1 M Na_2SO_4 and (f) AB 40 + Orange II, at EG-diamond composite electrode

4.3.5.1 Effect of supporting electrolyte on the degradation of AB 40 at EG and EG-diamond anodes

The presence of only inert ions in water is unrealistic, electro-active ions will most likely be present and these ions can form strong oxidising agents [35]. In particular, chloride ions are often present in liquid effluents and natural waters consequently making the involvement of active chlorine unavoidable in electrochemical treatment of such media [36]. There exist quite a number of reports on chlorine-mediated electrolysis of organics [37-39]. Indirect electrochemical oxidation via active chlorine is attractive as it offers

enhanced degradation of the target pollutant, but possible formation of recalcitrant and sometimes more toxic halogenated intermediates has been a concern [40].

In electrolyte containing chloride ions, oxidant species are formed at the anode via oxidation of chloride ions according to the following equations [35].

$$2Cl^- \longrightarrow Cl_2 + 2e^- \qquad (4.4)$$

$$Cl_2 + H_2O \longrightarrow HOCl + H^+ + Cl^- \qquad (4.5)$$

$$HOCl \longrightarrow H^+ + OCl^- \qquad (4.6)$$

The oxidant species present depends on the pH of the medium. In this work, the electrolysis of AB 40 was also carried out in 0.1 M NaCl at pH 7. After 20 minutes of electrolysis, complete decolourisation occurred at the EG electrode while it takes about 25 minutes to achieve complete decolourisation at the EG-diamond anode (Fig. 4.6d). The significant acceleration of the removal of the dye suggests involvement of secondary oxidant, chiefly active chlorine. The slightly slower removal rate obtained at the EG-diamond anode could be as a result of faster generation of active chlorine at the EG anode. And active chlorine probably plays the dominant role at the initial stage of oxidation of the pollutant at both electrodes. Formation of active chlorine has been shown to be more favoured at active electrodes than at non-active electrodes [35]. In the mediated electrolysis, the extent of mineralisation is however lower at the EG-diamond electrode than that obtained in the presence of sulphate supporting electrolyte. This observation can be attributed to the formation of chlorinated intermediates which are difficult to destroy [40].

4.3.6 Kinetics of degradation

Pseudo-first order kinetic model is usually used to describe the kinetics of electrochemical oxidation of organics, and most organics fit well into it [41]. The equation is as given below:

$$\frac{dC}{dt} = -k.C$$

Where C is the concentration of AB 40 in mgL^{-1}, t is the reaction time in minutes (min), and k is degradation rate constant in min^{-1}. The plot of $\ln(Co/Ct)$ against t (for electrolysis time of 180 min) was linear. And the kinetic rate constants obtained from the magnitude of the slopes were 2.34 x 10^{-3} min^{-1} with correlation coefficient of 0.9499 and 4.41 x 10^{-3} min^{-1} with correlation coefficient of 0.9945 for EG and EG-diamond electrodes respectively. The linear plot obtained on the EG-diamond electrode shows that the electrochemical oxidation of AB 40 follows pseudo first order kinetic model. The higher value of apparent rate constant obtained for the degradation at the EG-diamond proves that the process is enhanced at the composite electrode.

4.4 Sub-conclusion

Application of expanded graphite-diamond anode in the electrochemical oxidation of anthraquinonic and azo dyes (AB 40 and OG II) has been reported in this work. The results demonstrate that the incorporation of diamond into expanded graphite enhanced both the decolourisation and the mineralisation of the organic pollutants. Chlorine mediated electrolysis of AB 40 was performed and the two sided effects of the presence of chloride ion which on one hand enhances decolourisation and on the other hand hampers mineralisation was observed in this study. The anode materials used in

this work can be attractive owing to the low cost of both EG and diamond and also the ease of preparation.

4.5 References

[1] http://www.unwater.org/statistics/statistics-detail/fi/c/211800/. Accessed 04 June 2015

[2] Y.Y. Qin, C.K.M. Leung, A.O.W. Leung, S.C. Wu, J.S. Zheng, M.H. Wong, Persistent organic pollutants and heavy metals in adipose tissues of patients with uterine leiomyomas and the association of these pollutants with seafood diet, BMI, and age, Environmental Science and Pollution Research, 17 (2010) 229-240.

[3] D. Baderna, A. Colombo, G. Amodei, S. Cantù, F. Teoldi, F. Cambria, G. Rotella, F. Natolino, M. Lodi, E. Benfenati, Chemical-based risk assessment and in vitro models of human health effects induced by organic pollutants in soils from the Olona valley, Science of the Total Environment, 463 (2013) 790-801.

[4] A.V. Sergeev, D.O. Carpenter, Geospatial patterns of hospitalization rates for stroke with comorbid hypertension in relation to environmental sources of persistent organic pollutants: results from a 12-year population-based study, Environmental Science and Pollution Research, 18 (2011) 576-585.

[5] F.H. Fernandes, E. Bustos-Obregon, D.M.F. Salvadori, Disperse Red 1 (textile dye) induces cytotoxic and genotoxic effects in mouse germ cells, Reproductive Toxicology, 53 (2015) 75-81.

[6] D.M. Leme, G.A.R. de Oliveira, G. Meireles, T.C. dos Santos, M.V.B. Zanoni, D.P. de Oliveira, Genotoxicological assessment of two reactive dyes extracted from cotton fibres using artificial sweat, Toxicology in Vitro, 28 (2014) 31-38.

[7] E.N. Ngwa, A.-P. Kengne, B. Tiedeu-Atogho, E.-P. Mofo-Mato, E. Sobngwi, Persistent organic pollutants as risk factors for type 2 diabetes, Diabetology & metabolic syndrome, 7 (2015) 41.

[8] O. Ama, N. Mabuba, O. Arotiba, Synthesis, Characterization, and Application of Exfoliated Graphite/Zirconium Nanocomposite Electrode for the Photoelectrochemical Degradation of Organic Dye in Water, Electrocatalysis, 6 (2015) 390-397.

[9] E.J. Ruiz, C. Arias, E. Brillas, A. Hernández-Ramírez, J. Peralta-Hernández, Mineralization of Acid Yellow 36 azo dye by electro-Fenton and solar photoelectro-Fenton processes with a boron-doped diamond anode, Chemosphere, 82 (2011) 495-501.

[10] A. Ahmad, S.H. Mohd-Setapar, C.S. Chuong, A. Khatoon, W.A. Wani, R. Kumar, M. Rafatullah, Recent advances in new generation dye removal technologies: novel search for approaches to reprocess wastewater, RSC Advances, 5 (2015) 30801-30818.

[11] P.B. Moraes, R.R. Pelegrino, R. Bertazzoli, Degradation of Acid Blue 40 dye solution and dye house wastewater from textile industry by photo-assisted electrochemical process, Journal Of Environmental Science And Health Part A, 42 (2007) 2131-2138.

[12] S. Malato, P. Fernández-Ibáñez, M.I. Maldonado, J. Blanco, W. Gernjak, Decontamination and disinfection of water by solar photocatalysis: recent overview and trends, Catalysis Today, 147 (2009) 1-59.

[13] E. Brillas, C. Arias, P.-L. Cabot, F. Centellas, J. Garrido, R. Rodríguez, Degradation of organic contaminants by advanced electrochemical oxidation methods, Portugaliae electrochimica acta, 24 (2006) 159-189.

[14] I. Sirés, E. Brillas, M.A. Oturan, M.A. Rodrigo, M. Panizza, Electrochemical advanced oxidation processes: today and tomorrow. A review, Environmental Science and Pollution Research, 21 (2014) 8336-8367.

[15] L. Yan, Y. Wang, J. Li, H. Ma, H. Liu, T. Li, Y. Zhang, Comparative study of different electrochemical methods for petroleum refinery wastewater treatment, Desalination, 341 (2014) 87-93.

[16] M. Turabik, N. Oturan, B. Gözmen, M.A. Oturan, Efficient removal of insecticide "imidacloprid" from water by electrochemical advanced oxidation processes, Environmental Science and Pollution Research, 21 (2014) 8387-8397.

[17] C.A. Martínez-Huitle, L.S. Andrade, Electrocatalysis in wastewater treatment: recent mechanism advances, Quimica Nova, 34 (2011) 850-858.

[18] Y. Wang, Z. Shen, Y. Li, J. Niu, Electrochemical properties of the erbium–chitosan–fluorine–modified PbO_2 electrode for the degradation of 2, 4-dichlorophenol in aqueous solution, Chemosphere, 79 (2010) 987-996.

[19] B.P. Chaplin, Critical review of electrochemical advanced oxidation processes for water treatment applications, Environmental Science: Processes & Impacts, 16 (2014) 1182-1203.

[20] E. Brillas, C.A. Martínez-Huitle, Decontamination of wastewaters containing synthetic organic dyes by electrochemical methods. An updated review, Applied Catalysis B: Environmental, 166 (2015) 603-643.

[21] P. Ramesh, G. Suresh, S. Sampath, Selective determination of dopamine using unmodified, exfoliated graphite electrodes, Journal of Electroanalytical Chemistry, 561 (2004) 173-180.

[22] J. Skowroński, P. Krawczyk, Enhanced electrochemical activity of regenerated expanded graphite electrode after exhaustion in the process of phenol oxidation, Chemical Engineering Journal, 152 (2009) 464-470.

[23] V. Uvarov, I. Popov, Metrological characterization of X-ray diffraction methods at different acquisition geometries for determination of crystallite size in nano-scale materials, Materials Characterization, 85 (2013) 111-123.

[24] Y.-S. Yang, C.-Y. Wang, M.-M. Chen, Z.-Q. Shi, J.-M. Zheng, Facile synthesis of mesophase pitch/exfoliated graphite nanoplatelets nanocomposite and its application as anode materials for lithium-ion batteries, Journal of Solid State Chemistry, 183 (2010) 2116-2120.

[25] I. Afanasov, O. Shornikova, D. Kirilenko, I. Vlasov, L. Zhang, J. Verbeeck, V. Avdeev, G. Van Tendeloo, Graphite structural transformations during intercalation by HNO 3 and exfoliation, Carbon, 48 (2010) 1862-1865.

[26] Y.-C. Chen, L. Chang, Chemical vapor deposition of diamond on an adamantane-coated sapphire substrate, RSC Advances, 4 (2014) 18945-18950.

[27] P. Ramesh, S. Sampath, Electrochemical characterization of binderless, recompressed exfoliated graphite electrodes: Electron-transfer kinetics and diffusion characteristics, Analytical chemistry, 75 (2003) 6949-6957.

[28] T. Ndlovu, A.T. Kuvarega, O.A. Arotiba, S. Sampath, R.W. Krause, B.B. Mamba, Exfoliated graphite/titanium dioxide nanocomposites for photodegradation of eosin yellow, Applied Surface Science, 300 (2014) 159-164.

[29] A.C. Ferrari, Raman spectroscopy of graphene and graphite: disorder, electron–phonon coupling, doping and nonadiabatic effects, Solid state communications, 143 (2007) 47-57.

[30] S. Sun, X. Jia, B. Yan, F. Wang, N. Chen, Y. Li, H.-a. Ma, Synthesis and characterization of hydrogen-doped diamond under high pressure and high temperature, CrystEngComm, 16 (2014) 2290-2297.

[31] J. Hodkiewicz, Characterizing carbon materials with Raman spectroscopy, Thermo Scientific Application Note, 51946 (2010).

[32] C. Wen, Z. Jin, X. Liu, D. Sun, X. Li, G. Zhou, J. Lin, Z. Hao, Synthesis of diamond using nano-graphite and Fe powder under high pressure and high temperature, Materials Letters, 60 (2006) 3507-3510.

[33] K. Fabisiak, R. Torz-Piotrowska, E. Staryga, M. Szybowicz, K. Paprocki, P. Popielarski, F. Bylicki, A. Wrzyszczyński, Cyclic voltammetry response of an undoped CVD diamond electrodes, Materials Science and Engineering: B, 177 (2012) 1243-1247.

[34] I. Duo, A. Fujishima, C. Comninellis, Electron transfer kinetics on composite diamond (sp^3)–graphite (sp^2) electrodes, Electrochemistry communications, 5 (2003) 695-700.

[35] H.T. Madsen, E.G. Søgaard, J. Muff, Study of degradation intermediates formed during electrochemical oxidation of pesticide residue 2, 6-dichlorobenzamide (BAM) in chloride medium at boron doped diamond (BDD) and platinum anodes, Chemosphere, 120 (2015) 756-763.

[36] O. Scialdone, S. Randazzo, A. Galia, G. Silvestri, Electrochemical oxidation of organics in water: role of operative parameters in the absence and in the presence of NaCl, Water research, 43 (2009) 2260-2272.

[37] M. Panizza, G. Cerisola, Direct and mediated anodic oxidation of organic pollutants, Chemical reviews, 109 (2009) 6541-6569.

[38] A.H. Degaki, G.F. Pereira, R.C. Rocha-Filho, N. Bocchi, S.R. Biaggio, Effect of specific active chlorine species and temperature on the electrochemical degradation of the reactive blue 19 dye using a boron-doped diamond or DSA anode in a flow reactor, Electrocatalysis, 5 (2014) 8-15.

[39] F. Zaviska, P. Drogui, J.-F. Blais, G. Mercier, In situ active chlorine generation for the treatment of dye-containing effluents, Journal of applied electrochemistry, 39 (2009) 2397-2408.

[40] R. Yuan, S.N. Ramjaun, Z. Wang, J. Liu, Effects of chloride ion on degradation of Acid Orange 7 by sulfate radical-based advanced oxidation process: implications for formation of chlorinated aromatic compounds, Journal of hazardous materials, 196 (2011) 173-179.

[41] J. Peralta-Hernández, Y. Meas-Vong, F.J. Rodríguez, T.W. Chapman, M.I. Maldonado, L.A. Godínez, Comparison of hydrogen peroxide-based processes for treating dye-containing wastewater: decolorization and destruction of Orange II azo dye in dilute solution, Dyes and Pigments, 76 (2008) 656-662.

CHAPTER FIVE

ELECTRO-OXIDATION OF 2,4-DICHLOROPHENOL ON A TERNARY COMPOSITE ELECTRODE OF DIAMOND, GRAPHENE AND POLYANILINE[1]

5.1 Introduction

The need for rapid, efficient and effective monitoring of high priority, recalcitrant organic pollutants in the environment has given rise to many research efforts. Many methods especially in the chromatographic and spectroscopic domains have been developed to determine and analyse a myriad of organic contaminants which often find their way into the environment [1-4]. In particular, analytical techniques and procedures involving the use of chromatographic and/or spectroscopic instruments for selective and sensitive determination of phenolic compounds have been advanced [5, 6]. These methods have over the time proved to be reliable; they however have some drawbacks, the basic ones being cost of equipment, expertise to operate and inappropriateness for on-site analysis [7-9]. Over time, electrochemical approach has been indicated as a viable choice for monitoring many organic and inorganic pollutants in water. Electrochemical devices for monitoring analytes of interest offer benefits such as high sensitivity and selectivity, simplicity and ease of operation, comparably low cost and portability amongst others [8, 10].

[1] This chapter has been published as: Peleyeju, M.G.; Idris, A.O.; Umukoro, E.H.; Babalola, J.O.; Arotiba, O.A.* Electrochemical detection of 2,4-dichlorophenol on a ternary composite of diamond, graphene and polyaniline electrode *ChemElectroChem*, **2017**, 4, 1074–1080

A key component of any electrochemical sensor is the sensing platform, the electrode surface. The surface of the electrode, where interaction with the analyte occurs, is prepared and designed to maximise necessary communication between the surface and the target substance. Commonly, electrode modifiers are often sought to enhance the needed sensitivity and reproducibility [11, 12]. These modifiers may be enzyme or non-enzyme materials. Enzyme-based sensors for the determination of phenols have been explored, and good sensitivity and stability were reported [13-15]. Detection of phenols on enzyme-based sensors is attractive, however, complicated enzyme immobilisation procedures, susceptibility of enzymes to denaturation and deactivation under extreme conditions of pH and temperature, and blockage of the active site by species which may be present in the sample matrix, are disadvantages [16].

Successful attempts have been made on non-enzymatic detection of phenols. A metal-organic framework, $[Cu_3(BTC)_2]$, has been used as a modifier for carbon paste electrode for the determination of 2,4-dichlorophenol. The modified electrode demonstrated high sensitivity and good stability towards the chlorinated phenol. The authors attributed the high sensitivity of the modified electrode to the large surface area, high adsorption capacity and good electron transfer efficiency of the $[Cu_3(BTC)_2]$ [16]. Also, Gan *et al.* employed a hybrid of carbon spheres, silver nanoparticles and graphene oxide to modify glassy carbon electrode for sensitive determination of four chlorinated phenols. The high sensitivity of this sensor was related to the fast electron transfer kinetics and high accumulation efficiency on the nanocomposite modifier [17]. Similarly, Yu *et al.* developed a sensor based on the composite of carbon dots (C dots), hexadecyltrimethyl ammonium bromide (CTAB) and chitosan for the determination of 2,4-dichlorophenol. The adsorption affinity of CTAB for phenols and the electrocatalytic property of C dots were explored in the work [18].

The success or otherwise of an electrochemical sensor depends largely on the sensitivity and stability of the electrode. Sensing platforms for some organics such as phenolic

compounds need to be carefully chosen, this is because many phenols including 2,4-dichlorophenol form an insulating film during electroanalysis, leading to fouling or passivation of the electrode surface. The gradual loss of activity at the surface of the electrode adversely impacts on the sensitivity and reliability of the sensor. As a result, many researchers design their phenols sensors with the aim to mitigate this phenomenon [19-22].

In this investigation, a ternary composite of diamond, graphene and polyaniline (DGP) is used as an electrode modifier for the sensitive detection of 2,4-dichlorophenol (2,4-DCP), a substance that has been designated by the United States Environmental Protection Agency as a priority pollutant. 2,4-DCP finds application in a number of industrial and agricultural processes such as production of pesticides, herbicides etc. and has been discovered in ground and surface water [23, 24]. It is deemed to cause a variety of health issues [25-27]. 2,4-DCP, like other phenolics, is notorious for passivating electrode during analysis [28, 29].

Diamond is an sp^3 hybridised allotrope of carbon which exhibits many outstanding properties such as excellent mechanical strength, high thermal conductivity, electrical resistance, wide spectral range optical transparency, large band gap and chemical inertness. The motivation for the application of diamond-based electrodes in electrochemical studies include wide potential window, low signal-to-background current ratio, tunable electrical resistivity, high oxygen evolution potential, excellent chemical stability, and considerable resistance to fouling, of diamond [30]. In a report by Terashima *et al.*, boron-doped diamond was used for the analysis of chlorophenols, the stability and sensitivity of the electrode remained impressive even at a high concentration of the analyte and after a prolonged use. They attributed these results to the low proclivity of diamond for adsorption of the oxidation products [31]. Also, Swain and co-workers noted the superior performance of both microcrystalline and nanocrystalline diamond electrodes to glassy carbon electrode in a study where these

electrodes were applied for the amperometric detection of chlorinated phenols. They related the better performance of diamond electrode to its excellent electrochemical response and high resistance to fouling [30].

Graphene, consisting of sp^2 hybridised carbon atoms, is one of the most researched and applied materials in many fields of science and technology in the last decade. Graphene is an exciting material to an electrochemist owing to its exceptional electrical conductivity, excellent electronic transport properties and high surface area. These properties have informed investigations on its use in many electrochemical devices, including sensors. Specifically, a graphene related material (reduced graphene oxide) has been used as electrode modifier for the determination of phenolics [7]. Li *et al.* reported a high electrocatalytic activity on a nanocomposite of reduced graphene graphene oxide for the determination of 2,4-dichlorophenol[10]. Also, Higson and co-workers observed a lower electron transfer resistance and improved electrochemical activity upon modification of screen printed electrodes with graphene [32].

Polyaniline (PANI) is a polymer which has been explored for sensing applications, this is essentially on account of its conducting nature. PANI has a good environmental stability and its synthesis is relatively easy. Seo *et al.* reported a phenol sensor based on PANI nanosheets, the sensor showed a considerable electrocatalytic activity towards the analyte [33].

In this work, the numerous inherent excellent properties of diamond and graphene were explored for the sensitive detection of 2,4-dichlorophenol with PANI used as a fixative.

5.2 Experimental

5.2.1 Chemical reagents and Materials

Sodium nitrate ($NaNO_3$), potassium permanganate ($KMnO_4$), sulphuric acid (H_2SO_4, 98%), hydrogen peroxide (H_2O_2, 30 %), hydrochloric acid (HCl, 35%), nitric acid (HNO_3, 65%), sodium sulphate (Na_2SO_4), sodium chloride (NaCl), dimethylformamide (DMF), hydrated potassium ferricyanide ($K_3Fe(CN)_6.3H_2O$), potassium nitrate (KNO_3), 2,4-dichlorophenol (2,4-DCP), ammonium persulfate (APS) and natural graphite powder were purchased from Sigma Aldrich (South Africa). Aniline and diamond powder were obtained from Merck and Element six (South Africa) respectively.

5.2.2 Characterisations

Fourier Transform Infrared Spectroscopy (FTIR) of KBr pellet of the sample was done on PerkinElmer Spectrum 100 spectrometer (USA), Raman spectra were obtained on Raman Microscope (PerkinElmer RamanMicro 200, USA) with ×50 objective. X-ray diffractometry investigation of the samples were done on Rigaku Smartlab x-ray diffractometer (USA), the surface area analysis was performed on Micrometrics ASAP 2020 surface area and porosity analyser (USA). The micrographs of the materials were obtained using scanning electron microscope (TESCAN, Vega 3 XMU, Czech Republic) and transmission electron microscope (JEOL 2100 HRTEM 200V, Japan).

5.2.3 Synthesis of Reduced graphene oxide

Graphene oxide (GO) was synthesised using Hummer's method. 5 g of graphite powder and 2.5 g of sodium nitrate were added into three-mouthed round bottom flask containing 115 mL of sulfuric acid and the mixture stirred. The flask was then transferred into an ice bath where 15 g of potassium permanganate was added bit by bit to the mixture, with continuous stirring. Thereafter, the reaction mixture was left

standing at room temperature for 4 hours after which it was heated to 35 °C for 30 min. The reaction mixture was then poured into a flask containing 250 mL of deionised water and further heated to 70 °C and maintained for 15 min. It was then poured into 1 L of deionised water and hydrogen peroxide was added. The material was washed several times with water by centrifugation. The resulting slurry was dried at 70 °C in an air furnace.

The grey powder obtained was subjected to thermal treatment in a tube furnace at a temperature of 500 °C in an inert atmosphere (argon) for 20 min. The flow rate was set at 100 mL/min. The low density, black powder obtained was collected and kept for use.

5.2.4 Synthesis of diamond/graphene/PANI (DGP) composite

A 0.9 mL of previously vacuum distilled aniline was added to 50 mL of 1 M hydrochloric acid. Diamond powder (1 g) and reduced graphene oxide (1 g) were thoroughly mixed and subsequently added to the aniline solution and magnetically stirred. A 50 mL volume of 0.25 M ammonium persulfate was then added drop-wise while maintaining the reaction mixture at 5 °C. The mixture was then transferred into a refrigerator and kept at 4 °C for 48 h. The solid obtained was washed repeatedly with deionised water and air dried for 72 h.

5.2.5 Electrode preparation and electrochemical experiments

Electrochemical measurements were performed on an Ivium Technologies Compactstat potentiostat (Netherlands) using three electrodes system, comprising glassy carbon (and modified glassy carbon), Ag/AgCl (3M KCl) and platinum wire as working, reference and counter electrodes respectively.

Prior to modification with DGP, a glassy carbon electrode (GCE) was polished with alumina slurry, rinsed with water and subsequently sonicated in water for 5 min. DGP was dispersed in DMF and sonicated for 10 min. 20 μL of the dispersion was pipetted onto the cleaned GCE and allowed to air-dry for 3 hr. Preparation of unitary and binary modifiers was done following similar protocols.

Cyclic voltammetry (CV) and electrochemical impedance spectroscopy (EIS) of the bare and modified GCE were carried out using 5 mM solution of $[Fe(CN)_6]^{3-/4-}$ prepared in 0.1 M KCl, as an electrochemical redox probe. Solutions for electrochemical measurements were purged with ultra-pure argon for 5 min.

5.3 Results and discussion

5.3.1 FTIR spectroscopy

The FTIR spectra of reduced graphene oxide and DGP are shown in Figure 5.1. For the graphene sheet, absorption bands at around 3410, 2925 and 2841, 1617 and 1155 cm^{-1} are assigned to O-H stretch, C-H stretch, aromatic C=C, and C-H in plane bending vibration respectively. In the spectrum of the composite material, absorption bands at around 1483 and 1567 cm^{-1} correspond to benzenoid rings and quinonoids rings vibrations (C=C stretching deformations) respectively. The band due to benzenoid ring at around 1483 cm^{-1} has higher intensity than the quinonoid ring band at 1567 cm^{-1}, as is often observed [34]. The peak at around 1303 cm^{-1} represents the C-N stretching vibration of secondary aromatic amine and the peak at around 1127 cm^{-1} shows the N=Q=N stretching, (Q = quinonoid ring). The absorption bands at around 1567, 1483 and 1127 cm^{-1} indicate the formation of PANI on graphene sheets.

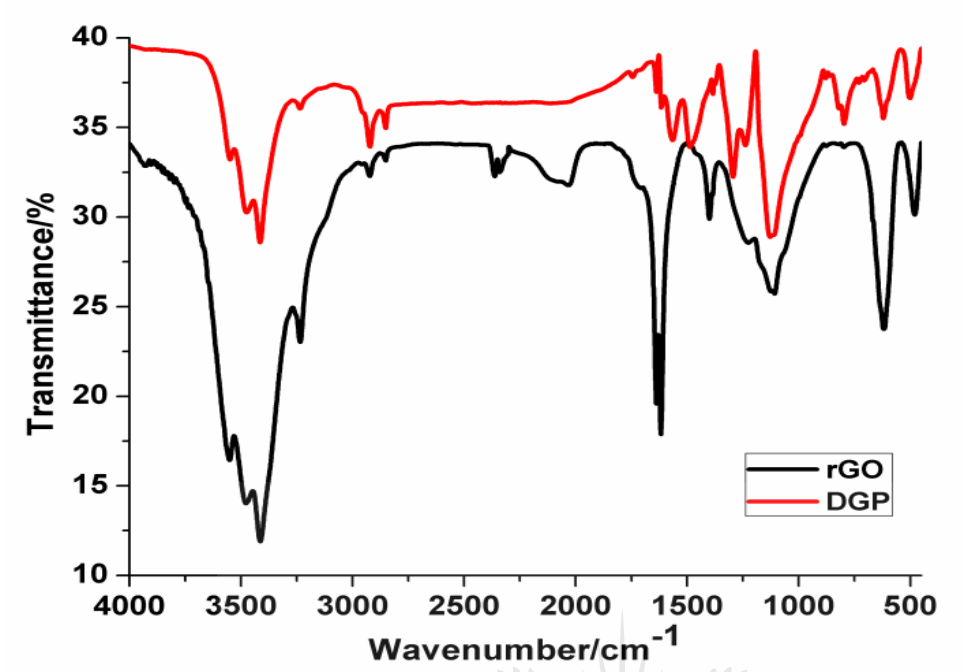

Fig. 5. 1. FTIR spectra of rGO and DGP

5.3.2 Raman analysis

Raman spectroscopy is an excellent tool for studying structural changes in carbon materials. It is often used to obtain valuable information on crystal structure and defects in graphene-based materials. The Raman spectra of graphene oxide, graphene, diamond and DGP are presented in Figure 5.2a. The G and D bands for GO are at around 1598 and 1338 cm^{-1} respectively. The G band arises from the vibration of sp^2 carbon atoms in a hexagonal ring structure and the D band often indicates the presence of defects in graphene/graphene-like materials. The G and D peaks in thermally reduced GO are centered at around 1588 and 1328 cm^{-1} respectively. Both the G and D peaks of GO are slightly red-shifted upon thermal treatment, indicating structural transformation. This is often observed when there is removal of oxygen functionalities from GO layers. There is an increase in the ratio of the D peak intensity to the G peak intensity (I_D/I_G) of the thermally reduced GO when compared with GO. The intensity of the D peak is related to the size of the in-plane sp^2 domains and increased I_D/I_G of GO upon reduction has

been linked to increased number of sp^2 cluster in the material. The Raman spectrum of diamond can be observed in Figure 5.2b, an intense and sharp peak at approximately 1327 cm^{-1} is seen. This D band is associated with the diamond T_{2g} vibration mode at the centre of the Brilliouin zone. The Raman spectrum of the diamond shows that graphitic impurities are absent. The Raman spectrum of the ternary composite shows a sharp D and slightly broadened G bands at around 1327 and 1585 cm^{-1} respectively. The small intensity of the G peak can be attributed to the presence of the highly intense diamond peak. No observable peaks are present for PANI, this may be due to peaks of PANI being too weak and/or there is overlap of the peaks with the peaks of other components in the composite. Similar observation was made by Kumar *et al.* in a study involving composite of PANI and reduced graphene oxide [34].

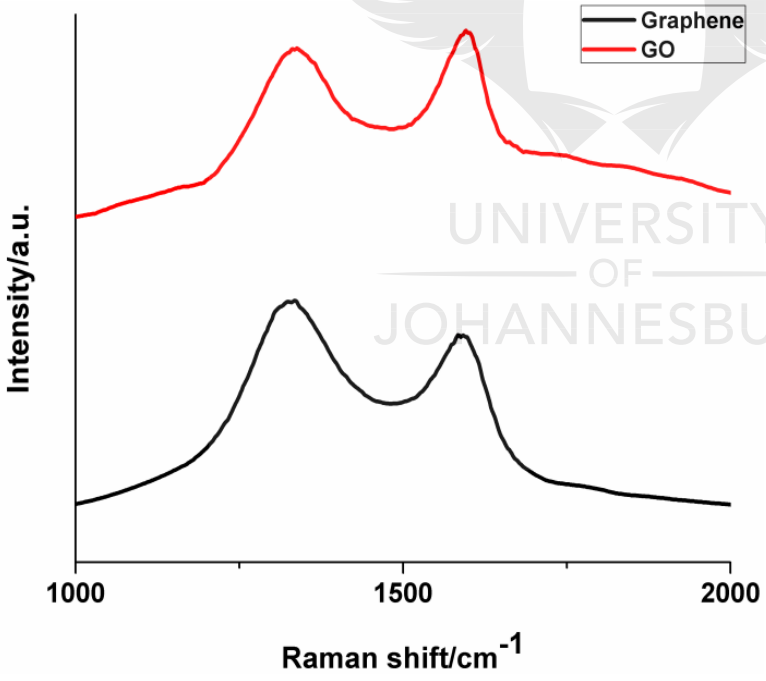

a)

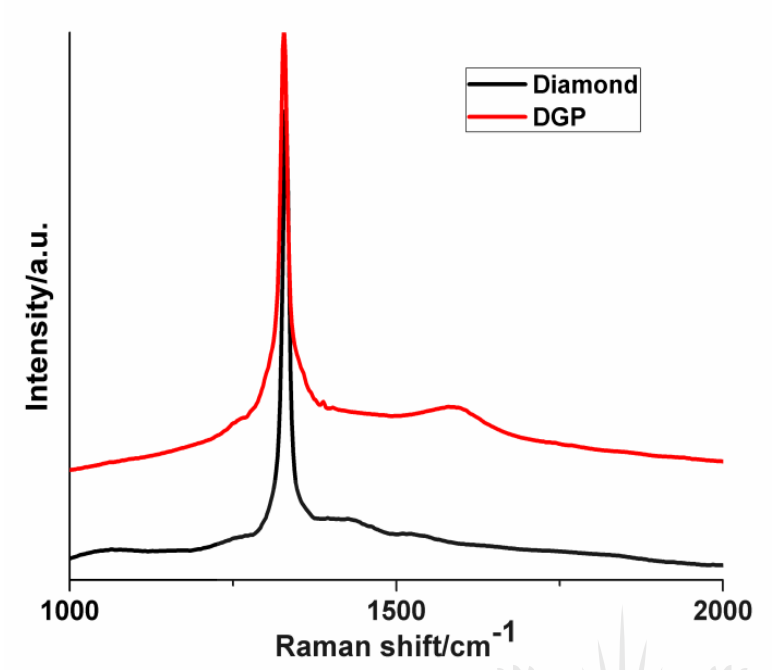

b)

Fig. 5. 2. Raman spectra of a) GO and rGO, b) diamond and DGP

5.3.3 X-ray diffraction analysis

The XRD patterns of GO, graphene, PANI and DGP are as shown in figure 5.3. In the spectrum of GO, there is a sharp and well-defined peak at 2θ = 11.1 ° which corresponds to (001) diffraction mode [35]. This peak is absent in the spectrum of the thermally reduced GO and there appears a new broad peak at around 24 °, which is related to the (002) mode of stacked reduced graphene oxide nanosheets [36]. The XRD pattern of PANI reveals three characteristic peaks centered at 14.7, 20.2 and 25.4 ° corresponding to (011), (020) and (200) crystal planes respectively. The peaks at around 20 and 25 ° have been attributed to periodicity parallel and perpendicular to the polymer chains of PANI, respectively [37]. In the spectrum of the composite material, the intense and sharp diamond peak at 43.6 ° (111) and 75.1 ° (220) can be clearly observed [38]. The characteristic peaks of PANI are still seen in the composite spectrum, while that of graphene appears to have overlapped with that of PANI.

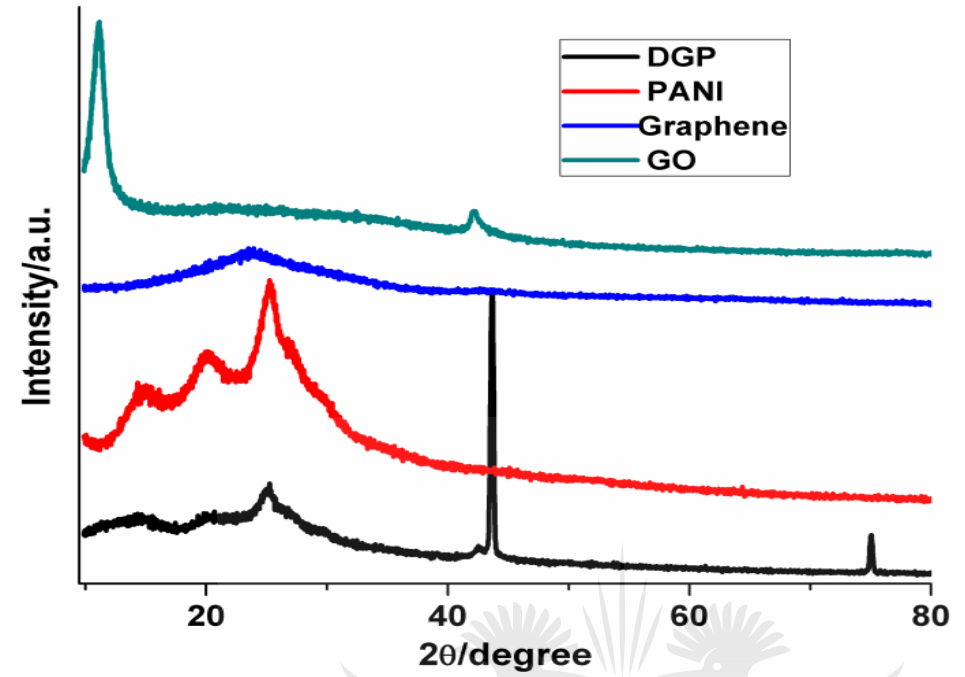

Fig. 5. 3. XRD patterns of GO, graphene, PANI and DGP

5.3. 4 Morphology and BET surface area analyses

The SEM and TEM images of diamond particles, DGP, graphene and PANI are shown in figure 5.4, The SEM image of DGP (Fig. 5.4b) reveals that the diamond particles, graphene sheets and PANI are properly 'fused' together. Nitrogen adsorption-desorption isotherm was used to investigate the specific surface area of diamond, graphene and DPG. Figures 5.4(f-h) show N_2 adsorption isotherms of diamond, graphene and DGP at standard temperature and pressure, and Table 5.1 reveal their various textural parameters. The presence of hysteresis loop in the isotherm of graphene confirms its mesoporous nature. The Brunauer-Emmett-Teller (BET) surface area of graphene is significantly much higher than those of both diamond and the composite. The presence of graphene resulted in improved surface area of the composite material when compared to pristine diamond.

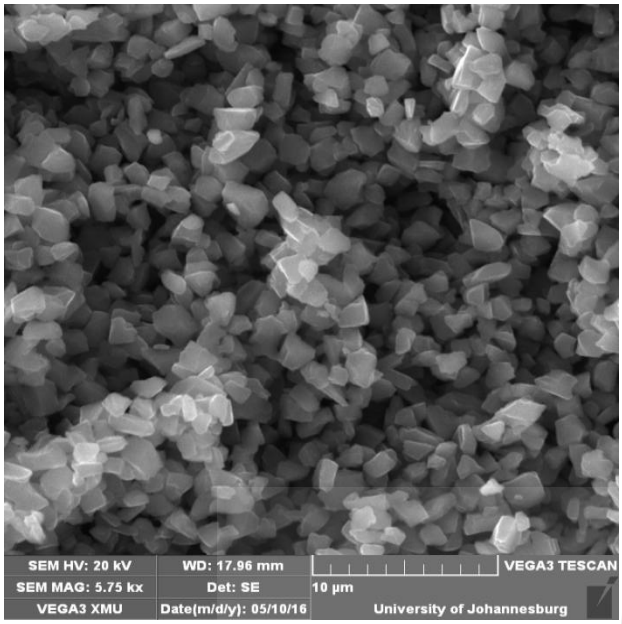
SEM HV: 20 kV
WD: 17.96 mm
VEGA3 TESCAN
SEM MAG: 5.75 kx
Det: SE
10 µm
VEGA3 XMU
Date(m/d/y): 05/10/16
University of Johannesburg

a)

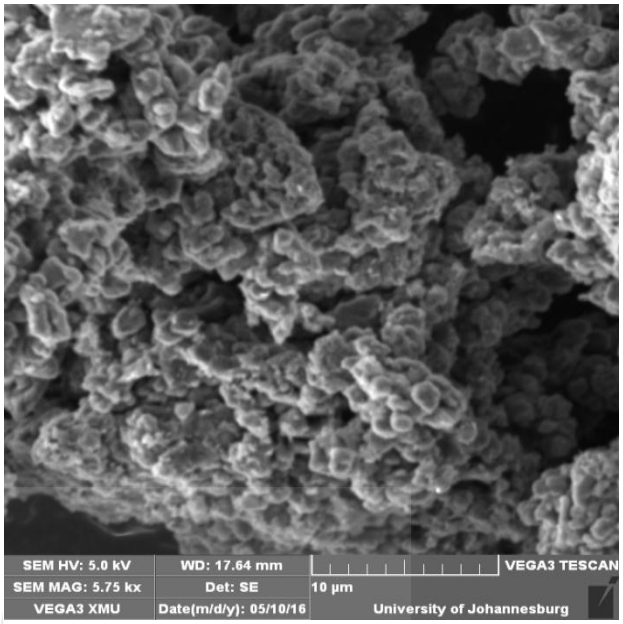
SEM HV: 5.0 kV
WD: 17.64 mm
VEGA3 TESCAN
SEM MAG: 5.75 kx
Det: SE
10 µm
VEGA3 XMU
Date(m/d/y): 05/10/16
University of Johannesburg

b)

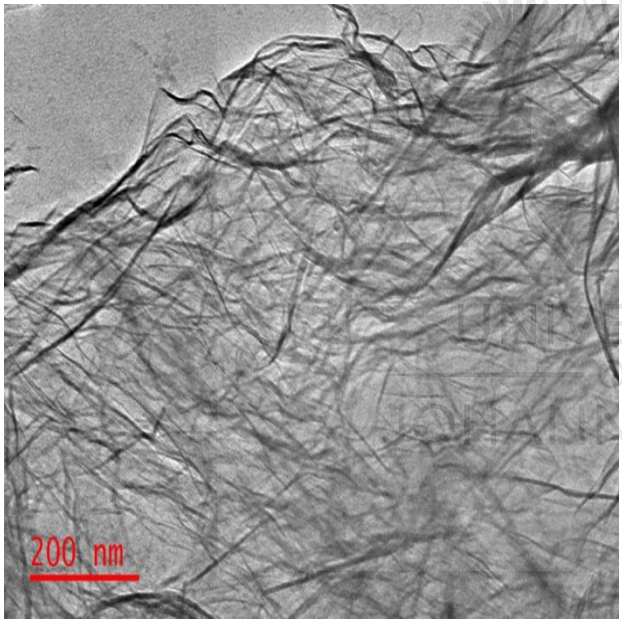
200 nm

c)

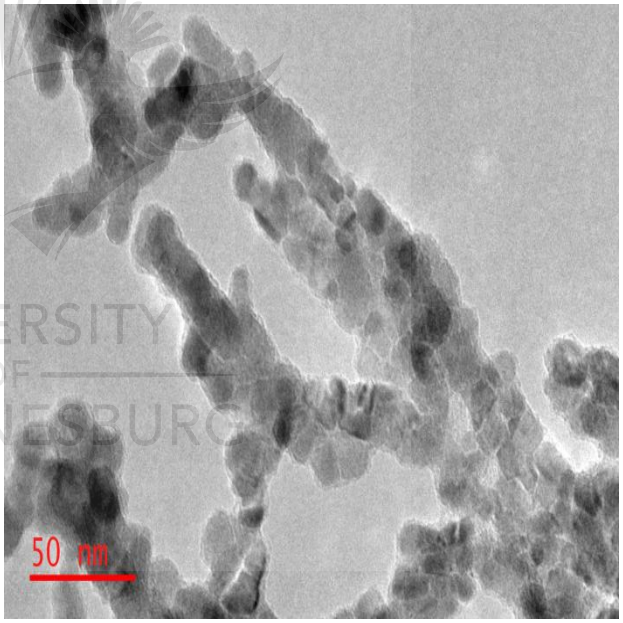
50 nm

d)

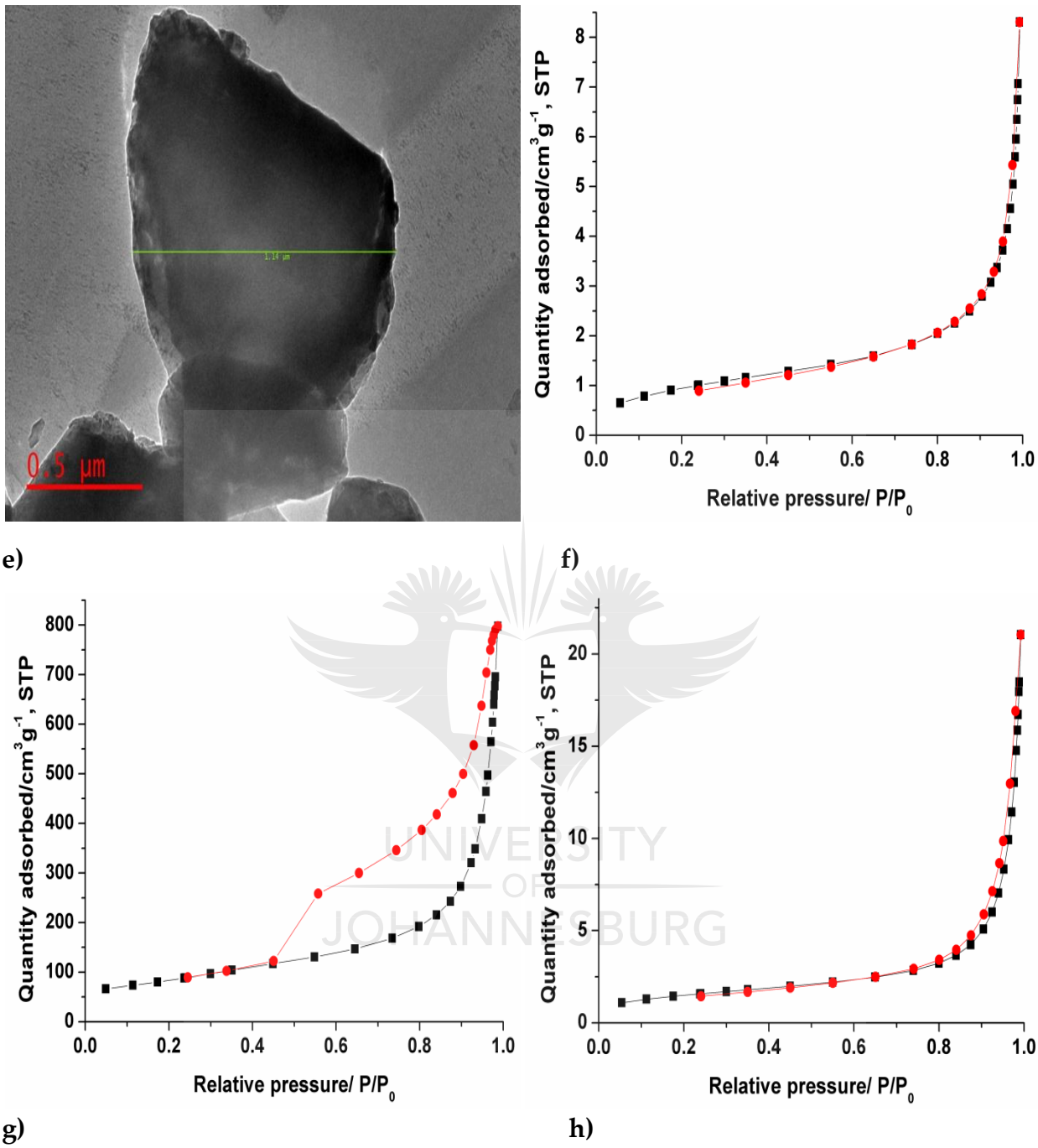

Fig. 5. 4. SEM micrographs of (a) Diamond particles (b) DGP, and TEM micrographs of (c) graphene (d) PANI (e) Diamond particles, Nitrogen adsorption-desorption isotherms of (f) Diamond particles (g) Graphene (h) DGP

Table 5.1. Physical properties of diamond, graphene and DGP obtained from N_2 adsorption

Sample	Surface area/m^2g^{-1}	Pore volume ($x10^{-3}$)/cm^3g^{-1}	Pore size/nm
Diamond	3.49	8.40	9.64
Graphene	298.04	1222	16.41
DGP	5.33	26.15	19.62

5.3.5 Electrochemical characterisations

The cyclic voltammograms of bare GCE and DGP modified GCE are shown in Figure 5.5a. The modification of GCE with DGP resulted in a remarkably high peak current. This increase can be related to the increased electro-active surface of the electrode as a result of modification with the composite material and this is beneficial for electro-analysis given the improved sensitivity of the sensing platform. The performance of the GCE-DGP was compared to other binary (GCE-DP and GCE-GP) and unitary (GCE-G) electrodes (Fig. 5.5b). The highest current signal was obtained on the ternary composite electrode in comparison to the other electrodes. It should be noted that if background current is accounted for, the current of the GCE-DGP is somewhat higher than that of the graphene-PANI (GCE-GP). The Nyquist diagrams obtained from electrochemical impedance spectroscopy (EIS) measurements usually provide valuable information on electron transfer kinetics at the electrode

interface. Nyquist plots often include a semicircle portion (depicting charge transfer resistance) and a linear portion for a Faradaic system. In Figure 5.5c, the Nyquist diagrams obtained from the EIS analysis of GCE and GCE-DPG reveal a marked difference between the semicircle portions of the two electrodes. The almost linear Nyquist plot of the modified GCE shows that it presents much higher electron mobility

than the bare GCE. This improved electron transfer rate can be attributed to the highly conductive nature of graphene.

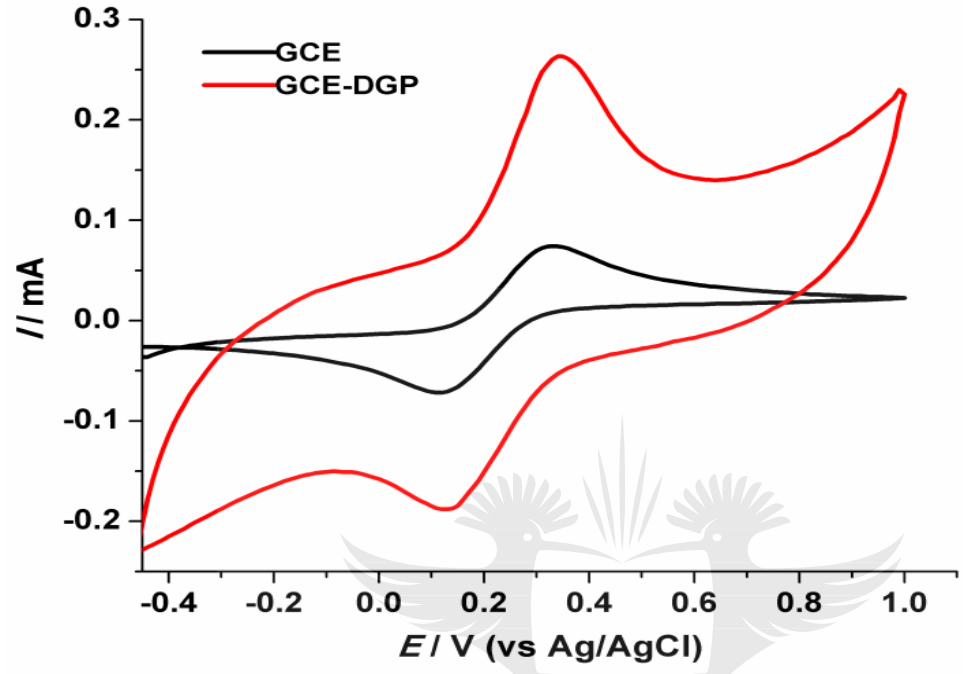

a)

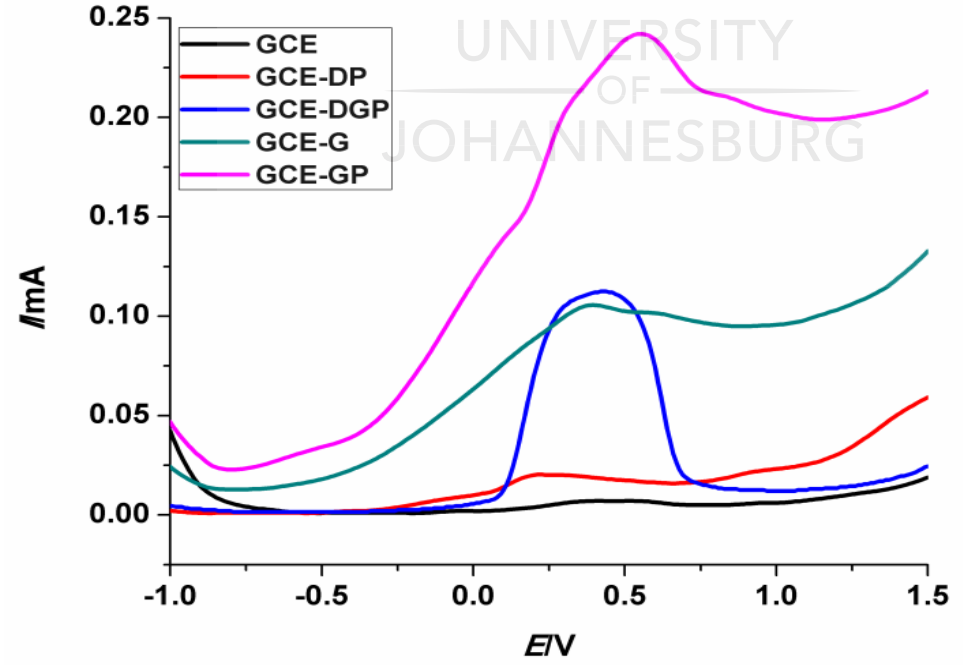

b)

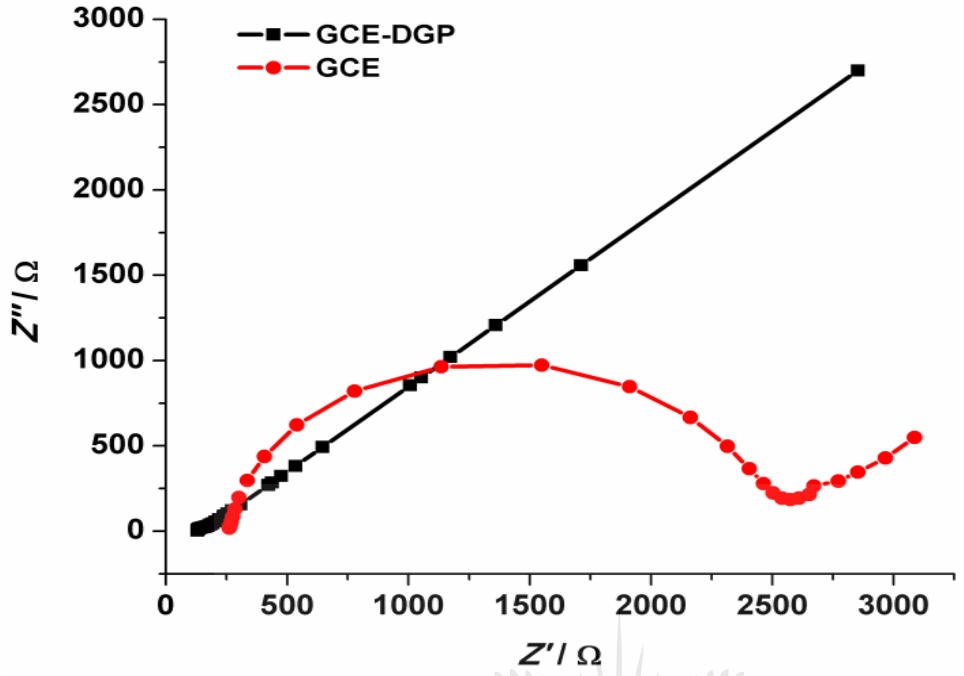

Fig. 5. 5. a) Cyclic voltammograms of GCE and GCE-DGP in 5.0 mM $K_3Fe(CN)_6$ at a scan rate of 0.05 Vs^{-1} , b) Square wave voltammograms of GCE, GCE-DP, GCE-DGP, GCE-G and GCE-GP in 80 μM 2,4-DCP, and c) Nyquist plots of GCE and GCE-DPG in 5.0 mM $K_3Fe(CN)_6$

5.3.5.1 Effects of pH and supporting electrolytes on the detection of 2,4-DCP

The pH of the analyte solution is an important parameter in electrochemical sensing. Therefore, the current response of 80 μM 2,4-DCP was examined at pH values of 1, 3, 5, 7, 9 and 12. The results are displayed in figure 5.6a. As can be observed, the highest current was obtained at pH 1. The current signal decreases with increasing pH. At alkaline pH, the current signal is not only smaller but a cathodic shift in the peak potential can also be observed. Furthermore, figure 5.6b reveals the effects of different electrolytes on the current response of 2,4-DCP at GCE-DGP, the signals in acidic solutions are markedly higher than those obtained in near neutral solutions of chloride and sulphate. Generally, when pH > pKa, the molecule would exist predominantly in

the anionic form, the molecule remains undissociated at a pH lower than its pKa. With pKa value of 7.89, 2,4-DCP is predominantly neutral at acidic pHs and ionised at alkaline pHs. The relatively low current signals obtained at increasing pH values suggest that the interaction between 2,4-DCP and the modifier is π-π and not electrostatic. The extensive π electrons system in both graphene and PANI favours their interaction with aromatic compounds.

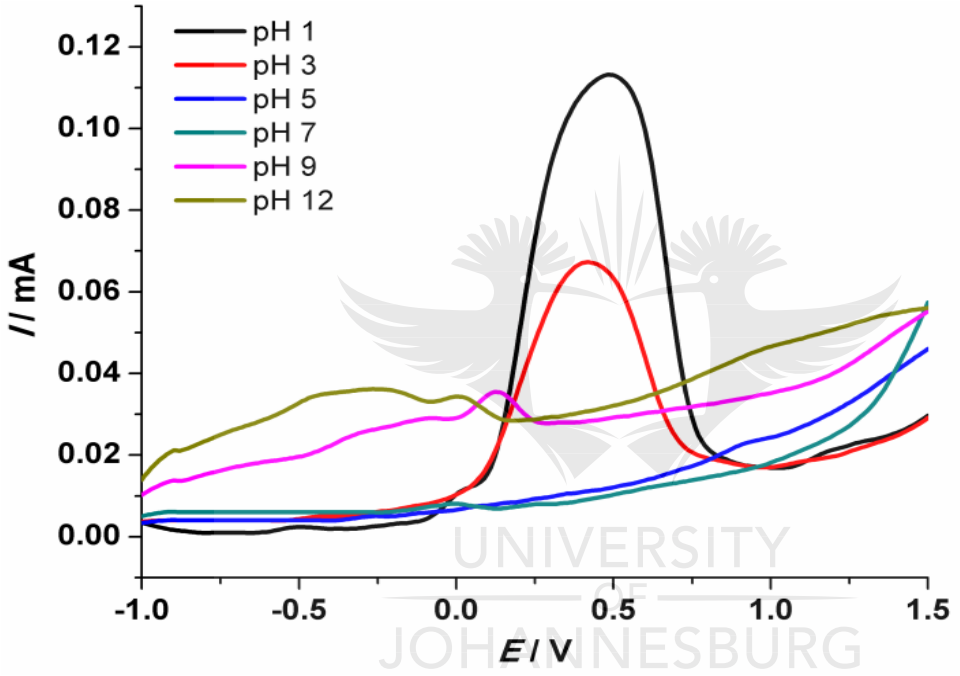

a)

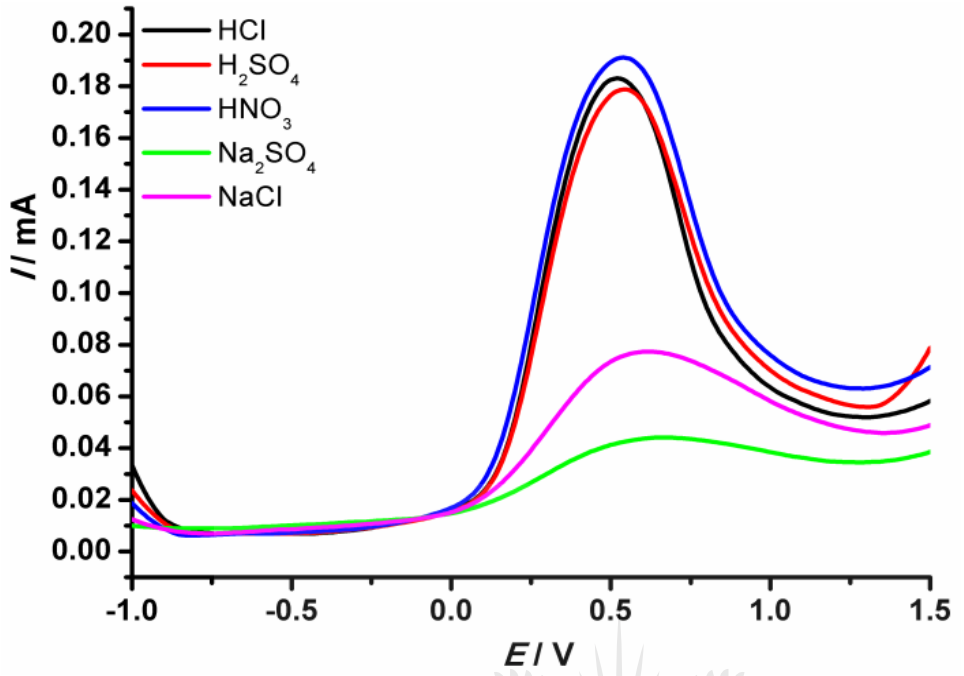

b)

Fig. 5. 6. a) square wave voltammograms of DGP-GCE in 80 µM 2,4-DCP at different pH, b) Effects of supporting electrolytes on the detection of 2,4-DCP using 123 µM solution, the concentration of each electrolyte was 0.1 M.

5.3.6 Square Wave Voltammetric (SWV) detection of 2,4-DCP

The determination of 2,4-DCP was achieved using square wave voltammetry. Increase in the oxidation current signals of 2,4-DCP with increasing concentration from 5 - 80 µM, can be observed (fig. 5.7). The linear regression equation from the calibration plot was

$y = 1.1075X + 2.5840 \times 10^{-5}$ ($R^2 = 0.9935$) and the limit of detection was calculated to be 0.25 µM. A comparison of the performance of the electrode with some previously reported electrodes for the determination of 2,4-DCP reveal that this electrode offered good sensitivity [16, 18, 39, 40]. The fabricated sensor was applied for the detection of 2,4-DCP in domestic wastewater obtained from Daasport Wastewater treatment,

Pretoria, South Africa. Before analysis, the water sample was filtered and the pH adjusted with HNO_3. The results obtained are displayed in Table 2. These data show that DGP based sensor is suitable for the determination of 2,4-DCP in environmental samples.

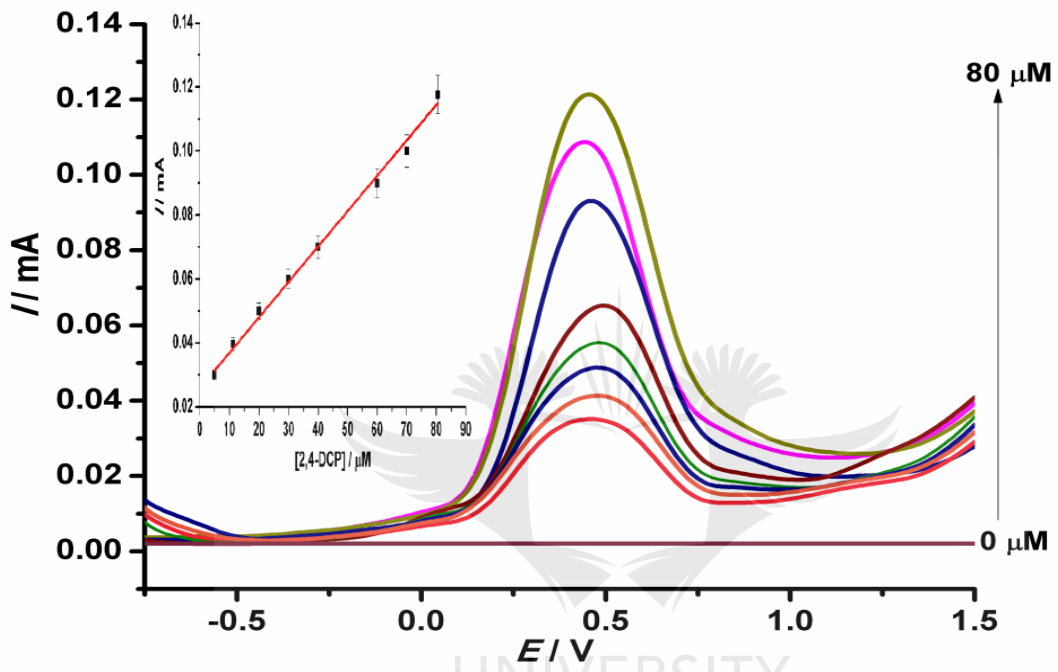

Fig. 5. 7. Square wave voltammograms of GCE-DGP in different concentrations of 2-DCP [5, 10, 20, 40, 60,70 and 80 μM] (prepared in 0.1 M HNO_3) Inset: plot of [2,4-DCP] vs peak current

Table 2. Recovery of 2,4-DCP in wastewater sample (n = 3)

Sample	Added (μM)	Detected (μM)	Recovery (%)	RSD (%)
1	2	2.164	108.200	3.8
2	10	10.067	100.670	2.2
3	20	21.955	109.775	1.5

5.3.7 Stability of GCE-DGP

To examine the stability of the electrode, ten successive measurements were taken using 80 μM 2,4-DCP (Fig. 5.8a). The relative standard deviation of the peak current for the ten measurements was found to be 2.8%. It can be reasonably asserted that the electrode is stable and applicable for the analysis of 2,4-DCP in aqueous media. The electroanalysis of 2,4-DCP (and other phenols) often presents the challenge of fouling, with the oxidation products adhering to the surface of the electrode. The ternary electrode was found to show the best antifouling behavior towards phenol oxidation. To further illustrate this, Figures 5.7a and 5.7b present a 20-scan run in the presence of 2,4 DCP for the ternary electrode GCE-DGP and the graphene-PANI electrode (GCE-GP). A variation (reduction) in the peak currents of the first and last scan suggests that the GCE-DGP (Fig. 5.8a) has a better resistance to fouling than the GCE-GP (Fig. 5.8b). The GCE-DGP was found to be the most stable of all the electrodes. The background currents of each of the 20 scans of the GCE-DGP remained constant (leading to a better current resolution), while variations can be observed for the GCE-GP as the number of scans increase. This observation is also indicative of the better stability of the ternary electrode.

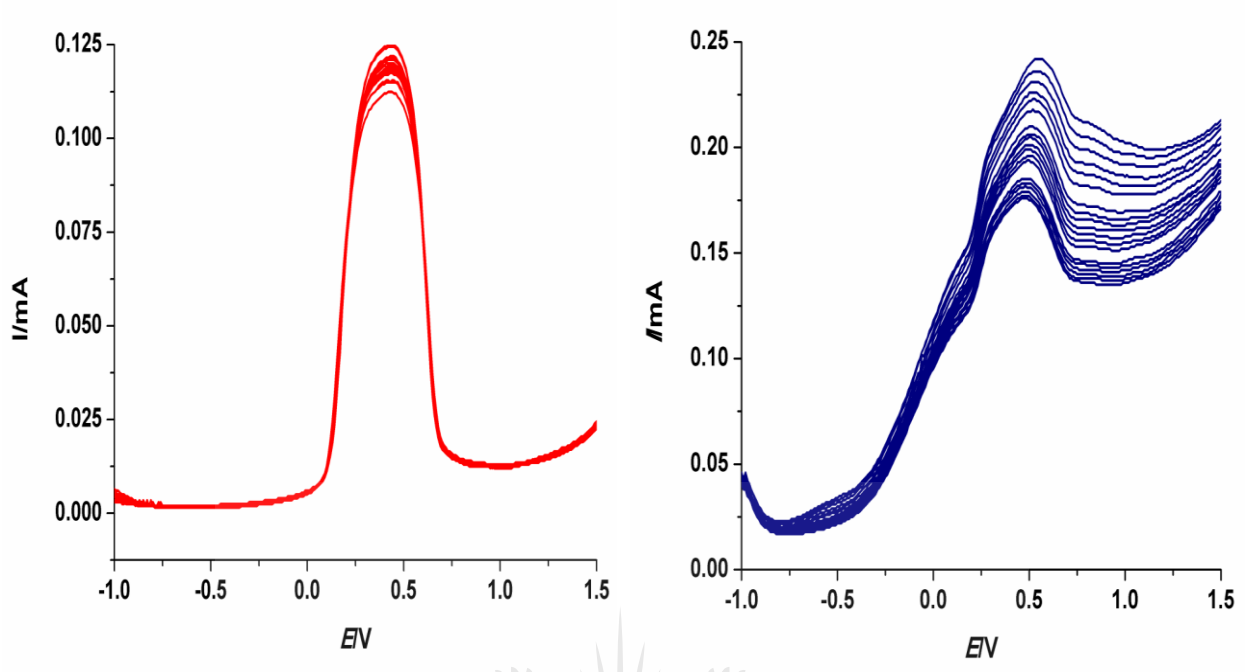

a) b)

Fig. 5. 8. Square wave voltammograms of a) GCE-DGP (b graphene-PANI modified GCE in 80 μM 2,4-DCP (20 runs for each electrode)

5.3.8 Selectivity studies

Furthermore, the selectivity of the proposed sensor was investigated by measuring the electrochemical response of 2,4-DCP in the presence of two other phenols, phenol and 4-chlorophenol (4-CP). The concentrations of 2,4-DCP, Phenol and 4-CP are 80 μM each in the mixture. As can be seen in figure 5.8 , the presence of both phenol and 4-CP in 2,4-DCP solution led to an increase in the current signal of 2,4-DCP. The oxidation of some phenolic compounds at a similar potential has been reported before [24] and these reports reveal the challenge of selectivity while sensing such compounds. After the addition of other phenols, the peak current increase was very minimal, therefore this sensor shows high sensitivity toward 2,4 DCP and thus can still find use for the detection of chlorophenols in aqueous media. The selectivity of this sensor is further

strengthened by the excellent recoveries calculated (Table 2) when used in real wastewater sample with a more complex matrix.

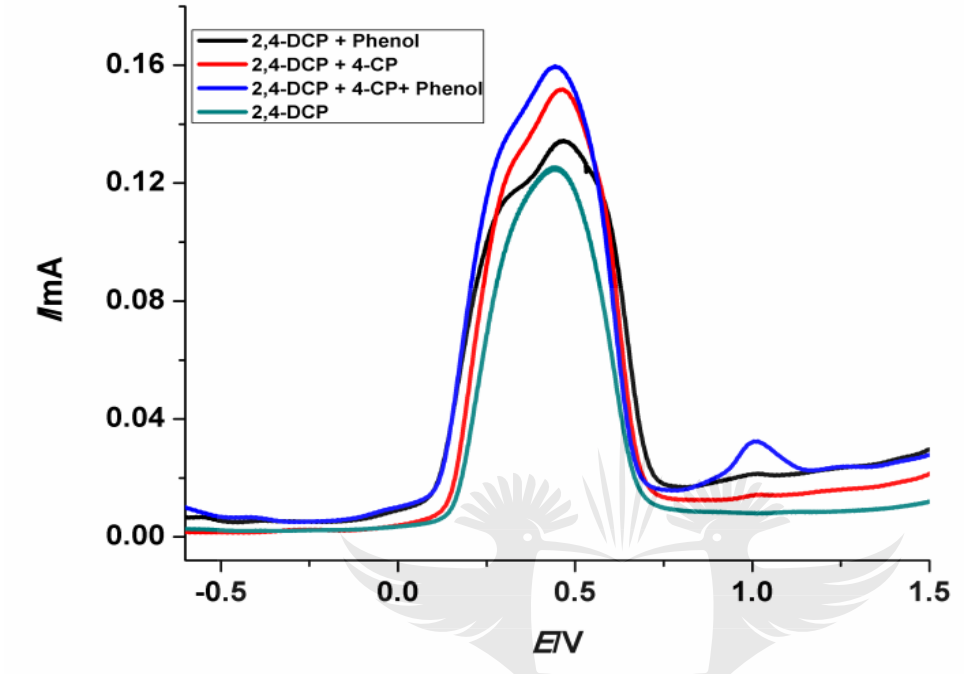

Fig. 5. 9. Square wave voltammograms of 2,4-DCP in the presence of other phenolic compounds

5.4 Sub-conclusion

DGP was prepared by in situ oxidative polymerisation of aniline in the presence of diamond and graphene. The DPG modified GCE showed remarkably improved electrochemical properties compared to the bare GCE. The modified electrode was applied for the determination of 2,4-DCP in standard and real samples. The results obtained reveal that the sensor is suitable for analytical application. Graphene and PANI were deemed to enhance interaction between the analyte and the sensor by means of π-π interactions, while diamond was believed to act as anti-passivating agent. This is because of its low susceptibility to passivation. The electrode may represent a promising platform for the determination of 2,4-DCP in environmental samples.

5.5 References

[1] L. Kong, K. Kadokami, S. Wang, H.T. Duong, H.T.C. Chau, Monitoring of 1300 organic micro-pollutants in surface waters from Tianjin, North China, Chemosphere 122 (2015) 125-130.

[2] R.L. Pérez, G.M. Escandar, Experimental and chemometric strategies for the development of Green Analytical Chemistry (GAC) spectroscopic methods for the determination of organic pollutants in natural waters, Sustainable Chemistry and Pharmacy 4 (2016) 1-12.

[3] S. Sandron, A. Rojas, R. Wilson, N.W. Davies, P.R. Haddad, R.A. Shellie, P.N. Nesterenko, B.P. Kelleher, B. Paull, Chromatographic methods for the isolation, separation and characterisation of dissolved organic matter, Environmental Science: Processes & Impacts 17 (2015) 1531-1567.

[4] B. Vrana, L. Komancová, J. Sobotka, Calibration of a passive sampler based on stir bar sorptive extraction for the monitoring of hydrophobic organic pollutants in water, Talanta 152 (2016) 90-97.

[5] M. Antolovich, P. Prenzler, K. Robards, D. Ryan, Sample preparation in the determination of phenolic compounds in fruits, Analyst 125 (2000) 989-1009.

[6] M.J. George, L. Marjanovic, D.B.G. Williams, Solvent-Assisted Headspace Sampling Using Solid Phase Microextraction for the Analysis of Phenols in Water, Analytical chemistry 87 (2015) 9559-9562.

[7] N.I. Ikhsan, P. Rameshkumar, N.M. Huang, Controlled synthesis of reduced graphene oxide supported silver nanoparticles for selective and sensitive electrochemical detection of 4-nitrophenol, Electrochimica Acta 192 (2016) 392-399.

[8] Z. Zhang, S. Zhai, M. Wang, L. He, D. Peng, S. Liu, Y. Yang, S. Fang, H. Zhang, Electrochemical sensor based on a polyaniline-modified SnO_2 nanocomposite for detecting ethephon, Analytical Methods 7 (2015) 4725-4733.

[9] X. Wang, X. Lu, L. Wu, J. Chen, Direct electrochemical tyrosinase biosensor based on mesoporous carbon and Co3O4 nanorods for the rapid detection of phenolic pollutants, ChemElectroChem 1 (2014) 808-816.

[10] J. Li, D. Miao, R. Yang, L. Qu, P.d.B. Harrington, Synthesis of poly (sodium 4-styrenesulfonate) functionalized graphene/cetyltrimethylammonium bromide (CTAB) nanocomposite and its application in electrochemical oxidation of 2, 4-dichlorophenol, Electrochimica Acta 125 (2014) 1-8.

[11] E. Er, H. Çelikkan, N. Erk, A novel electrochemical nano-platform based on graphene/platinum nanoparticles/nafion composites for the electrochemical sensing of metoprolol, Sensors and Actuators B: Chemical 238 (2017) 779-787.

[12] K.P. Prathish, R.C. Carvalho, C.M. Brett, Electrochemical characterisation of poly (3, 4-ethylenedioxythiophene) film modified glassy carbon electrodes prepared in deep eutectic solvents for simultaneous sensing of biomarkers, Electrochimica Acta 187 (2016) 704-713.

[13] C. Apetrei, M. Rodríguez-Méndez, J. De Saja, Amperometric tyrosinase based biosensor using an electropolymerized phosphate-doped polypyrrole film as an immobilization support. Application for detection of phenolic compounds, Electrochimica Acta 56 (2011) 8919-8925.

[14] J.H. Kim, S.-G. Hong, H.J. Sun, S. Ha, J. Kim, Precipitated and chemically-crosslinked laccase over polyaniline nanofiber for high performance phenol sensing, Chemosphere 143 (2016) 142-147.

[15] C. Wu, Z. Liu, H. Sun, X. Wang, P. Xu, Selective determination of phenols and aromatic amines based on horseradish peroxidase-nanoporous gold co-catalytic strategy, Biosensors and Bioelectronics 79 (2016) 843-849.

[16] S. Dong, G. Suo, N. Li, Z. Chen, L. Peng, Y. Fu, Q. Yang, T. Huang, A simple strategy to fabricate high sensitive 2, 4-dichlorophenol electrochemical sensor based on metal organic framework Cu 3 (BTC) 2, Sensors and Actuators B: Chemical 222 (2016) 972-979.

[17] T. Gan, Z. Lv, J. Sun, Z. Shi, Y. Liu, Preparation of graphene oxide-wrapped carbon sphere@ silver spheres for high performance chlorinated phenols sensor, Journal of hazardous materials 302 (2016) 188-197.

[18] L. Yu, X. Yue, R. Yang, S. Jing, L. Qu, A sensitive and low toxicity electrochemical sensor for 2, 4-dichlorophenol based on the nanocomposite of carbon dots, hexadecyltrimethyl ammonium bromide and chitosan, Sensors and Actuators B: Chemical 224 (2016) 241-247.

[19] B.L. Hanssen, S. Siraj, D.K. Wong, Recent strategies to minimise fouling in electrochemical detection systems, Reviews in Analytical Chemistry 35 (2016) 1-28.

[20] M.M. Hossain, L. Aldous, Polyoxometalates as solution-phase electrocatalytic mediators for reduced electrode fouling and the improved oxidative response of phenols, Electrochemistry Communications 69 (2016) 32-35.

[21] A. Safavi, N. Maleki, F. Tajabadi, Highly stable electrochemical oxidation of phenolic compounds at carbon ionic liquid electrode, Analyst 132 (2007) 54-58.

[22] A.N. Kawde, M.A. Morsy, N. Odewunmi, W. Mahfouz, From electrode surface fouling to sensitive electroanalytical determination of phenols, Electroanalysis 25 (2013) 1547-1555.

[23] J. Gao, L. Liu, X. Liu, H. Zhou, S. Huang, Z. Wang, Levels and spatial distribution of chlorophenols–2, 4-dichlorophenol, 2, 4, 6-trichlorophenol, and pentachlorophenol in surface water of China, Chemosphere 71 (2008) 1181-1187.

[24] S. Chiron, C. Minero, D. Vione, Occurrence of 2, 4-dichlorophenol and of 2, 4-dichloro-6-nitrophenol in the Rhône river delta (Southern France), Environmental science & technology 41 (2007) 3127-3133.

[25] S.M. Amer, F.A. Aly, Genotoxic effect of 2, 4-dichlorophenoxy acetic acid and its metabolite 2, 4-dichlorophenol in mouse, Mutation Research/Genetic Toxicology and Environmental Mutagenesis 494 (2001) 1-12.

[26] M. Bors, B. Bukowska, R. Pilarski, K. Gulewicz, J. Oszmiański, J. Michałowicz, M. Koter-Michalak, Protective activity of the Uncaria tomentosa extracts on human erythrocytes in oxidative stress induced by 2, 4-dichlorophenol (2, 4-DCP) and catechol, Food and chemical toxicology 49 (2011) 2202-2211.

[27] S. Yang, R.S. Wu, R.Y. Kong, Physiological and cytological responses of the marine diatom Skeletonema costatum to 2, 4-dichlorophenol, Aquatic Toxicology 60 (2002) 33-41.

[28] M. Ferreira, H. Varela, R.M. Torresi, G. Tremiliosi-Filho, Electrode passivation caused by polymerization of different phenolic compounds, Electrochimica Acta 52 (2006) 434-442.

[29] M. Ureta-Zanartu, P. Bustos, C. Berrıos, M. Diez, M. Mora, C. Gutiérrez, Electrooxidation of 2, 4-dichlorophenol and other polychlorinated phenols at a glassy carbon electrode, Electrochimica Acta 47 (2002) 2399-2406.

[30] G.W. Muna, N. Tasheva, G.M. Swain, Electro-oxidation and amperometric detection of chlorinated phenols at boron-doped diamond electrodes: a comparison of microcrystalline and nanocrystalline thin films, Environmental science & technology 38 (2004) 3674-3682.

[31] C. Terashima, T.N. Rao, B. Sarada, D. Tryk, A. Fujishima, Electrochemical oxidation of chlorophenols at a boron-doped diamond electrode and their determination by high-performance liquid chromatography with amperometric detection, Analytical chemistry 74 (2002) 895-902.

[32] N.J. Walch, F. Davis, N. Langford, J.L. Holmes, S.D. Collyer, S.P. Higson, Enhancement of electrode performance by a simple casting method using sonochemically exfoliated graphene, Analytical chemistry 87 (2015) 9273-9279.

[33] H.-K. Seo, S. Ameen, M.S. Akhtar, H.S. Shin, Structural, morphological and sensing properties of layered polyaniline nanosheets towards hazardous phenol chemical, Talanta 104 (2013) 219-227.

[34] N.A. Kumar, H.-J. Choi, Y.R. Shin, D.W. Chang, L. Dai, J.-B. Baek, Polyaniline-grafted reduced graphene oxide for efficient electrochemical supercapacitors, ACS nano 6 (2012) 1715-1723.

[35] C. Fu, G. Zhao, H. Zhang, S. Li, Evaluation and characterization of reduced graphene oxide nanosheets as anode materials for lithium-ion batteries, Int. J. Electrochem. Sci 8 (2013) 6269-6280.

[36] J. Cao, Y. Zhu, X. Yang, Y. Chen, Y. Li, H. Xiao, W. Hou, J. Liu, The promising photo anode of graphene/zinc titanium mixed metal oxides for the CdS quantum dot-sensitized solar cell, Solar Energy Materials and Solar Cells 157 (2016) 814-819.

[37] U. Bogdanović, V. Vodnik, M. Mitrić, S. Dimitrijević, S.o.D. Skapin, V. Žunič, M. Budimir, M. Stoiljković, Nanomaterial with High Antimicrobial Efficacy© Copper/Polyaniline Nanocomposite, ACS applied materials & interfaces 7 (2015) 1955-1966.

[38] M. Peleyeju, E. Umukoro, J. Babalola, O. Arotiba, Electrochemical Degradation of an Anthraquinonic Dye on an Expanded Graphite-Diamond Composite Electrode, Electrocatalysis 7 (2016) 132-139.

[39] J. Zhang, J. Lei, H. Ju, C. Wang, Electrochemical sensor based on chlorohemin modified molecularly imprinted microgel for determination of 2, 4-dichlorophenol, Analytica chimica acta 786 (2013) 16-21.

[40] Y. Sun, L. Wang, H. Liu, Myoglobin functioning as cytochrome P450 for biosensing of 2, 4-dichlorophenol, Analytical Methods 4 (2012) 3358-3363.

[41] J. Li, X. Li, R. Yang, L. Qu, P.d.B. Harrington, A sensitive electrochemical chlorophenols sensor based on nanocomposite of ZnSe quantum dots and cetyltrimethylammonium bromide, Analytica chimica acta, 804 (2013) 76-83.

[42] L. Yu, X. Yue, R. Yang, S. Jing, L. Qu, A sensitive and low toxicity electrochemical sensor for 2, 4-dichlorophenol based on the nanocomposite of carbon dots, hexadecyltrimethyl ammonium bromide and chitosan, Sensors and Actuators B: Chemical, 224 (2016) 241-247.

[43] J. Li, D. Miao, R. Yang, L. Qu, P.d.B. Harrington, Synthesis of poly (sodium 4-styrenesulfonate) functionalized graphene/cetyltrimethylammonium bromide (CTAB) nanocomposite and its application in electrochemical oxidation of 2, 4-dichlorophenol, Electrochimica Acta, 125 (2014) 1-8.

CHAPTER SIX

PHOTOELECTROCATALYTIC WATER TREATMENT SYSTEMS: DEGRADATION, KINETICS AND INTERMEDIATE PRODUCTS STUDIES OF SULFAMETHOXAZOLE ON A TIO_2-EXFOLIATED GRAPHITE ELECTRODE[1]

6.1 Introduction

Antibiotics have been and are being used in the treatment of a broad range of infections caused by bacteria, saving man and animals from pain, distress and death. In recent time, however, there has been a growing concern over the proliferation of antibiotic-resistant bacteria and it is believed that the presence of antibacterial agents in the environment has contributed to the emergence of these bacteria strains [1, 2]. A number of these substances are not easily biodegradable and thus they persist in the environment. The detection of antibiotics in surface and ground waters is well documented and sulfamethoxazole (SMX), a sulfonamide, is among the most frequently detected [3-7]. SMX finds a wide application in human and veterinary medicine for treatment of infections [8]. Incomplete metabolism in the body and ineffective treatment of wastewater from pharmaceutical industries may result in the accumulation of this substance and its metabolites in the environment.

There have been a large number of investigations on the destruction of organic pollutants via electrochemical approach [9-12]. In particular, direct or indirect oxidation

[1] This chapter has been published as: Peleyeju, M.G., Umukoro, E.H., Tshwenya, L., Moutloali, R., Babalola, J.O., Arotiba, O.A.* Photoelectrocatalytic water treatment systems: degradation, kinetics and intermediate products studies of sulfamethoxazole on a TiO2–exfoliated graphite electrode. *RSC Advances*, **2017**, 7, 40571-40580

involving the generation of hydroxyl radicals at a feasible potential has been shown to be promising for the remediation of water contaminated by organic substances [13, 14]. The development of photoelectrochemical process to enhance oxidation of organic pollutants at the anode renders this approach more effective and more attractive. A typical photoelectrochemical cell is equipped with an anode that is photoactive; such that the generation of the powerful hydroxyl radicals, which react unselectively with many recalcitrant organic pollutants, is maximised in the presence of light. In photoelectrocatalytic system, the challenges often associated with the traditional photocatalytic process are minimised. For instance, the problem of electrons and holes recombination [15] is reduced as the electrons generated are driven away via the external circuit [16, 17]. Similarly, recovering of the photocatalyst from the suspension after treatment is not required as it is immobilised/localised on a substrate. The synergistic benefit of electrical energy and solar energy also makes the photoelectrocatalytic method more suitable for oxidising organic contaminants in wastewater.

Photocatalytic semiconductors have been immobilised onto conductive substrates and employed as photoanodes for treating water polluted by organic substances. In a recent report by Li et al., a phosphate modified BiOCl photocatalyst was immobilised onto FTO glass and the resulting photoanode was employed for water oxidation and methyl orange degradation [18]. Similarly, Zeng *et al.* prepared a film of WO_3 nanoplates on FTO glass and applied the anode for the photoelectrochemical degradation of methylene blue [19]. In another study by Lin and co-workers, Bi_2WO_6 film was formed on ITO glass and the electrode was utilised for the photo-assisted anodic oxidation of rhodamine B [20]. TiO_2 is one of the most explored photoactive materials in many photocatalytic applications [21]. It has received considerable attention as a choice material for the preparation of anodes for use in photoelectrochemical processes. TiO_2 is preferred because of its high photocatalytic activity, chemical stability, low cost and

non-toxicity. In a report by Su *et al.*, TiO_2 photoanode was prepared by treating Ti foil in a solution of titanium (IV) chloride and nitric acid. The electrode was used for the degradation of sulfamethoxazole in the presence of UV light, and it was reported to be effective for the degradation of the pharmaceutical especially when chloride was used as supporting electrolyte [17]. In another investigation by Kondalkar *et al.*, TiO_2 was immobilised onto FTO glass substrate by dip coating and the photoanode reportedly showed good electrocatalytic activity towards the oxidation of the antibiotic, cefotaxime, under UV irradiation [22]. Also, Wei *et al.* prepared a film of TiO_2/g-C_3N_4 hybrid heterostructure on ITO glass by surface hybridisation and dip-coating approach. The anode reportedly exhibited good photoelectrocatalytic property towards phenol oxidation [23]. Efforts have been made to trap TiO_2 nanoparticles in the pores of certain carbon materials. For instance, a few reports have emerged on the use of graphite rods and expanded graphite as supports for the immobilisation of TiO_2. In these studies, the photoanodes were used for the degradation of phenols and dyes [24-27]. In particular, the porous and the compressible nature of expanded graphite were advantageous for the trapping of the photocatalyst. In addition, factors such as low cost, ease of preparation, and high conductivity also encouraged the use of graphite-based supports for TiO_2 photoanode. The impressive electron transport property of exfoliated graphite is desirable for channeling away the photogenerated electrons [28], consequently, the lifespan of the charges can be prolonged. In essence, this promotes the production of the powerful hydroxyl radicals which are required for the oxidation of the organic compounds in water.

In this work, a nanocomposite of TiO_2 and exfoliated graphite (EG) was prepared via sol-gel and microwave techniques. The composite material was fabricated into electrode and employed for the photoelectrochemical oxidation of sulfamethoxazole for the first time.

6.2 Experimental

6.2.1 Reagents and materials

Natural graphite flakes, nitric acid, sulphuric acid, n-butanol, titanium butoxide, potassium ferricyanide, potassium nitrate, sodium sulphate, sulfamethoxazole, formic acid and acetonitrile were purchased from Sigma-Aldrich (South Africa) and used as obtained. All solutions were prepared with deionised water.

6.2.2 Characterisations

X-ray diffraction (XRD) patterns were obtained on Rigaku Smartlab x-ray diffractometer (USA) with Cu kα radiation. Raman analyses were performed on Witec alpha300 R confocal Raman microscope (Germany). Electron images were obtained on scanning electron microscope (TESCAN, Vega3 XMU, Czech Republic) and transmission electron microscope (JEM 2100 TEM, 200 kV, Japan). UV-Vis spectra of the aliquots of SMX withdrawn from the reaction cell at fixed time intervals were recorded on Agilent Cary 60 spectrophotometer (Malaysia) and the chemical oxygen demand was determined on HACH DR3900 spectrophotometer. SMX degradation intermediates were identified using Shimadzu LCMS 8030 (triplequad) equipped with a Shimadzu LC-30AD Nexera Liquid Chromatography, a Shimadzu SIL-30 AC Nexera autosampler, and a Shimadzu CTO-20 AC Prominence Column Oven. The analytical column was a C18 column (Shimadzu 2 μm, 2.1 mm × 100 mm) which was maintained at 40° C. The flow rate was 0.2 mL.min^{-1} and injection volume was 5 μL, the mobile phases were acetonitrile and 0.1% formic acid.

6.2.3 Preparation of EG and TiO_2-EG

Preparation of EG was done according to a method reported earlier [29]. Firstly, sieving of natural graphite flakes was achieved by 300 micron sieve. The uniformly sized graphite flakes were then dispersed in a mixture of nitric acid and sulfuric acid (1:3 v/v). The mixture was kept at ambient conditions for 24 h, after which the resulting acid intercalated material was washed with deionised water until a near neutral pH was achieved. The material was then air dried and subsequently subjected to a thermal treatment at 800 °C for 60 s. The product obtained is a puffed up material with a large volume-to-mass ratio.

In a typical preparation of the nanocomposite of EG and TiO_2, 2 g of EG was dispersed in a 30 mL of n-butanol, and the mixture was stirred magnetically for 5 min. Thereafter, 6 mL of titanium butoxide was added to the mixture, and the hydrolysis of the titanium butoxide was achieved by drop-wise addition of 5 mL of water to the mixture while stirring vigorously. The sol formed was subsequently transferred into a reaction vessel and placed in Anton Paar microwave synthesis reactor operated at 600 W for 10 min. The material obtained was calcined at 400 °C for 2 h. Pristine TiO_2 was prepared following the same procedure except that EG was not added.

6.2.4 Fabrication of electrodes

The TiO_2-EG prepared was compressed into 15.0 mm pellets at high pressure using a hydraulic press. A clean copper wire of diameter 1.0 mm and resistivity 1.673 μΩcm was coiled at one end to form a flat surface, conductive silver glue was applied onto this surface and the pellet was subsequently placed. It was then left to air dry at room temperature for 30 minutes. The edges of the pellets were then covered with non-conductive epoxy resin and the electrode was then placed in a glass rod and sealed with

the resin and teflon tape, exposing only the electrode surface and the terminal copper wire.

6.2.5 Electrochemical and photoelectrochemical experiments

Electrochemical experiments were carried out on a computer-controlled potentiostat/galvanostat (autolab, PGSTAT 302N model). Three electrode configuration was used with EG (or TiO_2-EG), platinum foil and Ag/AgCl (3 M KCl) as working, auxiliary and reference electrodes respectively. The diameter of the working electrode was 1.5 cm. Cyclic voltammograms were obtained in a 5 mM (with KCl as supporting electrolyte) solution of ferricyanide. Electrochemical and photoelectrocatalytic oxidation of sulfamethoxazole was carried out in an undivided cell (with quartz window) using chronopotentiometry. Typically, a 75 mL of 25 mgL^{-1} SMX prepared in 0.1 M Na_2SO_4 was electrolysed in an experiment and the electrolytic solution was magnetically stirred during the course of electrolysis. The pH of the SMX solution was maintained at 6.3 prior to degradation. Simulated sunlight was from a solar simulator, Oriel LCA-100 equipped with a 100 W xenon lamp and an Air Mass 1.5 Global filter which produces 100 $mWcm^{-2}$. The surface of the electrode was made to align with the light source and the distance between the electrochemical cell and the lamp was 10 cm.

6.3 Results and discussion

6.3.1 XRD analysis

The XRD patterns of TiO_2 and TiO_2-EG are shown in Figure 6.1, TiO_2 gave sharp and well defined peaks at 25.3, 37.8, 47.9, 54.5, 62.7, 69.5 and 75.0° which correspond to (101), (004), (200), (211), (204), (220) and (215) crystal lattice planes of anatase TiO_2

respectively (JCPDS No. 21-1272). A new peak at 26.4° can be observed in the spectrum of the nanocomposite material, this reflection peak corresponds to (002) crystal plane of expanded graphite [29].

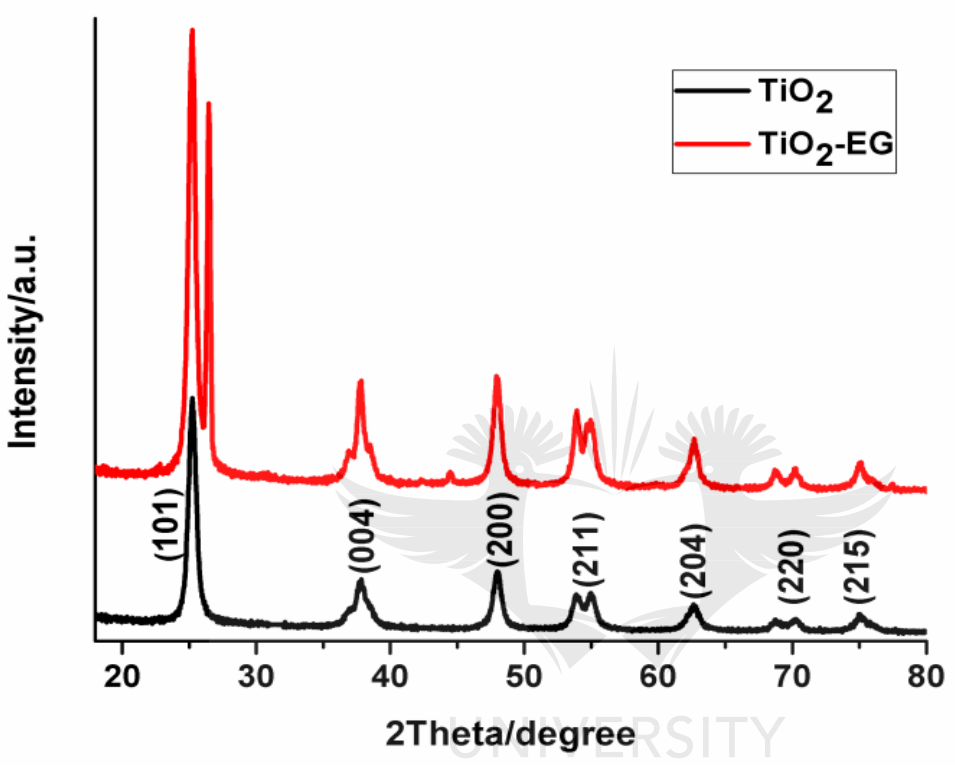

Fig. 6. 1. XRD patterns of TiO_2 and EG-TiO_2

6.3.2 Raman spectroscopy

Raman analyses of the materials were carried out to investigate the structural features of the electrode materials. Figures 6.2a and 6.2b display the Raman spectra of TiO_2 and TiO_2-EG. The characteristic bands of anatase TiO_2 can be seen at around 146, 398, 521 and 643 cm^{-1} corresponding to E_g, B_{1g}, A_{1g} and E_g Raman lattice vibrations of the metal oxide semiconductor respectively [30-32]. The spectrum of the nanocomposite shows the signature peaks of TiO_2 which are present in the spectrum of the pristine material, while a new peak centred at 1589 cm^{-1} can also be seen. This new peak is the G band of

the EG material which arises from the vibration of sp^2 carbon atoms. The D band which is due to defect in the lattice structure of the graphitic material has a very low intensity and therefore cannot be clearly seen in the spectrum of the composite material, it is however present in the spectrum of the pristine EG shown in the inset.

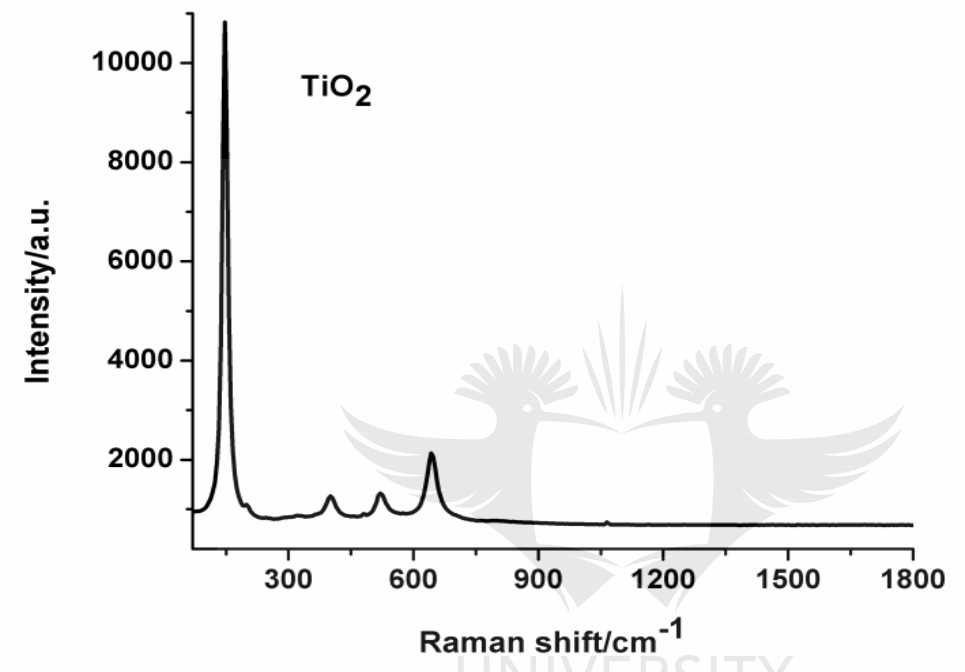

a)

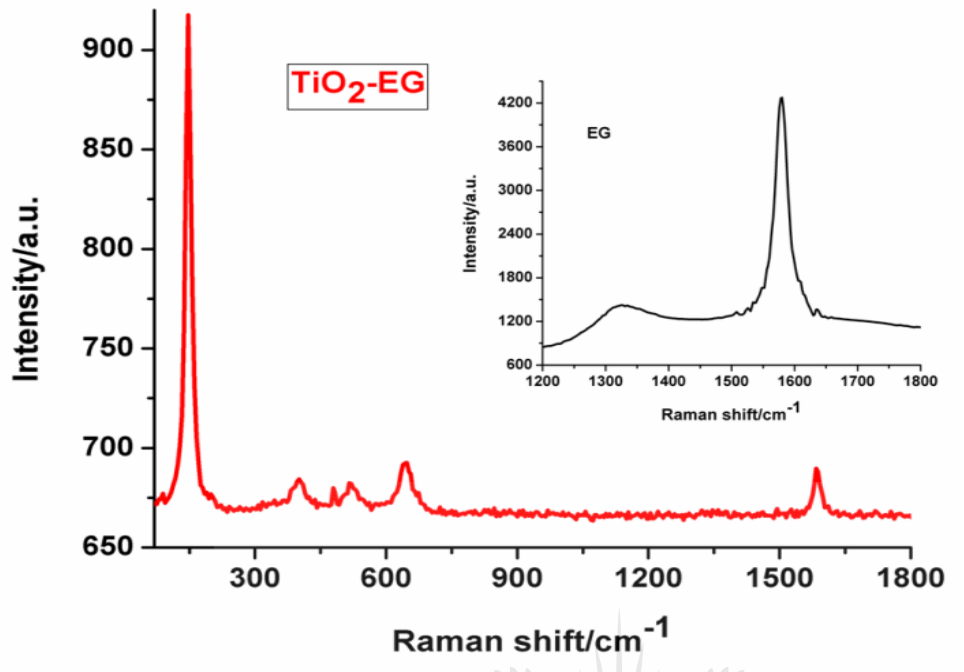

b)

Fig. 6. 2. Raman spectra of TiO_2 and TiO_2-EG (inset: spectrum of EG)

6.3.3 FTIR spectroscopy

The FTIR spectra of TiO_2 and TiO_2-EG can be seen in figure 6.3, the peak at around 550 cm^{-1} in the spectrum of pristine TiO_2 can be attributed to the vibration of the Ti-O bonds in the TiO_2 lattice. In the spectrum of the composite material, peaks at 1634 and 1068 cm^{-1} can be ascribed to C=C and C-O-C stretch of the EG. Also, the weak bands at 2924 and 2854 cm^{-1} are due to C-H stretch. The broad peak at 3408 cm^{-1} can be assigned to the vibration of hydroxyl groups of adsorbed water.

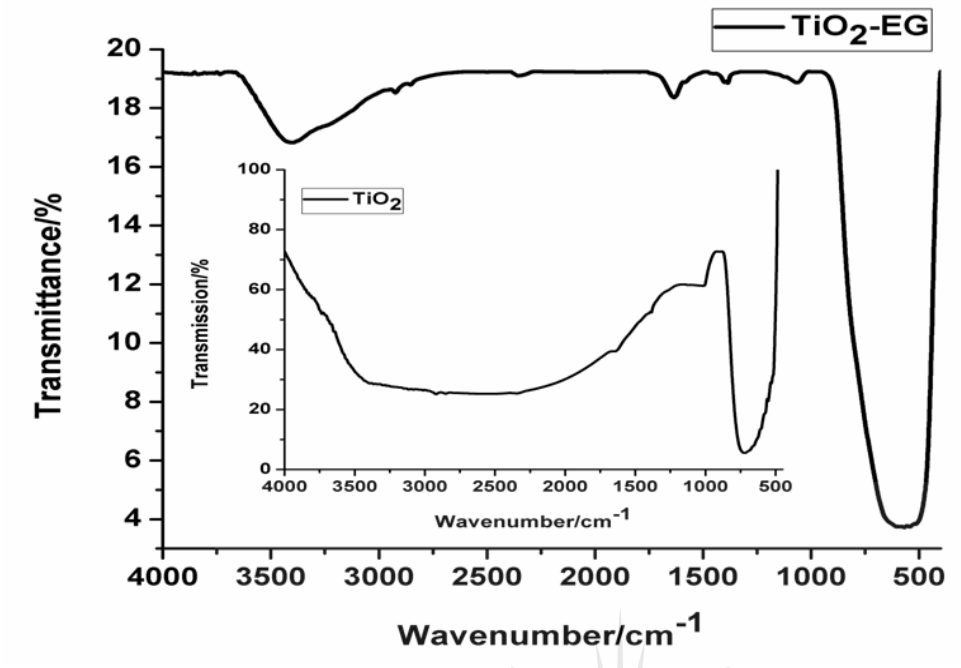

Fig. 6. 3. FTIR spectrum of TiO_2-EG (inset: spectrum of TiO_2)

6.3.4 Morphologies of electrode materials

The electron micrographs of TiO_2 and TiO_2-EG are presented in figure 6.4. From the SEM image of TiO_2 (Fig. 6.4a), it can be reasonably assumed that the nanoparticles are uniformly sized. The TEM image (Fig 6.4c) reveals that there is agglomeration of the particles; this can also be deduced from the SEM image as the particles are closely situated. In the TEM image of the TiO_2-EG (Fig. 6.4d), however, the TiO_2 particles are seen to sit on the graphite sheets, and agglomeration of the particles are minimal. Also, the SEM image of TiO_2-EG (fig. 6.4b) shows that the graphite layers are decorated by the TiO_2 particles.

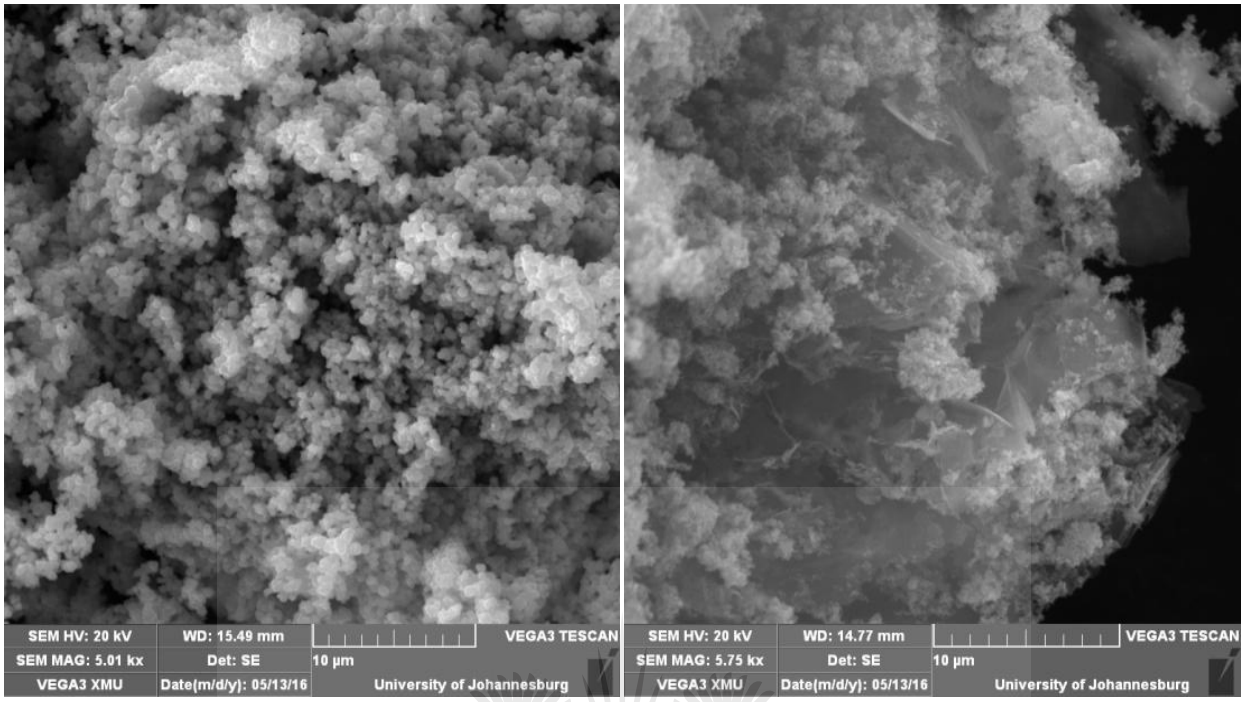

a) b)

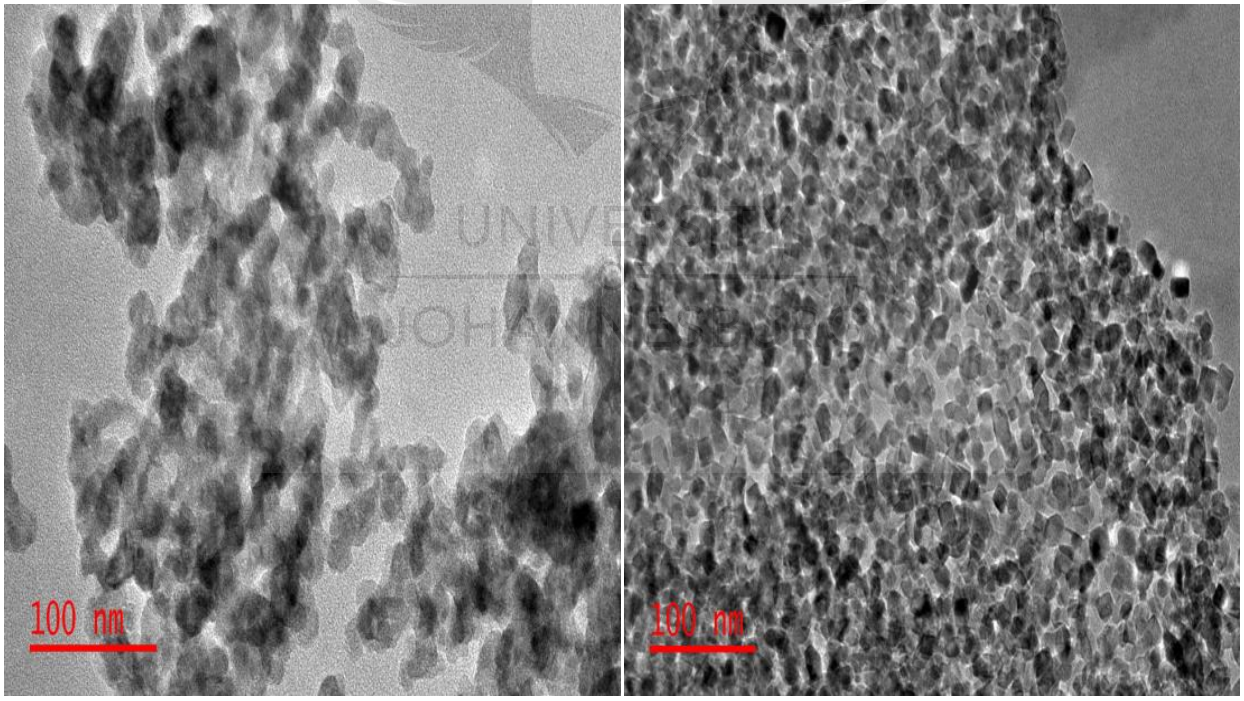

c) d)

Fig. 6. 4. SEM images of a) TiO_2, b) TiO_2-EG and TEM images of c) TiO_2, d)TiO_2-EG

6.3.5 Cyclic voltammetric measurements

Cyclic voltammetry is a widely used technique which offers qualitative information on electrochemical reactions. The voltammograms obtained from the cyclic voltammetric studies of the electrodes carried out using potassium ferricyanide as a redox probe are presented in figure 6.5. The separation between the peak potentials for a reversible couple (at 298 K) is given by

$$\Delta E_p = 0.059/n \qquad (6.1)$$

where n is the number of electrons transferred. A process in which ΔE_p is approximately 59 mV is considered to be fast (reversible) while a larger value of ΔE_p depicts a slow electrode kinetics. ΔE_p deduced from the voltammograms of EG and TiO_2-EG are 307 and 352 mV respectively. The much slower kinetics (when compared with 59 mV) at the EG electrode can be due to the presence of non-metal impurities and surface oxides resulting from the intercalation process. The ΔE_p value for the TiO_2-EG electrode is larger than that of EG electrode; this indicates that the electrochemical process is slower at the composite electrode. This is not surprising given the presence of the relatively low conducting TiO_2 in the composite, which dilutes the better conducting EG. In spite of the large values of ΔE_p, the scan rate study at the composite electrode (Fig. 6.5c) shows that the process is not irreversible since there is no significant shift in the position of the peak potentials at the different scan rates. Notably, the total current obtained at EG-TiO_2 electrode is higher than the value obtained at EG electrode. This can be attributed to the larger surface area provided by the TiO_2 nanoparticles which enhanced the interaction of the redox probe with the electrode. However, the faradaic current obtained at the EG electrode is of higher magnitude than that obtained at the EG-TiO_2 electrode (the composite electrode displayed higher capacitive current).

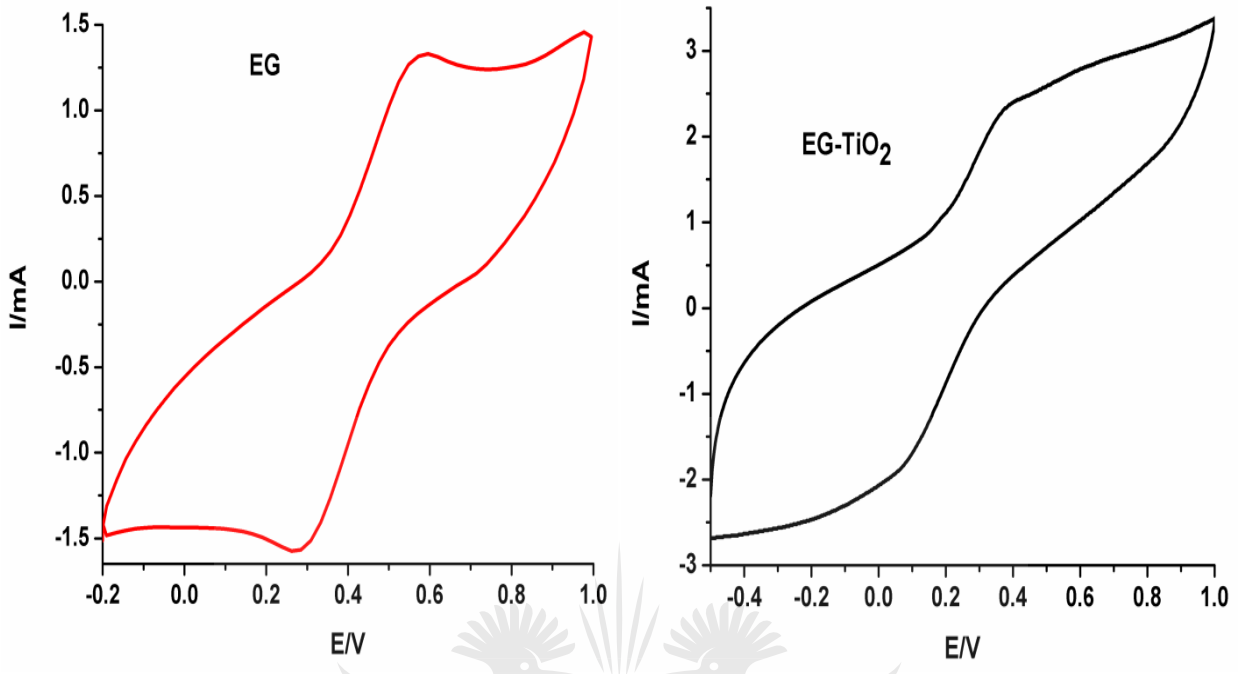

a)

b)

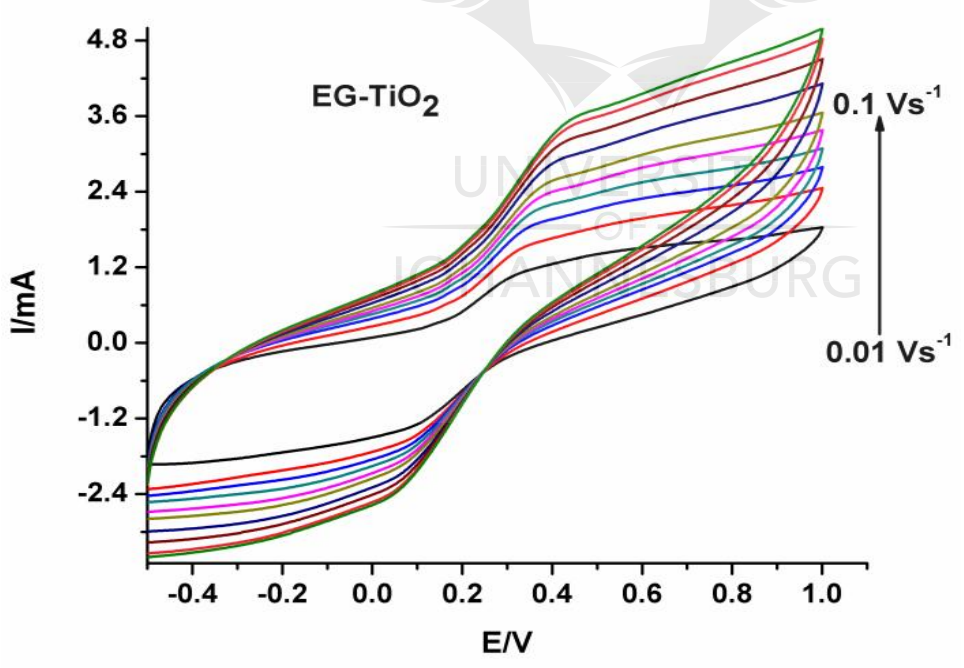

c)

Fig. 6. 5. Cyclic voltammograms of a) EG and b) EG-TiO_2 recorded at a scan rate of 0.05 Vs^{-1} and c) EG-TiO_2 at different scan rates, in 5 mM ferricyanide solution

6.3.6 Degradation of SMX at EG and TiO_2-EG electrodes

Oxidation of the analyte was monitored on UV-Vis spectrophotometer at its wavelength of maximum absorption (λ_{max} = 257 nm). In both electrochemical and photoelectrochemical processes at the TiO_2-EG electrode, there was a gradual but very significant reduction (with time) in the absorbance of the antibiotic at the λ_{max} (Fig. 6.6a). This confirmed its degradation in the processes. However, a much higher degradation efficiency was obtained in the photo-assisted process (Fig. 6.6b). It is also noteworthy that the composite electrode exhibited a higher removal efficiency of the analyte than the pristine electrode in the electrochemical process (Fig. 6.6c). The improved degradation obtained in the photoelectrochemical process at the TiO_2 based electrode can be attributed to the photocatalytic behaviour of the semiconductor and the combined effect of electrical energy and solar energy which are beneficial for generating the hydroxyl radicals required to destroy the pollutant. Upon irradiation with light, the photo-generated holes in TiO_2 react with water to produce hydroxyl radicals, this powerful oxidant attacks and degrades the pollutant molecules until they are mineralised. Similarly, the holes also act as oxidant, attacking the organic species until it is completely broken down. Furthermore, when the applied potential is sufficiently high, oxidation of water on the surface of the anode to form the hydroxyl radicals takes place. The enhanced performance of EG-TiO_2 compared to EG in the electrochemical process can be related to the higher electro-active surface area of the EG-TiO_2 which provides a greater number of sites for the oxidation of water to generate the oxidant. In addition, since direct electron transfer from the contaminant to the anode often occurs simultaneously with the indirect oxidation [33, 34], a larger electro-active surface area favours the oxidation of SMX at the anode. This observation is in agreement with the

results of the cyclic voltammetric experiments in which higher peak current was obtained at the composite electrode.

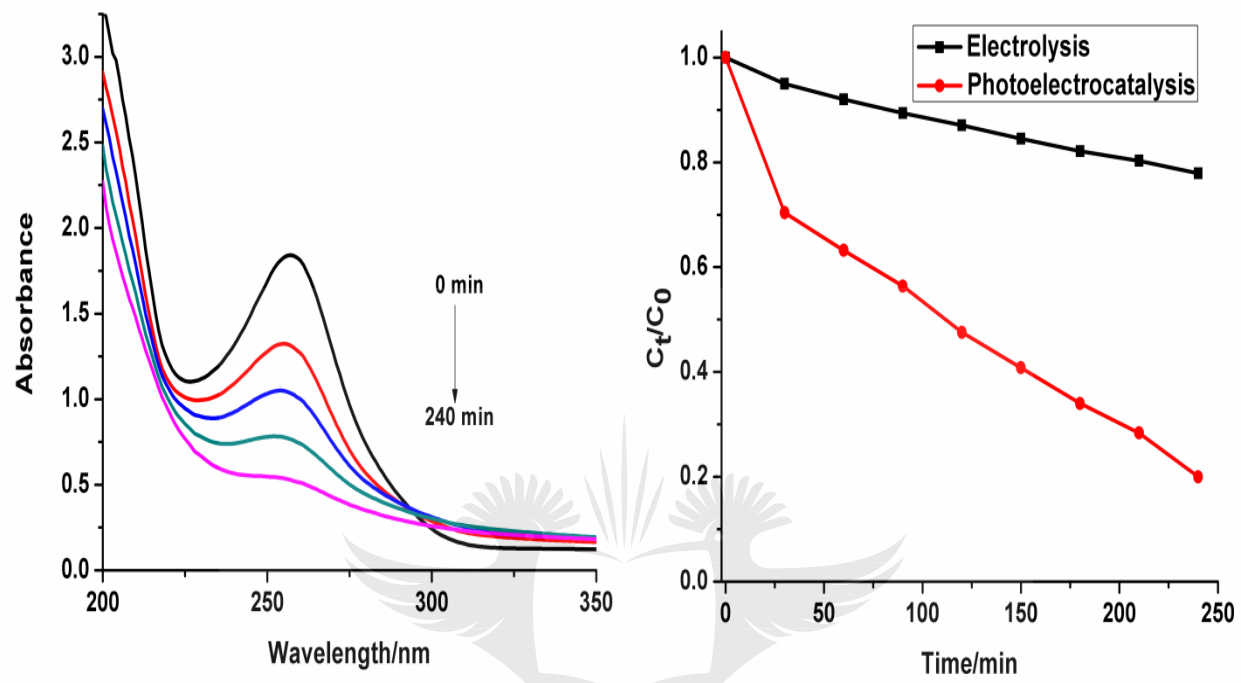

a) b)

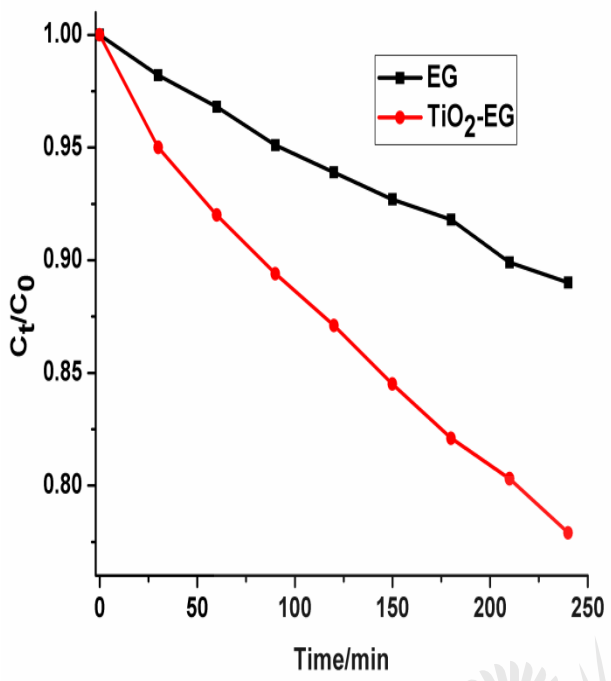

c)

Fig. 6. 6. a) UV-Vis spectra of oxidised SMX solution, and normalised plots of concentration abatement for b) electrochemical and photoelectrocatalytic degradation of SMX at TiO_2-EG photoelectrode c) electrochemical degradation of SMX at EG and TiO_2-EG anodes

6.3.6.1 Effect of current density on the degradation of SMX

The influence of current density on the degradation process was investigated. Oxidation of the analyte was achieved at the initial current density of 7 $mAcm^{-2}$. There was however improvement in the process when the value was increased to 10 $mAcm^{-2}$. Further increase to 13 $mAcm^{-2}$ did not lead to appreciable increase in the degradation efficiency (Fig. 4d). This trend suggests that the oxidation of SMX is mainly achieved by holes and hydroxyl radicals in the photoelectrochemical process. It is also believed that the anodic potential (1.8 V) at 10 $mAcm^{-2}$ is optimal to prevent recombination of photogenerated charges and that further increase in potential is unutilised.

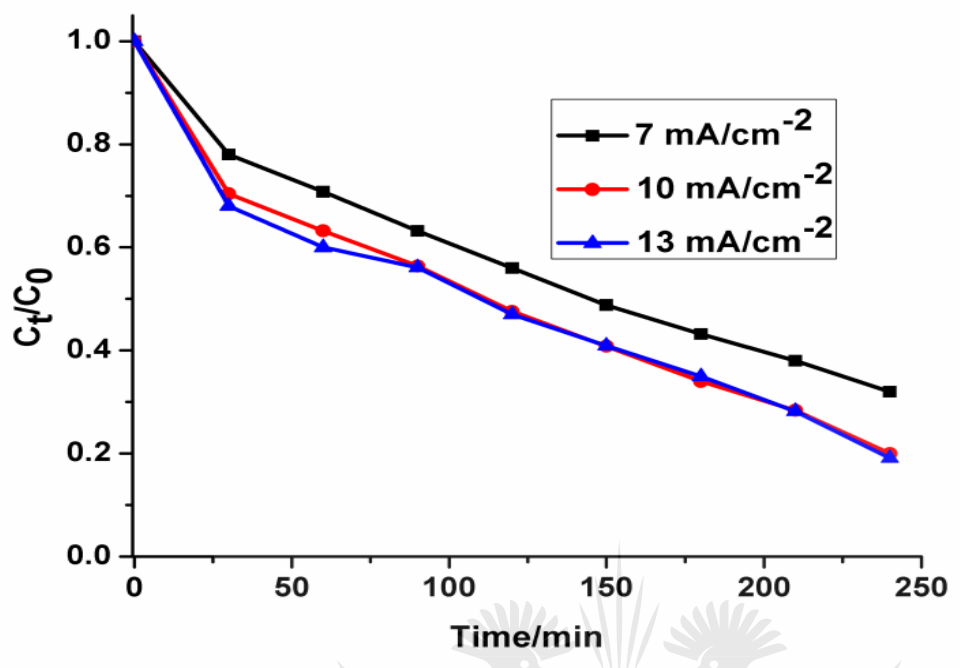

Fig. 6.6. 1.Current-dependence of SMX degradation

6.3.6.2 Effect bulk solution pH on the degradation of SMX

The effect of pH of the bulk solution on the degradation of SMX was studied. It can be observed that the rate of oxidation is higher at acidic pH (Fig. 6.6.2), with the rate at pH 3.1 being slightly higher than the rate at pH 6.3. The Pk_{a1} and Pk_{a2} values of SMX are 1.7 and 5.6 respectively [35]. Below and above these values SMX is either positively or negatively charged respectively. The proportion of cationic or anionic form of SMX present in a solution at a time depends on the pH of the solution. At pH 3, SMX molecules are expected to be in neutral form and since the degradation efficiency at this pH is higher than at the other two pH values, it can be said that the degradation of the analyte in this process is favoured when the molecules are uncharged. The difference between the rates at pH 3 and pH 6 is not very large, thus it can be asserted that there is still a considerable amount of the neutral molecules at pH 6. Furthermore, although the

degradation of SMX at pH 6.3 is a little slower, the pH of the electrolytic solution can still be maintained at 6.3 since it is milder.

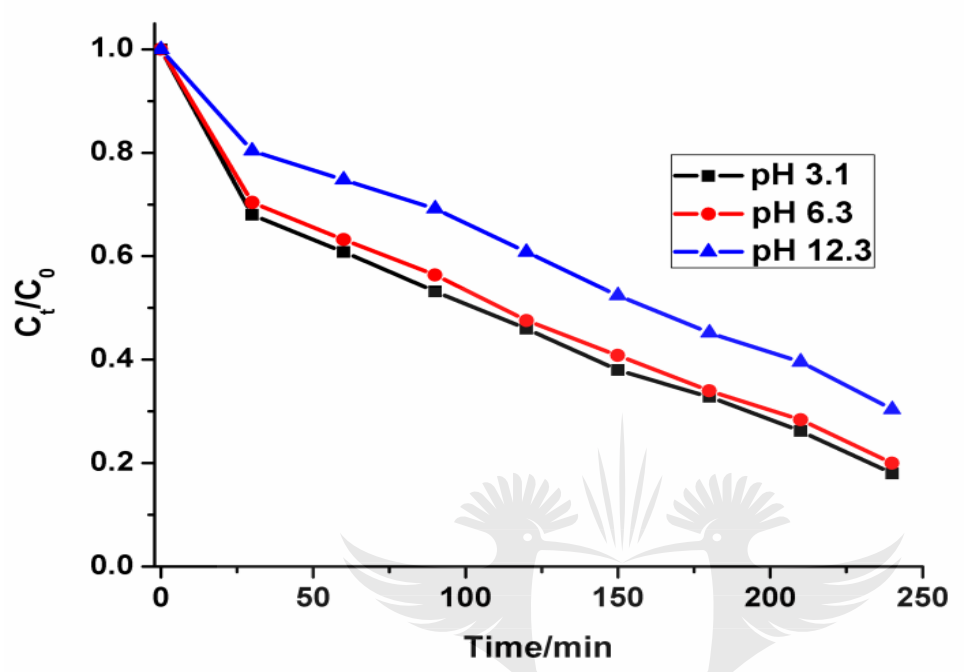

Fig. 6.6. 2. Effect of bulk solution pH on SMX degradation.

6.3.7 Kinetics of SMX degradation, COD decay and current efficiency at TiO_2-EG photoanode

Hydroxyl radicals mediated degradation of organic contaminants can be described by the Langmuir-Hinselwood model, specifically the simplified pseudo-first order equation can be used to examine the kinetics in the degradation process. The equation is given as:

$$ln\ C/C_0 = -\ k.t \qquad (6.2)$$

C and C_0 are the concentrations (in mgL^{-1}) of the pollutant at time t = t and t = 0 respectively, and t is time in minute. A plot of $ln\ C_0/C$ against t presented a good linearity and the rate constant, k of the reaction was calculated from slope of the line. The apparent rate constant obtained for the degradation process carried out at a current density of 10 $mAcm^{-2}$ and pH 6.3 was 5.74 x 10^{-3} min^{-1}. This value of k is smaller compared to that obtained in a related study by Su *et al.*, however, when factors such as electrode surface area, supporting electrolyte are taken into consideration, the rate of SMX decay in this work can be said to be appreciably good.

An efficient wastewater treatment technique is expected to lead to a significant reduction in the chemical oxygen demand (COD) of the water at a reasonable energy input. The removal of COD in this investigation was calculated using the relations:

$$\textbf{COD decay (\%)} = (COD_0 - COD_t)/COD_0 * 100\% \qquad (6.3)$$

where COD_0 and COD_t are the values (in mgL^{-1}) of chemical oxygen demand at time, t = 0 and t = t respectively. After 6 hr of electrolysis and light irradiation at the optimum conditions, a 90% COD removal was obtained at the photoanode.

Using the COD approach, the current efficiency for the degradation of SMX was calculated using the following equation [36]:

$$\textbf{Total Current Efficiency (TCE)} = FV.\ (COD_0 - COD_t)/8I\Delta t \qquad (6.4)$$

where COD_0 and COD_t are the COD (in gL^{-1}) at time t = 0 and t = t, F is the Faraday constant (96487 $Cmol^{-1}$), V is the volume of the electrolytic solution (in Litres), I is the current (A) and t is the electrolysis time (s). The TCE calculated for the degradation of

SMX at optimum conditions was 0.674. This value indicates that a fairly high proportion of the electrical energy applied was utilised for the decay of the contaminant.

6.3.8 Identification of intermediate products during the degradation of SMX

LCMS analysis of standard sample and aliquots of degraded SMX solution were carried out. The chromatograms obtained are given in figure 6.7**.** The major aromatic intermediates identified are m/z = 94, 157, 172. These species can result from the γ-, β-, δ- and ε- cleavages of the sulfamethoxazole molecules [37]. The peak at m/z = 94 can be considered to be protonated aniline, as it has been reported in a number of studies dealing with oxidation of SMX by hydroxyl radicals[3, 37-39]. It can be thought to be formed by the attack of hydroxyl radicals on sulfonated moiety, leading to release of SO_4^{2-} [38]. The formation of a product having m/z = 157 has been attributed to the cleavage of the S-N bond in the parent molecule [40], and the m/z = 172 may be a sulfanilamide or ionic form of sulfanilic acid resulting from ε- cleavage [37, 41]. The peaks at m/z = 270 and 286 have been indicated to result from the mono- and di-hydroxylated products of SMX [42, 43]. It can therefore be reasonably suggested that the photoelectrocatalytic oxidation of SMX is by cleavage of the S-N bond and hydroxylation and opening of ring systems in the molecule. A schematic representation of the proposed degradation route of SMX is presented in figure 6.8.

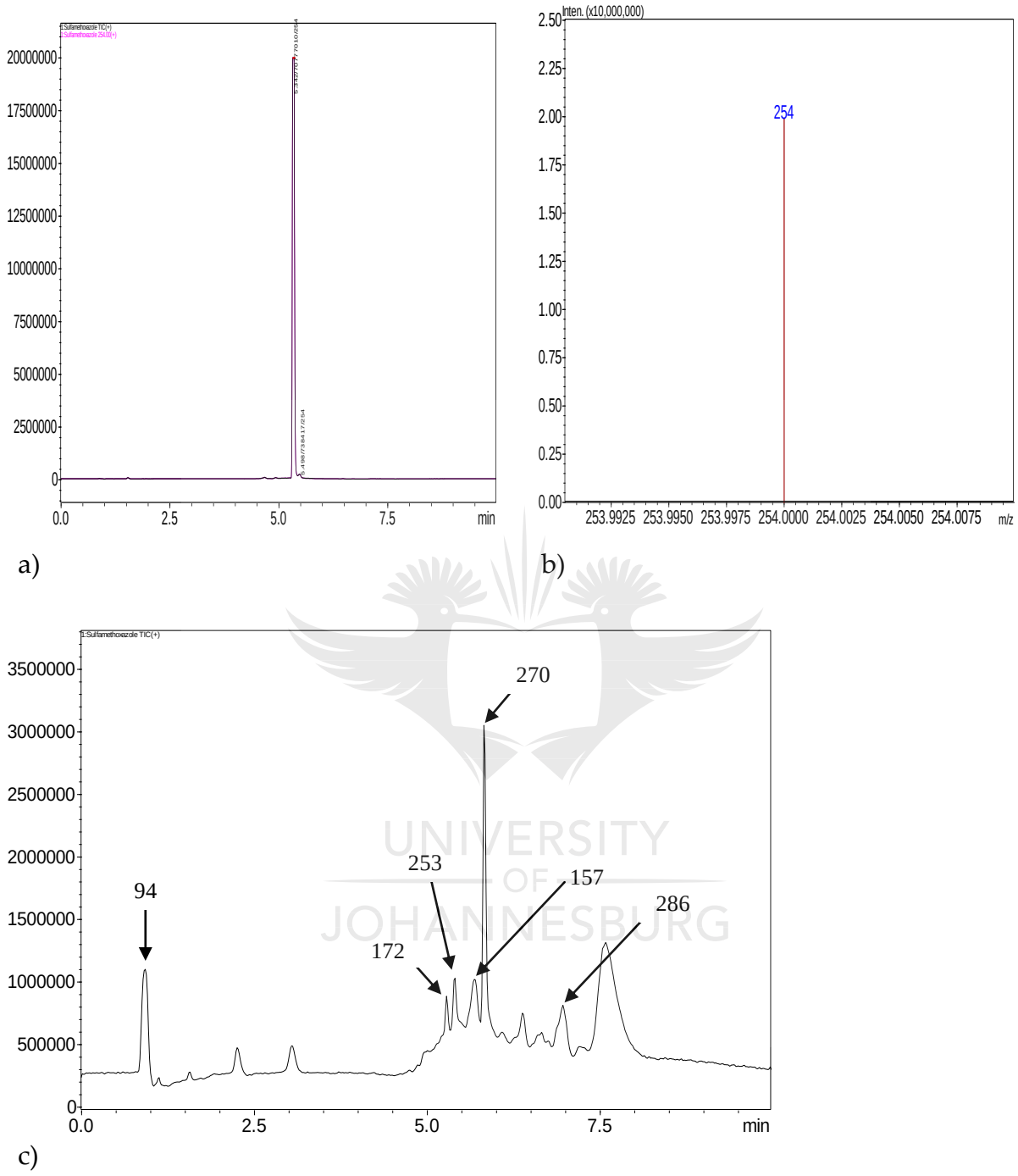

Fig. 6. 7. a) Chromatogram of SMX solution b) mass spectrum of SMX solution c) chromatogram of degraded SMX solution.

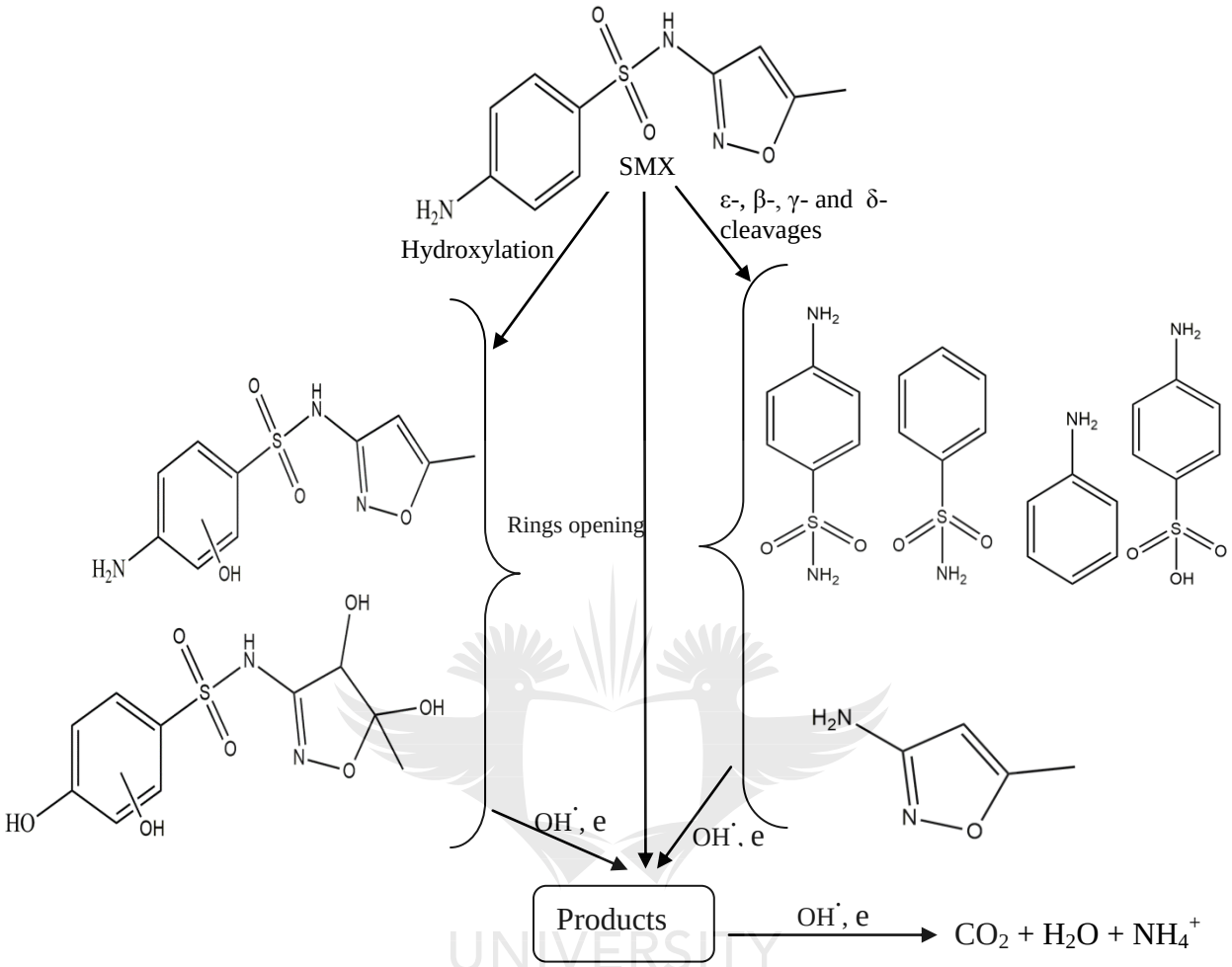

Fig. 6. 8. Proposed degradation route of SMX by photoelectrochemical process.

6.4 Sub-conclusion

The applicability of TiO_2-EG electrode for the oxidation of SMX via photoelectrocatalytic process was demonstrated in this study. The performance of the photoanode was enhanced in the presence of simulated sunlight, with a fourfold increase in the removal efficiency of the contaminant. The degradation of SMX at the electrode was dependent on pH of the solution and applied current, pH 6.3 and current density 10 $mAcm^{-2}$ were taken as optimum. After 6 h of the process at the optimum conditions, 90% of the COD of the solution was removed. LC-MS analysis of the

degraded SMX revealed the formation of aniline and other by-products which are believed to result from the interaction of the photoelectrochemically generated hydroxyl radicals and electrons with the parent molecule.

Given the ease of preparation, low cost and performance of the TiO_2-EG anode, it can be further explored for the removal of pharmaceuticals from wastewater.

6.5 References

[1] D. Lucas, M. Badia-Fabregat, T. Vicent, G. Caminal, S. Rodríguez-Mozaz, J. Balcazar, D. Barcelo, Fungal treatment for the removal of antibiotics and antibiotic resistance genes in veterinary hospital wastewater, Chemosphere 152 (2016) 301-308.

[2] C. Stange, J. Sidhu, A. Tiehm, S. Toze, Antibiotic resistance and virulence genes in coliform water isolates, International Journal of Hygiene and Environmental Health 219 (2016) 823-831.

[3] S. Hussain, S. Gul, J.R. Steter, D.W. Miwa, A.J. Motheo, Route of electrochemical oxidation of the antibiotic sulfamethoxazole on a mixed oxide anode, Environmental Science and Pollution Research 22 (2015) 15004-15015.

[4] N. Voulvoulis, D. Barceló, P. Verlicchi, in: Pharmaceuticals in the Environment, (2015).

[5] B.E. Haggard, J.M. Galloway, W.R. Green, M.T. Meyer, Pharmaceuticals and other organic chemicals in selected north-central and northwestern Arkansas streams, Journal of environmental quality 35 (2006) 1078-1087.

[6] A.K. Brown, C.S. Wong, Simultaneous quantification of propranolol and sulfamethoxazole and major human metabolite conjugates 4-hydroxy-propranolol sulfate and sulfamethoxazole-β-glucuronide in municipal wastewater—A framework for multiple classes of drugs and conjugates, Journal of Chromatography A 1471 (2016) 34-44.

[7] P. Rodríguez-Escales, X. Sanchez-Vila, Fate of sulfamethoxazole in groundwater: Conceptualizing and modeling metabolite formation under different redox conditions, Water Research 105 (2016) 540-550.

[8] L. Xu, G. Wang, F. Ma, Y. Zhao, N. Lu, Y. Guo, X. Yang, Photocatalytic degradation of an aqueous sulfamethoxazole over the metallic silver and Keggin unit codoped titania nanocomposites, Applied Surface Science 258 (2012) 7039-7046.

[9] F.C. Moreira, R.A. Boaventura, E. Brillas, V.J. Vilar, Electrochemical advanced oxidation processes: a review on their application to synthetic and real wastewaters, Applied Catalysis B: Environmental 202 (2017) 217-261.

[10] E. Brillas, C.A. Martínez-Huitle, Decontamination of wastewaters containing synthetic organic dyes by electrochemical methods. An updated review, Applied Catalysis B: Environmental 166 (2015) 603-643.

[11] X. He, Z. Chai, F. Li, C. Zhang, D. Li, J. Li, J. Hu, Advanced treatment of biologically pretreated coking wastewater by electrochemical oxidation using Ti/RuO_2–IrO_2 electrodes, Journal of Chemical Technology and Biotechnology 88 (2013) 1568-1575.

[12] B. Ntsendwana, B.B. Mamba, S. Sampath, O.A. Arotiba, Synthesis, characterisation and application of an exfoliated graphite–diamond composite electrode in the electrochemical degradation of trichloroethylene, RSC Advances 3 (2013) 24473-24483.

[13] B.P. Chaplin, Critical review of electrochemical advanced oxidation processes for water treatment applications, Environmental Science: Processes & Impacts 16 (2014) 1182-1203.

[14] M. Turabik, N. Oturan, B. Gözmen, M.A. Oturan, Efficient removal of insecticide "imidacloprid" from water by electrochemical advanced oxidation processes, Environmental Science and Pollution Research 21 (2014) 8387-8397.

[15] D. Zhou, Z. Chen, Q. Yang, C. Shen, G. Tang, S. Zhao, J. Zhang, D. Chen, Q. Wei, X. Dong, Facile Construction of g-C_3N_4 Nanosheets/TiO_2 Nanotube Arrays as Z-Scheme

Photocatalyst with Enhanced Visible-Light Performance, ChemCatChem 8 (2016) 3064-3073.

[16] E.H. Umukoro, M.G. Peleyeju, J.C. Ngila, O.A. Arotiba, Towards wastewater treatment: Photo-assisted electrochemical degradation of 2-nitrophenol and orange II dye at a tungsten trioxide-exfoliated graphite composite electrode, Chemical Engineering Journal 317 (2017) 290-301.

[17] Y.-f. Su, G.-B. Wang, D.T.F. Kuo, M.-l. Chang, Y.-h. Shih, Photoelectrocatalytic degradation of the antibiotic sulfamethoxazole using TiO_2/Ti photoanode, Applied Catalysis B: Environmental 186 (2016) 184-192.

[18] Z. Li, Y. Qu, K. Hu, M. Humayun, S. Chen, L. Jing, Improved photoelectrocatalytic activities of BiOCl with high stability for water oxidation and MO degradation by coupling RGO and modifying phosphate groups to prolong carrier lifetime, Applied Catalysis B: Environmental 203 (2017) 355-362.

[19] Q. Zeng, J. Li, J. Bai, X. Li, L. Xia, B. Zhou, Preparation of vertically aligned WO_3 nanoplate array films based on peroxotungstate reduction reaction and their excellent photoelectrocatalytic performance, Applied Catalysis B: Environmental 202 (2017) 388-396.

[20] J. Li, X. Zhang, Z. Ai, F. Jia, L. Zhang, J. Lin, Efficient visible light degradation of rhodamine B by a photo-electrochemical process based on a Bi_2WO_6 nanoplate film electrode, The Journal of Physical Chemistry C 111 (2007) 6832-6836.

[21] S. Sarkar, R. Das, H. Choi, C. Bhattacharjee, Involvement of process parameters and various modes of application of TiO_2 nanoparticles in heterogeneous photocatalysis of pharmaceutical wastes–a short review, RSC Advances 4 (2014) 57250-57266.

[22] V.V. Kondalkar, S.S. Mali, R.M. Mane, P. Dandge, S. Choudhury, C.K. Hong, P.S. Patil, S.R. Patil, J.H. Kim, P.N. Bhosale, Photoelectrocatalysis of cefotaxime using nanostructured TiO_2 photoanode: Identification of the degradation products and determination of the toxicity level, Industrial & Engineering Chemistry Research 53 (2014) 18152-18162.

[23] Z. Wei, F. Liang, Y. Liu, W. Luo, J. Wang, W. Yao, Y. Zhu, Photoelectrocatalytic degradation of phenol-containing wastewater by TiO_2/gC_3 N 4 hybrid heterostructure thin film, Applied Catalysis B: Environmental 201 (2017) 600-606.

[24] G. Palmisano, V. Loddo, H.H. El Nazer, S. Yurdakal, V. Augugliaro, R. Ciriminna, M. Pagliaro, Graphite-supported TiO_2 for 4-nitrophenol degradation in a photoelectrocatalytic reactor, Chemical Engineering Journal 155 (2009) 339-346.

[25] D. Li, J. Jia, Y. Zhang, N. Wang, X. Guo, X. Yu, Preparation and characterization of Nano-graphite/TiO_2 composite photoelectrode for photoelectrocatalytic degradation of hazardous pollutant, Journal of Hazardous Materials 315 (2016) 1-10.

[26] B. Ntsendwana, S. Sampath, B. Mamba, O. Arotiba, Photoelectrochemical oxidation of p-nitrophenol on an expanded graphite–TiO_2 electrode, Photochemical & Photobiological Sciences 12 (2013) 1091-1102.

[27] X. Yu, Y. Zhang, X. Cheng, Preparation and photoelectrochemical performance of expanded graphite/TiO_2 composite, Electrochimica Acta 137 (2014) 668-675.

[28] T. Ndlovu, A.T. Kuvarega, O.A. Arotiba, S. Sampath, R.W. Krause, B.B. Mamba, Exfoliated graphite/titanium dioxide nanocomposites for photodegradation of eosin yellow, Applied Surface Science 300 (2014) 159-164.

[29] M. Peleyeju, E. Umukoro, J. Babalola, O. Arotiba, Electrochemical Degradation of an Anthraquinonic Dye on an Expanded Graphite-Diamond Composite Electrode, Electrocatalysis 7 (2016) 132-139.

[30] F. Hardcastle, Raman spectroscopy of titania (TiO_2) nanotubular water-splitting catalysts, Journal of the Arkansas Academy of Science 65 (2011) 43-48.

[31] O. Frank, M. Zukalova, B. Laskova, J. Kürti, J. Koltai, L. Kavan, Raman spectra of titanium dioxide (anatase, rutile) with identified oxygen isotopes (16, 17, 18), Physical Chemistry Chemical Physics 14 (2012) 14567-14572.

[32] G. Zhu, H. Yin, C. Yang, H. Cui, Z. Wang, J. Xu, T. Lin, F. Huang, Black Titania for Superior Photocatalytic Hydrogen Production and Photoelectrochemical Water Splitting, ChemCatChem 7 (2015) 2614-2619.

[33] J.-F. Zhi, H.-B. Wang, T. Nakashima, T.N. Rao, A. Fujishima, Electrochemical incineration of organic pollutants on boron-doped diamond electrode. Evidence for direct electrochemical oxidation pathway, The Journal of Physical Chemistry B 107 (2003) 13389-13395.

[34] A. Donaghue, B.P. Chaplin, Effect of select organic compounds on perchlorate formation at boron-doped diamond film anodes, Environmental science & technology 47 (2013) 12391-12399.

[35] H. Chen, B. Gao, H. Li, L.Q. Ma, Effects of pH and ionic strength on sulfamethoxazole and ciprofloxacin transport in saturated porous media, Journal of contaminant hydrology 126 (2011) 29-36.

[36] M. Zhou, Q. Dai, L. Lei, C.a. Ma, D. Wang, Long life modified lead dioxide anode for organic wastewater treatment: electrochemical characteristics and degradation mechanism, Environmental science & technology 39 (2005) 363-370.

[37] K.P. de Amorim, L.L. Romualdo, L.S. Andrade, Electrochemical degradation of sulfamethoxazole and trimethoprim at boron-doped diamond electrode: performance, kinetics and reaction pathway, Separation and Purification Technology 120 (2013) 319-327.

[38] G. Liu, X. Li, B. Han, L. Chen, L. Zhu, L.C. Campos, Efficient degradation of sulfamethoxazole by the Fe(II)/HSO_5^- process enhanced by hydroxylamine: Efficiency and mechanism, Journal of Hazardous Materials 322 (2017) 461-468.

[39] H.Y. Kim, T.-H. Kim, S.M. Cha, S. Yu, Degradation of sulfamethoxazole by ionizing radiation: Identification and characterization of radiolytic products, Chemical Engineering Journal 313 (2017) 556-566.

[40] W. Zhu, F. Sun, R. Goei, Y. Zhou, Facile fabrication of RGO-WO_3 composites for effective visible light photocatalytic degradation of sulfamethoxazole, Applied Catalysis B: Environmental 207 (2017) 93-102.

[41] L. Hu, P.M. Flanders, P.L. Miller, T.J. Strathmann, Oxidation of sulfamethoxazole and related antimicrobial agents by TiO_2 photocatalysis, Water Research 41 (2007) 2612-2626.

[42] E. Ioannidou, Z. Frontistis, M. Antonopoulou, D. Venieri, I. Konstantinou, D.I. Kondarides, D. Mantzavinos, Solar photocatalytic degradation of sulfamethoxazole over tungsten–Modified TiO_2, Chemical Engineering Journal 318 (2017) 143-152.

[43] J. Radjenovic, M. Petrovic, Removal of sulfamethoxazole by electrochemically activated sulfate: Implications of chloride addition, Journal of Hazardous Materials 333 (2017) 242-249.

CHAPTER SEVEN

SYNTHESIS, CHARACTERISATION AND PHOTOELECTROCATALYTIC APPLICATION OF CND/B-$BiVO_4$/WO_3 NANOSTRUCTURED ELECTRODE FOR DEGRADATION OF ORANGE II DYE.[1]

7.1 Introduction

Anodic materials that are employed in PEC setup for water decontamination are semiconductors with desirable properties for production of the needed oxidant species. TiO_2 is undoubtedly the most experimented semiconductor for photocatalytic applications [1]. So far, it has also claimed number one position as anodic material for photoelectrocatalytic degradation of organic pollutants [2, 3]. But the photoactivity of TiO_2 is largely limited to the UV region of the solar spectrum owing to its wide band gap. Hence it is unsuitable for harnessing the abundant sunlight energy. Utilisation of solar energy in tackling environmental and energy issues is attractive because sunlight is naturally available and abundant in many parts of the world. Therefore, photocatalysts which are sensitive in the visible region of the solar spectrum have received considerable attention as anodic materials for PEC application. $BiVO_4$ and its composites have been used as photoanodes in PEC system for hydrogen production via water splitting and organic contaminants decomposition. Having a narrow band gap of 2.4 eV, $BiVO_4$ is an ideal semiconductor for visible-light driven processes. It is non-toxic, stable to photocorrosion, inexpensive and can be obtained via simple synthetic routes. However, apart from the rapid recombination of electron-hole pairs, $BiVO_4$ also suffers

[1] Manuscript to be submitted to Applied Catalysis B

from poor electrical conductivity and low adsorptive performance [4]. These drawbacks make $BiVO_4$ an inefficient photocatalyst for pollutants degradation. Studies have shown that photocatalytic/photoelectrocatalytic degradation of organic pollutants at pristine $BiVO_4$ presented low removal efficiency [5-8].

WO_3 is another semiconductor which has been explored in a number of applications including electrochromic devices, dye sensitised solar cells, photoelectrochemical water splitting, etc. WO_3 can harvest a reasonably large fraction of the solar spectrum because of its relatively small band gap (2.5 - 2.8 eV) [9-11]. WO_3 is inexpensive, demonstrates low susceptibility to photocorrosion, exhibits appreciable stability in acidic and oxidative conditions, and is non-toxic [12]. Importantly, WO_3 is being explored as a potential photocatalyst for the destruction of organic pollutants because of the high oxidation power of its valence-bound holes [13]. In spite of its impressive properties, the photocatalytic activity of WO_3 is poor owing to its relatively low conduction band edge. The position of the conduction band edge is unfavourable for one-electron reduction of adsorbed oxygen molecules [14]. This leads to accumulation of photogenerated electrons, and their consequent recombination with the holes which are needed for oxidation of target compounds. As a result, improving the photocatalytic activity of WO_3 by modifying its electronic structure has been the focus of many researches. It has been reported that tuning the morphology/structure of WO_3 can yield a catalyst with enhanced charge separation and improved photoactivity [12, 15-18]. Theerthagiri *et al.*, Zhang *et al.* and Yao *et al.*, in separate studies, showed that WO_3 nanorods possess suitable physico-chemical properties for enhanced photocatalytic performance [11, 19, 20].

Fabricating a hybrid of two or more semiconductors has been hinted as one of the plausible approaches to overcoming the challenges of electron and hole recombination and some other limitations associated with individual photocatalyst [21-25]. The resulting nanocomposite catalysts have been reported to display much higher activity

than the individual materials. Xia *et al.* reported the oxidation of phenol on a $Fe_2O_3/BiVO_4$ thin film anode via photoelectrocatalytic process [26]. The composite photoanode demonstrated superior performance to the pristine $BiVO_4$ anode. The authors attributed the enhanced degradation performance to the ultra-thin iron oxide which minimised charge carriers recombination in $BiVO_4$. In another report by Martins *et al.* [27], WO_3 modified TiO_2 nanotube array (NTAs) exhibited better mineralisation efficiency than the unmodified TiO_2 (NTAs) when both electrodes were employed for the photoelectrocatalytic degradation of the endocrine disrupting compound propyl paraben. Similarly, Wei *et al.* [28] reported that decontamination of coking wastewater containing phenolic compounds was much more efficient at heterostructured TiO_2/g-C_3N_4 than at pure TiO_2 and g-C_3N_4. The improvement in the photoelectrocatalytic efficiency was attributed partly to the heterojunction that is formed between the two photocatalysts which suppresses the recombination rate of electrons and holes.

In this work, $BiVO_4$ has been modified with carbon nanodots and boron to obtain a photocatalyst denoted as CND/B-$BiVO_4$. This catalyst was then coupled to WO_3 nanorods and the resulting nanocomposite was immobilised on Ti plate. The photoanode, CND/B-$BiVO_4/WO_3$ was then employed for the catalytic oxidation of selected substances. A few studies have reported the use of $BiVO_4/WO_3$ as anodic material in photoelectrocatalytic experiments [21, 29, 30]. In this study we hypothesised that modification of $BiVO_4$ with substances such as CND and B would impact positively on the photocatalytic performance of the semiconductor. In addition, we envisaged that coupling this modified material to WO_3 nanorods will provide a nanocomposite anode with desirable properties for photoelectrocatalytic applications.

7.2 Experimental

7.2.1 Chemicals and materials

Sodium tungstate dihydrate ($Na_2WO_4.2H_2O$), bismuth nitrate pentahydrate ($Bi(NO_3)_3.5H_2O$), sodium metavanadate ($NaVO_3$), sodium chloride (NaCl), sodium sulphate (Na_2SO_4), sodium hydrogen carbonate ($NaHCO_3$), sodium hydroxide (NaOH), orange II sodium salt, polyethylene glycol (PEG), boric acid (H_3BO_3) and ethanol were purchased from Sigma-Aldrich (South Africa). All solutions were prepared with deionised water. Titanium sheets were supplied by Williams Gregor Limited, UK.

7.2.2 Synthesis of WO_3 nanorods

The synthesis of WO_3 nanorods is as follows: 2.62 g of $Na_2WO_4.2H_2O$ was dissolved in 80 mL of deionised water and this was followed by addition of 1.0 g of NaCl. The homogeneous mixture obtained was then acidified with HCl until the pH was 2.06. Upon the addition of HCl, the mixture turned to a white precipitate and this precursor solution was transferred to a 100 mL teflon-lined autoclave. The autoclave was sealed and maintained at 180 °C in an oven for 24 h. After cooling to room temperature, the synthesised material was transferred to centrifuge tubes and washed by centrifugation repeatedly with deionised water and then ethanol. The material was then dried at 80 °C in air oven for 8 h. The powder material obtained after drying was kept for use.

7.2.3 Preparation of carbon nanodots

Carbon nanodots (CNDs) were prepared from oats purchased from a local market in Johannesburg, South Africa. A 5 g mass of oats was powdered by grinding. The powder was then put into a crucible and transferred into a muffle furnace maintained at 400 °C for 2 h. The black material formed was allowed to cool to room temperature,

pulverised and subsequently dispersed in deionised water. The dispersion was centrifuged and the supernatant was decanted into a clean beaker. This process was repeated several times to obtain more supernatants. The water in the supernatant was evaporated and the solid particles left in the beaker were collected and kept for use.

7.2.4 Synthesis of $BiVO_4$ and CND/B-$BiVO_4$

To synthesise pristine $BiVO_4$, 0.61 g of $NaVO_3$ was dissolved in about 40 mL of deionised water and 2.43 g of $Bi(NO_3)_3.5H_2O$ were dissolved in 0.1 M HNO_3. The $NaVO_3$ solution was then gradually added to the $Bi(NO_3)_3$ solution. The yellow precursor solution formed was transferred into a teflon-lined autoclave, sealed and put into the stainless steel shell. This was then maintained 180 °C for 24 h in an oven. After cooling, the material was transferred into centrifuge tubes and washed a few times with water. The yellow substance obtained after decantation was dried in an air oven at 80 °C for 8 h. Preparation of CND/B-$BiVO_4$ followed the same procedure except that 1.0 g of H_3BO_3 and 10 mg of CND were added to the solution of $NaVO_3$ prior to mixing with $Bi(NO_3)_3.5H_2O$ solution.

7.2.5 Characterisations

Powder x-ray diffraction analysis of the catalysts was done on Rigaku Smartlab x-ray diffractometer (USA) equipped with Cu kα radiation and operated at 40 kV and 40 mA. Raman spectra of the materials were obtained on Raman Microscope (PerkinElmer RamanMicro 200, USA) with objective lens 50x. Fourier Transform Infrared Spectroscopy (FTIR) of KBr pellet of the samples was carried on PerkinElmer Spectrum 100 spectrometer (USA), BET surface area analysis was performed on Micrometrics ASAP 2020 surface area and porosity analyser (USA). The electron images were obtained on scanning electron microscope (TESCAN, Vega 3 XMU, Czech Republic) and transmission electron microscope ((JEOL 2100 HRTEM 200V, Japan). EDX analysis

was performed on an analyser attached to SEM. Diffuse reflectance spectroscopy was done on UV/Visible spectrophotometer (Shimadzu 2450, Japan), Concentration abatement of the dye was monitored on UV/Visible spectrophotometer (Agilent Cary 60, Malaysia) at its wavelength of maximum absorption. Chemical oxygen demand was determined on HACH DR3900 spectrophotometer.

7.2.6 Fabrication of electrodes

Ti sheets were first degreased in 40% m/m NaOH solution heated to 80°C and maintained for 2 h. Etching of the sheets was then carried out in a 18% v/v HCl solution maintained at 98% for 2 h.

The dispersions of $BiVO_4$, CND/B-$BiVO_4$ and WO_3 were prepared by weighing 0.2 g of each of the catalysts into an ethanolic solution of polyethylene glycol (PEG) (containing 2 mL of ethanol and 1 mL of PEG). A solution of both CND/B-$BiVO_4$ and WO_3 was also prepared by dispersing 0.1 g each of the catalysts in ethanolic solution of PEG. The dispersions were ultrasonicated for 60 min.

A 100 μL of the dispersion was drop cast onto both sides of the prepared Ti sheets with exposed area 4 cm^2. The coated sheets were dried in an oven at a temperature of 250°C. The coating was repeated once more and the sheets were sintered at 500°C in a muffle furnace.

7.2.8 Electrochemical experiments

Electrochemical measurements were done on a computer-controlled potentiostat (autolab PGSTAT 302N) using three-electrode system. The working electrodes used include $BiVO_4$/Ti, CND/B-$BiVO_4$/Ti, WO_3/Ti and CND/B-$BiVO_4$/WO_3/Ti , the reference electrode was Ag/AgCl (3M KCl) and the counter electrode was coiled platinum wire. Linear sweep voltammetric measurements were carried out in 0.1 M solution of Na_2SO_4 and amperometric measurements in the presence and in the absence of photons were

performed in 5 mgL^{-1} solution of orange II sodium salt (prepared in 0.1 M Na_2SO_4). Electrochemical oxidation of the dye was carried out in a quartz photoelectrochemical cell in the presence and in the absence of light. Typically, 250 mL of the simulated wastewater (containing 5 mgL^{-1} of the analyte) was electrolysed in an experiment with continuous stirring of the electrolytic solution. The solar light source was Oriel solar simulator. The simulator has a xenon lamp of 100 W and a UV cut-off filter (Air Mass 1.5 Global filter). The distance between the photoelectrochemical cell and the light source was about 5 cm.

7.3 Results and discussions

7.3.1 XRD analysis

The XRD patterns of the electrode materials are shown in Figure 7.1. The peaks in the XRD patterns of pure $BiVO_4$ (Fig. 7.1a) can be indexed to monoclinic scheelite structure of $BiVO_4$ (JCPDS card No. 14-0688) [31, 32]. The average crystallite size of $BiVO_4$ can be estimated from Scherrer formula (equation 7.1) using the line width analysis of the peak at around 29.0° (which corresponds to (121) crystal plane) [33].

$$L = \frac{K\lambda}{\beta Cos\theta} \qquad (7.1)$$

where K is the dimensionless shape factor, λ is the wavelength of the Cu K_α radiation, β is the crystallite size contribution to the peak width (integral or full width at half maximum) in radians, and θ is the Bragg angle. The crystallite size of the prepared $BiVO_4$ is displayed in table 7.1.

The XRD patterns of CND shows a characteristic broad peak centered at around 24.8° and another broad but much less intense peak at around 43.7° with corresponding

interlayer spacing of 0.3585 and 0.2051 nm respectively. The peak at 24.8° can be assigned to the (002) planes of graphite [34]. The XRD of WO_3 is shown in figure 7.1d, the diffraction peaks at 2θ = 14.1, 22.9, 28.2, 36.5, 49.9 and 55.4° correspond to the (100), (001), (200), (201), (220) and (221) crystal planes respectively of the hexagonal structure of WO_3 (JCPDS card No. 75-2187) [35, 36].

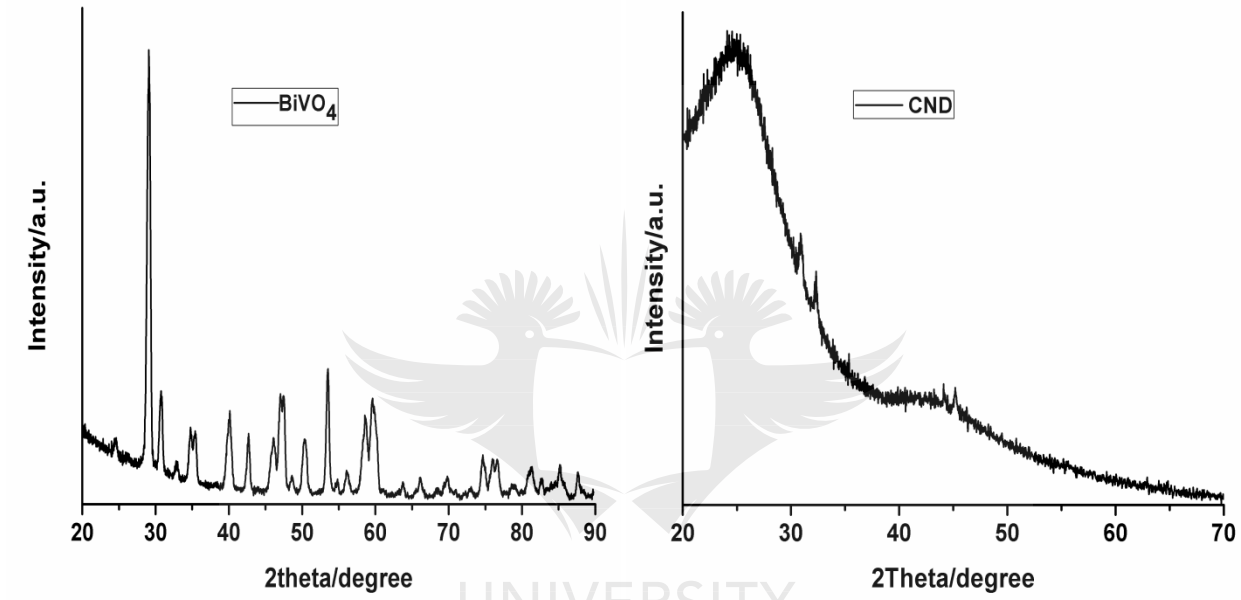

a) b)

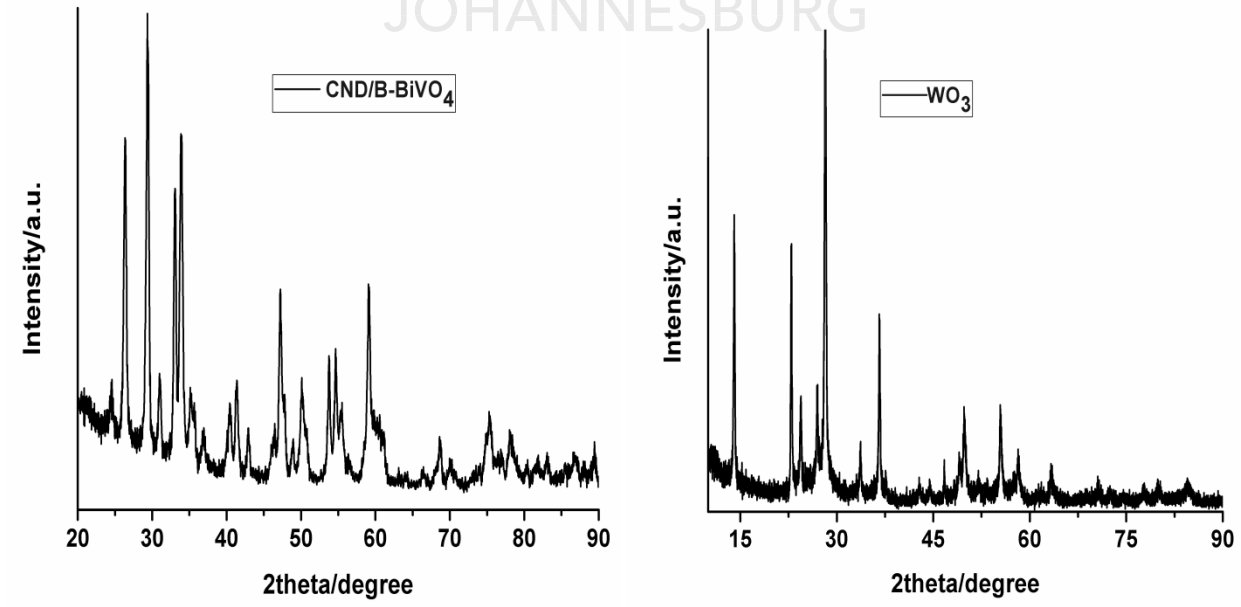

c) **d)**

Fig. 7. 1. Powder XRD patterns of a) $BiVO_4$, b) CND, c) CND/B-$BiVO_4$ and d) WO_3

7.3.2 FTIR spectroscopy

The FTIR spectra of the anodic materials are displayed in Figure 7.2. The characteristic peak of $BiVO_4$ can be seen at around 732 cm^{-1} (Fig. 7.2a). This strong band is due to the stretching of the V-O bond in the semiconductor [37, 38]. The spectrum of CND is displayed in Fig. 7.2b, the IR bands are at 1164, 1587, 2914 and 3415 cm^{-1} which may be attributed to C-O bond stretch, C-C double bond stretch, C-H stretch and O-H stretch of adsorbed water molecules respectively [39, 40]. The spectrum of the composite material shows the peaks of the constituents (FIg. 7.2c). The bands depicting the presence of CND are much less intense compared to the characteristic peak of $BiVO_4$. This may be correlated to the small amount of the carbon material in the composite. The spectrum of WO_3 shown in Fig. 7.2d has IR peaks centered at 770, 1414, 1601, 2962 and 3433 cm^{-1}. The broad band at around 770 cm^{-1} can be assigned to the W-O stretch while the bands at 1414 and 3433 cm^{-1} can be indexed to the O-H bending and stretching modes respectively, of the adsorbed water molecules [41, 42].

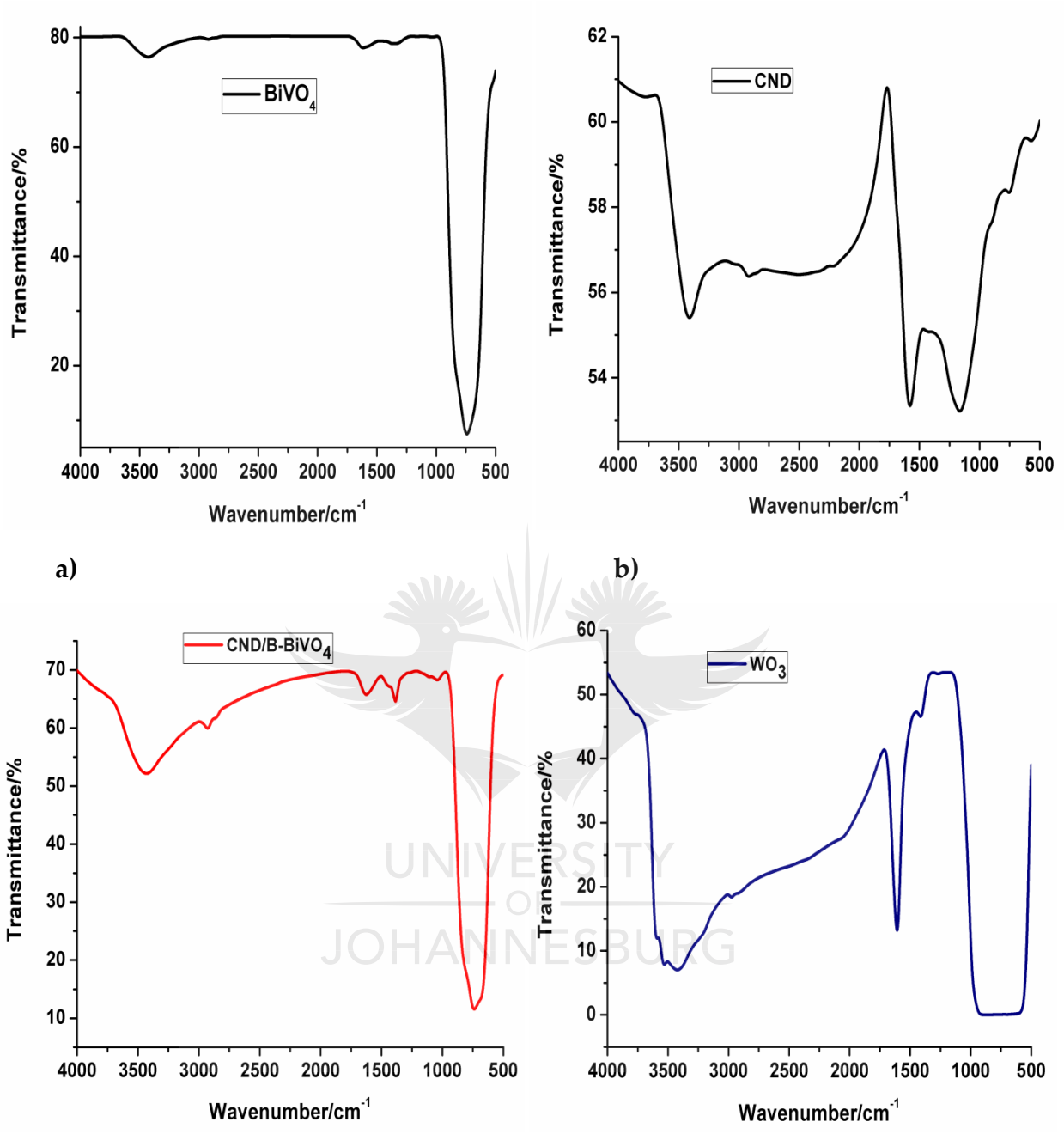

Fig. 7. 2. FTIR spectra of a) $BiVO_4$, b) CND, c) CND/B-$BiVO_4$ and d) WO_3

7.3.3 Raman spectroscopy

The Raman spectra of $BiVO_4$, CND, CND/B-$BiVO_4$ and WO_3 are shown in Figure 7.3. The spectrum of $BiVO_4$ (Fig. 7.3a) displays a well-defined and intense peak at 828 cm^{-1} which corresponds to the symmetric stretching of the V-O bond [43]. The weak shoulder at 709 cm^{-3} can be assigned to the anti-symmetric stretching mode of the V-O bond [44]. The bands at 364 and 325 cm^{-1} can be attributed to the symmetric and antisymmetric bending modes of the VO_4 tetrahedrons while the band at 212 cm^{-1} can be assigned to external rotation modes [45, 46]. Figure 7.3b shows the spectrum of CND with the G and D bands centered at 1570 and 1343 cm^{-1} respectively. The ratio of the intensity of D band to the intensity of G band (D_I/G_I) is approximately unity. This indicates that there is a significant amount of defects in the CND. Figure 7.3d shows the Raman peaks of pure WO_3 nanorods. The strong and intense band centered at 780 cm^{-1} can be assigned to the stretching of the W-O bonds in the metal oxide. The band at 287 cm^{-1} is due to the bending mode of W-O bond.

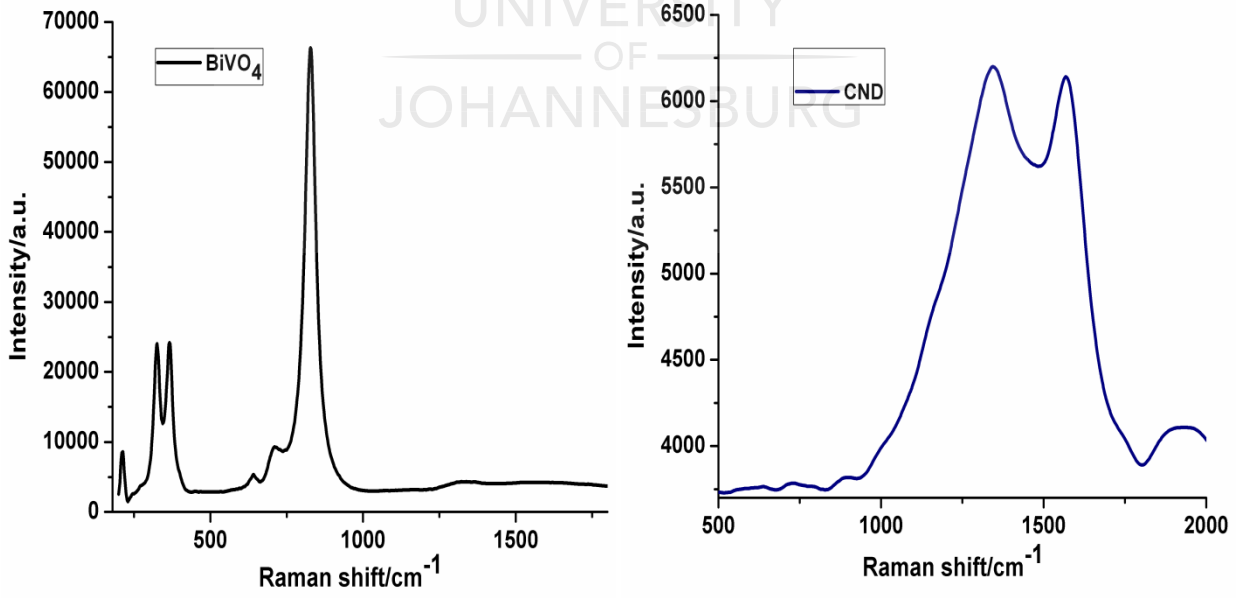

a) b)

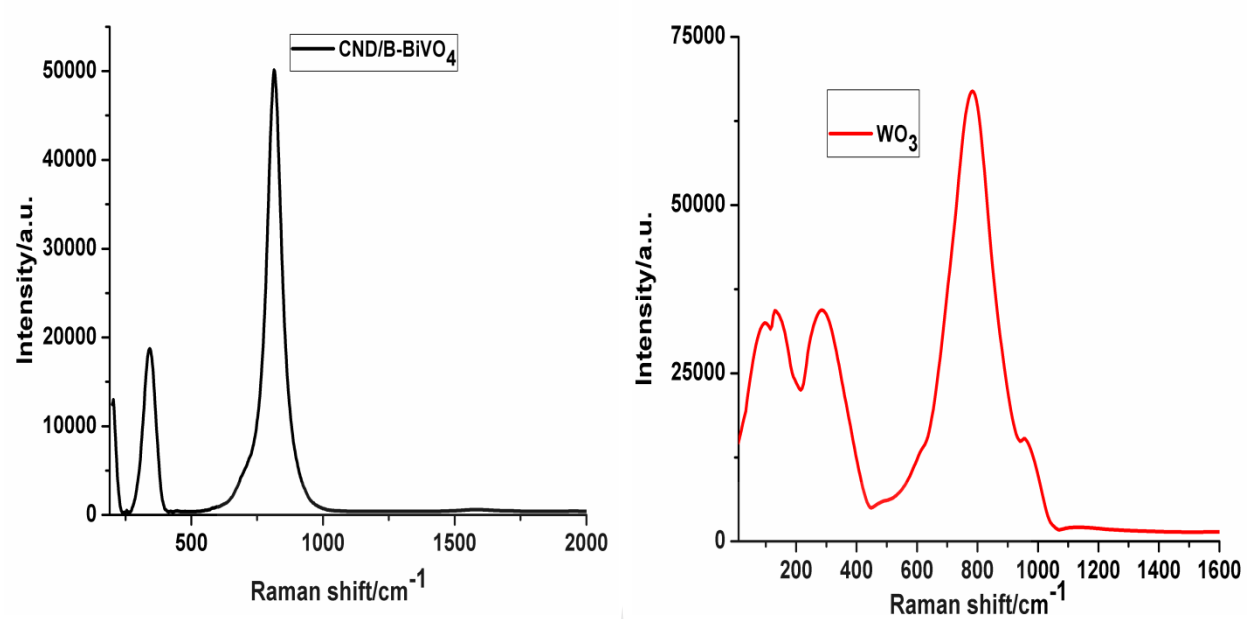

c) d)

Fig. 7. 3. Raman spectra of a) $BiVO_4$, b)CND, c) CND/B-$BiVO_4$ and d) WO_3

7.3.4 Diffuse reflectance spectroscopy

Diffuse reflectance spectroscopy (DRS) is a valuable technique that can be used to gain insights into the electronic states of semiconducting materials. The UV-Vis absorption spectra of $BiVO_4$, WO_3 and CND/B-$BiVO_4$ are shown in figure 7.4. The intrinsic absorption bands of both the pristine $BiVO_4$ and doped $BiVO_4$ span over UV and visible light regions. The doped $BiVO_4$ demonstrates superior visible light absorption compared to pristine $BiVO_4$. In addition, the absorption edge of the CND and B co-doped $BiVO_4$ can be seen to exhibit red-shift. The extension of the absorption edge of the doped material may be as a result of band transitions occurring due to the presence of impurities in the forbidden band [47]. The spectrum of WO_3 shows that the semiconductor exhibits photoabsorption above 400 nm which is in agreement with earlier reports [48, 49].

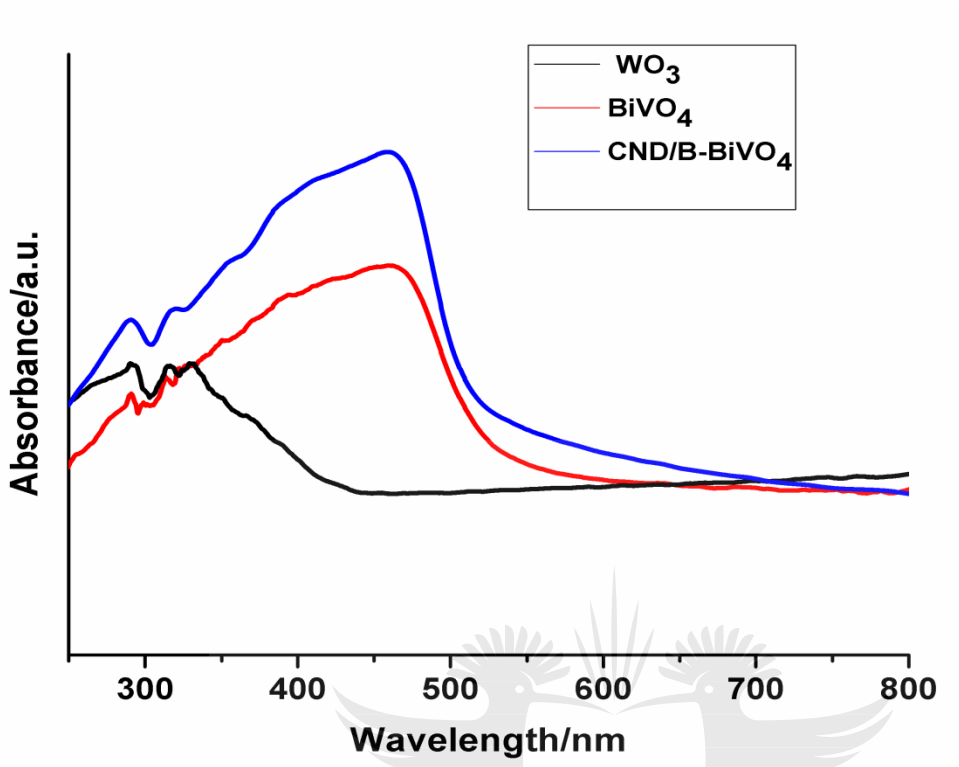

Fig. 7. 4. UV-Vis absorption spectra of $BiVO_4$, WO_3 and CND/B-$BiVO_4$

7.3.5 BET surface area analysis

Nitrogen adsorption-desorption experiment was carried out to determine the BET surface area of the anodic materials. The adsorption isotherms of $BiVO_4$, CND, CND/B-$BiVO_4$ and WO_3 are presented in figure 7.5. and the specific BET surface area can be found in table 7.1. From the values of the BET surface area, it is clear that incorporation of CND into the lattices of $BiVO_4$ lead to increase in the surface area of the photocatalyst. Improved surface area is advantageous for the interaction of the organic pollutant with the photocatalyst and this will aid overall degradation efficiency. Similarly, the comparatively high BET surface area of WO_3 nanorods will contribute

significantly to the adsorption capability of the heterojunction photoanode, this will enhance its catalytic performance.

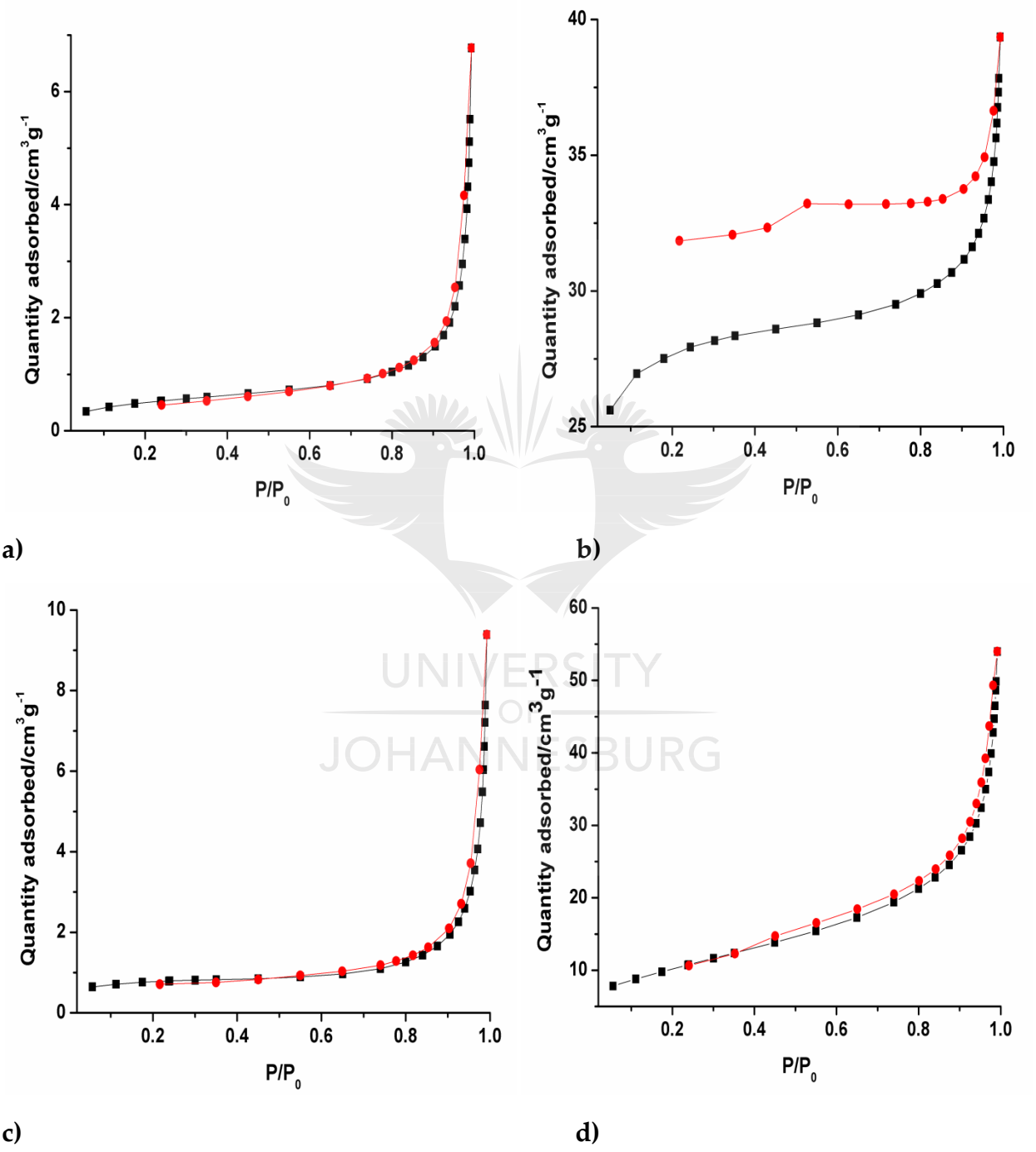

Fig. 7. 5. Nitrogen adsorption-desorption isotherms of a) Pristine $BiVO_4$, b) CND c) CND/B-$BiVO_4$ and d) WO_3

Table 7.1 Some physical properties of pristine $BiVO_4$, CND, doped $BiVO_4$ and WO_3

Sample	BET Surface area/m^2g^{-1}	Average Crystallite size/nm
$BiVO_4$	1.81	42
CND	84.32	4
CND/B-$BiVO_4$	2.49	-
WO_3	36.26	-

7.3.6 Morphology investigation, EDS analysis and elemental mapping

The SEM and TEM images, EDS spectra and element maps are presented in figure 7.6. From the SEM image of pristine $BiVO_4$ (Fig. 7.6a), it can be observed that the nanoparticles formed, to a large extent, have uniformly distributed sizes. The particles are seen to be closely packed. The EDS spectrum (Fig. 7.6b) of $BiVO_4$ reveals the constituent elements of the catalyst. The SEM image (Fig. 7.6c) of the doped $BiVO_4$ shows the morphology characteristic of a composite material. It has no regular structure or shape, but the constituents can be seen to be well integrated. The EDS spectrum (Fig. 7.6d) shows the presence of B, although it has a very low intensity owing to its very low concentration compared with the other component elements. The elemental map (Fig. 7.6e) further confirms the presence of B in the nanocomposite, with the element uniformly distributed within the material. The SEM image (Fig. 7.6g) of the WO_3 prepared shows that the material has rod morphology, with many clusters. The TEM image at 1 μm (Fig. 7.6i) reveals that the rods are of different lengths, but the diameter can be seen to be essentially the same.

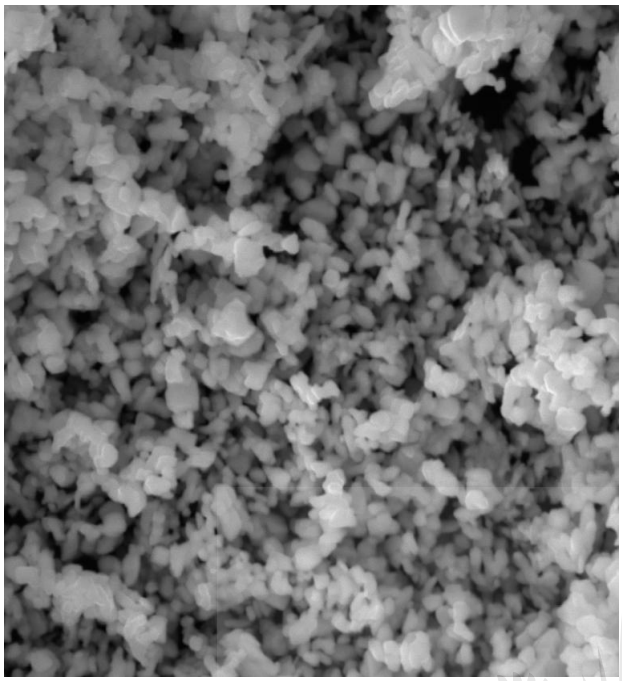

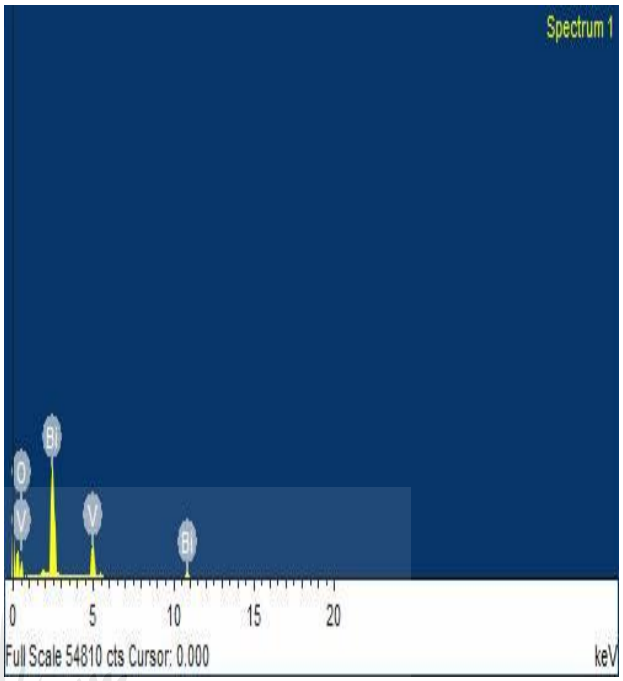

a) b)

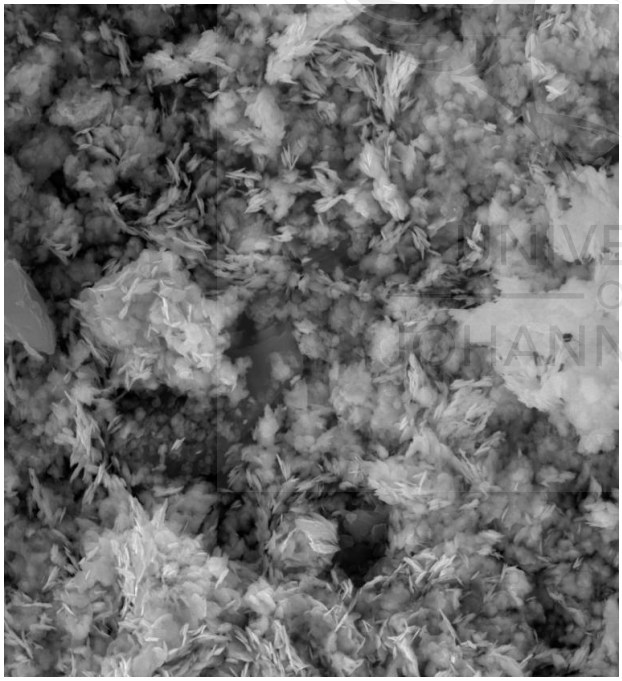

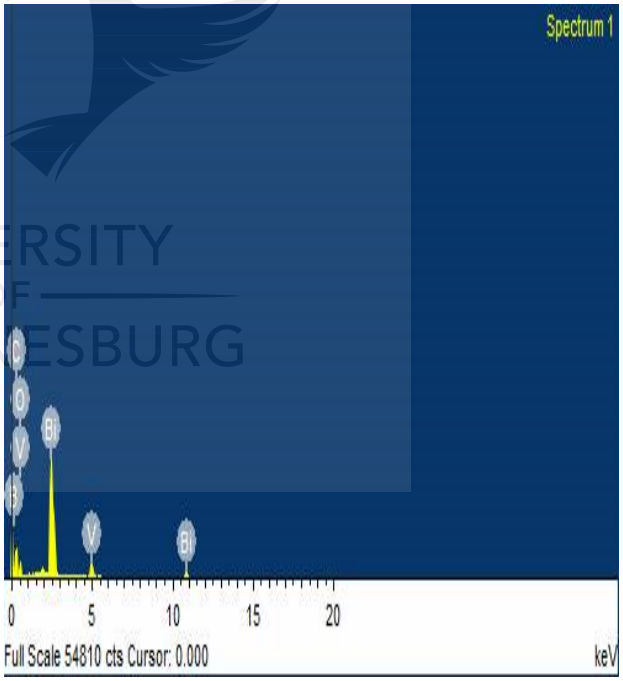

c) d)

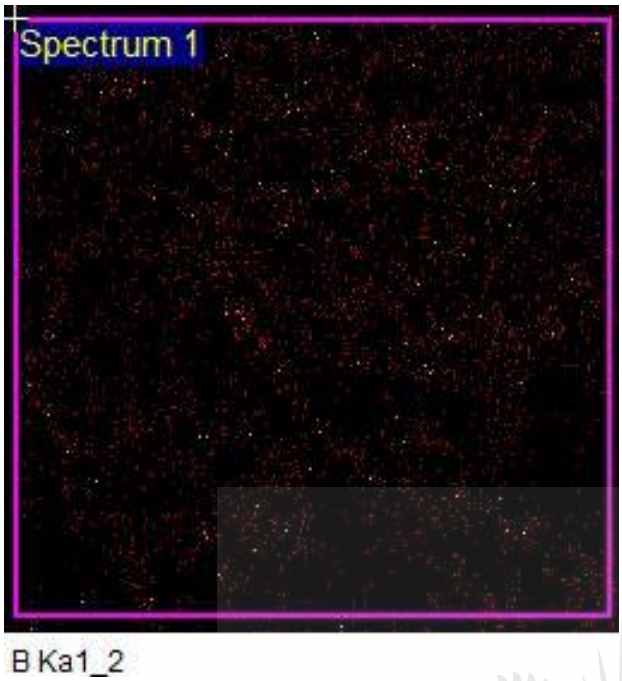
Spectrum 1
B Ka1_2

e)

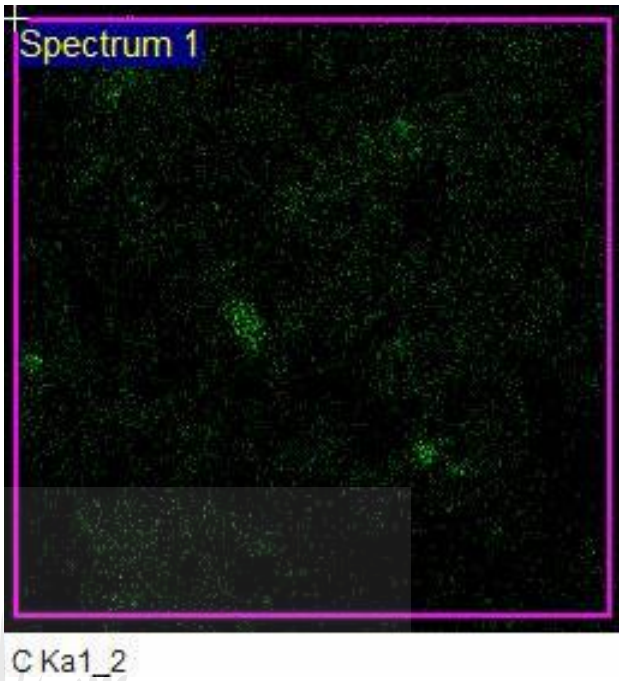
Spectrum 1
C Ka1_2

f)

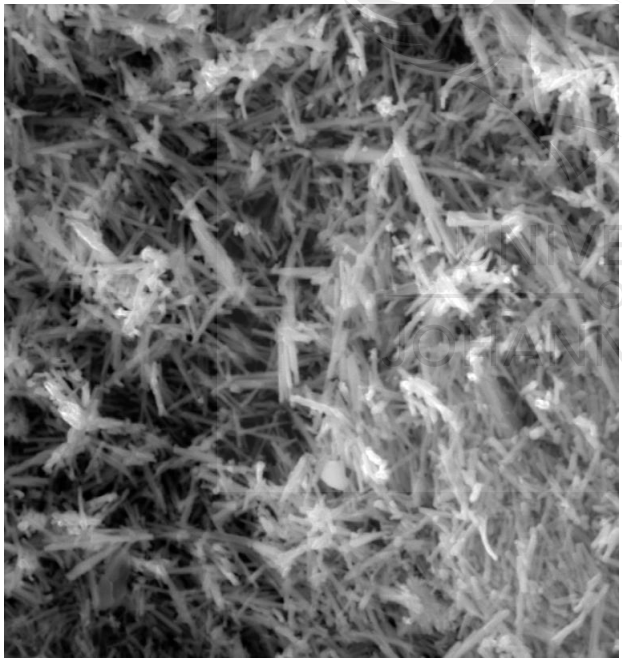

g)

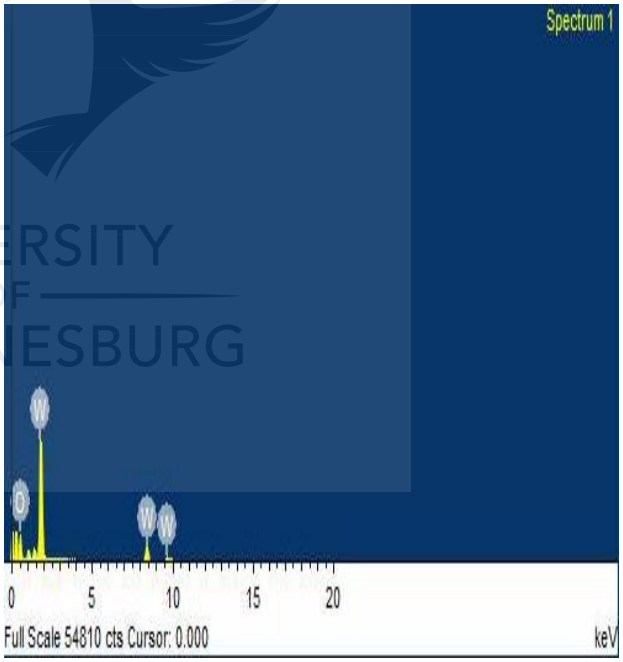
Spectrum 1
O
W
W
W
0
5
10
15
20
Full Scale 54810 cts Cursor: 0.000
keV

h)

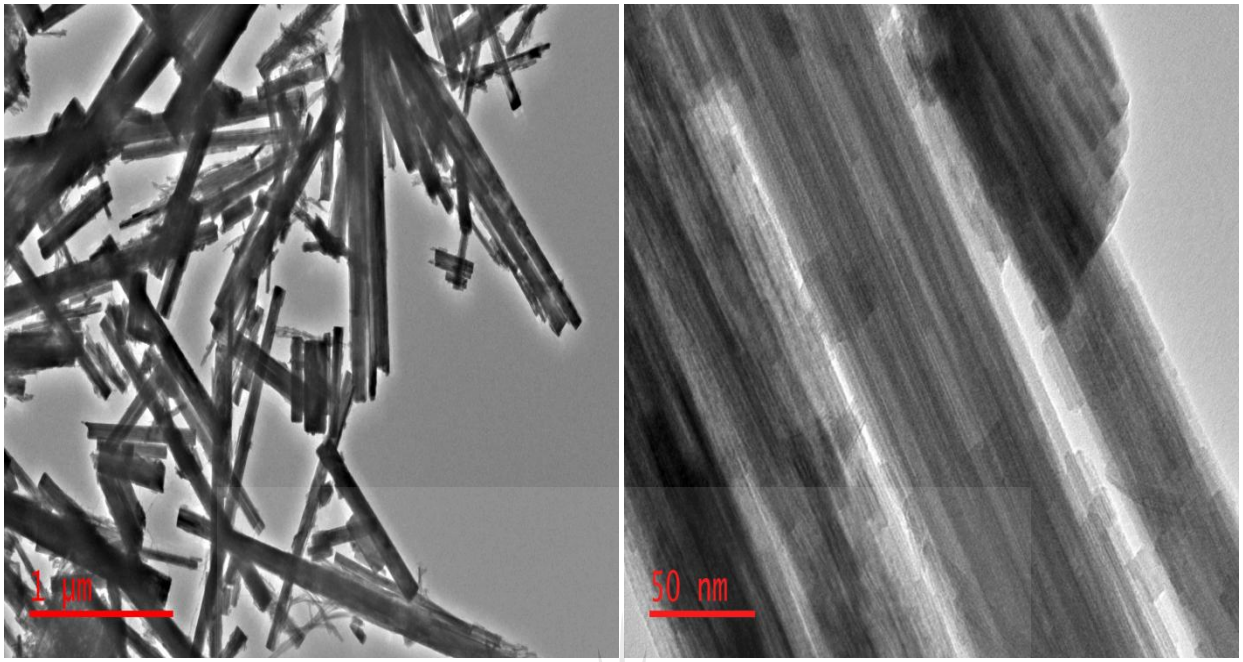

i) j)

Fig. 7. 6. a) SEM image $BiVO_4$, b) EDS spectrum of $BiVO_4$, c) SEM image of CND/B-$BiVO_4$, d) EDS spectrum of CND/B-$BiVO_4$, Elemental maps for e) B and f) C, g) SEM image of WO_3, h) EDS spectrum of WO_3, i & f) TEM images of WO_3

7.3.7 Linear sweep voltammetry and photo-current response

The linear sweep voltammograms of the fabricated photoanodes were obtained in the dark and in the presence of light. As shown in figure 7.7a, the current responses of both CND/B-$BiVO_4$ and CND/B-$BiVO_4$/WO_3 in the dark are not significantly different until reaching the potential of about 1.2 V, with the bi-component electrode displaying a slightly higher current than the doped $BiVO_4$ electrode. Apparently, the presence of WO_3 contributed to the current signal of the bi-component electrode. It is well known that WO_3 exhibit better charge-transfer property than $BiVO_4$ [50, 51]. In the presence of light, the photoanodes showed markedly higher photocurrent than those recorded under dark condition. The significant photocurrent enhancement recorded by the coupled semiconductors anode can be attributed to synergistic effects of the $BiVO_4$ and

WO_3. The excellent charge transport property of the WO_3 and the high visible light activity of the $BiVO_4$ are beneficial for improved photoactivity. In addition, in both doped $BiVO_4$ and coupled electrodes, photocurrent can be seen to increase with increasing anodic potential. This is characteristic of n-type semiconductors.

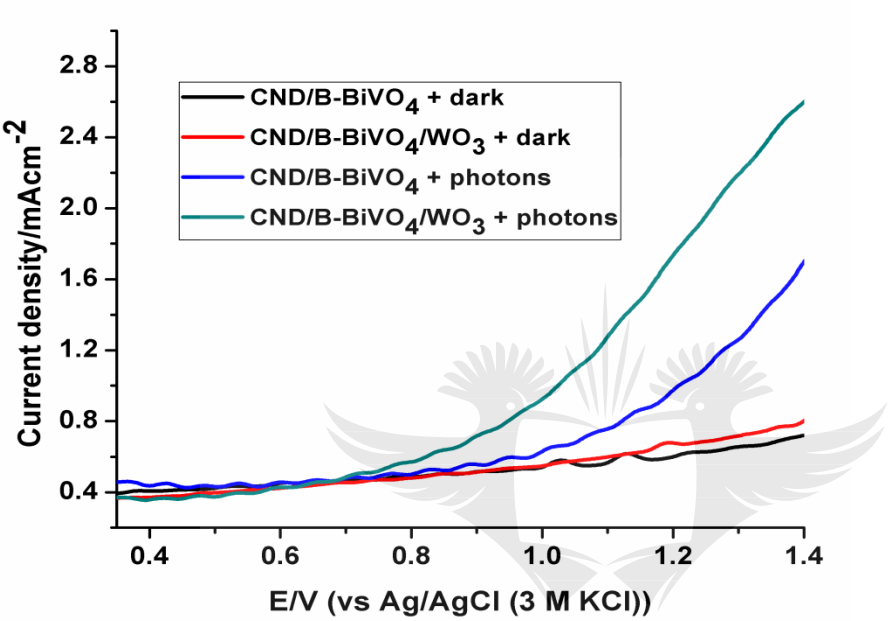

a)

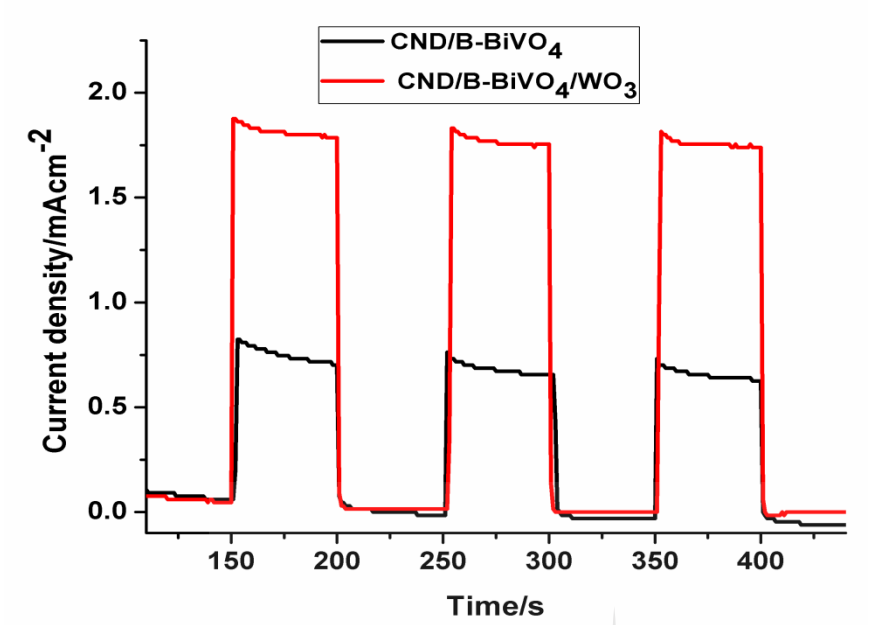

b)

Fig. 7. 7. a) Linear sweep voltammograms of photoanodes measured in 0.1 M Na_2SO_4, b) Photocurrent response of CND/B-$BiVO_4$ and CND/B-$BiVO_4$/WO_3 obtained in 5 mgL^{-1} orange II dye (prepared in 0.1 M Na_2SO_4) at a potential of 1.2 V

7.3.8 Photoelectrocatalytic degradation experiments

The degradation of orange II sodium salt (Fig. 7.8) was carried out at the fabricated electrodes to evaluate their photoelectrocatalytic performance.

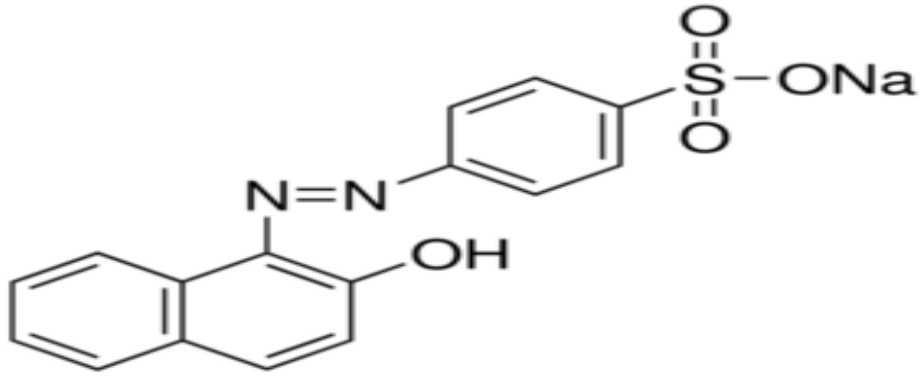

Fig. 7. 8. The chemical structure of Orange II sodium salt.

The oxidation process was performed at applied anodic potential of 2.0 V. And the degradation of the dye was monitored using UV-Vis spectrophotometer at its wavelength of maximum absorption, λ_{max} = 483 nm.

As can be seen in Figure 7.9a, the CND/B-$BiVO_4$/WO_3 electrode exhibited the highest degradation efficiency with 92 % removal of the dye in 3 h of the photoelectrocatalytic process. The performance of the photoanodes follows the order $BiVO_4$ < WO_3 < CND/B-$BiVO_4$ < CND/B-$BiVO_4$/WO_3. The performance of pristine $BiVO_4$ is inferior to that of the pure WO_3 nanorods despite the former being a better absorber of visible light. The poor conductivity and low adsorption capability of $BiVO_4$ are some of the factors responsible for its low photoelectrocatalytic performance. On the other hand, the large surface area of WO_3 and its excellent conductivity are favourable for the degradation of organic pollutants. Notably, the CND and B co-doped $BiVO_4$ showed much more enhanced performance. It has been suggested that interstitial boron doping can increase the number of oxygen vacancies and V^{4+}, leading to red-shifting of the absorption edge (Fig. 7.4) and consequently improved photocatalytic performance in the visible light region [52]. Also, incorporation of CND into the structure of $BiVO_4$ could lead to improved charge transport property and enhanced adsorption capability of the photocatalyst. Apparently, the CND/B-$BiVO_4$/WO_3 performed best because of the synergistic effects of the various constituent materials. The kinetic rate constants obtained by fitting the degradation experimental data into the Langmuir Hinshelwood kinetic model are 0.0924, 0.1812, 0.254 and 0.845 h^{-1} respectively. Figure 7.9b displays the plots of normalised concentration abatement of the dye via photolysis, electrolysis and photocatalysis. It can be seen that the coupled process offers a far more efficient removal of the dye than the individual processes. This observation further affirms the superiority of photoelectrocatalytic oxidation process to both electrochemical oxidation

and photocatalytic oxidation processes. The COD decay after 3 h of the photoelectrocatalytic process at the preferred anode was 58%.

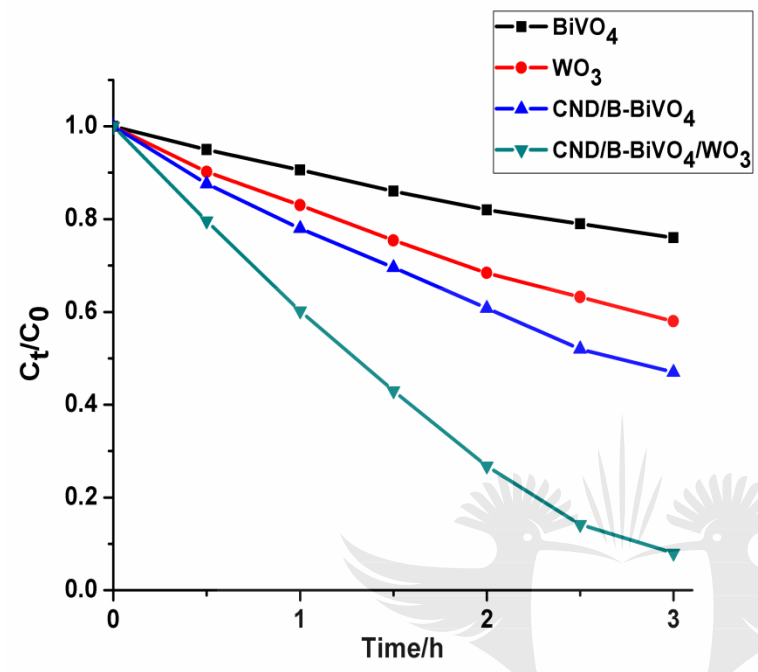

a)

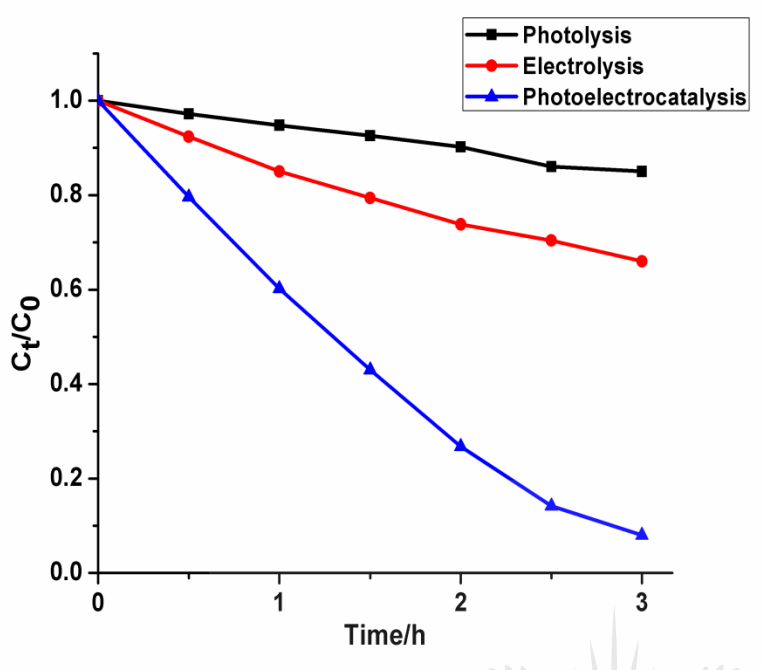

b)

Fig. 7. 9. a) Degradation profiles of orange II sodium salt a) at different photoanodes, b) by different oxidation processes.

7.4 Sub-conclusion

Two visible-light sensitive semiconductors, namely, $BiVO_4$ and WO_3 have been synthesised, characterised and applied for the degradation of a model organic pollutant, orange II dye. The $BiVO_4$ was modified with CND and B to improve its charge transport property and adsorption behaviour so as to increase its photoelectrocatalytic efficiency. The kinetic rate constants calculated for the degradation of the contaminants at $BiVO_4$ and WO_3 photoanodes were 0.0924 and 0.1812 h^{-1} respectively. The much better performance of WO_3 nanorods compared to the undoped $BiVO_4$ may not be unrelated to its morphology which can retard recombination of photogenerated electron-hole pairs. Doping CND and B into the structure of $BiVO_4$ led to significant improvement in its photoelectrocatalytic performance. Coupling the doped $BiVO_4$ to WO_3 yielded a heterostructured anodic material which showed much more excellent properties than

the individual components. The higher performance of this electrode can be linked to the formation of n-n heterojunction which promotes separation of charges and generation of large amount of the valence-bound holes which are needed for the oxidation of the pollutant. This study shows that $BiVO_4$ and WO_3 based anodes have prospects for water remediation via photoelectrocatalysis.

References

[1] M.G. Peleyeju, E.H. Umukoro, L. Tshwenya, R. Moutloali, J.O. Babalola, O.A. Arotiba, Photoelectrocatalytic water treatment systems: degradation, kinetics and intermediate products studies of sulfamethoxazole on a TiO_2–exfoliated graphite electrode, RSC Advances 7 (2017) 40571-40580.

[2] Y. Zhang, X. Xiong, Y. Han, X. Zhang, F. Shen, S. Deng, H. Xiao, X. Yang, G. Yang, H. Peng, Photoelectrocatalytic degradation of recalcitrant organic pollutants using TiO_2 film electrodes: an overview, Chemosphere 88 (2012) 145-154.

[3] S. Garcia-Segura, E. Brillas, Applied photoelectrocatalysis on the degradation of organic pollutants in wastewaters, Journal of Photochemistry and Photobiology C: Photochemistry Reviews (2017).

[4] Z. He, Y. Shi, C. Gao, L. Wen, J. Chen, S. Song, BiOCl/$BiVO_4$ p–n heterojunction with enhanced photocatalytic activity under visible-light irradiation, The Journal of Physical Chemistry C 118 (2013) 389-398.

[5] Y. Sun, B. Qu, Q. Liu, S. Gao, Z. Yan, W. Yan, B. Pan, S. Wei, Y. Xie, Highly efficient visible-light-driven photocatalytic activities in synthetic ordered monoclinic $BiVO_4$ quantum tubes–graphene nanocomposites, Nanoscale 4 (2012) 3761-3767.

[6] M. Shang, W. Wang, S. Sun, J. Ren, L. Zhou, L. Zhang, Efficient visible light-induced photocatalytic degradation of contaminant by spindle-like PANI/$BiVO_4$, The Journal of Physical Chemistry C 113 (2009) 20228-20233.

[7] Y. Geng, P. Zhang, N. Li, Z. Sun, Synthesis of Co doped $BiVO_4$ with enhanced visible-light photocatalytic activities, Journal of Alloys and Compounds 651 (2015) 744-748.

[8] J. Sun, Y. Guo, Y. Wang, D. Cao, S. Tian, K. Xiao, R. Mao, X. Zhao, H_2O_2 assisted photoelectrocatalytic degradation of diclofenac sodium at gC_3N_4/$BiVO_4$ photoanode under visible light irradiation, Chemical Engineering Journal (2017).

[9] V. Cristino, S. Marinello, A. Molinari, S. Caramori, S. Carli, R. Boaretto, R. Argazzi, L. Meda, C.A. Bignozzi, Some aspects of the charge transfer dynamics in nanostructured WO_3 films, Journal of Materials Chemistry A 4 (2016) 2995-3006.

[10] L. Huang, H. Xu, Y. Li, H. Li, X. Cheng, J. Xia, Y. Xu, G. Cai, Visible-light-induced WO_3/gC_3 N_4 composites with enhanced photocatalytic activity, Dalton Transactions 42 (2013) 8606-8616.

[11] S. Yao, F. Qu, G. Wang, X. Wu, Facile hydrothermal synthesis of WO_3 nanorods for photocatalysts and supercapacitors, Journal of Alloys and Compounds 724 (2017) 695-702.

[12] P. Dong, G. Hou, X. Xi, R. Shao, F. Dong, WO_3-based photocatalysts: morphology control, activity enhancement and multifunctional applications, Environmental Science: Nano 4 (2017) 539-557.

[13] B. Weng, J. Wu, N. Zhang, Y.-J. Xu, Observing the role of graphene in boosting the two-electron reduction of oxygen in graphene–WO_3 nanorod photocatalysts, Langmuir 30 (2014) 5574-5584.

[14] Y. Sakai, A. Shimanaka, M. Shioi, S. Kato, S. Satokawa, T. Kojima, A. Yamasaki, Fabrication of high-sensitivity palladium loaded tungsten trioxide photocatalyst by photodeposite method, Catalysis Today 241 (2015) 2-7.

[15] Z.F. Huang, J. Song, L. Pan, X. Zhang, L. Wang, J.J. Zou, Tungsten oxides for photocatalysis, electrochemistry, and phototherapy, Advanced Materials 27 (2015) 5309-5327.

[16] T. Zhang, J. Su, L. Guo, Morphology engineering of WO_3/$BiVO_4$ heterojunctions for efficient photocatalytic water oxidation, CrystEngComm 18 (2016) 8961-8970.

[17] N. Dirany, M. Arab, C. Leroux, S. Villain, V. Madigou, J. Gavarri, Effect of WO_3 nanoparticles morphology on the catalytic properties, Materials Today: Proceedings 3 (2016) 230-234.

[18] B. Ahmed, S. Kumar, A.K. Ojha, P. Donfack, A. Materny, Facile and controlled synthesis of aligned WO_3 nanorods and nanosheets as an efficient photocatalyst material, Spectrochimica Acta Part A: Molecular and Biomolecular Spectroscopy 175 (2017) 250-261.

[19] J. Theerthagiri, R. Senthil, A. Malathi, A. Selvi, J. Madhavan, M. Ashokkumar, Synthesis and characterization of a CuS–WO_3 composite photocatalyst for enhanced visible light photocatalytic activity, RSC Advances 5 (2015) 52718-52725.

[20] J. Zhang, Y. Ma, Y. Du, H. Jiang, D. Zhou, S. Dong, Carbon nanodots/WO_3 nanorods Z-scheme composites: Remarkably enhanced photocatalytic performance under broad spectrum, Applied Catalysis B: Environmental 209 (2017) 253-264.

[21] L. Xia, J. Bai, J. Li, Q. Zeng, X. Li, B. Zhou, A highly efficient $BiVO_4$/WO_3/W heterojunction photoanode for visible-light responsive dual photoelectrode photocatalytic fuel cell, Applied Catalysis B: Environmental 183 (2016) 224-230.

[22] S. Ho-Kimura, S.J. Moniz, A.D. Handoko, J. Tang, Enhanced photoelectrochemical water splitting by nanostructured $BiVO_4$–TiO_2 composite electrodes, Journal of Materials Chemistry A 2 (2014) 3948-3953.

[23] E.S. Kim, H.J. Kang, G. Magesh, J.Y. Kim, J.-W. Jang, J.S. Lee, Improved photoelectrochemical activity of $CaFe_2O_4$/$BiVO_4$ heterojunction photoanode by reduced surface recombination in solar water oxidation, ACS applied materials & interfaces 6 (2014) 17762-17769.

[24] S. Wang, J.-H. Yun, B. Luo, T. Butburee, P. Peerakiatkhajohn, S. Thaweesak, M. Xiao, L. Wang, Recent progress on visible light responsive heterojunctions for photocatalytic applications, Journal of Materials Science & Technology 33 (2017) 1-22.

[25] Y.-J. Yuan, F. Wang, B. Hu, H.-W. Lu, Z.-T. Yu, Z.-G. Zou, Significant enhancement in photocatalytic hydrogen evolution from water using a MoS_2 nanosheet-coated ZnO heterostructure photocatalyst, Dalton Transactions 44 (2015) 10997-11003.

[26] L. Xia, J. Bai, J. Li, Q. Zeng, L. Li, B. Zhou, High-performance $BiVO_4$ photoanodes cocatalyzed with an ultrathin α-Fe_2O_3 layer for photoelectrochemical application, Applied Catalysis B: Environmental 204 (2017) 127-133.

[27] A.S. Martins, L. Nuñez, M.R. de Vasconcelos Lanza, Enhanced photoelectrocatalytic performance of TiO_2 nanotube array modified with WO_3 applied to the degradation of the endocrine disruptor propyl paraben, Journal of Electroanalytical Chemistry 802 (2017) 33-39.

[28] Z. Wei, F. Liang, Y. Liu, W. Luo, J. Wang, W. Yao, Y. Zhu, Photoelectrocatalytic degradation of phenol-containing wastewater by TiO 2/gC_3N_4 hybrid heterostructure thin film, Applied Catalysis B: Environmental 201 (2017) 600-606.

[29] Q. Zeng, J. Li, L. Li, J. Bai, L. Xia, B. Zhou, Synthesis of WO_3/$BiVO_4$ photoanode using a reaction of bismuth nitrate with peroxovanadate on WO_3 film for efficient photoelectrocatalytic water splitting and organic pollutant degradation, Applied Catalysis B: Environmental (2017).

[30] P. Chatchai, A.Y. Nosaka, Y. Nosaka, Photoelectrocatalytic performance of WO_3/$BiVO_4$ toward the dye degradation, Electrochimica Acta 94 (2013) 314-319.

[31] Y. Liu, B. Huang, Y. Dai, X. Zhang, X. Qin, M. Jiang, M.-H. Whangbo, Selective ethanol formation from photocatalytic reduction of carbon dioxide in water with $BiVO_4$ photocatalyst, Catalysis Communications 11 (2009) 210-213.

[32] Y. Yan, S. Sun, Y. Song, X. Yan, W. Guan, X. Liu, W. Shi, Microwave-assisted in situ synthesis of reduced graphene oxide-$BiVO_4$ composite photocatalysts and their enhanced photocatalytic performance for the degradation of ciprofloxacin, Journal of hazardous materials 250 (2013) 106-114.

[33] M. Wang, H. Zheng, Q. Liu, C. Niu, Y. Che, M. Dang, High performance B doped $BiVO_4$ photocatalyst with visible light response by citric acid complex method, Spectrochimica Acta Part A: Molecular and Biomolecular Spectroscopy 114 (2013) 74-79.

[34] M. Peleyeju, E. Umukoro, J. Babalola, O. Arotiba, Electrochemical Degradation of an Anthraquinonic Dye on an Expanded Graphite-Diamond Composite Electrode, Electrocatalysis 7 (2016) 132-139.

[35] S. Adhikari, D. Sarkar, High efficient electrochromic WO_3 nanofibers, Electrochimica Acta 138 (2014) 115-123.

[36] L.J. Zhang, S. Li, B.K. Liu, D.J. Wang, T.F. Xie, Highly efficient CdS/WO_3 photocatalysts: Z-scheme photocatalytic mechanism for their enhanced photocatalytic H2 evolution under visible light, ACS Catalysis 4 (2014) 3724-3729.

[37] I. Khan, S. Ali, M. Mansha, A. Qurashi, Sonochemical assisted hydrothermal synthesis of pseudo-flower shaped Bismuth vanadate ($BiVO_4$) and their solar-driven water splitting application, Ultrasonics Sonochemistry 36 (2017) 386-392.

[38] F. Chen, Q. Yang, Y. Wang, J. Zhao, D. Wang, X. Li, Z. Guo, H. Wang, Y. Deng, C. Niu, Novel ternary heterojunction photcocatalyst of Ag nanoparticles and gC 3 N 4 nanosheets co-modified $BiVO_4$ for wider spectrum visible-light photocatalytic degradation of refractory pollutant, Applied Catalysis B: Environmental 205 (2017) 133-147.

[39] H. Xu, L. Yan, V. Nguyen, Y. Yu, Y. Xu, One-step synthesis of nitrogen-doped carbon nanodots for ratiometric pH sensing by femtosecond laser ablation method, Applied Surface Science 414 (2017) 238-243.

[40] X. Wen, L. Shi, G. Wen, Y. Li, C. Dong, J. Yang, S. Shuang, Green synthesis of carbon nanodots from cotton for multicolor imaging, patterning, and sensing, Sensors and Actuators B: Chemical 221 (2015) 769-776.

[41] S. Zhang, H. Li, Z. Yang, Controllable synthesis of WO_3 with different crystalline phases and its applications on methylene blue removal from aqueous solution, Journal of Alloys and Compounds (2017).

[42] J. Sun, X. Shu, Y. Tian, Z. Tong, S. Bai, R. Luo, D. Li, A. Chen, Preparation of polypyrrole@ WO_3 hybrids with pn heterojunction and sensing performance to

triethylamine at room temperature, Sensors and Actuators B: Chemical 238 (2017) 510-517.

[43] Z.J. Zhang, Q.C. Zheng, L. Sun, Synthesis of 2-D nanostructured $BiVO_4$: Ag hybrid as an efficient electrode material for supercapacitors, Ceramics International (2017).

[44] K. Trzciński, M. Szkoda, K. Siuzdak, M. Sawczak, A. Lisowska-Oleksiak, Enhanced photoelectrochemical performance of inorganic–organic hybrid consisting of $BiVO_4$ and PEDOT: PSS, Applied Surface Science 388 (2016) 753-761.

[45] A. Zhang, J. Zhang, The effect of hydrothermal temperature on the synthesis of monoclinic bismuth vanadate powders, Mater. Sci.-Poland 27 (2009) 1015-????.

[46] L. Tang, J.-j. Wang, C.-t. Jia, G.-x. Lv, G. Xu, W.-t. Li, L. Wang, J.-y. Zhang, M.-h. Wu, Simulated solar driven catalytic degradation of psychiatric drug carbamazepine with binary $BiVO_4$ heterostructures sensitized by graphene quantum dots, Applied Catalysis B: Environmental 205 (2017) 587-596.

[47] F. Li, L. Zhang, X. Chen, Y. Liu, S. Xu, S. Cao, Synergistically enhanced photocatalytic reduction of CO_2 on N–Fe codoped $BiVO_4$ under visible light irradiation, Physical Chemistry Chemical Physics 19 (2017) 21862-21868.

[48] J. Luo, X. Zhou, L. Ma, X. Xu, Enhanced visible-light-driven photocatalytic activity of WO_3/BiOI heterojunction photocatalysts, Journal of Molecular Catalysis A: Chemical 410 (2015) 168-176.

[49] L. Cui, X. Ding, Y. Wang, H. Shi, L. Huang, Y. Zuo, S. Kang, Facile preparation of Z-scheme WO_3/gC_3N_4 composite photocatalyst with enhanced photocatalytic performance under visible light, Applied Surface Science 391 (2017) 202-210.

[50] S.J. Hong, S. Lee, J.S. Jang, J.S. Lee, Heterojunction $BiVO_4$/WO_3 electrodes for enhanced photoactivity of water oxidation, Energy & Environmental Science 4 (2011) 1781-1787.

[51] M.G. Lee, D.H. Kim, W. Sohn, C.W. Moon, H. Park, S. Lee, H.W. Jang, Conformally coated $BiVO_4$ nanodots on porosity-controlled WO_3 nanorods as highly efficient type II heterojunction photoanodes for water oxidation, Nano Energy 28 (2016) 250-260.
[52] M. Wang, Y. Che, C. Niu, M. Dang, D. Dong, Effective visible light-active boron and europium co-doped $BiVO_4$ synthesized by sol–gel method for photodegradion of methyl orange, Journal of hazardous materials 262 (2013) 447-455.

CHAPTER EIGHT

8.0 CONCLUSION AND RECOMMENDATION

8.1 Conclusion

This dissertation sought to investigate the electro-oxidation/degradation of organic contaminants at anodes fabricated from diamond (and some other forms of carbon) and metal oxide semiconductors.

Diamond particles were trapped in the layers of exfoliated graphite and the resulting composite was fabricated into electrodes. Characterisations of the materials confirmed their identities. The composite electrode was effective for the decontamination of water polluted by synthetic dyes. Bulk electrolysis in SO_4^{2-} supported cell yielded better mineralisation than the Cl^- containing cell. The latter however yielded faster decolourisation. In essence, EG-diamond is a promising composite material for anodic oxidation of organic contaminants in water.

Furthermore, a composite of diamond, graphene and polyaniline was also synthesised and applied for the electro-oxidation of 2,4-dichlorophenol for the first time. The composite modifier exhibited excellent electrocatalytic properties. A nanocomposite of graphene and PANI gave an impressive current signal but displayed a significant background current. Electro-oxidation of the analyte at the ternary modifier, however, gave a very low background current. In addition, fouling of the ternary platform was very minimal. Therefore, the cheap, easy-to-prepare and stable diamond-based electrode modifier offers an opportunity for rapid and sensitive monitoring of phenolic compounds in water samples.

A nanocomposite comprising TiO_2 and EG was synthesised by sol-gel and microwave techniques. The photoanode fabricated from the material showed excellent performance

for the degradation of an emerging pollutant, sulfamethoxazole. Photoelectrocatalytic oxidation was superior to electrochemical oxidation in removing the antibiotic from the simulated wastewater. The LC-MS analysis of the degraded solutions revealed that generated hydroxyl radicals played significant roles in the degradation process.

To further explore semiconductor-based anodes for water purification, a photoelectrocatalytic water treatment system equipped with a novel $BiVO_4$ nanocomposite anode was utilised for remediation of dye-contaminated water. The visible-light sensitive anode showed significant photoactivity and proved to be very effective for the degradation of the pollutant. This anode has huge potential for large-scale application given its performance with relatively large quantity of laboratory sample experimented with in this study.

In conclusion, this work has shown that anodes fabricated using low-cost carbon materials and metal oxide semiconductors can be utilised for monitoring and removing organic pollutants from water via electrochemical and photoelectrocatalytic processes.

8.2 Recommendations

Diamond-based anodes are not only effective and efficient for the degradation of organic contaminants, but are also excellent and reliable tools for the determination of a wide range of analytes. Given the performance, easy preparation method and low cost of the EG-diamond utilised in this study, its further application for anodic oxidation of other emerging contaminants and even electrochemical detection of chemical and biological analytes is recommended. Furthermore, diamond and graphene composites of varied sp^3 and sp^2 components can be considered as platforms for the electrochemical detection of priority contaminants. Such composites may present exciting

electrocatalytic properties. In addition, studies can be carried out to improve the selectivity of the diamond and graphene based sensor towards phenols determination.

Coupling of anodic oxidation and photocatalysis is one of the upcoming advanced oxidation processes that holds tremendous promise for remediation of water contaminated by organic substances. Anodic materials which are capable of utilising a large fraction of sunlight for this process are still being developed. EG-TiO_2 and $BiVO_4$ nanocomposite can be further explored for this purpose. Reports on the development and application of diamond and semiconductors composites for photoelectrocatalytic degradation of organic pollutants are very limited. It is recommended that doped diamond and semiconductors can be composited and studied for their photoelectrocatalytic performance. Furthermore, a nanocomposite of $BiVO_4$ and WO_3 can be further investigated for the oxidation of more organic substances. Further modification of $BiVO_4$ can be attempted to improve its conductivity and adsorption capability. In addition, research efforts can be geared towards the synthesis of WO_3 to obtain morphologies with desirable characteristics for photoelectrocatalytic applications.